

University of Nottingham
School of Physics & Astronomy



University of
Nottingham
UK | CHINA | MALAYSIA

**Investigation of the Electrical Properties of
Transparent Conductive Oxides Thin
Semiconductor Films Grown by Various
Techniques**

by

FAISAL S. AL MASHARY

M. Sc (Physics)

Thesis submitted to University of Nottingham
for the degree of Doctor of Philosophy
March 2019

ABSTRACT

The main motivation of this thesis was to investigate the electrical properties of In-doped TiO₂, Er-doped TiO₂ and Er-doped In₂O₃ thin films.

The effect of the growth techniques on the structural, electrical and optical properties of In-doped TiO₂ thin films grown by pulsed laser deposition (PLD) and sputtering techniques were investigated. X-ray diffraction (XRD) and Raman revealed both rutile and anatase phases for the sputtered samples whereas only the anatase phase was observed for the PLD samples. Photoluminescence (PL) spectra unveiled several peaks which were explained by defect related optical transitions. The PLD samples were found to have better electrical properties and lower number of electrically active defects than those of the sputtered samples.

The structural, optical and electrical properties of In-doped TiO₂ grown on (100) and (311)B GaAs substrates by PLD were investigated. In doping was found to adversely affect the electrical properties of (100) samples, whereas it enhanced those of (311)B samples. XRD and PL measurements showed that samples grown on (311)B planes have better crystallographic properties when compared to samples grown on the conventional (100) plane. Two shallow defects were detected in all samples except for sample 15 (311)B where three shallow defects were observed. A red-shifted emission was also observed in sample 15 (311)B which was due to the presence of more shallow defects in this sample as compared to the other samples. As there is no significant difference in the electrical properties, it could be concluded that sample 15 (311)B is the best among all samples investigated in this work due to the red-shift that makes it more suitable for solar cell applications as compared to the other samples.

ABSTRACT

Er-doped TiO₂ thin films (Er:TiO₂ TFs) have also been grown on p-type silicon substrates via a combination of an easy sol-gel process and spin coating technique. The obtained results provide strong evidence that Er doping improve the electrical properties and annihilates oxygen-related defects, especially for the highly doped samples. Hence, an enhancement in the sensitivity of UV detectors for Er doped samples is expected.

In₂O₃ and Er doped In₂O₃ (Er:In₂O₃) thin films were grown on p-type Si (100) substrates by a spin-on technique. It was found that the less doped sample has the lowest leakage current density and better electrical properties while the undoped In₂O₃ sample has the highest leakage current density. It was also found that as the atomic fraction of Er increases, the reverse current density increases. The undoped In₂O₃ sample reveals four defects whereas only one defect could be detected in the less doped sample. The removal of oxygen related defects and the improvement of the electrical properties of the doped samples, especially for the less doped sample, would enhance the sensitivity of UV detectors for Er doped samples as compared to the undoped In₂O₃ samples.

PUBLICATIONS

1. Investigation of the Structural, Optical and Electrical Properties of Indium-Doped TiO₂ Thin Films Grown by Pulsed Laser Deposition Technique on Low and High GaAs Planes
Faisal. S. Al mashary, Jorlandio. F. Felix, Sukarno O. Ferreira, Daniele de Souza, Yara. G. Gobato, Jasbinder Chauhan, Natalia Alexeeva, Mohamed Henini, Abdulrahman M. Albadri, Ahmed. Y. Alyamani
Submitted to Materials Science and Engineering: B
2. Investigation of the Effect of Erbium Doping on the Electrically Active Defects in TiO₂ Thin Films Prepared by Sol-Gel Process
Faisal S. Al mashary, Aniruddha Mondal, Sanjib Mondal, Anupam Ghosh, Jorlandio F. Felix, Sultan Alhassan, Maryam M. Al huwayz, Mohamed Henini
Submitted to Thin Solid Films
3. Effect of indium doping on the electrical and structural properties of TiO₂ thin films used in MOS devices
A. Djeghlouf, D. Hamri, A. Teffahi, A. Saidane, **F. S. Al Mashary**, M.M. Al Huwayz, M. Henini, I. Orak, A. M. Albadri, A. Y. Alyamani
Journal of Alloys and Compounds 775, 202 (2019)
4. Effect of Growth Techniques on the Structural, Optical and Electrical Properties of Indium Doped TiO₂ Thin Films
F. S. Al Mashary, S. de Castro, A. F. da Silva, J. F. Felix, M. R. Piton, H. V. A. Galeti, A. D. G. Rodrigues, Y. G. Gobato, N. Al Saqri, M. Henini, M. M. Al Huwayz, A. M. Albadri, A. Y. Alyamani, H. A. Albrithen, S. A. Alhusaini, K. M. Aljaber, A. Z. Alanazi, F. S. Alghamdi
Journal of Alloys and Compounds 766, 194 (2018)
5. The role of defects on the efficiency of intermediate band solar cells based on III-V semiconductors
Lida Janeth Collazos Paz, Maryam Al Huwayz, **Faisal S. Al mashary**, Luciana Dornelas, Mohamed Henini, Patricia de Souza, Mauricio Pires
Paper presented at the PROCEEDINGS OF BRAZILIAN WORKSHOP ON SEMICONDUCTOR PHYSICS, 2017.
Available from: <https://proceedings.science/bwsp/papers/the-role-of-defects-on-the-efficiency-of-intermediate-band-solar-cells-based-on-iii-v-semiconductors?lang=en>
6. Investigation of defects in indium doped TiO₂ thin films using electrical and optical techniques
Noor Alhuda Al Saqri, Aniruddha Mondal, Jorlandio Francisco Felix, Yara Galvão Gobato, Vanessa Orsi Gordo, Hind Albalawi, Dler Jameel, Haifaa

PUBLICATIONS

- Alghamdi, **Faisal Al Mashary**, David Taylor, Mahmmoud Abd El-sadek, Mohamed Henini
Journal of Alloys and Compounds 698, 883 (2017)
7. Electrical performance of conducting polymer (SPAN) grown on GaAs with different substrate orientations
D. A. Jameel, M. Aziz, J. F. Felix, N. Al Saqri, D. Taylor, H. Albalawi, H. Alghamdi, **F. Al Mashary**, M. Henini
Applied Surface Science 387, 228 (2016)
8. Electrical Behavior of MBE Grown Interfacial Misfit GaSb/GaAs Heterostructures With and Without Te-Doped Interfaces
Mohsin Aziz, Jorlandio Francisco Felix, Noor Al Saqri, Dler Jameel, **Faisal Saleh Al Mashary**, Hind Mohammed Albalawi, Haifaa Mohammed Abdullah Alghamdi, David Taylor, Mohamed Henini
IEEE Transactions on Electron Devices 62, 3980 (2015)
9. High-performance organic/inorganic hybrid heterojunction based on Gallium Arsenide (GaAs) substrates and a conjugated polymer
D. A. Jameel, J. F. Felix, M. Aziz, N. Al Saqri, D. Taylor, W. M. De Azevedo, E. F. da Silva, H. Albalawi, H. Alghamdi, **F. Al Mashary**, M. Henini
Applied Surface Science 357, 2189 (2015)
10. Rapid thermal annealing: An efficient method to improve the electrical properties of tellurium compensated Interfacial Misfit GaSb/GaAs heterostructures
Mohsin Aziz, Jorlandio F. Felix, Dler Jameel, Noor Al Saqri, **Faisal S. Al Mashary**, Haifaa M. Alghamdi, Hind M. Albalawi, David Taylor, Mohamed Henini
Superlattices and Microstructures 88, 80 (2015)
11. Investigation of the effects of gamma radiation on the electrical properties of dilute GaAs $1-x$ N x layers grown by Molecular Beam Epitaxy
N. Al Saqri, J. F. Felix, M. Aziz, D. Jameel, C. I. L. de Araujo, H. Albalawi, **F. Al Mashary**, H. Alghamdi, D. Taylor, M. Henini
Current Applied Physics 15, 1230 (2015)

CONFERENCE PRESENTATIONS

ORAL TALK

- “The Effect of Indium Contents on the Electrical Active Defects in Indium Doped TiO₂ Thin Films”
The 19th International Conference on Extended Defects in Semiconductors (EDS2018), Thessaloniki, Greece (24-29 June 2018)
- “The Effect of Growth Techniques on the Electrical Active Defects in Indium Doped TiO₂ Thin Films”
The 18th Brazilian Workshop on Semiconductor Physics (18th BWSP), Sao Sebastiao, Brazil (14-18 August 2017)

POSTER PRESENTATIONS

- “Investigation of electrical properties of Erbium-doped TiO₂ thin films prepared by sol-gel spin-on technique”
The UK Semiconductors 2018 Conference (UKS 18), Sheffield, United Kingdom (4-5 July 2018)
- “Electrical characterization of defects in In-doped TiO₂ thin films”
The 18th International Conference on Extended Defects in Semiconductors (EDS2016), Les Issambres, France (25-29 September 2016)

ACKNOWLEDGEMENTS

“All praise is due to Allah, the Almighty, the most gracious, and the most merciful, for blessing me and giving me the strength to complete this thesis”

First of all I would like to express my deepest gratitude and thankfulness to my supervisor, Prof Mohamed Henini, for giving me the opportunity to join his group and work under his supervision. I am really grateful for the tremendous support, guidance and help during my PhD studies. His encouragement gave me the confidence to present my work in many international conferences and collaborate with different groups worldwide. I would also like to acknowledge the financial support from Qassim University, Saudi Arabia, for my PhD studies at University of Nottingham.

I would like to thank Dr J. F. Felix (University of Brasilia, Brazil) for structural characterization, Prof Y. G. Gobato (Federal University of São Carlos, Brazil) for PL characterization, Dr A. Albadri (King Abdulaziz City for Science and Technology, Riyadh) and Dr A. Mondal (National Institute of Technology, India) for providing me with many samples that were investigated in this thesis. I would like also to thank all my colleagues and collaborators for the useful and valuable discussions.

I am thankful to the technicians in the School of Physics & Astronomy, Mr D. Taylor, Mr J. Chauhan and Dr N. Alexeeva for their help in the processing of the samples investigated in this thesis. I would also like to thank all my friends, especially Dr Mazen Alhuwaimel, for their support during my PhD.

ACKNOWLEDGEMENTS

I would like to express my special and sincere gratefulness and gratitude to my father, Saleh, and mother, Hussah, for the encouragement and support, not just during my PhD study but throughout my life. I wish also to thank my brother and sisters for their support and encouragement.

Finally, I would like to express my sincere gratitude to my beloved wife, Norah, for the care and love. Without her encouragement and support I would not have been able to complete this thesis.

ACRONYMS

The following acronyms will be used throughout the thesis:

I-V	Current-Voltage
C-V	Capacitance-Voltage
DLTS	Deep Level Transient Spectroscopy
Laplace DLTS	Laplace Deep Level Transient Spectroscopy
PL	Photoluminescence

TABLE OF CONTENTS

CHAPTER 1: INTRODUCTION1

1.1 INTRODUCTION 1

1.2 MOTIVATION3

1.3 LAYOUT OF THE THESIS5

REFERENCES.....8

CHAPTER 2: FUNDAMENTAL CONCEPTS OF SEMICONDUCTORS..11

2.1 SEMICONDUCTORS 11

2.1.1 UNDOPED AND DOPED SEMICONDUCTORS 12

2.2 CRYSTAL STRUCTURE 13

2.3 DENSITY OF STATES 17

2.4 ENERGY BANDGAP 18

2.4.1 DIRECT AND INDIRECT ENERGY BANDGAP 19

2.4.2 EFFECT OF TEMPERATURE ON ENERGY BANDGAP20

2.5 HETEROJUNCTION STRUCTURES21

2.5.1 LATTICE MISMATCH21

2.5.2 ATOM SIZE AND ELECTRONEGATIVITY22

2.5.3 BAND ALIGNMENT23

2.6 GENERAL PROPERTIES OF NOMINATED SEMICONDUCTORS24

2.6.1 TITANIUM DIOXIDE (TiO₂)24

2.6.2 INDIUM OXIDE (In₂O₃)26

TABLE OF CONTENTS

REFERENCES.....	27
CHAPTER 3: DEFECTS IN SEMICONDUCTORS AND THEIR PROPERTIES	32
3.1 CLASSIFICATION OF SEMICONDUCTOR DEFECTS	32
3.1.1 POINT DEFECTS	32
3.1.2 COMPLEXES OF POINT DEFECTS	34
3.1.3 LINEAR DEFECTS	36
3.2 DEFECTS AND THEIR CARRIER KINETICS	37
3.2.1 SHALLOW AND DEEP LEVELS IMPURITIES	37
3.2.2 SHOCKLEY-READ-HALL THEORY.....	39
3.3 DEFECTS IN COMPOUND SEMICONDUCTORS.....	44
3.3.1 DEFECTS IN TITANIUM DIOXIDE (TiO ₂).....	45
3.3.2 DEFECTS IN INDIUM OXIDE (In ₂ O ₃).....	46
REFERENCES.....	48
CHAPTER 4: EXPERIMENTAL TECHNIQUES.....	53
4.1 SCHOTTKY DIODE.....	54
4.1.1 DEPLETION REGION	56
4.1.2 SCHOTTKY DIODE UNDER BIAS CONDITIONS	57
4.2 CAPACITANCE – VOLTAGE (C-V) MEASUREMENTS.....	59
4.3 CURRENT – VOLTAGE (I-V) MEASUREMENTS	60
4.4 DEEP LEVEL TRANSIENT SPECTROSCOPY (DLTS).....	62
4.4.1 CAPACITANCE TRANSIENTS	63

TABLE OF CONTENTS

4.4.2 CONVENTIONAL DLTS	66
4.5 LAPLACE DLTS	68
4.6 DLTS HARDWARE SETUP	70
4.6.1 CRYOSTAT AND TEMPERATURE CONTROLLER	71
4.6.2 CAPACITANCE METER	73
4.6.3 CURRENT-VOLTAGE SOURCE METER	73
4.6.4 DATA ACQUISITION AND BNC CONNECTOR BOX	73
4.6.5 COMPUTER INTERFACE	74
4.7 SYSTEM SOFTWARE	74
4.7.1 CONVENTIONAL DLTS MODE	74
4.7.2 LAPLACE TRANSIENT PROCESSING (LAPLACE DLTS) MODE	75
4.8 PHOTOLUMINESCENCE	75
4.9 X-RAY DIFFRACTION (XRD)	77
4.10 RAMAN SPECTROSCOPY	78
4.11 ABSORPTION	79
REFERENCES	81
CHAPTER 5: EXPERIMENTAL DETAILS	83
5.1 SAMPLES INVESTIGATED IN THIS THESIS	83
5.1.1 INDIUM DOPED TiO ₂ GROWN ON SILICON SUBSTRATES BY TWO DIFFERENT TECHNIQUES	83
5.1.2 INDIUM DOPED TiO ₂ GROWN BY PLD TECHNIQUE ON LOW AND HIGH INDEX GaAs PLANES	86

TABLE OF CONTENTS

5.1.3 ERBIUM DOPED TiO ₂ GROWN ON SILICON SUBSTRATES BY SOL-GEL TECHNIQUE.....	87
5.1.4 ERBIUM DOPED In ₂ O ₃ GROWN ON SILICON SUBSTRATES BY SPIN-ON TECHNIQUE.....	89
5.2 MEASUREMENTS DETAILS	91
5.2.1 I-V MEASUREMENTS	91
5.2.2 C-V MEASUREMENTS.....	91
5.2.3 DLTS MEASUREMENTS.....	91
5.2.4 LAPLACE DLTS MEASUREMENTS.....	92
5.2.5 PHOTOLUMINESCENCE (PL) MEASUREMENTS	92
5.2.6 XRD AND RAMAN MEASUREMENTS.....	93
CHAPTER 6: EFFECT OF GROWTH TECHNIQUES ON THE STRUCTURAL, OPTICAL AND ELECTRICAL PROPERTIES OF INDIUM DOPED TiO₂ THIN FILMS	94
6.1 INTRODUCTION	94
6.2 RESULTS AND DISCUSSION	95
6.2.1 SAMPLE DETAILS.....	95
6.2.2 STRUCTURAL AND OPTICAL INVESTIGATIONS	96
6.2.3 CURRENT-VOLTAGE MEASUREMENTS.....	102
6.2.4 CAPACITANCE-VOLTAGE MEASUREMENTS	108
6.2.5 OPTICAL PROPERTIES	109
6.2.6 DLTS AND LAPLACE DLTS MEASUREMENTS	116

TABLE OF CONTENTS

6.3 CONCLUSION	121
REFERENCES.....	122
CHAPTER 7: INVESTIGATION OF THE STRUCTURAL, OPTICAL AND ELECTRICAL PROPERTIES OF INDIUM-DOPED TiO₂ THIN FILMS GROWN BY PULSED LASER DEPOSITION TECHNIQUE ON LOW AND HIGH INDEX GaAs PLANES	127
7.1 INTRODUCTION	127
7.2 RESULTS AND DISCUSSION	129
7.2.1 SAMPLE DETAILS	129
7.2.2 STRUCTURAL MEASUREMENTS	130
7.2.3 CURRENT-VOLTAGE MEASUREMENTS.....	133
7.2.4 CAPACITANCE-VOLTAGE MEASUREMENTS	142
7.2.5 PL MEASUREMENTS	144
7.2.6 DLTS AND LAPLACE DLTS MEASUREMENTS	148
7.3 CONCLUSION	153
REFERENCES.....	155
CHAPTER 8: INVESTIGATION OF ELECTRICAL PROPERTIES OF ERBIUM-DOPED TiO₂ THIN FILMS PREPARED BY SOL-GEL PROCESS.....	161
8.1 INTRODUCTION	161
8.2 RESULTS AND DISCUSSION	162
8.2.1 SAMPLE DETAILS	162

TABLE OF CONTENTS

8.2.2 CAPACITANCE -VOLTAGE MEASUREMENTS	163
8.2.3 CURRENT-VOLTAGE MEASUREMENTS.....	164
8.2.4 DLTS AND LAPLACE DLTS MEASUREMENTS	170
8.3. CONCLUSION.....	177
REFERENCES.....	179
CHAPTER 9: INVESTIGATION OF THE ELECTRICAL PROPERTIES OF ERBIUM-DOPED In₂O₃ THIN FILMS	184
9.1 INTRODUCTION	184
9.2 RESULTS AND DISCUSSION	186
9.2.1 SAMPLE DETAILS	186
9.2.2 CURRENT-VOLTAGE MEASUREMENTS.....	186
9.2.3 CAPACITANCE-VOLTAGE MEASUREMENTS	193
9.2.4 DLTS AND LAPLACE DLTS MEASUREMENTS	194
9.3 CONCLUSION.....	200
REFERENCES.....	202
CHAPTER 10: CONCLUSION AND FUTURE WORK.....	207
10.1 CONCLUSION.....	207
10.1.1 INDIUM DOPED TiO ₂ THIN FILMS GROWN BY PLD AND SPUTTERING TECHNIQUES ON SILICON SUBSTRATES	207
10.1.2 INDIUM DOPED TiO ₂ THIN FILMS GROWN BY PLD TECHNIQUE ON LOW AND HIGH INDEX GaAs PLANES	209

TABLE OF CONTENTS

10.1.3 ERBIUM DOPED TiO ₂ THIN FILMS GROWN BY A COMBINATION OF AN EASY SOL-GEL PROCESS AND SPIN COATING METHOD	211
10.1.4 ERBIUM DOPED In ₂ O ₃ THIN FILMS GROWN BY SPIN-ON TECHNIQUE	212
10.2 SUGGESTIONS FOR FUTURE WORK.....	213

INTRODUCTION

Chapter 1 will introduce a brief introduction to the semiconductor materials investigated as well as the motivations and structure of the thesis.

1.1 INTRODUCTION

Semiconductor materials have had an enormous impact in the electronics and optoelectronics industry. The ability of manipulating the electrical and optical properties of semiconductors by doping is an essential feature that make them preferable over conductors. In 1874, F. Braun discovered for the first time the rectification behaviour of metal-semiconductor contacts where the current is nonlinear and rather flows only in one bias direction [1]. However, the invention of the transistor in 1947 by W. Shockley, J. Bradeen and W. Barttain at Bell laboratories was a remarkable breakthrough in the history of semiconductors [2]. The first transistor was fabricated using germanium (Ge). This was followed by another major breakthrough in the industry of semiconductors [1, 2], namely the innovation of integrated circuits (ICs) in 1958 by J. Kilby. Silicon is the most studied semiconductor element and is the basis of most ICs while GaAs is the workhorse of compound semiconductors that are used in optoelectronics devices.

TiO₂ is a wide bandgap semiconductor material and is one of the conducting transparent oxides (TCOs) family [3]. TiO₂ is known to be an n-type semiconductor due to oxygen related defects (oxygen vacancy and titanium interstitial) which are donor defects [4-6]. Oxygen vacancies introduce energy levels in the bandgap near the conduction band [7]. However, Nowotny et al. observed p-type conductivity in undoped TiO₂ at very high temperature and this was attributed to titanium vacancies

CHAPTER 1

which are acceptor defects [8]. The conduction band of TiO₂ is formed mainly from titanium 3d and the valence band mainly from oxygen 2p. In the case of no oxygen vacancy, the four valence electrons from titanium atom fill the empty 2p orbitals of oxygen (two electrons for one oxygen atom and the other two for the other oxygen atom). However, if an oxygen atom is missing (an oxygen vacancy), the two titanium valence electrons donated to the missing oxygen atom will occupy the titanium 3d orbitals in the conduction band and hence increase the free electrons in the conduction band [7, 9]. This mechanism leads to the n-type conductivity of TiO₂. It is a core material in many technological applications such as photocatalysis, water and air purification, solar cells and photo-electrochemical (PEC) water splitting [10-14] due to its significant electrical and optical properties. Its wide bandgap (3.0 - 3.4 eV [15, 16]) makes it only sensitive to UV light and transparent for visible light which therefore degrade its efficiency for solar cell applications. Doping TiO₂ with metal ions, such as indium [17], can alter some of its electrical and optical properties and hence makes it sensitive to visible light.

In₂O₃ is also an n-type wide bandgap semiconductor (3.6 – 3.75 eV) and one of the most studied TCO material [18]. It is worth mentioning that the n-type property of In₂O₃ is also due to oxygen related defects as in TiO₂ [19, 20]. As it is a TCO material, it is used as a transparent conducting film in photovoltaic devices, but it has also applications in flat panel displays, gas sensors and UV detectors [21-23]. The enhancement of the band gap of TCOs materials can improve UV detectors performance. However, one of the disadvantages of TCOs materials, which adversely affect their performance as UV detectors, is the oxygen related defects [18].

The oxygen related defects degrade the efficiency of In_2O_3 and TiO_2 as UV detectors because visible light is absorbed by these defects which have energy states within the bandgap [24, 25]. Er doping of In_2O_3 [26] and TiO_2 [27] has been reported to remove the oxygen defects and enhance the bandgap which result in better UV detection performance. The enhancement of the bandgap may be due to a decrease of the maximum energy of the valence band and an increase of the minimum energy of the conduction band which occur as a result of Er ions substituting In and Ti ions in the In_2O_3 and TiO_2 lattices, respectively [26, 28]. Er can also be incorporated interstitially and occupy an oxygen vacancy site. This can lead to the elimination of oxygen vacancies defects [26].

Semiconductor structures, generally, possess many types of defects that alter the electrical and optical properties of the structures. Defects can be introduced into the semiconductor lattice intentionally, by doping, or unintentionally, during the growth and fabrication processes. Some of these defects create deep levels within the bandgap of the materials and therefore affect the performance of the devices. Much effort is needed to understand these defects to help in controlling their presence in the materials. Deep level transient spectroscopy (DLTS) is a powerful technique for investigating the electrically active defects in semiconductor materials [29].

1.2 MOTIVATION

The electrically active defects play an important role in the performance of electronic and optoelectronic devices. The main motivation of this thesis is to study the electrically active defects in some wide band gap semiconductor structures, namely TiO_2 and In_2O_3 . TiO_2 thin films (TFs) were doped with Indium in order to

CHAPTER 1

tailor the band gap of TiO_2 and hence make it suitable for solar cell applications. Here TiO_2 has been grown on Si substrates by two different techniques, namely pulsed laser deposition (PLD) and sputtering, in order to study the effect of the growth technique on the structural, optical and electrical (especially the electrically active defects) properties in In-doped TiO_2 TFs. Indium doped TiO_2 TFs have also been grown by PLD on low [(100)] and high [(311)B] GaAs planes to investigate the effect of the orientation of the GaAs substrates, i.e. (100) and (311)B, on the properties of In-doped TiO_2 TFs. Erbium-doped TiO_2 and In_2O_3 TFs, grown by the sol-gel process followed by spin coating, have been investigated with the aim to remove the oxygen related defects and enhance the band gap which consequently increase the sensitivity of detecting the UV light. DLTS has also been used to investigate the electrically active defects in Er doped TiO_2 and Er doped In_2O_3 TFs.

In addition to DLTS, current-voltage (I-V) and capacitance-voltage (C-V) measurements have been used to study the electrical properties of the devices under investigation. Moreover, X-ray diffraction (XRD) and photoluminescence (PL) techniques were employed to study the structural and optical properties of In doped TiO_2 grown on Si substrates by PLD and sputtering which are presented in Chapter 6 and In doped TiO_2 grown on GaAs substrates by PLD which are presented in Chapter 7.

1.3 LAYOUT OF THE THESIS

The thesis is structured as follows:

Chapter 2: FUNDAMENTAL CONCEPTS OF SEMICONDUCTORS

Describes the fundamental concepts of semiconductors, crystal structure, principles of heterostructure devices and the properties of TiO₂ and In₂O₃ materials.

Chapter 3: DEFECTS IN SEMICONDUCTORS AND THEIR PROPERTIES

Aims to cover the crystal defects in semiconductors and theoretical background of carrier kinetics.

Chapter 4: EXPERIMENTAL TECHNIQUES

Describes the experimental techniques used in this thesis such as capacitance-voltage (C-V), current-voltage (I-V), DLTS, Laplace DLTS and Photoluminescence (PL). In addition, the hardware and software required to implement these methods are also presented.

Chapter 5: EXPERIMENTAL DETAILS

Gives the details of the samples investigated in the thesis and the experimental procedures.

Chapter 6: EFFECT OF GROWTH TECHNIQUES ON THE STRUCTURAL, OPTICAL AND ELECTRICAL PROPERTIES OF INDIUM DOPED TiO₂ THIN FILMS

Describes the effect of the growth techniques on the electrically active defects of In-doped TiO₂ using DLTS and Laplace DLTS techniques. In addition, X-Ray Diffraction (XRD) and Raman have been used to investigate the structure of the samples. I-V and C-V measurements were carried out and the optical properties of the samples studied using the PL technique.

Chapter 7: INVESTIGATION OF THE STRUCTURAL, OPTICAL AND ELECTRICAL PROPERTIES OF INDIUM-DOPED TiO₂ THIN FILMS GROWN BY PULSED LASER DEPOSITION TECHNIQUE ON LOW AND HIGH INDEX GaAs PLANES

In this chapter, the electrical properties of In-doped TiO₂ grown by PLD technique on (100) and (311)B n-type GaAs substrates were investigated. I-V, C-V, DLTS and Laplace DLTS measurements are presented for these samples. Moreover, XRD and PL techniques were also used to investigate the structural and optical properties, respectively.

Chapter 8: INVESTIGATION OF ELECTRICAL PROPERTIES OF ERBIUM-DOPED TiO₂ THIN FILMS PREPARED BY SOL-GEL PROCESS

Electrical properties of (Er³⁺) doped TiO₂ thin films (Er:TiO₂ TFs) grown by sol-gel technique on silicon (p-type) substrate were investigated using I-V, C-V, DLTS and Laplace DLTS.

CHAPTER 1

Chapter 9: INVESTIGATION OF ELECTRICAL PROPERTIES OF ERBIUM-DOPED In₂O₃ THIN FILMS

In this chapter, the electrically active defects in Er-doped In₂O₃ grown by spin-on technique on p-type Si (100) substrates are studied using I-V, C-V, DLTS and Laplace DLTS.

Chapter 10: CONCLUSION AND FUTURE WORK

Includes an overall summary of the work presented in this thesis in addition to suggestions for future work.

REFERENCES

1. Grundmann, M., *The physics of semiconductors: an introduction including nanophysics and applications*. 2015: Springer.
2. Neamen, D.A., *Semiconductor physics and devices*. Vol. 3. 1997: McGraw-Hill New York.
3. Duenas, S., et al., *A comparative study of the electrical properties of TiO₂ films grown by high-pressure reactive sputtering and atomic layer deposition*. *Semiconductor science and technology*, 2005. **20**(10): p. 1044.
4. Blumenthal, R., J. Baukus, and W. Hirthe, *Studies of the Defect Structure of Nonstoichiometric Rutile, TiO_{2-x}*. *Journal of The Electrochemical Society*, 1967. **114**(2): p. 172-176.
5. Nowotny, J., et al., *Titanium dioxide for solar-hydrogen I. Functional properties*. *International journal of hydrogen energy*, 2007. **32**(14): p. 2609-2629.
6. Nowotny, M.K., et al., *Observations of p-type semiconductivity in titanium dioxide at room temperature*. *Materials Letters*, 2010. **64**(8): p. 928-930.
7. Ramamoorthy, M., R. King-Smith, and D. Vanderbilt, *Defects on TiO₂ (110) surfaces*. *Physical Review B*, 1994. **49**(11): p. 7709.
8. Nowotny, M., et al., *Titanium vacancies in nonstoichiometric TiO₂ single crystal*. *physica status solidi (b)*, 2005. **242**(11): p. R88-R90.
9. Nie, X., et al., *Doping of TiO₂ polymorphs for altered optical and photocatalytic properties*. *International Journal of Photoenergy*, 2009. **2009**.
10. Henderson, M.A., *A surface science perspective on photocatalysis*. *Surface Science Reports*, 2011. **66**(6): p. 185-297.

CHAPTER 1

11. Fujishima, A., X. Zhang, and D.A. Tryk, *TiO₂ photocatalysis and related surface phenomena*. Surface Science Reports, 2008. **63**(12): p. 515-582.
12. Diebold, U., *The surface science of titanium dioxide*. Surface science reports, 2003. **48**(5): p. 53-229.
13. Fujishima, A. and K. Honda, *Electrochemical photolysis of water at a semiconductor electrode*. nature, 1972. **238**(5358): p. 37-38.
14. Park, N.v., J. Van de Lagemaat, and A. Frank, *Comparison of dye-sensitized rutile-and anatase-based TiO₂ solar cells*. 2000, National Renewable Energy Laboratory (NREL), Golden, CO.
15. Amtout, A. and R. Leonelli, *Optical properties of rutile near its fundamental band gap*. Physical Review B, 1995. **51**(11): p. 6842.
16. Tang, H., et al., *Urbach tail of anatase TiO₂*. Physical Review B, 1995. **52**(11): p. 7771.
17. Al mashary, F.S., et al., *Effect of growth techniques on the structural, optical and electrical properties of indium doped TiO₂ thin films*. Journal of Alloys and Compounds, 2018. **766**: p. 194-203.
18. Kim, H.S., et al., *High performance solution-processed indium oxide thin-film transistors*. Journal of the American Chemical Society, 2008. **130**(38): p. 12580-12581.
19. Ko, T.-S., et al., *Tunable light emissions from thermally evaporated In₂O₃ nanostructures grown at different growth temperatures*. Journal of crystal growth, 2008. **310**(7-9): p. 2264-2267.
20. Bierwagen, O., *Indium oxide—a transparent, wide-band gap semiconductor for (opto) electronic applications*. Semiconductor Science and Technology, 2015. **30**(2): p. 024001.

CHAPTER 1

21. Ghosh, A., et al., *Detailed investigation of defect states in Erbium doped In₂O₃ thin films*. Materials Research Bulletin, 2018. **99**: p. 211-218.
22. Li, C., et al., *In₂O₃ nanowires as chemical sensors*. Applied Physics Letters, 2003. **82**(10): p. 1613-1615.
23. Murali, A., et al., *Synthesis and characterization of indium oxide nanoparticles*. Nano Letters, 2001. **1**(6): p. 287-289.
24. Liang, C., et al., *Catalytic growth of semiconducting In₂O₃ nanofibers*. Advanced Materials, 2001. **13**(17): p. 1330-1333.
25. Srivastava, A., et al., *Tunable nanostructures and crystal structures in titanium oxide films*. Nanoscale research letters, 2009. **4**(1): p. 54.
26. Ghosh, A., et al., *Removal of oxygen related defects from chemically synthesized In₂O₃ thin film doped with Er by spin-on technique*. Journal of Alloys and Compounds, 2017. **695**: p. 1260-1265.
27. Mondal, S., et al., *Investigation of optical and electrical properties of erbium-doped TiO₂ thin films for photodetector applications*. Journal of Materials Science: Materials in Electronics, 2018. **29**(22): p. 19588-19600.
28. Lahiri, R., et al., *Performance of Erbium-doped TiO₂ thin film grown by physical vapor deposition technique*. Applied Physics A, 2017. **123**(9): p. 573.
29. Lang, D., *Deep-level transient spectroscopy: A new method to characterize traps in semiconductors*. Journal of applied physics, 1974. **45**(7): p. 3023-3032.

FUNDAMENTAL CONCEPTS OF SEMICONDUCTORS

In this chapter, the fundamental properties of semiconductors, such as doped and undoped semiconductors structures, crystal structures, density of states, energy bandgap, temperature dependent energy gap, heterostructures and carrier mobility, are discussed. In addition, some of the important properties of TiO_2 and In_2O_3 are also presented in this chapter.

2.1 SEMICONDUCTORS

Semiconductors are very important materials as they are the foundation of modern electronics industry. They are considered as the building blocks in the fabrication of electrical and optical devices. Semiconductor materials are found in many devices such as computers (CPUs, memory), optical-storage media (CD, DVD), communication infrastructure (optical-fibre technology, mobile communication) and lighting (LEDs) [1].

Semiconductors are materials which have electrical conductivities that lies between insulators and conductors. The resistivity of a semiconductor ranges from 10^{-2} to $10^9 \Omega\text{-cm}$.

Semiconductor materials can be classified into two categories, namely elementary and compound semiconductors. The elemental semiconductors are made of a single element from the periodic table. Silicon (Si) and germanium (Ge), which are elements from group IV, are examples of elemental semiconductors. Compound semiconductors are made of two or more elements from the periodic table. Compound semiconductors are called binary compounds if they are made of

two elements, such as GaAs, and called ternary compounds if they are made of three elements, such as InGaAs [2].

2.1.1 UNDOPED AND DOPED SEMICONDUCTORS

Undoped semiconductors, which are called intrinsic semiconductors, are those which have no impurities. Undoped semiconductors can be elemental or compound semiconductors. In intrinsic semiconductors, the number of electrons in the conduction band equals the number of holes in the valence band. Thus, undoped semiconductors behave as insulators at 0 K temperature because the valence band is completely filled, and the conduction band is completely empty and hence no carriers flow is observed.

In the case of doped semiconductors, which are also known as extrinsic semiconductors, some impurities are added to alter the electrical properties of the host materials. Depending on the impurities, the semiconductors are classified into n-type and p-type doped semiconductors, when there is an excess of electrons and holes, respectively. An example of an n-type semiconductor is when Si (element from group IV) is doped with As (element from group V). In this case, As (which has five electrons in the outer shell) is replacing an atom of Si (which has four electrons in the outer shell) and a free electron is introduced into the lattice. The As atom is known here as a donor. For p-type semiconductor, if boron (which has three electrons in the outer shell) is used as a dopant in Si, a boron atom will substitute a Si atom and the three valence electrons of boron will form covalent bonds with three surrounding Si atoms leaving the fourth surrounding Si atom with a deficiency (hole). Therefore, a p-type semiconductor is formed with excess holes and the boron atom is called an acceptor [2, 3].

2.2 CRYSTAL STRUCTURE

A crystal structure is formed by placing atoms or molecules in an arrangement that forms a three-dimensional periodic array structure without any impurities added intentionally or accidentally during the process of growing the structure. Therefore, a precise crystal structure is crucial for a high-performance semiconductor device. A lattice is defined as the arrangement of atoms in a crystal. A unit cell, which is the basic building block of a crystal structure, is the smallest assembled set of atoms or molecules which can be repeated to form the whole crystal structure [2]. Fig. 2.1 shows a simple cubic (sc), body-centred cubic (bcc) and face-centred cubic (fcc) which are examples of the basic unit cells. In a simple cubic structure, there is an atom located in each corner of the cube, whereas the body-centred cubic structure has an additional atom located in the centre of the cube. In addition to the atoms in each corner, there is an additional atom at each face of the cube for face-centred cubic structure [4].

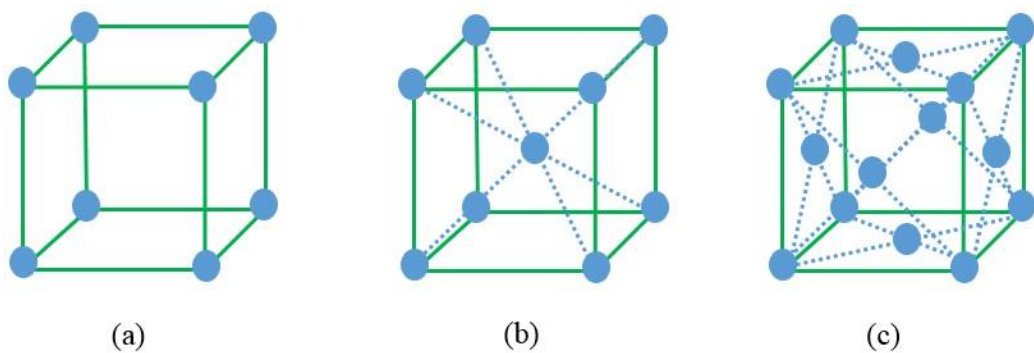


Fig. 2.1: unit cells (a) simple cubic, (b) body-centred cubic and (c) faced-centred cubic.

The most important crystal structures in semiconductors are diamond and zinc blende structures. Most of the structures in semiconductors are classified into these two types of structures. Both structures can be generated by the interpenetration of two fcc lattices where one is displaced along the body diagonal by one-quarter of the distance. In both structures, the atoms are organized together to form a tetrahedron and each atom is covalently bonded to four neighbour atoms. The difference between the diamond structure and zinc blende structure is that diamond structure has only one type of atoms (e.g. Ge, Si and C), whereas two different types of atoms are required in the zinc blende structure (e.g. GaAs, GaSb and InAs). Fig. 2.2 shows both diamond and zinc blende structures [2].

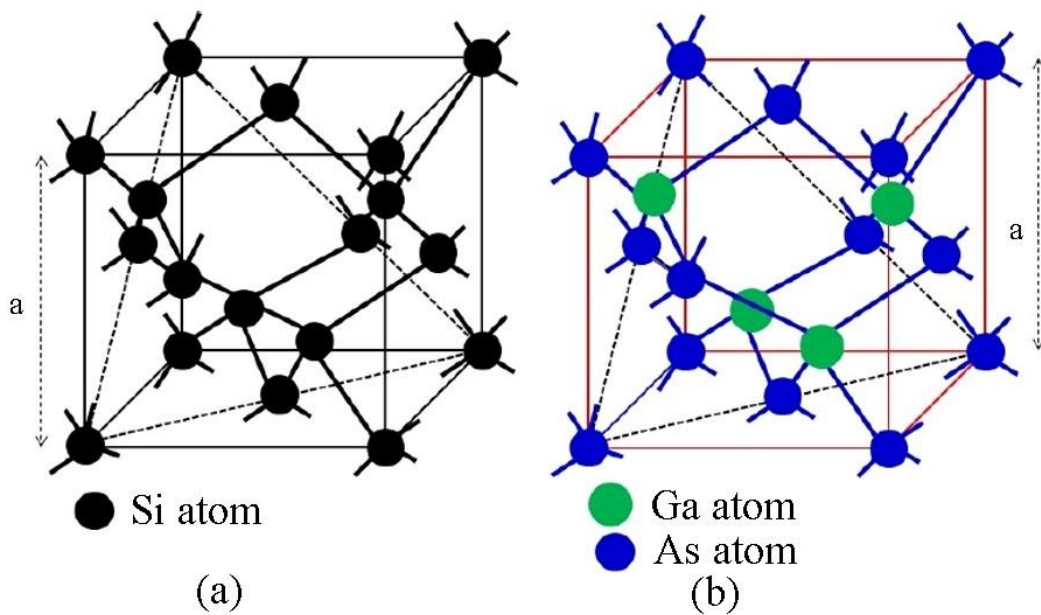


Fig. 2.2: (a) diamond structure for Si. (b) Zinc blende structure for GaAs [2].

CHAPTER 2

The orientation of the crystal planes plays an important role in the fabrication of semiconductor devices since they are built on the surface or near the surface of the crystal. Knowing the plane on which a device will be fabricated is essential because it can affect the electrical and optical properties of the device. Miller indices are usually used to define the planes of a crystal. Miller indices (hkl) of a plane can be identified by finding the intercepts of the plane along the x, y and z directions, then taking the reciprocals of the intercepts and finally reducing them to the smallest integers [5]. Fig. 2.3 shows Miller indices of some planes in a cubic crystal. A direction of a crystal surface can be determined by a set of h, k and l as follows:

1. (hkl) for a plane that has intercepts at $1/h$, $1/k$ and $1/l$ on the x, y and z axis, respectively.
2. $(\bar{h}kl)$ for a plane that intercepts the negative x axis.
3. $\{hkl\}$ for a full set of planes.
4. $[hkl]$ for a direction of a crystal such as $[100]$ for the x axis.
5. $\langle hkl \rangle$ for a full set of directions.

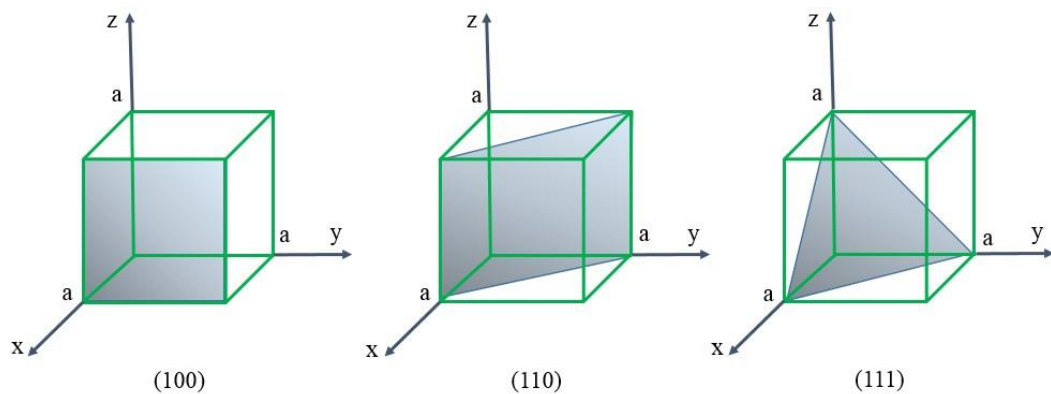


Fig. 2.3: Miller indices of some planes in a cubic crystal.

CHAPTER 2

There are three primitive basis vectors (\mathbf{a} , \mathbf{b} and \mathbf{c}) which are used to describe the crystalline solid along the x, y and z directions. A crystal structure will remain the same under any translation through a direct lattice vector (\mathbf{R}), which is the sum of these primitive vectors as

$$\mathbf{R} = m\mathbf{a} + n\mathbf{b} + p\mathbf{c} \quad (2.1)$$

where m , n and p are integers.

A set of reciprocal basis vectors (\mathbf{a}^* , \mathbf{b}^* and \mathbf{c}^*) can be defined by the primitive basis vectors as:

$$\mathbf{a}^* = 2\pi \frac{\mathbf{b} \times \mathbf{c}}{\mathbf{a} \cdot \mathbf{b} \times \mathbf{c}} \quad (2.2)$$

$$\mathbf{b}^* = 2\pi \frac{\mathbf{c} \times \mathbf{a}}{\mathbf{a} \cdot \mathbf{b} \times \mathbf{c}} \quad (2.3)$$

$$\mathbf{c}^* = 2\pi \frac{\mathbf{a} \times \mathbf{b}}{\mathbf{a} \cdot \mathbf{b} \times \mathbf{c}} \quad (2.4)$$

where $\mathbf{a} \cdot \mathbf{a}^* = 2\pi$, $\mathbf{a} \cdot \mathbf{b}^* = 0$, and so on.

Note that the denominators are alike because $\mathbf{a} \cdot \mathbf{b} \times \mathbf{c} = \mathbf{b} \cdot \mathbf{c} \times \mathbf{a} = \mathbf{c} \cdot \mathbf{a} \times \mathbf{b}$ and they define the volume enclosed by these vectors (\mathbf{a} , \mathbf{b} and \mathbf{c}). The general reciprocal lattice vector (\mathbf{G}) is defined as:

$$\mathbf{G} = h\mathbf{a}^* + k\mathbf{b}^* + l\mathbf{c}^* \quad (2.5)$$

where h , k and l are integers.

The relationship between the direct lattice vector (\mathbf{R}) and the reciprocal lattice vector (\mathbf{G}) is given by [5]:

$$\mathbf{G} \cdot \mathbf{R} = 2\pi \times \text{integer} \quad (2.6)$$

It is worth mentioning that the planes (100), (110) and (111) are called low index planes and any plane that has at least one index higher than 0 and 1 (i.e. 2 or higher) is called a high index plane.

2.3 DENSITY OF STATES

Density of states $N(E)$ is the number of electronic states at a certain energy level that are available to be occupied by carriers, i.e. the number of states per unit volume per unit energy that are available for the carriers to occupy. It is essential to determine the distribution of the carriers and their concentrations in a semiconductor. The interaction between atoms due to the close space between them lead to splitting of the quantified energy levels into a finite number of energy states [6].

Electrons tend to occupy the lowest energy levels available. The highest two occupied energy bands are called valence and conduction bands. The valence band is completely occupied with electrons at 0 Kelvin and the electronic states in the conduction band are empty. The conduction and valence bands are separated by a bandgap, which is a range of energy where no allowed states can exist. During the conduction process, when electrons possess enough energy to overcome the bandgap, they are excited to the conduction band leaving vacancies (holes) in the valence band. These electrons need available states in the conduction band for them to occupy. The allowed states at certain energy levels are defined as the density of states. The density of states depends on the confinement of the carriers and their degree of freedom. The degree of freedom of the carriers depends on the material structure. Semiconductors materials can be categorized according to their dimensions into four types: bulk or three dimensions (3D), two-dimensions (2D), one-dimension (1D) and zero-dimension (0D) materials. Fig. 2.4 [7] shows the density of states for these materials as a function of energy. The density of states of a bulk material is proportional to the square root of energy, whereas it is a step-like function in case of 2D material (like a quantum well). In 1D material such as a

quantum wire, the density of states is a function of $(E)^{-1/2}$ and in the case of 0D material (i.e. quantum dot) it is described with a delta function.

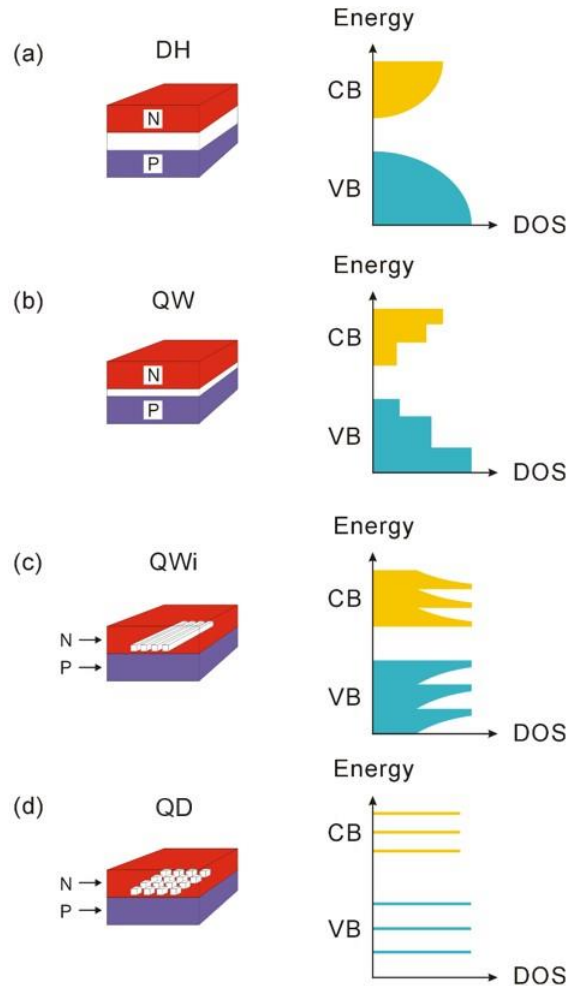


Fig. 2.4: density of states for (a) bulk material (3D), (b) quantum well (2D), (c) quantum wire (1D) and (d) quantum dot (0D) [7].

2.4 ENERGY BANDGAP

In solid state physics, materials are classified into three types which are insulators, semiconductors and metals. This classification depends on the size of the energy bandgap (E_g) which is the difference between the energy of the highest valence band (E_v) and the energy of the lowest conduction band (E_c). In particular,

the energy bandgap of metals is ~ 0 eV, whereas in semiconductors it ranges from ~ 0.17 eV (InSb) to ~ 6 eV (AlN) and for insulators E_g is very high (e.g. $E_g > 6$ eV) [4]. The energy-wave vector (E-k) is used to represent the bandgap of semiconductors. The conduction band and the valence band near $K = 0$ is approximately parabolic in shape and their energies are given by

$$E_C = E_g + \frac{\hbar^2 k^2}{8\pi^2 m_e^*}, E_v = -\frac{\hbar^2 k^2}{8\pi^2 m_h^*} \quad (2.7)$$

where \hbar is the Planck's constant, k is Boltzmann constant, m_e^* and m_h^* are the effective mass of electron and hole, respectively.

The electrons are confined in the valence band at a very low temperature (~ 0 K) because they do not have sufficient energy to overcome the bandgap into the conduction band. Hence, at this low temperature, semiconductors behave as insulators [8].

2.4.1 DIRECT AND INDIRECT ENERGY BANDGAP

Semiconductors can be classified according to the nature of their bandgap, namely direct and indirect bandgap semiconductors. This classification depends on the position of the minimum energy of the conduction band and the maximum energy of the valence band with respect to the wave vector (k). If the minimum energy of the conduction band and the maximum energy of the valence band have the same k value, i.e. $k=0$ (Γ point), the semiconductor is called a direct bandgap semiconductor (e.g. GaAs). However, in case of an indirect bandgap semiconductor (e.g. Si), the minimum of the conduction band and the maximum of the valence band do not occur at the same value of wave vector [8]. An illustration of (E-k) relationship for the most common direct and indirect bandgap semiconductors GaAs and Si, respectively is shown in Fig. 2.5 [5].

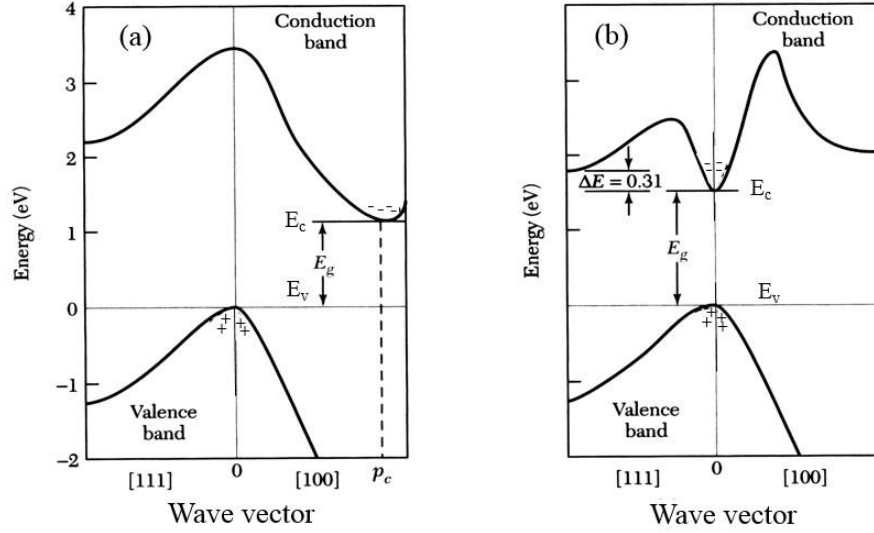


Fig. 2.5: energy band structure (E-k diagram) for (a) Si and (b) GaAs. Electrons and holes are represented by (-) and (+), respectively. E_v and E_c are the energy of the highest valence band and the energy of the lowest conduction band, respectively [2].

2.4.2 EFFECT OF TEMPERATURE ON ENERGY BANDGAP

As the temperature of a semiconductor increases, its energy bandgap decreases. At 0 K, the bandgap energy of GaAs and Si are 1.52 eV and 1.17 eV, respectively. However, at room temperature, the bandgap decreases to 1.42 eV and 1.12 eV for GaAs and Si, respectively [5]. This reduction of the bandgap is attributed to the dilation of the lattice constant. The inter-atomic spacing increases with the increase of the thermal vibration of the atoms which leads to a decrease in the potential seen by electrons, hence the bandgap is reduced. Another reason for the temperature dependence of the bandgap is the electron-phonon (or electron-lattice) interaction [9]. The dependence of bandgap on temperature can be expressed by [10]

$$E_g(T) = E_g(0) - \frac{\alpha T^2}{T + \beta} \quad (2.8)$$

where $E_g(0)$ is the energy of the bandgap at 0 K, α and β are constants and depend on the material. For example, $\alpha = 0.49$ meV/K and $\beta = 655$ K for Si [5].

2.5 HETEROJUNCTION STRUCTURES

Semiconductor structures can be either homojunction or heterojunction structures. In a homojunction structure, two identical semiconductor materials are grown on top of each other (e.g. p-n junction). However, when a semiconductor material is grown on top of a dissimilar semiconductor, a heterojunction structure is formed. It is worth mentioning that the semiconductor materials of a heterojunction have different properties (e.g. bandgap and lattice constant) [4].

2.5.1 LATTICE MISMATCH

It is important for a heterojunction structure to be lattice matched (Fig. 2.6 (a)) and this can be achieved when the lattice constants of the constituent materials are the same. If the lattice constants of the materials forming the heterojunction are different, a lattice mismatched structure is formed. Then, dislocations will be introduced in the interface which leads to the formation of defects at the interface. In addition, strain occurs at the interface due to the difference in the lattice constants. The lattice-mismatch is defined by [5]

$$\frac{\Delta a}{a} = \frac{a_{sub} - a_{layer}}{a_{sub}} \quad (2.9)$$

where a_{layer} is the lattice constant of the epitaxial layer and a_{sub} is the lattice constant of the substrate.

Compressive and tensile are the two strain types that may occur in a mismatched structure. If a layer of a semiconductor with a large lattice constant (called epilayer) is grown on top of a substrate of a smaller lattice constant, the strain is compressive as shown in Fig. 2.6 (b). On the other hand, the strain is known as tensile strain when the lattice constant of the substrate is greater than that of the epilayer (Fig. 2.6 (c)).

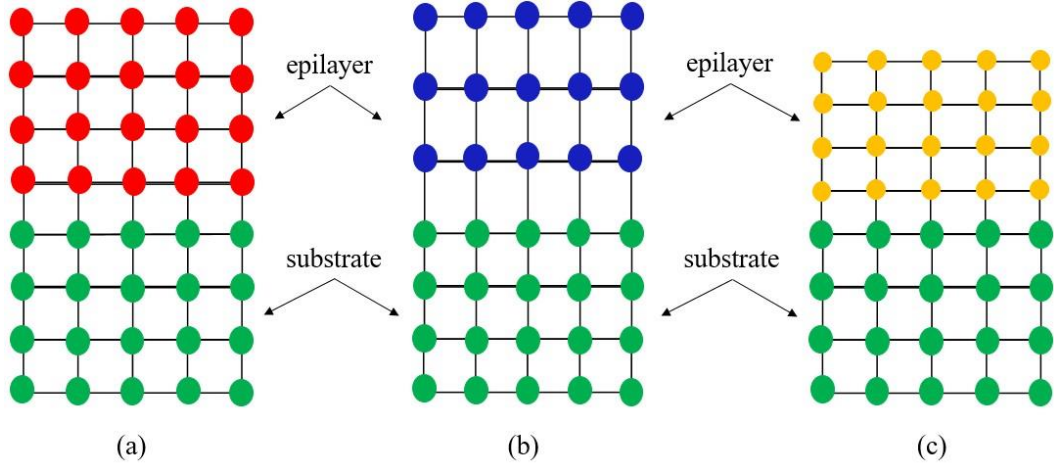


Fig. 2.6: graphic illustration of (a) lattice matched, (b) compressive strain and (c) tensile strain.

2.5.2 ATOM SIZE AND ELECTRONEGATIVITY

In addition to the lattice matching, the size of the atoms of the two different semiconductor materials that form a heterojunction is an important feature in the growth process of heterojunction structures. As the lattice-mismatch causes a strain in the structure, the difference in the atom size can also produce strain.

Electronegativity (χ), which is the ability of an atom within a molecule to attract electrons to itself and form a chemical bond, also plays an important role in the growth process [5]. The electronegativity is usually defined in the Pauling's electronegativity scale (in 1932, the electronegativity was studied for the first time by Linus Pauling) [11]. According to Pauling's electronegativity scale, the electronegativity difference between two different materials (A and B), which form the heterojunction structure, is giving by

$$\chi_A - \chi_B = [(eV)^{-\frac{1}{2}}] \sqrt{E_D(AB) - \frac{[E_D(AA) + E_D(BB)]}{2}} \quad (2.10)$$

where χ_A and χ_B are the electronegativity of material A and B, respectively. $E_D(AB)$, $E_D(AA)$ and $E_D(BB)$ are the dissociation energies in eV between the atoms AB, AA

and BB, respectively. Note that the electronegativity is a unitless quantity and the term $[(eV)^{-\frac{1}{2}}]$ is introduced to make the electronegativity unitless.

2.5.3 BAND ALIGNMENT

The aim of growing a heterojunction structure is to control the behaviour of the carriers through the band alignment. The band alignment of conduction and valence bands of two semiconductor materials A and B can be constructed using Anderson's rule [12]. This theory of Anderson is based on the electron affinity of the materials that form the heterojunction. If two semiconductors (A and B) are used to form a heterojunction, their vacuum levels have to be lined up as stated by Anderson's rule. As a result of lining up the vacuum levels, the difference in the electron affinities of A and B ($\kappa_A - \kappa_B$) leads to an offset of both conduction band (ΔE_c) and valence band (ΔE_v) as follows [6]:

$$\kappa_B - \Delta E_c - \kappa_A = 0 \quad (2.11)$$

$$\Delta E_c = \kappa_B - \kappa_A \text{ and } \Delta E_v = \Delta E_g - \Delta \kappa \quad (2.12)$$

Heterojunction structures are categorized according to their band alignment into three types. Type I (straddling) heterojunction is formed when the bandgap of semiconductor B (has lower bandgap than A) is enclosed within the bandgap of semiconductor A. InGaAs/InP is an example of type I heterojunction. In type II, staggered heterojunction, the conduction band edge and the valence band edge of semiconductor A are above the corresponding conduction and valence band edges of semiconductor B. An example of this type is InAlAs/InP. When both the conduction and valence band edges of semiconductor B is below the valence band edge of semiconductor A, the bandgaps, in this case, do not overlap and type III

(broken-gap) heterojunction is formed. GaSb/InAs is an example of Type III heterojunction [6]. The three types of heterojunctions are illustrated in Fig. 2.7 [5].

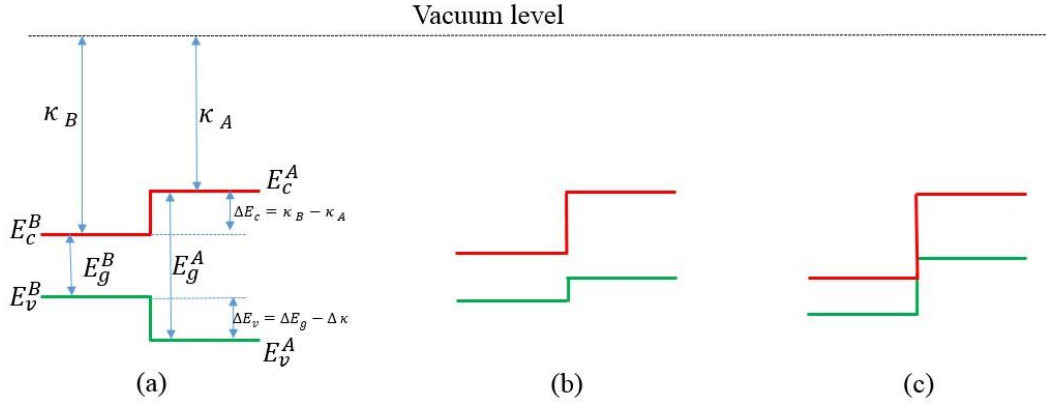


Fig. 2.7: band alignment of (a) Type I (straddling), (b) type II (staggered) and (c) type III (broken-gap) heterojunctions.

2.6 GENERAL PROPERTIES OF NOMINATED SEMICONDUCTORS

This section contains some general properties of semiconductor materials that have been investigated in this thesis.

2.6.1 TITANIUM DIOXIDE (TiO₂)

Titanium dioxide, also known as titania, is considered as an n-type wide bandgap semiconductor [13]. It occurs in nature in three main polymorphs: anatase, rutile and brookite phases [14]. Both anatase and rutile phases have a tetragonal structure (but different space group) and brookite is an orthorhombic structure [15, 16]. It is worth pointing out that the two most common phases of TiO₂ which are used to fabricate devices are anatase and rutile [16]. However, it is difficult to employ brookite phase for device application due to its metastability[16, 17]. Fig.

CHAPTER 2

2.8 [18] shows the crystal structures of anatase and rutile. The energy bandgaps of anatase [19] and rutile [20] TiO_2 phases are 3 eV and 3.4 eV, respectively. Furthermore, the anatase phase possesses an indirect bandgap [21] while the rutile has a direct bandgap [22]. Rutile phase in bulk is known to be the most thermodynamically stable phase of TiO_2 [18]. Anatase, with heat treatment around 550 °C, can be converted into the rutile phase [23].

TiO_2 has been one of the most extensively studied semiconductor materials in the last decades due to its high stability, non-toxicity and low cost [24-26]. TiO_2 has significant electrical and optical properties, thus it has been widely used in photocatalysis [27], water and air purification [28], as a solar cell [29, 30] and photo-electrochemical (PEC) water splitting [31].

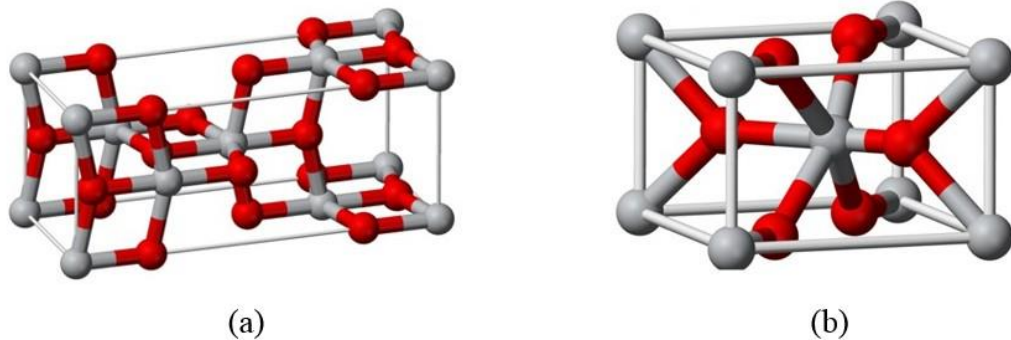


Fig. 2.8: crystal structures of two phases of TiO_2 , namely (a) anatase and (b) rutile. Here, Oxygen atoms are represented by red circles and Titanium atoms are in grey colour [18].

2.6.2 INDIUM OXIDE (In_2O_3)

Indium oxide (In_2O_3) is one of the most studied transparent conducting oxides (TCOs) [32]. It is a direct wide bandgap (3.6–3.75 eV) n-type semiconductor [33] and is known for its high electrical conductivity and high optical transparency [34]. Oxygen related defects, oxygen vacancies and indium interstitials, which behave as donors are the source of n-type conductivity [35]. It is used as a transparent conducting film in photovoltaic devices [36], in flat panel displays, electrochromic mirror [37] and UV light detectors [38]. It can also be used as a gas sensor due to its sensitivity to the ambient conditions [39].

At ambient conditions, In_2O_3 occurs in a cubic bixbyite type structure with a lattice constant of $a = 10.117 \text{ \AA}$ [40]. Four other polymorphs structures can be obtained at high pressure and temperature. One of these is rhombohedral corundum type and the other three are orthorhombic phases, namely Rh_2O_3 (II)-type, Rh_2O_3 (III)-type and orthorhombic $\alpha\text{-Gd}_2\text{S}_3$ -type [41, 42].

REFERENCES

1. Grundmann, M., *The Physics of Semiconductors: An Introduction Including Devices and Nanophysics*. 2006, Springer, Berlin.
2. Sze, S.M., *Semiconductor devices: physics and technology*. 2008: John Wiley & Sons.
3. Kittel, C., *Introduction to solid state physics*. 2005: Wiley.
4. Neamen, D.A., *Semiconductor Physics and Devices: Basic Principles*. 2012: McGraw-Hill Education.
5. Sze, S.M. and K.K. Ng, *Physics of semiconductor devices*. 2006: John wiley & sons.
6. Davies, J.H., *The physics of low-dimensional semiconductors: an introduction*. 1997: Cambridge university press.
7. Henini, M., *Quantum dot nanostructures*. *Materials today*, 2002. **5**(6): p. 48-53.
8. Colinge, J.-P. and C.A. Colinge, *Physics of semiconductor devices*. 2005: Springer Science & Business Media.
9. Fang, Z., et al., *Photoluminescence of InSb, InAs, and InAsSb grown by organometallic vapor phase epitaxy*. *Journal of Applied Physics*, 1990. **67**(11): p. 7034-7039.
10. Varshni, Y.P., *Temperature dependence of the energy gap in semiconductors*. *physica*, 1967. **34**(1): p. 149-154.
11. Pauling, L., *The nature of the chemical bond. IV. The energy of single bonds and the relative electronegativity of atoms*. *J. Am. Chem. Soc*, 1932. **54**(9): p. 3570-3582.

CHAPTER 2

12. Anderson, R., *Germanium-gallium arsenide heterojunctions [letter to the editor]*. IBM Journal of Research and Development, 1960. **4**(3): p. 283-287.
13. Forro, L., et al., *High mobility n-type charge carriers in large single crystals of anatase (TiO₂)*. Journal of Applied Physics, 1994. **75**(1): p. 633-635.
14. Howard, C., T. Sabine, and F. Dickson, *Structural and thermal parameters for rutile and anatase*. Acta Crystallographica Section B: Structural Science, 1991. **47**(4): p. 462-468.
15. Tang, H., et al., *Electrical and optical properties of TiO₂ anatase thin films*. Journal of applied physics, 1994. **75**(4): p. 2042-2047.
16. Landmann, M., E. Rauls, and W. Schmidt, *The electronic structure and optical response of rutile, anatase and brookite TiO₂*. Journal of physics: condensed matter, 2012. **24**(19): p. 195503.
17. Dambournet, D., I. Belharouak, and K. Amine, *Tailored preparation methods of TiO₂ anatase, rutile, brookite: mechanism of formation and electrochemical properties*. Chemistry of materials, 2009. **22**(3): p. 1173-1179.
18. Austin, R.H. and S.-f. Lim, *The Sackler Colloquium on promises and perils in nanotechnology for medicine*. Proceedings of the National Academy of Sciences, 2008. **105**(45): p. 17217-17221.
19. Tang, H., et al., *Urbach tail of anatase TiO₂*. Physical Review B, 1995. **52**(11): p. 7771.
20. Amtout, A. and R. Leonelli, *Optical properties of rutile near its fundamental band gap*. Physical Review B, 1995. **51**(11): p. 6842.

CHAPTER 2

21. Reddy, K.M., S.V. Manorama, and A.R. Reddy, *Bandgap studies on anatase titanium dioxide nanoparticles*. Materials Chemistry and Physics, 2003. **78**(1): p. 239-245.
22. Mo, S.-D. and W. Ching, *Electronic and optical properties of three phases of titanium dioxide: Rutile, anatase, and brookite*. Physical Review B, 1995. **51**(19): p. 13023.
23. Inagaki, M., et al., *Preparation of stable anatase-type TiO₂ and its photocatalytic performance*. International Journal of Inorganic Materials, 2001. **3**(7): p. 809-811.
24. Sarkar, M.B., et al., *Enlarged broad band photodetection using Indium doped TiO₂ alloy thin film*. Journal of Alloys and Compounds, 2014. **615**: p. 440-445.
25. Hashimoto, K., H. Irie, and A. Fujishima, *TiO₂ photocatalysis: a historical overview and future prospects*. Japanese journal of applied physics, 2005. **44**(12R): p. 8269.
26. Chinnamuthu, P., et al., *Band gap enhancement of glancing angle deposited TiO₂ nanowire array*. Journal of Applied Physics, 2012. **112**(5): p. 054315.
27. Henderson, M.A., *A surface science perspective on photocatalysis*. Surface Science Reports, 2011. **66**(6): p. 185-297.
28. Fujishima, A., X. Zhang, and D.A. Tryk, *TiO₂ photocatalysis and related surface phenomena*. Surface Science Reports, 2008. **63**(12): p. 515-582.
29. Diebold, U., *The surface science of titanium dioxide*. Surface science reports, 2003. **48**(5): p. 53-229.

CHAPTER 2

30. Park, N.v., J. Van de Lagemaat, and A. Frank, *Comparison of dye-sensitized rutile-and anatase-based TiO₂ solar cells*. 2000, National Renewable Energy Laboratory (NREL), Golden, CO.
31. Fujishima, A. and K. Honda, *Electrochemical photolysis of water at a semiconductor electrode*. *nature*, 1972. **238**(5358): p. 37-38.
32. King, P., et al., *Surface electron accumulation and the charge neutrality level in In₂O₃*. *Physical review letters*, 2008. **101**(11): p. 116808.
33. Kim, H.S., et al., *High performance solution-processed indium oxide thin-film transistors*. *Journal of the American Chemical Society*, 2008. **130**(38): p. 12580-12581.
34. Klein, A., *Electronic properties of In₂O₃ surfaces*. *Applied Physics Letters*, 2000. **77**(13): p. 2009-2011.
35. Dakhel, A., *Effect of ytterbium doping on the optical and electrical properties of intrinsic In₂O₃ thin films*. *Microelectronics Reliability*, 2010. **50**(2): p. 211-216.
36. Granqvist, C.G. and A. Hultåker, *Transparent and conducting ITO films: new developments and applications*. *Thin solid films*, 2002. **411**(1): p. 1-5.
37. Murali, A., et al., *Synthesis and characterization of indium oxide nanoparticles*. *Nano Letters*, 2001. **1**(6): p. 287-289.
38. Ghosh, A., et al., *Detailed investigation of defect states in Erbium doped In₂O₃ thin films*. *Materials Research Bulletin*, 2018. **99**: p. 211-218.
39. Li, C., et al., *In₂O₃ nanowires as chemical sensors*. *Applied Physics Letters*, 2003. **82**(10): p. 1613-1615.
40. Galazka, Z., et al., *Melt growth, characterization and properties of bulk In₂O₃ single crystals*. *Journal of Crystal Growth*, 2013. **362**: p. 349-352.

CHAPTER 2

41. Bekheet, M.F., et al., *Orthorhombic In₂O₃: a metastable polymorph of indium sesquioxide*. *Angewandte Chemie International Edition*, 2013. **52**(25): p. 6531-6535.
42. Sans, J., et al., *Structural and vibrational properties of corundum-type In₂O₃ nanocrystals under compression*. *Nanotechnology*, 2017. **28**(20): p. 205701.

DEFECTS IN SEMICONDUCTORS AND THEIR PROPERTIES

In this chapter, different types of defects in semiconductors are discussed. A classification of semiconductor defects in terms of their dimensions is presented. The effect of defects as generation and recombination centres on the carrier kinetics processes, and the deep level defects are also covered in this chapter. In addition, defects in TiO_2 and In_2O_3 semiconductors are also presented.

3.1 CLASSIFICATION OF SEMICONDUCTOR DEFECTS

A perfect crystal is ideally formed by a periodic repetition of unit cells along the three directions and doesn't contain imperfections. However, it is hard to grow such a perfect crystal without any imperfections within it. The imperfections are also called crystal defects and can be either intrinsic or extrinsic (due to the introduction of impurities into the crystal) defects. Extrinsic defects can be introduced intentionally (by doping) to reach some specified electrical and optical properties or can be unintentional during the growth processes. According to their dimensions, defects are categorized as point defect and extended defects. In this section, different types of defects will be covered.

3.1.1 POINT DEFECTS

A point defect, also known as zero dimension defect, is formed when a host atom is missing or an atom occupies an irregular site in the crystal. Point defects can be classified as follows [1, 2]:

- a) **Vacancy defect:** also known as Schottky defect is formed when an atom is missing from a regular site. An example of a vacancy defect is illustrated in Fig. 3.1 (a).
- b) **Substitutional defect:** this kind of defect is formed when a host atom is replaced by a foreign atom on a regular lattice site as shown in Fig. 3.1 (b). There is a special case of substitutional defect called antisite. This type occurs in compound semiconductors, where a host atom replaces and occupies a site of another host atom. Fig. 3.1 (c) shows an example of antisite where an As atom occupies a regular site of a Ga atom in GaAs material.
- c) **Interstitial defect:** is obtained when an atom is inserted into an irregular site in the lattice. There are two types of interstitial. An interstitial defect is called a self-interstitial when the atom is one of the host material and a foreign interstitial in case of a foreign or an impurity atom. Fig. 3.1 (d) shows both self and foreign interstitial defects.

These point defects not just disturb the periodicity of the crystal but also alter the electrical properties of the material and in some cases, play an important role in the conductivity of the material [2].

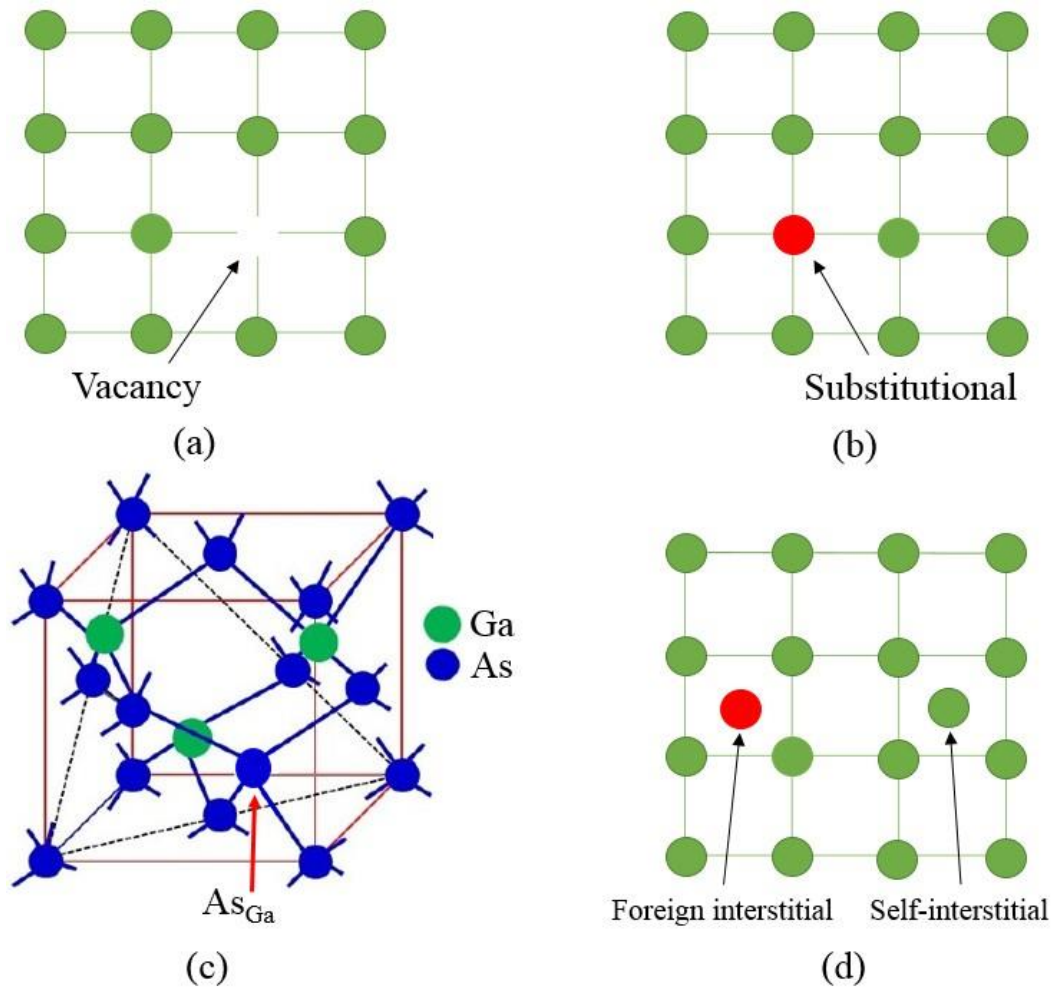


Fig. 3.1: Illustration of (a) vacancy, (b) substitutional, (c) antisite and (d) interstitial defects.

3.1.2 COMPLEXES OF POINT DEFECTS

A complex point defect is formed when at least two point defects interact with each other and form what is known as a pair defect. There are different types of complex point defects. A selection of these complex point defects is presented in this section [3].

- a) **Frenkel defect**: this defect is created when a vacancy and a self-interstitial defects are bonded together and form a complex defect as illustrated in Fig. 3.2 (a).

- b) Split-interstitial defect:** this is a type of complex defect where two interstitial defects, either the two are self-interstitials or foreign interstitials, form a pair as shown in Fig. 3.2 (b).
- c) Vacancy complexes:** there are three different kinds of vacancy complexes. A **Di-vacancy** is obtained when two vacancies form a pair. However, if two vacancies in addition to an interstitial form a pair, a complex vacancy called a **split vacancy** is created. The third type of complex vacancy is called a **vacancy-impurity complex** and is formed by a vacancy and a foreign interstitial. A diagram of these vacancy complexes is shown in Fig. 3.2 (c).
- d) Impurity pair:** this complex defect is formed by two impurity atoms, one of them is located in an interstitial site while the other one is replacing a host atom in a regular site in the lattice (substitutional impurity). An example of this kind of complex is shown in Fig. 3.2 (d).

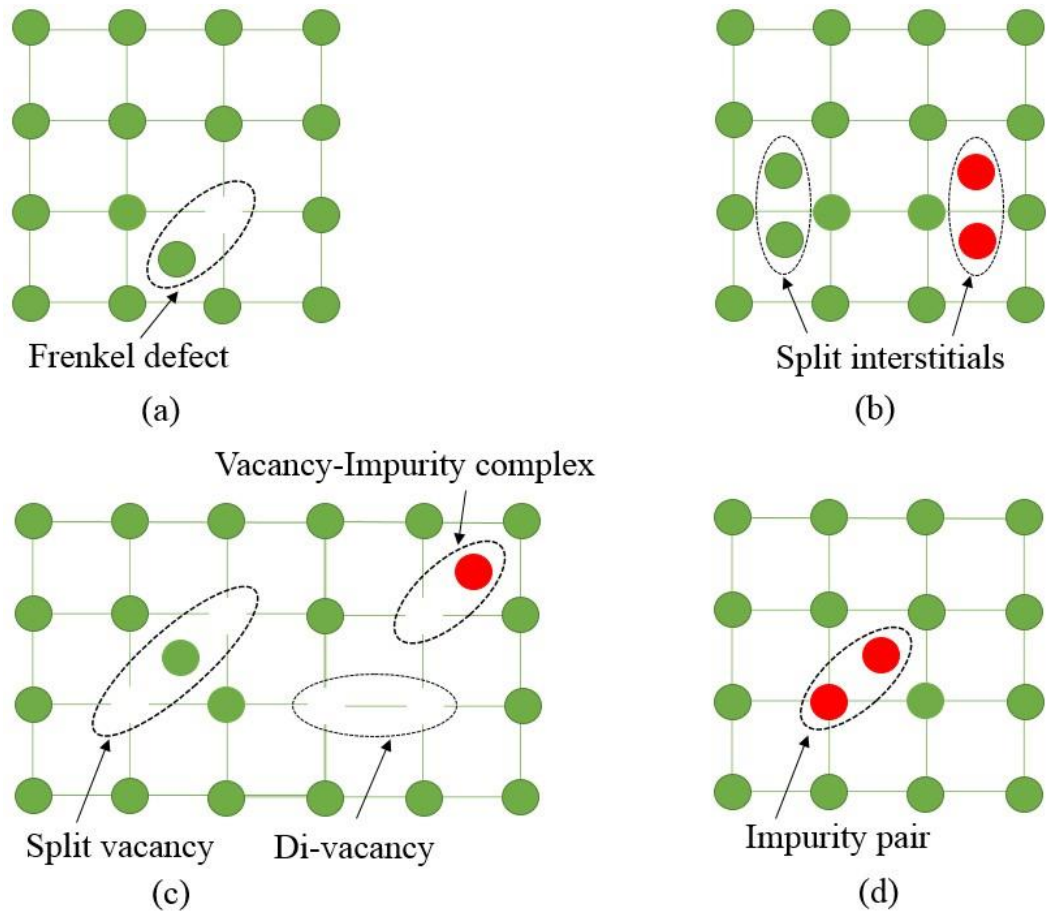


Fig. 3.2: complexes of point defects. (a) Frenkel defect, (b) Split-interstitials, (c) vacancy complexes and (c) Impurity pair.

3.1.3 LINEAR DEFECTS

In addition to the point defect, there are dislocation defects which are known as linear defects or one-dimensional defects. In these kinds of defects, not just an atom is moved from a regular lattice site but a line of atoms is displaced. Dislocation defects are common defects in semiconductors and interact with all other kinds of defects [4]. Among different types of dislocation, screw and edge dislocations are the two main types. A screw dislocation is formed when one part of the crystal is displaced with respect to the other as shown in Fig. 3.3 (a) [5]. However, Fig. 3.3 (b) shows an edge dislocation which occurs when an extra half

plane is inserted into the crystal and causes a dislocation of the surrounded atoms [1].

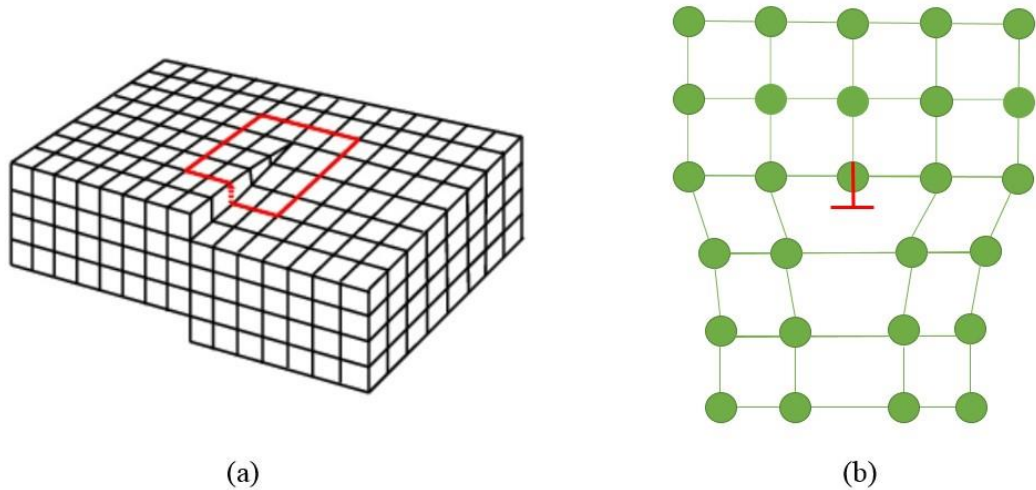


Fig. 3.3: Representation of (a) screw [5] and (b) edge dislocations.

3.2 DEFECTS AND THEIR CARRIER KINETICS

In this section, the classification of defects in terms of their energies will be discussed. In addition, the mechanism of the generation-recombination process will be explained in details.

3.2.1 SHALLOW AND DEEP LEVELS IMPURITIES

Any kind of impurity can play an important role in the electrical and optical properties of a semiconductor when it has its energy level within the bandgap of the semiconductor. Therefore, defects are categorized according to their positions with respect to the conduction and valence bands into shallow and deep levels [6]. Defects that have energy closer to the conduction band or valence band are called

CHAPTER 3

shallow level impurities. Shallow levels have low ionisation energies (< 0.025 eV) which can be easily ionised at room temperature, thus increasing the electrical conductivity of the material. Shallow level defects, which are due to dopant atoms that are intentionally incorporated into the semiconductor, are known as shallow donors if they donate electrons to the conduction band of the host material, or shallow acceptors if they donate holes to the valence band [7, 8]. On the other hand, defects with energy levels equal to or greater than 0.1 eV below the conduction band or above the valence band are called deep-level impurities [9, 10]. The contribution of these defects to the current flow is too small because they cannot be ionised at room temperature. Deep levels are very important and play a major role in semiconductors because they can behave as generation-recombination or trapping centres. Fig. 3.4 shows the shallow and deep levels within the bandgap of a semiconductor.

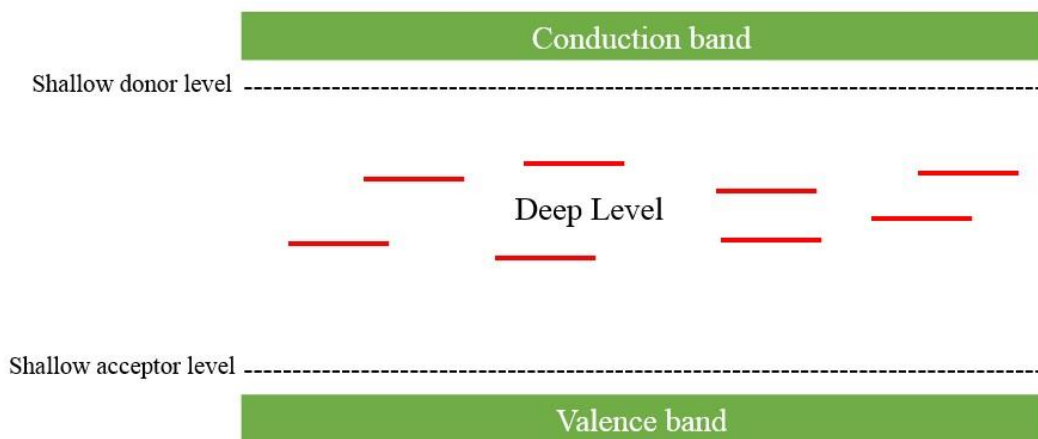


Fig. 3.4: A diagram of shallow and deep level impurities.

3.2.2 SHOCKLEY-READ-HALL THEORY

Deep-level impurities in a semiconductor are also known as trap centres and generation-recombination (G-R) centres. At equilibrium, the emission and capture rates of carriers are used to determine the occupancy of a deep level. Recombination of electrons and holes occurs in a semiconductor in two ways. Direct recombination, a band to band process, usually occurs in pure semiconductors, while indirect recombination happens via deep energy levels that are present within the bandgap of the material.

The mechanism of the generation and recombination of charge carriers through deep levels was explained by Shockley and Read [11]. This was also described, independently, by R. N. Hall [12]. Fig. 3.5 [13] is used to explain the generation-recombination process. Consider a deep-level impurity with energy E_T within the forbidden gap that has concentration N_T which is distributed throughout the semiconductor. First, assume an electron from the conduction band is captured by the centre (Fig. 3.5 (a)), this captured electron can be characterized by its electron capture coefficient (c_n). After that, the electron in the centre can be even emitted back to the conduction band (electron emission (e_n)), shown by Fig. 3.5 (b), or a hole from the valence band can be captured by the centre, which is called a hole capture (c_p) (Fig. 3.5 (c)). If either of these processes happen, the deep centre will be occupied by a hole, again with two possible results. The centre can emit the hole back to the valence band (hole emission e_p) as appears in Fig. 3.5 (d), or can capture an electron from the conduction band (Fig. 3.5 (a)). Note that process (d) is sometimes considered as electron emission from the valence band to the centre, represented by the dashed arrow in Fig. 3.5 (d). These four processes are the only possible processes that can happen between the conduction band, the impurity

CHAPTER 3

energy levels, and the valence band. When an electron is captured (Fig. 3.5 (a)) followed by capturing a hole (Fig. 3.5 (c)), this process is called a recombination. However, a generation process happens when an electron is emitted to the conduction band (Fig. 3.5 (b)) followed by emitting a hole to the valence band (Fig. 3.5 (d)). On the other hand, a third process called trapping can also occur, which is neither generation nor recombination. A deep level is called a trap centre when a capture of an electron is followed by emitting that electron back to the conduction band, or a capture of a hole is followed by emitting that hole back to the valence band. In the trapping process, only the conduction band or valence band participates in the process with the impurity level. In the recombination or generation process, both the conduction and valence bands, in addition to the impurity level, participate in the process [13].

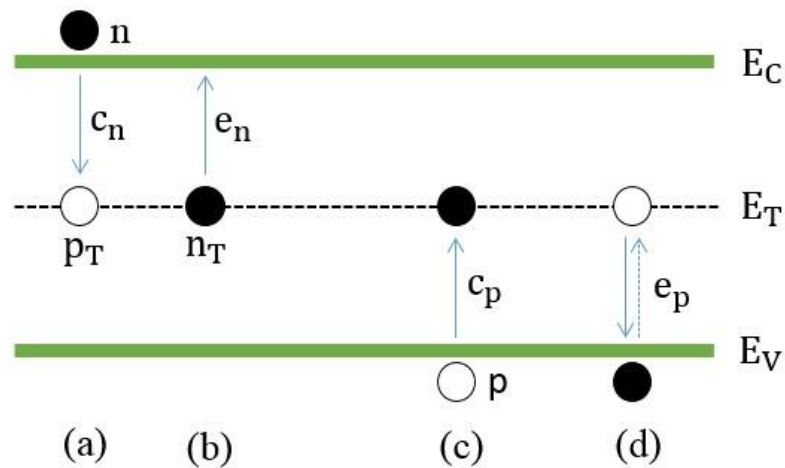


Fig. 3.5: (G-R) processes: (a) electron capture, (b) electron emission, (c) hole capture, and (d) hole emission.

CHAPTER 3

The centres located in the upper half of the bandgap usually have an electron emission rate much higher than the hole emission rate. Similarly, for the centres in the lower half, the hole emission rate is greater than the electron emission rate. Generally, for most centres, one emission rate usually dominates while the other can be neglected. A G-R centre can be either occupied by an electron or a hole. The centre is said to be in a n_T state when occupied by an electron, while it is in a p_T state when occupied by a hole. The n_T state is neutral and p_T is positive charge when the G-R centre is a donor. However, in the case of an acceptor centre, n_T is a negative charge and p_T is neutral. The total density of G-R centres (N_T) filled by electrons (n_T) or holes (p_T), note that a centre is either occupied by an electron or a hole, is given by

$$N_T = n_T + p_T \quad (3.1)$$

The density of electrons in the conduction band (n), the density of holes in the valence band (p) and the state of the centre n_T or p_T change together with time. It is important to know the rate of change with time of these parameters. Emission of electrons increases the density of electrons in the conduction band (n) while electron capture decreases them. So, the change of (n) with respect to time due to the G-R process can be written as

$$\left. \frac{dn}{dt} \right|_{G-R} = (b) - (a) = e_n n_T - n c_n p_T \quad (3.2)$$

where (a) and (b) are electron capture and electron emission processes.

Note that radiative and Auger processes are not considered in the above equation. Only the emission and capture processes that happen through the G-R centres are considered, as indicated by the G-R subscript. It should also be noted that there is no need for electrons in the conduction band (n) during the emission of electrons from the centre. This process depends only on the emission rate (e_n) and the

CHAPTER 3

electron density in the G-R centre (n_T). However, electrons in the conduction band (n) are necessary for the electron capture process to happen. In case of the hole density (p) in the valence band, the change of p over time is given by

$$\left. \frac{dp}{dt} \right|_{G-R} = (d) - (c) = e_p p_T - p c_p n_T \quad (3.3)$$

where (c) and (d) are hole capture and hole emission processes.

Note that the electron capture coefficient c_n (or hole capture coefficient c_p) depends on the electron (hole) thermal velocity $\langle v_n \rangle_{th}$ ($\langle v_p \rangle_{th}$) and the electron (hole) capture cross section of the G-R centre, so it is defined as

$$c_n = \sigma_n \langle v_n \rangle_{th} \quad (3.4)$$

Similarly, the hole capture coefficient is given by

$$c_p = \sigma_p \langle v_p \rangle_{th} \quad (3.5)$$

The density of a G-R centre changes with time when an electron or a hole is captured or emitted. This change with time is given by

$$\left. \frac{dn_T}{dt} \right|_{G-R} = \frac{dp}{dt} - \frac{dn}{dt} = (c_n n + e_p)(N_T - n_T) - (c_p p + e_n)n_T \quad (3.6)$$

In the steady-state case, the density is $\frac{dn_T}{dt} = 0$, so

$$(c_n n + e_p)(N_T - n_T) = (c_p p + e_n)n_T \quad (3.7)$$

And therefore,

$$n_T = \frac{(c_n n + e_p)N_T}{c_n n + e_n + c_p p + e_p} \quad (3.8)$$

Equation 3.8 is considered to be the base equation for most deep-level impurity measurements [13]. At thermal equilibrium, the rate of emission and the rate of capture are the same according to the detail balance principle. Thus,

$$e_n n_T = n c_n p_T \quad (3.9)$$

By using Equation 3.4, Equation 3.9 can be written as

CHAPTER 3

$$e_n n_T = n \sigma_n \langle v_n \rangle_{th} p_T \quad (3.10)$$

Similarly, in case of holes,

$$e_p p_T = p \sigma_p \langle v_p \rangle_{th} n_T \quad (3.11)$$

Considering the Fermi-Dirac distribution function (f) to be the number of states occupied by electrons, then the number of states occupied by holes is $(1-f)$. The Fermi-Dirac distribution function is given by

$$f = \left[\frac{1}{1 + \exp\left(\frac{E_T - E_f}{k_B T}\right)} \right] \quad (3.12)$$

where E_T , E_f , k_B and T are deep level energy, Fermi level energy, the Boltzmann constant and temperature, respectively. By using f , the total density of the centres (equation 3.1) can be given as

$$N_T = N_T f + N_T (1 - f) \quad (3.13)$$

Note that $n_T = N_T f$ and $p_T = N_T (1 - f)$. Equation 3.10 can be written by using Equations 3.12 and 3.13, as

$$e_n N_T f = n \sigma_n \langle v_n \rangle_{th} N_T (1 - f)$$

$$e_n = n \sigma_n \langle v_n \rangle_{th} \left(\frac{1 - f}{f} \right)$$

$$\text{where } \left(\frac{1 - f}{f} \right) = \exp\left(\frac{E_T - E_f}{k_B T}\right)$$

$$e_n = n \sigma_n \langle v_n \rangle_{th} \exp\left(\frac{E_T - E_f}{k_B T}\right) \quad (3.14)$$

The electron density in the conduction band (n) is given by

$$n = n_i \exp\left(\frac{E_f - E_i}{k_B T}\right) = N_c \exp\left(\frac{E_c - E_f}{k_B T}\right) \quad (3.15)$$

Note that $n_i = N_c \exp\left(\frac{E_i - E_c}{k_B T}\right)$ is the density of the states of the intrinsic material. By using Equation 3.15, the emission of electrons (Equation 3.14) and the emission of holes can be written as

$$e_n = N_c \sigma_n \langle v_n \rangle_{th} \exp\left(-\frac{E_c - E_T}{k_B T}\right) \quad (3.16)$$

$$e_p = N_v \sigma_p \langle v_p \rangle_{th} \exp\left(-\frac{E_T - E_v}{k_B T}\right) \quad (3.17)$$

Note that $N_c = 2\left(\frac{2\pi m_e^* k_B T}{h^2}\right)^{3/2}$ and $N_v = 2\left(\frac{2\pi m_h^* k_B T}{h^2}\right)^{3/2}$ are the density of states

in the conduction and valence bands, respectively. $\langle v_n \rangle_{th} = \frac{\sqrt{3k_B T}}{m_e^*}$ and $\langle v_p \rangle_{th} =$

$\frac{\sqrt{3k_B T}}{m_h^*}$ are the thermal velocity of electron and hole, respectively. Note that m_e^* and

m_h^* are the effective mass of the electrons and holes, respectively. Therefore,

Equations 3.16 and 3.17 can be rewritten as

$$e_n = AT^2 \sigma_n \exp\left(-\frac{E_c - E_T}{k_B T}\right) \quad (3.18)$$

$$e_p = BT^2 \sigma_p \exp\left(-\frac{E_T - E_v}{k_B T}\right) \quad (3.19)$$

where $A = 2\frac{\sqrt{3k_B}}{m_e^*} \left(\frac{2\pi m_e^* k_B}{h^2}\right)^{3/2}$ and $B = \frac{\sqrt{3k_B}}{m_h^*} \left(\frac{2\pi m_h^* k_B}{h^2}\right)^{3/2}$ are constants.

The activation energy of a deep-level defect (E_T) is considered to be the most important parameter since it shows the position of that defect within the bandgap.

The Arrhenius plot of $\left(\frac{e_{n,p}}{T^2}\right)$ versus $\left(\frac{1000}{T}\right)$ yields a straight line where the activation energy can be obtained from the slope of this line.

3.3 DEFECTS IN COMPOUND SEMICONDUCTORS

Semiconductor materials are widely used in electronic and optoelectronic devices. Different techniques can be used to grow the semiconductor devices. Unfortunately, none of these techniques can produce a perfect crystal. Hence, defects are present in almost all such devices. Usually, defects alter the electrical and optical properties and therefore affect the performance of the devices. It is, therefore, extremely important to investigate these defects and how to annihilate

them in order to grow and fabricate high-quality crystals and devices. In this section, a literature review of defects in TiO₂ and In₂O₃ will be presented.

3.3.1 DEFECTS IN TITANIUM DIOXIDE (TiO₂)

TiO₂ is a Transparent Conducting Oxides (TCO) material which has been extensively studied due to its interesting electrical and optical properties [14]. It has wide applications in terms of photocatalysis, water and air purification, solar cells and photo-electrochemical (PEC) water splitting [15-19]. In TCOs materials, point defects, especially vacancies and interstitials, are well known defects and they will alter the both the electronic structure and the chemical properties of the materials [20]. TiO₂ is an n-type semiconductor [21]. Oxygen vacancies and titanium interstitials defects are the cause of the n-type conductivity of a pure TiO₂ [22]. Oxygen vacancies are the predominant type of point defects in TiO₂ [23-26]. E. Wang *et al.* [27] studied indium doped TiO₂ containing different indium concentrations using sol-gel techniques. In this study, photoluminescence measurements have been carried out in a pure TiO₂ where two peaks around 480 nm and 525 nm have been observed. These peaks have been obtained as a result of the transition from oxygen vacancies with two trapped electrons and one trapped electron to the valence band of TiO₂. The energy levels of these oxygen vacancies were found to be 0.51 and 0.82 eV. However, for In doped TiO₂ samples, a surface state energy at 0.3 eV from the conduction band has been detected and the origin of this trap is assigned to O-In-Cl_x species. As In content increases, the absorption at 400-800 nm, which is due to electronic transition from valence band to the O-In-Cl_x species, is enhanced. In a different study, B. Morgan and G. Watson [28] have investigated the formation of native defects in anatase TiO₂ using density functional

theory and allocated two traps, 0.5 eV and 0.9 eV, to Ti^{+3} state and oxygen vacancy, respectively. T. Miyagi *et al.* [29] have used Deep Level Transient Spectroscopy (DLTS) technique to investigate the deep levels in Nb-doped anatase TiO_2 grown on a $SrTiO_3$ (001) substrate by metalorganic chemical vapour deposition. A trap with an activation energy of 0.13 eV has been observed in pure TiO_2 and the origin of this trap has been assigned to oxygen vacancies or Ti interstitial. However, in the Nb-doped TiO_2 films, two deep levels with 0.32 eV and 0.67 eV energies below the bottom of the conduction band have been detected and assigned to Nb ions. In a similar study, T. Miyagi *et al.* [30] have discovered a deep level of 0.96 eV below the conduction band with a large capture cross section of $8.3 \times 10^{-13} \text{ cm}^2$. The authors have suggested that this deep level is related to a line defect rather than a point defect due to the large value of the capture cross section. On the other hand, K. Kobayashi *et al.* [31] have used the admittance spectroscopic technique to investigate the deep levels in Nb-doped rutile TiO_2 . Two deep levels with energies of 0.24 and 0.37 eV have been observed. The origin of the trap 0.37 eV has been assigned to an oxygen vacancy, while Nb ions or impurity levels due to unintentional impurities are the two possible origins for the 0.24 eV trap.

3.3.2 DEFECTS IN INDIUM OXIDE (In_2O_3)

In_2O_3 is one of the most investigated Metal Oxide Semiconductor (MOS) material due to its high carrier mobility ($\sim 43.7 \text{ cm}^2/\text{V.s}$) as compared to other TCO materials [32]. It is an n-type semiconductor with a direct wide bandgap of 3.6 – 3.75 eV [33]. In_2O_3 can be used as a gas sensor due to its sensitivity to the ambient conditions [34]. It is also used as transparent conducting film in photovoltaic

devices [35], flat panel displays, electrochromic mirrors [36] and UV light detectors [37].

H. Zhu et al. [38] in their study of self-assembled 3D microflowery $\text{In}(\text{OH})_3$ architecture and its conversion to In_2O_3 have found a strong blue emission (422 nm) by photoluminescence (PL) technique. This was attributed to recombination of photoexcited holes and electrons occupying the oxygen vacancies. According to H. Zhu et al., these oxygen vacancies act as deep donor levels. Another PL investigation of In_2O_3 by M. S. Lee et al. [39] revealed a visible emission at 637 nm in their oxidized indium thin films using thermal treatment. This visible emission was assigned to oxygen vacancies formed within the bandgap of the In_2O_3 . P. Reunchan et al. [40] investigated the electronic and structural properties of oxygen and indium vacancies in In_2O_3 by first-principles calculations which are based on density functional theory (DFT). They reported a defect level at 0.2 eV and attributed it to an oxygen vacancy. Tomita et al. [41] have studied the origin of n-type conductivity in undoped In_2O_3 . They have detected two indium vacancies (0.083 and 0.094 eV) which form shallow acceptor levels. They have also found a defect with an energy of 0.1 eV and suggested the origin of this defect to be a complex of oxygen vacancy-indium interstitial. They suggested that the oxygen vacancies are deep levels and hence cannot act as native donors. However, indium interstitials are shallow donors and with the coexistence of oxygen vacancies can form even shallower donor levels and hence act as native donors [41].

REFERENCES

1. Kittel, C., *Introduction to solid state physics*. 2005: Wiley.
2. Neamen, D.A., *Semiconductor Physics and Devices: Basic Principles*. 2012: McGraw-Hill Education.
3. Bourgoin, J., *Point defects in Semiconductors II: Experimental aspects*. Vol. 35. 2012: Springer Science & Business Media.
4. Holt, D.B. and B.G. Yacobi, *Extended defects in semiconductors: electronic properties, device effects and structures*. 2007: Cambridge University Press.
5. de Juan, F., A. Cortijo, and M.A. Vozmediano, *Dislocations and torsion in graphene and related systems*. Nuclear physics B, 2010. **828**(3): p. 625-637.
6. Li, S.S., *Semiconductor physical electronics*. 2012: Springer Science & Business Media.
7. McCluskey, M.D. and E.E. Haller, *Dopants and defects in semiconductors*. 2012: CRC Press.
8. Grimmeiss, H., *Deep level impurities in semiconductors*. Annual Review of Materials Science, 1977. **7**(1): p. 341-376.
9. Keldysh, L., *Deep levels in semiconductors*. Sov. Phys. JETP, 1964. **18**(1): p. 253.
10. Willardson, R.K. and A.C. Beer, *Semiconductors and semimetals*. Vol. 12. 1977: Academic press.
11. Shockley, W. and W. Read Jr, *Statistics of the recombinations of holes and electrons*. Physical review, 1952. **87**(5): p. 835.
12. Hall, R.N., *Electron-hole recombination in germanium*. Physical review, 1952. **87**(2): p. 387.

CHAPTER 3

13. Schroder, D.K., *Semiconductor material and device characterization*. 2006: John Wiley & Sons.
14. Duenas, S., et al., *A comparative study of the electrical properties of TiO₂ films grown by high-pressure reactive sputtering and atomic layer deposition*. *Semiconductor science and technology*, 2005. **20**(10): p. 1044.
15. Henderson, M.A., *A surface science perspective on photocatalysis*. *Surface Science Reports*, 2011. **66**(6): p. 185-297.
16. Fujishima, A., X. Zhang, and D.A. Tryk, *TiO₂ photocatalysis and related surface phenomena*. *Surface Science Reports*, 2008. **63**(12): p. 515-582.
17. Diebold, U., *The surface science of titanium dioxide*. *Surface science reports*, 2003. **48**(5): p. 53-229.
18. Fujishima, A. and K. Honda, *Electrochemical photolysis of water at a semiconductor electrode*. *nature*, 1972. **238**(5358): p. 37-38.
19. Park, N.v., J. Van de Lagemaat, and A. Frank, *Comparison of dye-sensitized rutile-and anatase-based TiO₂ solar cells*. 2000, National Renewable Energy Laboratory (NREL), Golden, CO.
20. Ganduglia-Pirovano, M.V., A. Hofmann, and J. Sauer, *Oxygen vacancies in transition metal and rare earth oxides: Current state of understanding and remaining challenges*. *Surface Science Reports*, 2007. **62**(6): p. 219-270.
21. Forro, L., et al., *High mobility n-type charge carriers in large single crystals of anatase (TiO₂)*. *Journal of Applied Physics*, 1994. **75**(1): p. 633-635.
22. Mattioli, G., et al., *Deep versus shallow behavior of intrinsic defects in rutile and anatase TiO₂ polymorphs*. *The Journal of Physical Chemistry C*, 2010. **114**(49): p. 21694-21704.

CHAPTER 3

23. Ramamoorthy, M., R. King-Smith, and D. Vanderbilt, *Defects on TiO₂ (110) surfaces*. Physical Review B, 1994. **49**(11): p. 7709.
24. Wu, X., et al., *Oxygen vacancy mediated adsorption and reactions of molecular oxygen on the TiO₂ (110) surface*. Physical Review B, 2003. **68**(24): p. 241402.
25. Mackrodt, W., E.-A. Simson, and N. Harrison, *An ab initio Hartree-Fock study of the electron-excess gap states in oxygen-deficient rutile TiO₂*. Surface science, 1997. **384**(1-3): p. 192-200.
26. Hameeuw, K., et al., *Influence of surface and subsurface defects on the behavior of the rutile TiO₂ (110) surface*. physica status solidi (a), 2006. **203**(9): p. 2219-2222.
27. Wang, E., W. Yang, and Y. Cao, *Unique surface chemical species on indium doped TiO₂ and their effect on the visible light photocatalytic activity*. The Journal of Physical Chemistry C, 2009. **113**(49): p. 20912-20917.
28. Morgan, B.J. and G.W. Watson, *Polaronic trapping of electrons and holes by native defects in anatase TiO₂*. Physical Review B, 2009. **80**(23): p. 233102.
29. Miyagi, T., et al., *Photocatalytic property and deep levels of Nb-doped anatase TiO₂ film grown by metalorganic chemical vapor deposition*. Japanese journal of applied physics, 2004. **43**(2R): p. 775.
30. Miyagi, T., et al., *Deep level transient spectroscopy analysis of an anatase epitaxial film grown by metal organic chemical vapor deposition*. Japanese Journal of Applied Physics, 2001. **40**(4B): p. L404.

CHAPTER 3

31. Kobayashi, K., et al., *Investigation of trapping states in a Nb-doped rutile by admittance spectroscopy*. Journal of applied physics, 1986. **60**(12): p. 4191-4196.
32. Ghosh, A., et al., *Removal of oxygen related defects from chemically synthesized In₂O₃ thin film doped with Er by spin-on technique*. Journal of Alloys and Compounds, 2017. **695**: p. 1260-1265.
33. Kim, H.S., et al., *High performance solution-processed indium oxide thin-film transistors*. Journal of the American Chemical Society, 2008. **130**(38): p. 12580-12581.
34. Li, C., et al., *In₂O₃ nanowires as chemical sensors*. Applied Physics Letters, 2003. **82**(10): p. 1613-1615.
35. Granqvist, C.G. and A. Hultåker, *Transparent and conducting ITO films: new developments and applications*. Thin solid films, 2002. **411**(1): p. 1-5.
36. Murali, A., et al., *Synthesis and characterization of indium oxide nanoparticles*. Nano Letters, 2001. **1**(6): p. 287-289.
37. Ghosh, A., et al., *Detailed investigation of defect states in Erbium doped In₂O₃ thin films*. Materials Research Bulletin, 2018. **99**: p. 211-218.
38. Zhu, H., et al., *Self-assembled 3D microflowery In(OH)₃ architecture and its conversion to In₂O₃*. The Journal of Physical Chemistry C, 2008. **112**(39): p. 15285-15292.
39. Lee, M.-S., et al., *Characterization of the oxidized indium thin films with thermal oxidation*. Thin Solid Films, 1996. **279**(1-2): p. 1-3.
40. Reunchan, P., et al., *Vacancy defects in indium oxide: An ab-initio study*. Current Applied Physics, 2011. **11**(3): p. S296-S300.

CHAPTER 3

41. Tomita, T., et al., *The origin of n-type conductivity in undoped In₂O₃*.
Applied Physics Letters, 2005. **87**(5): p. 051911.

EXPERIMENTAL TECHNIQUES

Semiconductor materials have the ability to form many types of devices, all of which have contacts. Contacts can involve semiconductor-semiconductor contact (p-n junction), where a p-type semiconductor is brought into contact with an n-type semiconductor. An n-type and p-type semiconductor can be obtained by doping a semiconductor in such a way that makes electrons and holes the majority carriers, respectively [1]. Another form of contact is the metal-semiconductor contact, also referred to as a Schottky junction or Schottky barrier, where either the p-type or n-type in a p-n contact is replaced by a metal [2]. The main difference between a p-n contact and a Schottky barrier is in the depletion region. A depletion region formed in a p-n junction spreads to both sides when electrons in the n-type move towards the p-type and combine with the holes. This process leaves fixed negative ions on the p-type region and fixed positive ions on the n-type region. These opposite polarity ions on the two sides of the junction create a strong electric field which results in a depleted area which prevents further transfer of electrons. In the case of a Schottky barrier, the entire depletion region is on the semiconductor side since the depletion on the metal side is so small that it can be neglected. Both of these types of contacts are preferred for deep level transient spectroscopy (DLTS) measurements. In this chapter, a Schottky junction will be discussed. Furthermore, the electrical characterization techniques, namely current-voltage (I-V), capacitance-voltage (C-V), DLTS, Laplace DLTS and Photoluminescence (PL) techniques which have been used to investigate the samples in this thesis are discussed in this chapter.

4.1 SCHOTTKY DIODE

A Schottky diode is created when an appropriate metal with a work function Φ_m is brought into contact with a semiconductor having a work function Φ_s less than Φ_m , while the other side of the semiconductor is coated with a metal that creates an Ohmic contact, where the work function of the semiconductor is higher than the metal work function, with the semiconductor. Before the metal and semiconductor are brought into contact, their Fermi energy levels are different. However, when they brought into contact, the Fermi levels align due to the flow of electrons from the conduction band of the semiconductor, n-type in our case, to the metal side of the junction [2]. Fig. 4.1 schematically shows the energy bands diagrams for an isolated metal and semiconductor, whereas Fig. 4.2 represents the Schottky diode energy bands in equilibrium conditions.

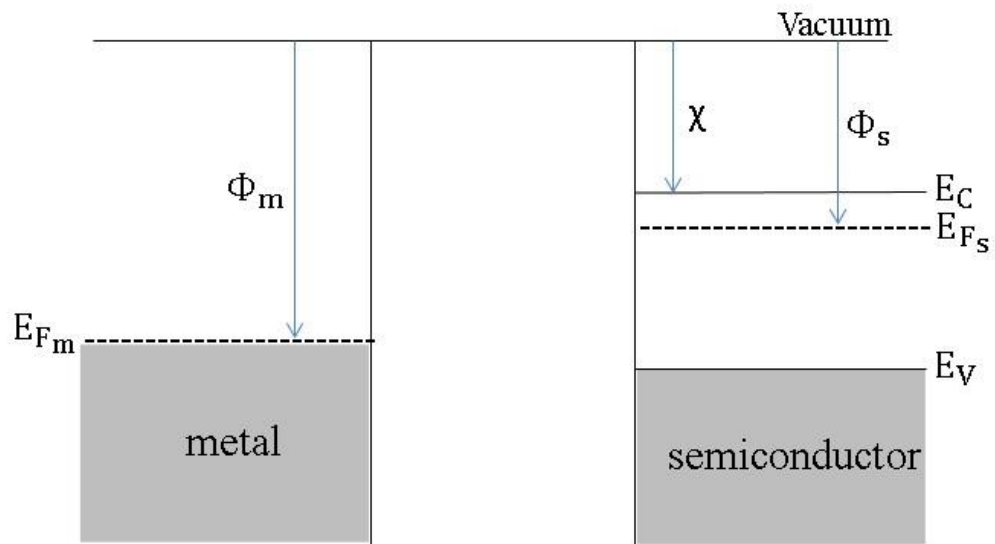


Fig. 4.1: Metal and semiconductor energy band diagrams.

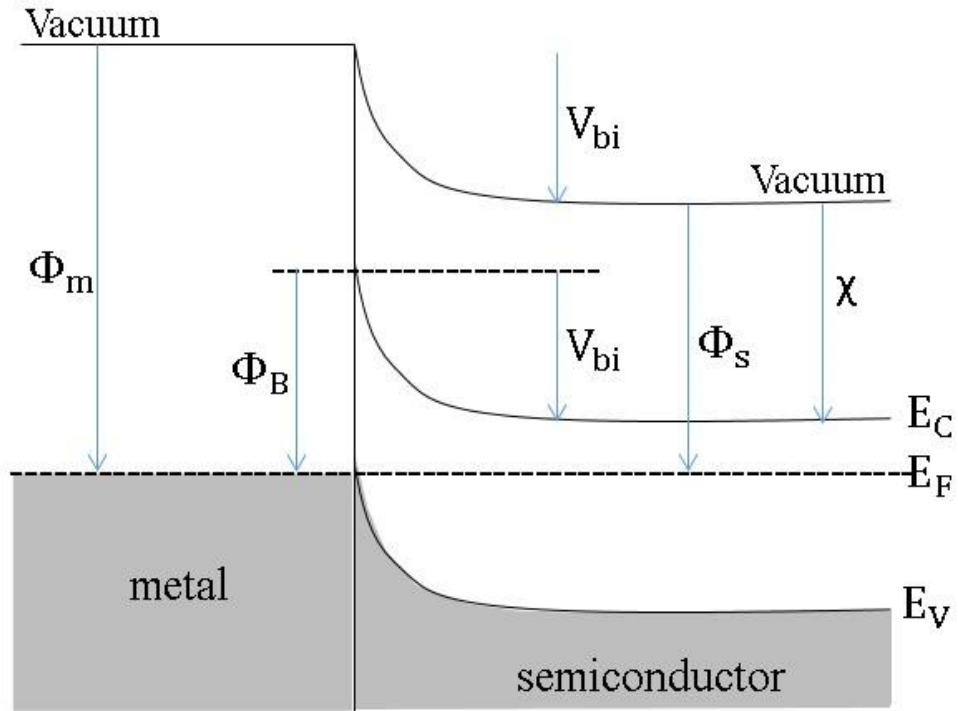


Fig. 4.2: Band diagram of a Schottky contact

Φ_m is the work function of the metal, which is the energy required to eject an electron located in the metal's Fermi level (E_{Fm}) from the metal. Φ_s is the semiconductor work function. E_C , E_V and E_F are the energies of the conduction band, valence band and Fermi level, respectively. In addition, electron affinity (χ) is the energy needed to extract an electron from the conduction band (E_C) to the vacuum. For an ideal Schottky diode, the barrier height (Φ_B) is the barrier that electrons face when moving from the metal to the semiconductor and is equal to

$$\Phi_B = \Phi_m - \chi \quad (4.1)$$

On the other hand, the curvature of the bands in the semiconductor side, which occurs due to the alignment of the Fermi level and the depletion region, creates what is called a built-in potential (V_{bi}), which prevents further electron flow from the semiconductor to the metal side of the junction. The built-in potential is given by:

$$V_{bi} = \Phi_m - \Phi_s \quad (4.2)$$

4.1.1 DEPLETION REGION

When a metal and an n-type semiconductor are brought into contact, electrons from the semiconductor start to migrate to the metal side until a balance in the Fermi levels for both the metal and semiconductor is reached. The migration of electrons leaves positively charged ions in the semiconductor, which creates a region with no free charge carriers called a depletion region. This depletion region is formed on the semiconductor side near the interface with the metal [1]. The width of this region (W) can be affected by V_{bi} , applied voltage and the doping concentration. By defining the interface of the junction as $x = 0$ to the beginning of the neutral region in the semiconductor as $x = W$, Poisson's equation can be used to determine the width of the depletion region (W).

$$V = \frac{1}{\epsilon_s} \int_0^W x \rho(x) dx \quad (4.3)$$

where V is the net potential, ϵ_s and x are the dielectric constant and the distance from the junction to the semiconductor, respectively. Charge density $\rho(x)$, when it is considered uniform, can be written as

$$\rho = qN_d \quad (4.4)$$

By using Equations 4.3 and 4.4, the width of the depletion region can be given as

$$W = \sqrt{\frac{2\epsilon_s V}{qN_d}} \quad (4.5)$$

where N_d is the ions' donor concentration in the depletion region. In the ideal case, the depletion region is completely free of charge carriers. This is called the depletion region approximation and assumes sharp boundaries between the neutral and depletion regions. However, in a real case, it is difficult to have a sharp

boundary due to the existence of some charges in the depletion region close to the neutral region. This region of charges in the depletion region is called the Debye length (L_D) and is given by:

$$L_D = \sqrt{\frac{\epsilon_s K T}{q^2 N_d}} \quad (4.6)$$

where K and T are the Boltzmann constant and temperature in Kelvins, respectively. For a low-doped semiconductor or when applying a large reverse bias, the width of the depletion region will be much larger than compared with the Debye Length. In this condition, the depletion region approximation is considered to be a good approach [3].

4.1.2 SCHOTTKY DIODE UNDER BIAS CONDITIONS

The equilibrium condition of a Schottky diode has been presented in Fig. 4.2. The diode will no longer be in this condition if an external voltage is applied. A current will flow through the junction and will depend on the voltage polarity that has been applied to the metal and the semiconductor. If a forward bias, + to the metal and – to the semiconductor, is applied ($V_F > 0$), the potential barrier on the semiconductor side (V_{bi}) decreases by V_F to ($V_{bi} - V_F$). The reduction in the built-in potential is due to the increase of the semiconductor Fermi level by V_F , which is shown in Fig. 4.3. On the other hand, if a reverse bias is applied ($V_R < 0$), the Fermi level of the semiconductor decreases by the applied voltage, which is shown in Fig. 4.4. Thus, the built-in potential will be increased by the amount of applied voltage to ($V_{bi} + V_R$) [1, 3].

The width of the depletion region is affected by the applied voltage. Under forward bias, the depletion region is reduced, and Equation 4.5 is given by:

CHAPTER 4

$$W = \sqrt{\frac{2\epsilon_s(V_{bi} - V_F)}{qN_d}} \quad (4.7)$$

However, if a reverse bias is applied, the depletion width will get wider and is given by:

$$W = \sqrt{\frac{2\epsilon_s(V_{bi} + V_R)}{qN_d}} \quad (4.8)$$

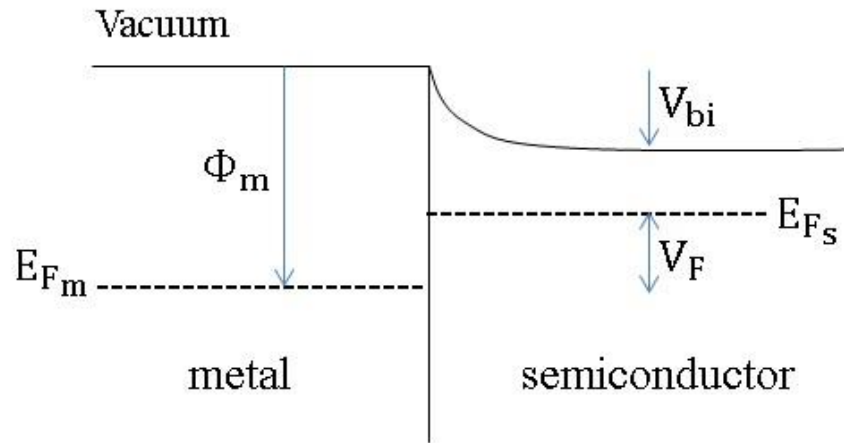


Fig. 4.3: Energy band diagram of a Schottky diode under a forward bias.

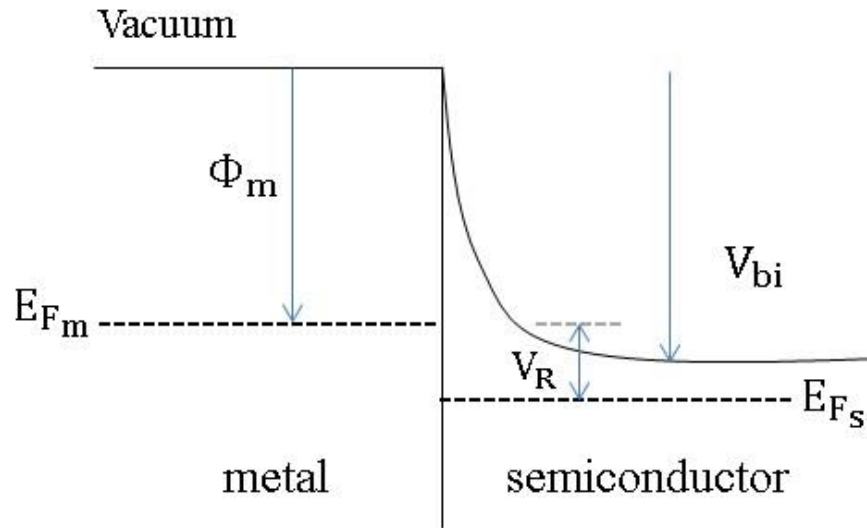


Fig. 4.4: Energy band diagram of a Schottky diode under a reverse bias.

4.2 CAPACITANCE – VOLTAGE (C-V) MEASUREMENTS

The capacitance of a Schottky diode can be seen as a capacitance of a parallel plate capacitor, which is given by:

$$C = \frac{dQ}{dV} \quad (4.9)$$

Here, dQ is the charge in the depletion region and dV is the applied voltage. The expression of the capacitance for the parallel plate capacitor can be used as the capacitance of the Schottky diode. Therefore, C can be written as:

$$C = \frac{A\epsilon_s}{W} \quad (4.10)$$

where A is the area of the diode and W is the width of the depletion region [4].

When a reverse bias is applied, Equation 4.10 can be rewritten using Equation 4.8

as

$$C = \frac{dQ}{dV_R} = \frac{A}{2} \sqrt{\frac{2\epsilon_s q N_d}{V_{bi} + V_R}} \quad (4.11)$$

CHAPTER 4

Note from this equation that the capacitance decreases as the reverse bias increases. As shown in Fig. 4.5, by plotting $(1/C^2)$ versus (V_R) , the doping concentration (N_d) and the built-in potential (V_{bi}) can be obtained from the slope and the intercept at $1/C^2 = 0$, respectively. The doping concentration is uniformly distributed throughout the depletion region if a linear relationship between $(1/C^2)$ and (V_R) is obtained. However, N_d is non-uniform in the case of a non-linear relationship.

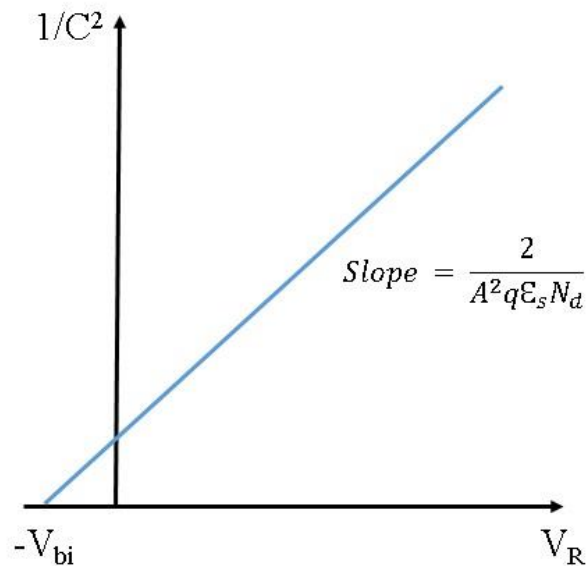


Fig. 4.5: Plot of $1/C^2$ versus reverse bias (V_R).

4.3 CURRENT – VOLTAGE (I-V) MEASUREMENTS

For an ideal Schottky or p-n junction, the I-V characteristics could be described by the thermionic emission model [5] that includes series resistance (R_S) as:

$$I = I_0 \left[\exp \left(\frac{q(V - IR_S)}{nKT} \right) - 1 \right] \quad (4.12)$$

CHAPTER 4

where q is the elementary charge, V is the applied voltage, n is the ideality factor, k is Boltzmann's constant, T is the temperature and I_0 is the saturation current which is given by:

$$I_0 = AA^*T^2 \exp\left(\frac{-q\phi_b}{KT}\right) \quad (4.13)$$

where A is the effective diode area, A^* is the effective Richardson's constant for the semiconductor material and ϕ_b is the barrier height. Note that I is the current from the semiconductor to the metal and it is due to the thermionic emission of the majority carriers from the semiconductor to the metal. The saturation current (I_0) is the current flow from the metal to the semiconductor and it is independent of the applied voltage.

When a forward bias is applied, $(V - IR_s) \gg KT$ and hence Equation 4.12 can be rewritten as:

$$I = I_0 \exp\left(\frac{q(V-IR_s)}{nKT}\right) \quad (4.14)$$

Taking the first derivative of I with respect to V results in the following:

$$dI/dV = I_0 \left(\frac{q}{nKT} \exp\left(\frac{q(V-IR_s)}{nKT}\right) - \frac{q}{nKT} \exp\left(\frac{q(V-IR_s)}{nKT}\right) R_s \frac{dI}{dV} \right) \quad (4.15)$$

Note that $dI/dV = G$, where G is the conductance. Equation 4.15 can be rewritten as:

$$G = \frac{q}{nKT} I_0 \exp\left(\frac{q(V-IR_s)}{nKT}\right) (1 - G.R_s) = \frac{q}{nKT} I (1 - G.R_s) \quad (4.16)$$

$$\frac{G}{I} = \frac{q}{nKT} - \frac{qR_s}{nKT} G \quad (4.17)$$

By plotting G/I versus G , a straight line is obtained as shown by Fig. 4.6. The ideality factor (n) and R_s could be extracted from the y-intercept and the slope, respectively. This method of extracting n and R_s experimentally is known as Werner's method [6].

CHAPTER 4

By taking the logarithm of Equation 4.14 and plotting $\ln(I)$ versus $(V - IR_s)$, I_0 could be extracted from the y-intercept. By taking the logarithm, Equation 4.14 is written as:

$$\ln(I) = \ln(I_0) + \frac{q(V - IR_s)}{nKT} \quad (4.17)$$

Then, by substituting I_0 value in Equation (4.13) where A , A^* and T are known, ϕ_b can be calculated.

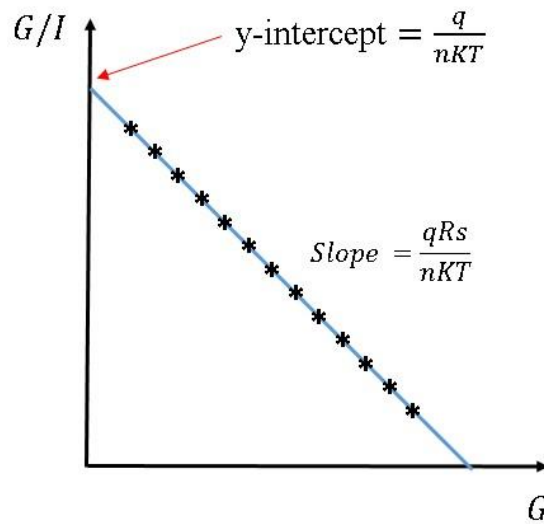


Fig. 4.6: Plot of G/I versus G .

4.4 DEEP LEVEL TRANSIENT SPECTROSCOPY (DLTS)

In 1974, D. V. Lang [7] introduced a novel technique, the so-called deep level transient spectroscopy (DLTS), to investigate the electrical active defects in semiconductors. This technique is based on a capacitance transient process occurring within the device. In this technique, the capacitance of a depletion region of a Schottky or a p-n junction is varied by changing the width of this region as a

function of temperature in order to determine the trap activation energy and capture cross-section.

4.4.1 CAPACITANCE TRANSIENTS

Since the DLTS technique is based on the concept of capacitance transient occurring in the depletion region (space charge region), a Schottky or a p-n junction is required. In this section, the capacitance transient of a Schottky junction is discussed.

Fig. 4.7 represents the energy band diagram of a Schottky junction under reverse bias (V_R) and the corresponding capacitance transient during a filling pulse (V_P).

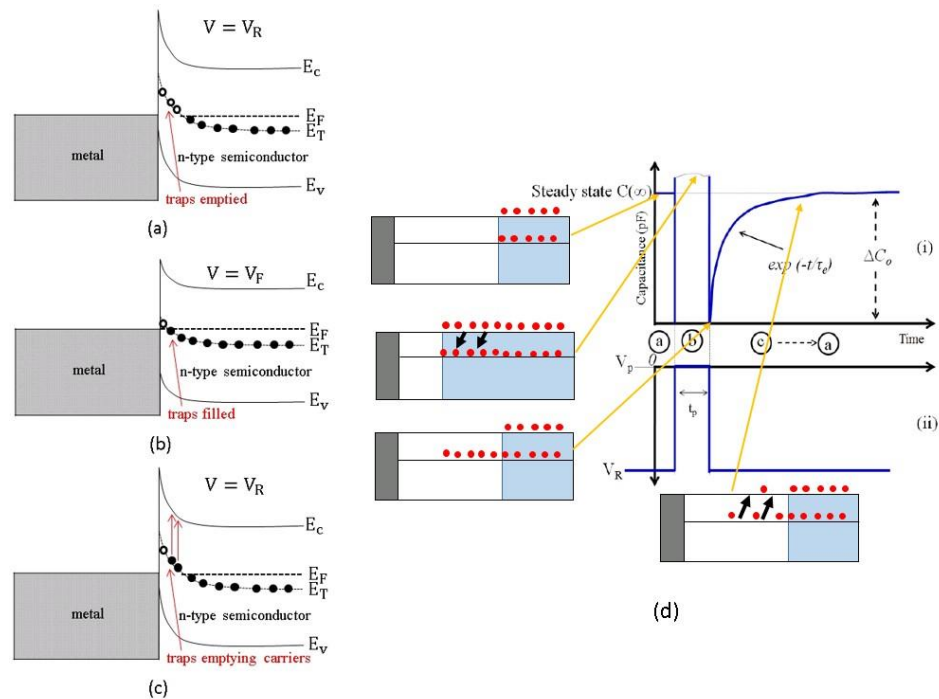


Fig. 4.7: plot of energy band diagram of Schottky junction showing the charge occupancy as (a) emptying traps during reverse bias ($V=V_R$), (b) filling traps during filling pulse ($V=V_F$), (c) traps thermally emitting electrons during reverse bias ($V=V_R$) and (d) DLTS pulses and corresponding capacitance transient.

CHAPTER 4

Initially (Fig. 4.7 (a)), the device is kept at a reverse bias in which a depletion region is formed and traps above the Fermi level are empty. Then, a filling pulse is applied (Fig. 4.7 (b)) with a duration of (t_P) which leads to the reduction of the width of the depletion region and hence allow the traps to capture electrons (filling traps). The rate at which the traps capture electrons is given by:

$$\frac{dn_T}{dt} = c_n(N_T - n_T) \quad (4.18)$$

where n_T , c_n and N_T are the number of trap states occupied by electrons, capture coefficient of the electrons and the total number of available trap states. The capture coefficient of the electrons (c_n) is given by:

$$c_n = \sigma_n \langle v_{th} \rangle n \quad (4.19)$$

where σ_n and $\langle v_{th} \rangle$ are the capture cross-section and thermal velocity of electrons. $n = N_d - N_T \cong N_d$ is the effective doping concentration.

After that, the reverse bias is restored (Fig. 4.7 (c)) and the depletion region is back to its initial width (steady state). In this case, the traps start thermally emitting the electrons back and the corresponding emission rate is given by:

$$\frac{dn_T}{dt} = e_p N_T - (e_p + e_n)n_T \quad (4.20)$$

where e_p and e_n are hole and electron emissions, respectively.

Assuming that the traps are electron interacting centres, the solution of Equation 4.18 (capture process) and Equation 4.20 (emission process) are given by exponential functions as follows [2]:

$$n_T = N_T(1 - \exp(-c_n t)), \quad c_n \gg e_n, e_p \text{ and } c_p \quad (4.21)$$

$$n_T = N_T \exp(-e_n t) = N_T \exp\left(\frac{-t}{\tau}\right), \quad e_n \gg c_n, e_p \text{ and } c_p \quad (4.22)$$

where c_p is the hole capture coefficient and $\tau = \frac{1}{e_n}$ is the inverse of the electron emission rate (also known as the time constant of the carrier emission).

CHAPTER 4

From the above equations, it is clear that the reduction of filled trap concentration follows an exponential trend with a time constant τ and hence this process leads to a capacitance transient as shown in Fig. 4.7 (d).

The change of occupancy of traps can be measured indirectly by monitoring the capacitance change. By adding the contribution of the filled traps, the capacitance of the Schottky junction (Equation 4.11) could be rewritten as:

$$C = \frac{dQ}{dV_R} = \frac{A}{2} \sqrt{\frac{2\epsilon_s q N_d^*}{V_{bi} + V_R}} \quad (4.23)$$

where $N_d^* = N_d - n_T$

For $n_T \ll N_d$, Equation 4.23 could be written as:

$$\Delta C = C_\infty \left(1 - \frac{n_T}{2N_d}\right) \quad (4.24)$$

where ΔC is the amplitude of the capacitance transient and $C_\infty = \frac{A}{2} \sqrt{\frac{2\epsilon_s q N_d}{V_{bi} + V_R}}$ is the steady state capacitance.

From Equations 4.22 and 4.24, information about time dependence of majority carrier traps could be obtained by the following:

$$\Delta C = C_\infty \left(1 - \frac{N_T}{2N_d} \exp\left(\frac{-t}{\tau}\right)\right) \quad (4.25)$$

It is worth mentioning that the minority carrier traps can also be deduced using the same procedures as for majority carrier traps. However, in the case of minority carrier traps, the sign of the capacitance transient is opposite to that of majority carrier traps.

4.4.2 CONVENTIONAL DLTS

The DLTS technique is based on the rate window concept, where the capacitance of the depletion region for a Schottky diode or a p-n junction is changed between two interval times, t_1 and t_2 ($t_1 < t_2$). The signal of DLTS ($S(T)$) is basically the difference in the capacitance ($\Delta C = C(t_1) - C(t_2)$) as a function of temperature and is given by:

$$S(T) = \Delta C = C(t_1) - C(t_2) = \Delta C_o [\exp(-e_n t_1) - \exp(-e_n t_2)] \quad (4.26)$$

Equation 4.26 can be rewritten using the inverse of emission rate (τ) as:

$$S(T) = \Delta C = C(t_1) - C(t_2) = \Delta C_o [\exp(\frac{-t_1}{\tau}) - \exp(\frac{-t_2}{\tau})] \quad (4.27)$$

where ΔC_o is the maximum change in the capacitance which corresponds to the maximum amplitude of DLTS signal and is given by:

$$\Delta C_o = \frac{C_\infty N_T}{2N_d} \quad (4.28)$$

It is worth pointing out that the trap concentration can be calculated by rewriting Equation 4.28 as shown below:

$$N_T = 2N_d \frac{\Delta C_o}{C_\infty} \quad (4.29)$$

where N_T and C_∞ are the trap concentration and the capacitance at maximum reverse bias (the capacitance when a trap is completely empty), respectively.

Equation 4.29 shows that the trap concentration is directly related to the DLTS peak amplitude.

The DLTS technique will respond and generate a maximum peak for $S(T)$ only when a transient happens within the inverse of the emission rate $\tau \approx (t_1 - t_2)$. However, the DLTS signal will be small in case $\tau \gg (t_1 - t_2)$ or $\tau \ll (t_1 - t_2)$, as shown in Fig. 4.8 (a) [7]. When $S(T)$ is maximum, Equation 4.27 can be

CHAPTER 4

differentiated and the result set equal to zero [$\frac{dS(T)}{dT} = 0$] to obtain the maximum of the inverse of emission rate (τ_{max}):

$$\tau_{max} = \frac{t_2 - t_1}{\ln\left(\frac{t_2}{t_1}\right)} \quad (4.30)$$

Equation 4.30 is called the rate window. The value of the rate window can be changed by changing the values of t_1 and t_2 . Changing the rate window will generate different maximum peaks (DLTS peaks) at different temperatures, which are shown in Fig. 4.8 (b). The Arrhenius plot of the emission rates (from DLTS peaks) as a function of temperature is used to obtain the trap activation energy, as shown in Fig. 4.8 (c). The activation energy is extracted from the slope of the Arrhenius plot whereas the apparent capture cross-section can be obtained from the y-intercept.

Equations 4.27 and 4.30 show that the DLTS signals depend on the ratio between them $\left(\frac{t_2}{t_1}\right)$ but not on the absolute values of t_1 and t_2 .

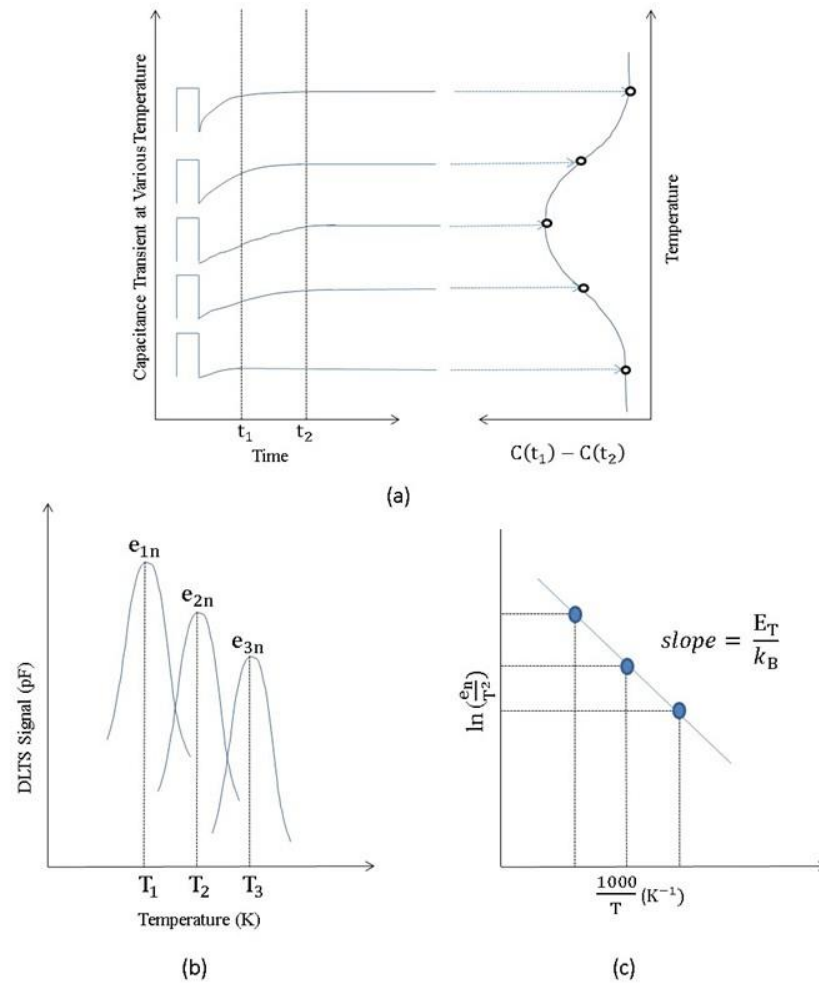


Fig. 4.8: schematics diagrams illustrating (a) the generation of DLTS peaks for one rate window, (b) DLTS peaks for different rate windows and (c) Arrhenius plot obtained from different rate windows.

4.5 LAPLACE DLTS

Although DLTS is a powerful technique for the investigation of deep-level defects, it has some problems that affect its resolution. One of the disadvantages of DLTS is the accuracy of temperature measurements during a thermal scanning process. Increasing or decreasing temperature causes inaccurate measurement of the traps' activation energies. Another disadvantage is the resolution of the time constant, as DLTS cannot distinguish between closely spaced defects that have

similar emission rates. This poor resolution leads to a broad peak on the DLTS spectrum [8]. The Laplace DLTS Technique is used to overcome these limitations in the conventional DLTS. Laplace DLTS is an isothermal technique where a diode is kept at a fixed temperature during the measurements. It considers the capacitance transients to be characterized by a spectrum of emission rates where the recorded transient $f(t)$ is given by:

$$f(t) = \int_0^{\infty} F(s)e^{-st} ds \quad (4.31)$$

Note that $f(t)$ and $F(s)$ are the recorded transient and the spectral density function, respectively. Equation 4.31 represents the transient capacitance as the Laplace transform of the actual spectral density function $F(s)$. The capacitance transient obtained from Laplace DLTS is shown in Fig. 4.9 (a). The real spectrum of emission rates within the transient is obtained by applying an appropriate mathematical algorithm which performs an inverse Laplace transform for the recorded transient $f(t)$ [9]. The Laplace DLTS technique uses three main algorithm routines, namely FLOG, CONTIN and FTIKREG, to solve Equation 4.31 [10]. As a result of using these algorithms, a spectrum of delta-like peaks is obtained as illustrated in Fig. 4.9 (b).

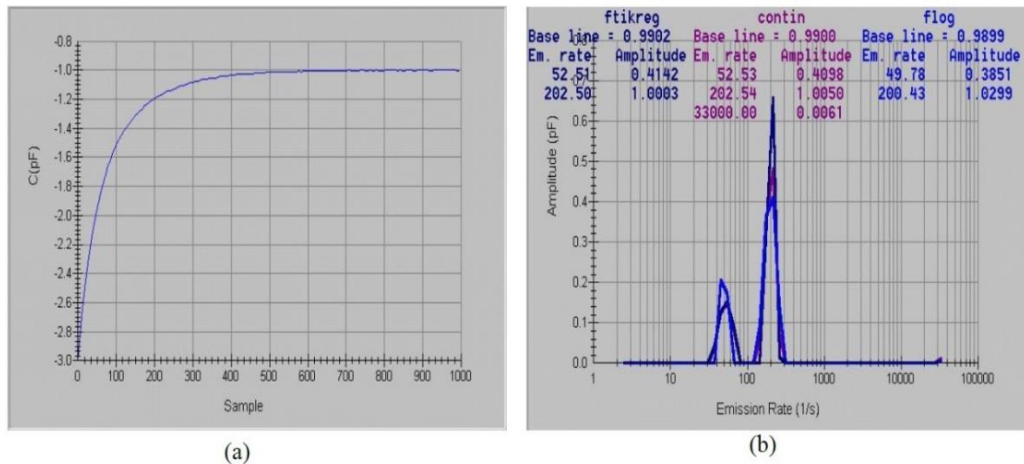


Fig. 4.9: (a) Laplace DLTS capacitance transient and (b) a spectrum of delta-like peaks [11].

4.6 DLTS HARDWARE SETUP

In this section, details of the equipment used for DLTS and I-V measurements are described. The DLTS system consists of the following equipment:

- I. Cryostat and temperature controller.
- II. Capacitance meter.
- III. Current-voltage source meter.
- IV. Data acquisition and BNC connector box for analogue Input (I)/Output (O).

All these apparatuses are controlled by a computer through a GPIB interface. Fig. 4.10 shows a photograph of the DLTS system and Fig. 4.11 illustrates the block diagram of the DLTS setup.

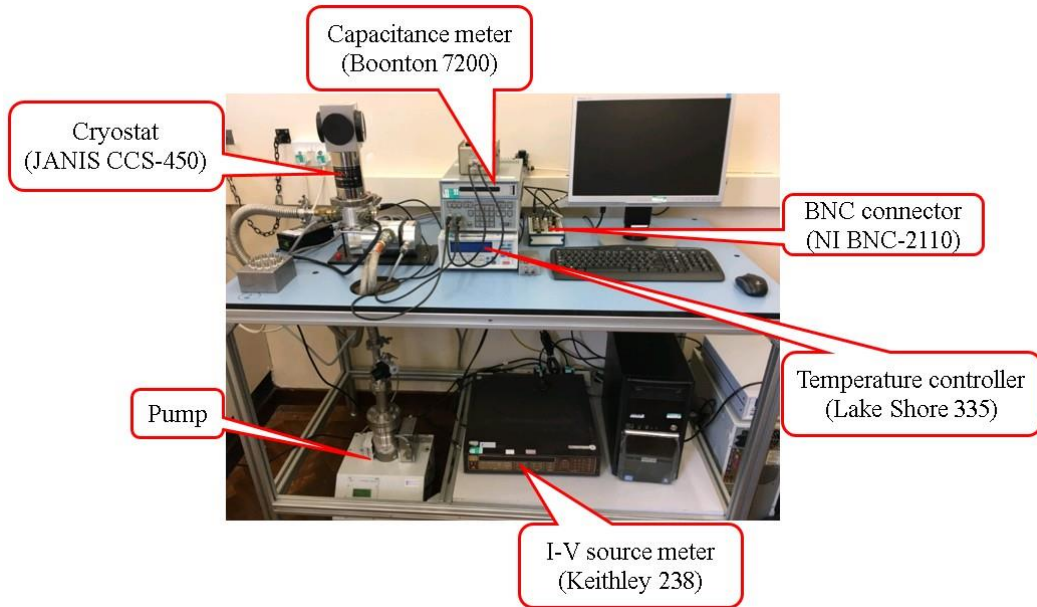


Fig. 4.10: Photograph of the DLTS system.

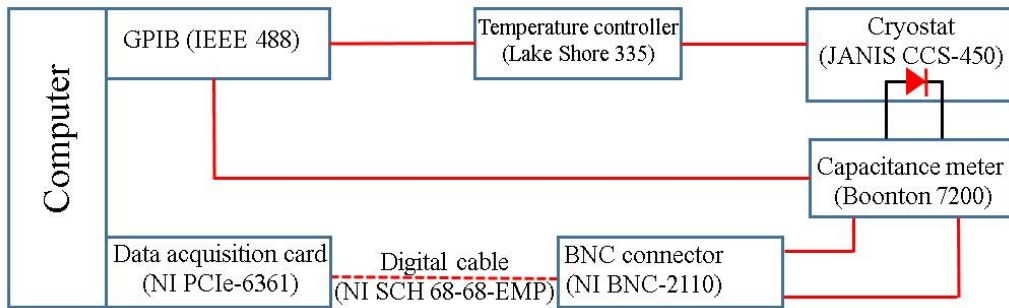


Fig. 4.11: Schematic diagram of the DLTS apparatus.

4.6.1 CRYOSTAT AND TEMPERATURE CONTROLLER

As discussed previously in this chapter, the emission of charge carriers from traps depends on the thermal energy of the carriers. Thus, a measured sample is placed inside a cryostat (JANIS CCS-450) which is connected to a temperature controller (Lake Shore 335) to control the sample's temperature. The cryostat is

CHAPTER 4

based on a helium (He) gas closed-loop cycle refrigeration where a high efficiency flexible six feet cryogen transfer line is used for the flow of the He gas. The operating temperature ranges from 10 to 450K with a stability of ± 1 K. The cryostat structure is shown in Fig. 4.12 which consists of the following:

- I. Lightweight aluminium vacuum shroud.
- II. Radiation shield.
- III. A cold finger attached to a sample holder.
- IV. Electrical ports for sample contacts.

The temperature controller is used to control two temperature sensors, one of which is placed very close to the sample in order to obtain a precise temperature for the sample under investigation.

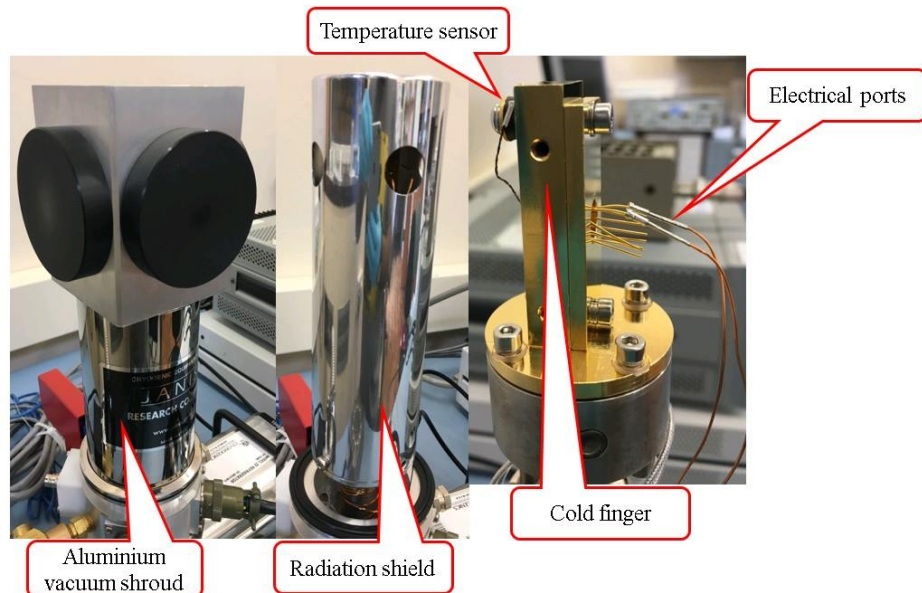


Fig. 4.12: Photograph of the cryostat structure.

4.6.2 CAPACITANCE METER

A high response time capacitance meter is essential for the capacitance transient measurements. Thus, the Boonton 7200 meter which has a response time of $\sim 120\mu\text{s}$ has been used. It has a fixed sampling frequency (1 MHz).

4.6.3 CURRENT-VOLTAGE SOURCE METER

I-V measurements were performed at different temperatures on each sample in this thesis in order to determine the diode parameters such as ideality factor (n), barrier height (ϕ_b) and series resistance (R_s). Moreover, a low reverse current, in the range of μA , is required for DLTS and Laplace DLTS measurements and hence I-V measurements are performed. Keithley 236 current source meter has been used to carry out the I-V measurements. It provides a source voltage ranging from 100 μV to 110 V with a sensitivity of $\pm 10\ \mu\text{V}$ and a source current in the range of 100 fA to 100 mA with a sensitivity of 10 fA.

4.6.4 DATA ACQUISITION AND BNC CONNECTOR BOX

Data acquisition card is a core component in the DLTS technique which is used for biasing and pulsing the diodes. A National Instruments (NI) PCIe-6321 card is used for this purpose which provides an input voltage of $\pm 10\ \text{V}$ and a pulse width starting from 0.5 μs . A BNC-2110 connector box is used to collect and send information from diodes to the computer for processing. The (NI) PCIe-6321 card and the BNC-2110 connector box are interfaced using a SHC68-68-EPM matching cable.

4.6.5 COMPUTER INTERFACE

General-purpose interface bus (GPIB) is used to connect all the equipment above to the computer with a high-speed communication. The GPIB allows the equipment to be controlled remotely through the provided software.

4.7 SYSTEM SOFTWARE

Laplace DLTS software was developed by a joint project “*Copernicus Project CIPA CT-94-0172 and The Foundation for Polish Science Serial No: C3.2.041*” between University of Manchester, Manchester, United Kingdom (Professor A. R. Peaker) and Institute of Physics of the Polish Academy of Sciences, Warsaw, Poland (the late Professor L. Dobaczewski). This software functions in two modes, i.e. conventional DLTS and Laplace Transient processing (Laplace DLTS) mode.

4.7.1 CONVENTIONAL DLTS MODE

In this mode, three different types of procedures can be used to perform conventional DLTS measurements. These are Multi-Rate Window, TrapView and Exponential Fitting which all work on the concept of rate window. The sample is scanned from a start to end points of temperatures with increasing steps (usually 2 K/minutes) in each one of these three procedures.

In Multi-Rate Window, nine different rate windows are simultaneously recorded and hence nine different DLTS signals are obtained. The different rate windows (5, 10, 20, 50, 100, 200, 500, 1000 and 2000 s⁻¹) are obtained by changing the value of t_1 and t_2 of each rate window.

In TrapView, a pair of rate windows has to be selected among five different pairs, i.e. (4, 10 s⁻¹), (20, 50 s⁻¹), (80, 200 s⁻¹), (400, 1000 s⁻¹) and (2000, 5000 s⁻¹).

In Exponential Fitting, only one rate window could be chosen for a single scan from the available rate windows (10, 20, 50, 100 and 200 s⁻¹). However, for this procedure, a lock-in mode can be chosen instead of rate window mode. Lock-in mode has a better resolution when compared to rate window mode but also has a poor signal to noise ratio. Moreover, the Arrhenius plot is generated during the temperature scan and allow to estimate traps activation energies.

In all mentioned procedures, the DLTS parameters, such as reverse bias, filling pulse and width of this pulse, can be set remotely.

4.7.2 LAPLACE TRANSIENT PROCESSING (LAPLACE DLTS) MODE

In this mode, the sample is held at a fixed temperature during the measurements. This mode is used to increase the signal to noise ratio. Three different algorithms are applied to generate Laplace DLTS peaks.

4.8 PHOTOLUMINESCENCE

Photoluminescence (PL) is one of many types of luminescence which is the emission of light from a material that is not heated. Hence, PL is the emission of light due to photon absorption. In this section, PL spectroscopy is discussed.

PL spectroscopy is a powerful non-destructive technique for the study of the optical properties of semiconductor materials [2]. A sample under investigation is exposed to an optical source such as a laser with an energy greater than the material bandgap ($h\nu > E_G$). The light from the laser source (photons) is absorbed and the excess energy is transferred to the material in a process known as photo-

excitation. Then, the material will emit the excess energy in the form of light known as PL spectrum. The intensity and the spectral content of the PL spectrum are used to obtain important information about the material properties, such as the bandgap, detecting impurity levels and measuring the quality of the material.

In the photo-excitation process, the electrons are excited to higher states and then relax back to their equilibrium states losing the difference in energy (between the excited and equilibrium states) in the form of light in a process called radiative recombination. However, a non-radiative process occurs when the difference in the energy is lost as heat. Fig. 4.13 shows the excitation of electrons, where non-equilibrium electrons tend to relax back into the equilibrium state (inter-band relaxation to band edge) and finally this is followed by emission of light due to an electron-hole radiative recombination.

It is worth mentioning that the PL measurements were carried out on the samples discussed in section 5.1.1 and 5.1.2.

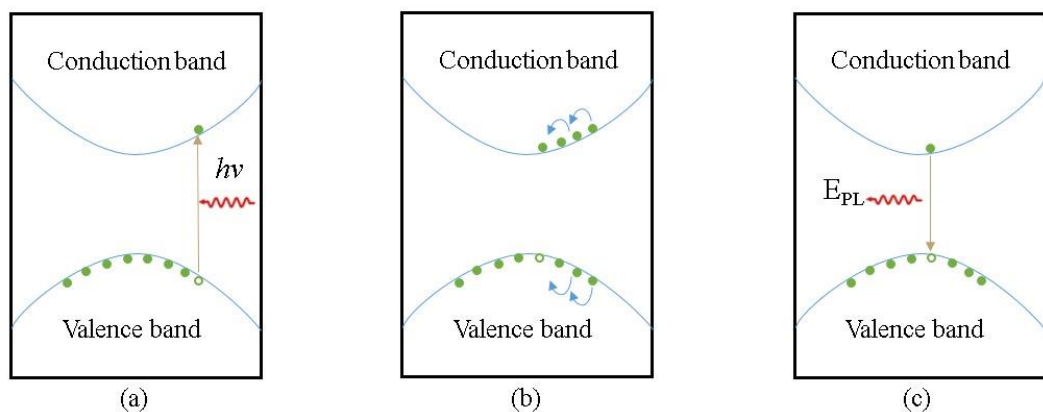


Fig. 4.13: Illustration of the processes involved in PL (a) photo-excitation from the valence band to the conduction band, (b) inter-band relaxation and (c) recombination which leads to PL emission.

4.9 X-RAY DIFFRACTION (XRD)

XRD is a technique that is used to determine the structural properties of materials, such as lattice parameters and phase identity. The XRD spectrum is compared with database (e.g. Joint Committee on Powder Diffraction Standards (JCPDS)) to identify the material under investigation easily. A sample under investigation is exposed to a beam of X-ray which will be diffracted at different angles. A constructive interference is obtained if they are in-phase as shown in Fig. 4.14. In this case Bragg's law is satisfied and a peak is generated. Bragg's law is defined as:

$$n\lambda = 2d \sin\theta \tag{4.32}$$

where n is integer, λ is the wavelength of the incident X-ray, d is the space between planes and θ is the incident angle.

The spacing between planes can be determine by knowing the angle at which the diffraction occurs and the wavelength. Hence, the material can be identified [12].

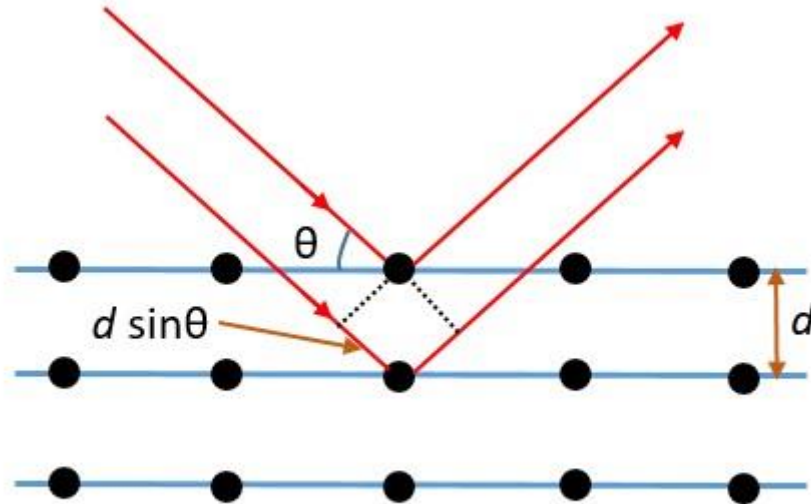


Fig. 4.14: illustration of diffractions.

4.10 RAMAN SPECTROSCOPY

Raman spectroscopy is used to probe different properties of materials, such as chemical structure and crystallinity. It is based on an inelastic scattering of light (Raman scattering) where the scattered light has different wavelength than the incident light. When a semiconductor is illuminated by a monochromatic light, most of the scattered light has unchanged wavelength. However, only a small amount of the scattered light has a different wavelength than the incident wavelength. If the scattered light loses energy (has energy less than the incident one), that is called Stokes scattering. However, if the scattered photon has higher energy, the scattering is called anti-Stokes. The difference in the energy will occur as a change in vibrational energy of the molecule that absorbs the light.

Raman spectra is a plot of the scattered light intensity versus the frequency which shows at which energies the light has been scattered. In this spectrum, peaks

are generated where their position and intensity can identify the material under investigation [13].

4.11 ABSORPTION

If a semiconductor with an energy bandgap of E_g is illuminated by a photon with an energy of $h\nu$ (h is Planck's constant and ν is the frequency of the photon), which is greater than E_g , a pair of electron and hole will be generated due to absorbing the photon by an electron. As Fig. 4.15 shows, the photon can be absorbed by an electron in the valence band which will be excited to the conduction band leaving a hole in the valence band. This process is called band to band transition [process (a) in Fig. 4.15]. The electron can also be excited to from the valence band to a defect level or from a defect level to the conduction band [(b) and (c) processes in Fig. 4.15]. Finally, the transition can occur between two defect levels [process (d) in Fig. 4.15].

Optical absorption spectrum is used to investigate the structural properties of semiconductor materials. In this process, the intensity of the transmitted light (I) is measured as follows [14]:

$$I(\lambda, t) = [1 - R(\lambda)]I_0(\lambda)e^{-\alpha(\lambda)t} \quad (4.33)$$

where λ is the wavelength of the incident light, t is the material's thickness, $R(\lambda)$ is reflection coefficient, I_0 the intensity of the incident light and $\alpha(\lambda)$ is the absorption coefficient.

In case of a direct bandgap semiconductor, $\alpha(\lambda)$ is given by:

$$\alpha(\lambda) = A[h\nu - E_g]^{1/2} \quad (4.34)$$

CHAPTER 4

where A is a constant which depends on the semiconductor material.

However, in case of indirect bandgap [15]:

$$\alpha h\nu = A[h\nu - E_g]^2 \quad (4.35)$$

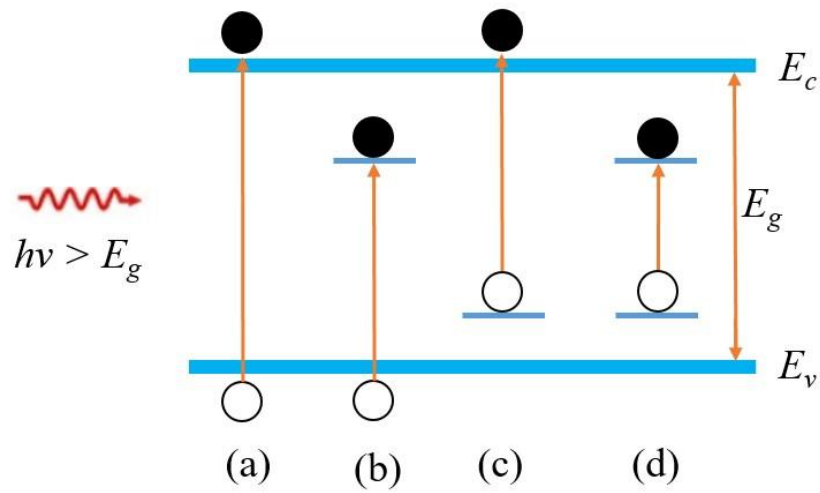


Fig. 4.15: optical absorption processes in a semiconductor.

REFERENCES

1. Colinge, J.-P. and C.A. Colinge, *Physics of semiconductor devices*. 2005: Springer Science & Business Media.
2. Schroder, D.K., *Semiconductor material and device characterization*. 2006: John Wiley & Sons.
3. Sze, S.M. and K.K. Ng, *Physics of semiconductor devices*. 2006: John Wiley & Sons.
4. Neamen, D.A., *Semiconductor physics and devices: basic principles*. 2003: McGraw Hill.
5. Sze, S.M. and M.K. Lee, *Semiconductor devices : physics and technology*. 2013, Singapore: Wiley.
6. Werner, J.H., *Schottky barrier and pn-junction I/V plots—Small signal evaluation*. Applied Physics A: Materials Science & Processing, 1988. **47**(3): p. 291-300.
7. Lang, D., *Deep-level transient spectroscopy: A new method to characterize traps in semiconductors*. Journal of applied physics, 1974. **45**(7): p. 3023-3032.
8. Dobaczewski, L., I. Hawkins, and A. Peaker, *Laplace transform deep level transient spectroscopy: new insight into defect microscopy*. Materials science and technology, 1995. **11**(10): p. 1071-1073.
9. Dobaczewski, L., et al., *Laplace transform deep-level transient spectroscopic studies of defects in semiconductors*. Journal of applied physics, 1994. **76**(1): p. 194-198.
10. Dobaczewski, L., A. Peaker, and K. Bonde Nielsen, *Laplace-transform deep-level spectroscopy: The technique and its applications to the study of*

CHAPTER 4

- point defects in semiconductors*. Journal of applied physics, 2004. **96**(9): p. 4689-4728.
11. Shafi, M., *Electrical and optical studies of dilute nitride and bismide compound semiconductors*. 2011, University of Nottingham.
 12. Cullity, B.D., *Elements of X-ray Diffraction*. 1978: Addison-Wesley.
 13. Larkin, P., *Infrared and Raman spectroscopy: principles and spectral interpretation*. 2017: Elsevier.
 14. Essick, J.M. and R.T. Mather, *Characterization of a bulk semiconductor's band gap via a near-absorption edge optical transmission experiment*. American journal of physics, 1993. **61**(7): p. 646-649.
 15. Murphy, A., *Band-gap determination from diffuse reflectance measurements of semiconductor films, and application to photoelectrochemical water-splitting*. Solar Energy Materials and Solar Cells, 2007. **91**(14): p. 1326-1337.

EXPERIMENTAL DETAILS

In this chapter, the growth and fabrication processes of all samples studied in this thesis are presented. Furthermore, the experimental procedures such as current-voltage (I-V), capacitance-voltage (C-V), conventional DLTS and Laplace DLTS, which have been used to investigate the samples are discussed.

5.1 SAMPLES INVESTIGATED IN THIS THESIS

The core motivation of this thesis is to investigate the electrically active defects in wide bandgap semiconductor materials, namely titanium dioxide (TiO₂) and indium oxide (In₂O₃).

5.1.1 INDIUM DOPED TiO₂ GROWN ON SILICON SUBSTRATES BY TWO DIFFERENT TECHNIQUES

Two series of samples were prepared for this study using two different growth methods. For the first series, a layer of 380 nm TiO₂ thin film, measured using cross-section scanning electron microscopy (SEM, HITACHI S4500), was deposited on (100) n-type silicon substrate using pulsed laser deposition (PLD/MBE 2100) from PVD products. The laser source was a KrF excimer Laser ($\lambda = 248$ nm, pulse width 20 ns, and repetition rate = 10 Hz) operating at 350 mJ to ablate the target under a vacuum of 10⁻⁶ Torr and oxygen background pressure of 5 × 10⁻³ Torr. The growth temperature was fixed at 500 °C and the distance from substrate to target was set at 55 mm. All PLD parameters which contribute to the growth rate were kept constant during the operating time. This series of samples is named 'PLD' sample. In the second series, RF magnetron sputtering technique was

CHAPTER 5

employed to deposit a 300 nm thin film of TiO₂ on (100) n-type silicon substrate. This series is labelled as ‘Sputtered’ sample. For the RF sputtering system, the samples were deposited using a 2-inch TiO₂ target at a temperature of 500 °C in an ambient of pure Argon without addition of oxygen. The chamber was evacuated to a high vacuum of less than 1×10^{-8} Torr. The substrate was rotated during the deposition at a low speed to enhance the thickness uniformity of the films. Substrates were mounted on 300 mm stainless steel rotating disk where the distance between target and substrate was 150 mm. High purity argon gas (99.999%) was introduced at a rate of 22 sccm as an inert gas for the plasma. Before deposition, the samples were pre-sputtered in argon plasma for 10 mins to remove any contaminants. The working pressure was set to 10^{-3} Torr and RF power was fixed at 150 W. By thermal evaporation, layers of indium (50 nm thick) were deposited on top of each set of samples in order to keep the same doping concentration of indium and investigate only the effect of the growth techniques on the electrical and optical properties of In doped TiO₂ thin films. In order to incorporate indium into the TiO₂ lattice, both series of samples were annealed under a flow of oxygen with a temperature ramp rate of 15°C/minute and a dwelling temperature of 500 °C for 30 minutes. This annealing process has been found as the best among many annealing processes and procedures investigated.

A third series of control samples, which do not contain In, were grown by sputtering and PLD techniques using the same procedures as described above. These control samples will help to understand and investigate the effect of In doping. These samples are labelled here as ‘Reference’ samples

To prepare the samples for electrical characterization, the devices were processed in the form of circular mesas with a diameter of 900 μm. The back sides

CHAPTER 5

of the silicon substrates were exposed to evaporated Aluminium to create back Ohmic contacts. Ti/Au was deposited by thermal evaporation on top of the In-doped TiO₂ layer to create Schottky contacts. Then the samples were mounted on TO5 headers ready for electrical measurements. Fig. 5.1 shows the growth and fabrication steps.

It is worth to mention that these samples have been grown in collaboration with the group of Dr Abdulrahman M. Albadri at King Abdulaziz City for Science and Technology, Saudi Arabia.

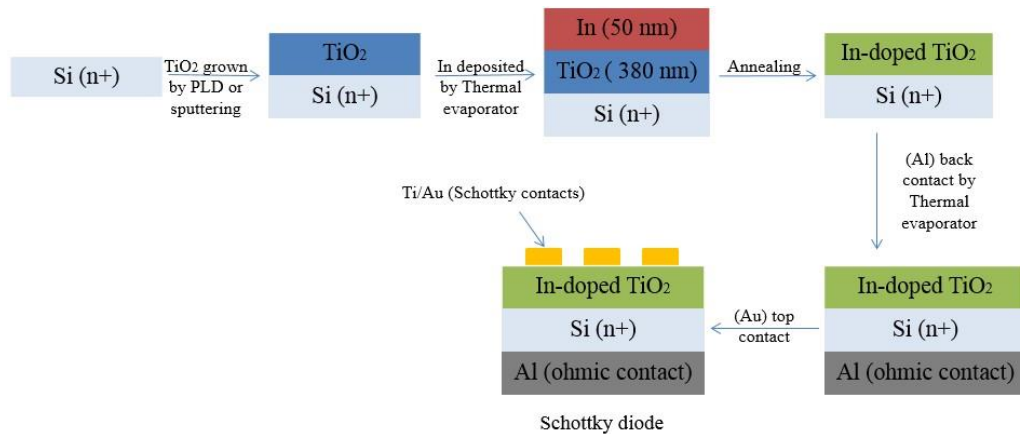


Fig. 5.1: Growth and fabrication steps.

5.1.2 INDIUM DOPED TiO₂ GROWN BY PLD TECHNIQUE ON LOW AND HIGH INDEX GaAs PLANES

Two series of samples were prepared for this study using low and high index n-type GaAs planes, namely (100) and (311)B, as substrates. The PLD growth and characterisation procedures are similar to those explained in section 5.1.1. The first series of samples is named '(100) sample'. By thermal evaporation, two layers of indium (15 and 5 nm thick) were deposited on top of two (100) substrates. In order to incorporate indium into the TiO₂ lattice, similar annealing procedures to those mentioned in section 5.1.1 were used. Therefore, for this series, two sub-series of samples, labelled as '15 (100)' and '5 (100)' for 15 nm In doped TiO₂/(100) n-type GaAs and 5 nm In doped TiO₂/(100) n-type GaAs, respectively.

The second series followed a similar pattern as the first '(100)' series but (311)B GaAs substrates were used instead of (100) GaAs. Also for this series, two samples labelled as '15 (311)B' and '5 (311)B' were prepared.

A third series of control samples, which do not contain In, were grown by PLD technique using the same procedures as described above in order to investigate the effect of In doping. The results obtained on these control samples are referred to as '(100) sample' for TiO₂/(100) GaAs and '(311)B sample' for TiO₂/(311)B GaAs.

To prepare the samples for electrical characterization, a shadow mask with circular mesas was used to deposit Au on top of the In-doped TiO₂ layer to create Schottky contacts. On the back sides of the GaAs substrates, Ge/Au/Ni/Au were deposited and then annealed at 390 °C for 20 seconds to form back Ohmic contacts. It is worth mentioning that the back contacts were deposited on the back of the

substrates before the growth of TiO₂ thin films. Fig. 5.2 shows the growth and fabrication steps.

It is worth to mention that these samples have been grown in collaboration with the group of Dr Abdulrahman M. Albadri at King Abdulaziz City for Science and Technology, Saudi Arabia.

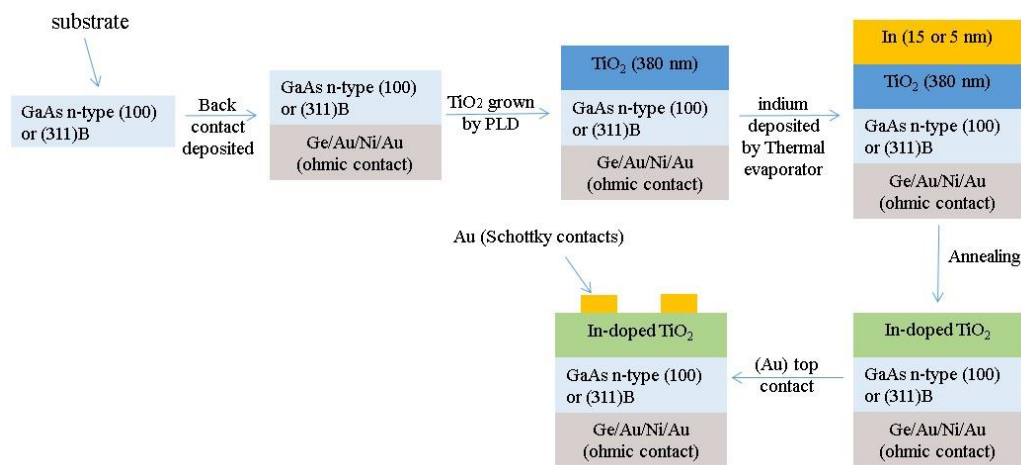


Fig. 5.2: Growth and fabrication steps.

5.1.3 ERBIUM DOPED TiO₂ GROWN ON SILICON SUBSTRATES BY SOL-GEL TECHNIQUE

Er-doped TiO₂ thin films (TFs) were deposited on p-type silicon (Si) substrates using sol-gel technique followed by spin coating. Titanium Isopropoxide (TTIP) was used as a precursor (Sigma Aldrich, purity $\geq 97\%$) of TiO₂ material. Erbium oxide nanopowder (Er₂O₃, Sigma Aldrich, purity $\geq 99.9\%$) was employed to dope TiO₂. To produce a proper solution for spin coating firstly, a homogeneous solution was prepared by mixing 10 ml ethanol (purity $\geq 99.9\%$, analytic reagent,

CHAPTER 5

Changshu Yanguan Chemical) and 2 ml glacial acetic acid (purity $\geq 99.8\%$, Merck) under ultra-sonication for 10 mins duration. Then, 2 ml TTIP was added to the solution. The final solution was ultra-sonicated for 30 mins and was left for 48 hours for ageing in a test tube to form the gel. To make Er:TiO₂ solutions, 0.04 g and 0.06 g Er₂O₃ nanopowder were mixed into two different TiO₂ solutions prepared by same compositions as mentioned before. The solutions were ultra-sonicated for 30 mins and were aged for a period of 48 hours to form the gel. The (100) p-type Si substrates (MTI, USA) were rinsed well with de-ionized water and finally cleaned with acetone followed by RCA (Radio Corporation of America) cleaning for Si substrates. The TFs were deposited by spin coating (spin NXG-P1, apexicindia) technique with substrate rotation speed of ~ 4000 rpm for 1.5 mins on Si substrates. The films were open-air annealed at 200 °C for 2 mins in a muffle furnace. To obtain uniform TFs, the entire coating and annealing process were repeated 3 times with final annealing at 450 °C for 1.5 hours in air atmosphere.

To prepare the samples for electrical characterization, the devices were processed in the form of circular mesas with a diameter of 1000 μm using the same procedure explained in section 5.1.1.

It is worth to mention that these samples have been grown in collaboration with the group of Dr Aniruddha Mondal at National Institute of Technology Durgapur, India.

5.1.4 ERBIUM DOPED In_2O_3 GROWN ON SILICON SUBSTRATES BY SPIN-ON TECHNIQUE

In_2O_3 and Er doped In_2O_3 (Er: In_2O_3) TFs were deposited p-type Si (100) substrates (resistivity $\sim 10 \Omega\text{-cm}$, MTI, USA) by spin-on technique using a chemical route. The sol-gel for In_2O_3 TF was prepared by dissolving 0.5 g Indium (III) Chloride (InCl_3) anhydrous powder (5 N purity, Sigma-Aldrich) into 30 mls of acetylacetone (purity $> 99\%$, Merck) under ultrasonication ($\sim 50^\circ\text{C}$, 15 min) and left for ageing for 24 hours. It was then spin coated (spin NXG-P1, apexicindia) on the p-Si substrates (rotation speed ~ 1000 rpm for 1 min). The as-deposited film was then annealed in a muffle furnace ($\sim 400^\circ\text{C}$ for 10 mins) under atmospheric air condition. The entire process was repeated four times in order to get a uniform film over the substrate with a final annealing at $\sim 400^\circ\text{C}$ for 30 mins. To prepare Er: In_2O_3 solution, Erbium (III) Oxide nano-powder (purity $\geq 99.9\%$, Aldrich) with different weights such as 0.01 g, 0.02 g and 0.04 g were dissolved in 10 mls sulfuric acid (H_2SO_4) by ultrasonication ($\sim 50^\circ\text{C}$, 15 min) and finally added to the previously prepared InCl_3 solution. These doped solutions were ultrasonicated ($\sim 50^\circ\text{C}$, 15 mins) and left for 48 hours for ageing. The Er: In_2O_3 sol-gels were then spin-coated on p-Si substrates (rotation speed ~ 6000 rpm for 2 mins) followed by 10 mins open air annealing ($\sim 400^\circ\text{C}$) for four times with final annealing at $\sim 400^\circ\text{C}$ for 30 mins as has already been described. The atomic fraction of Er in the doped films is estimated, using the energy dispersive X-ray spectroscopy (EDX), to be 0.15, 0.18 and 0.22 at. % for the 0.01 g, 0.02 g and 0.04 g Er_2O_3 containing TFs, respectively. Thus, the samples are labelled in this study as ‘undoped In_2O_3 ’, ‘0.15 at.% Er: In_2O_3 ’, ‘0.18 at.% Er: In_2O_3 ’ and ‘0.22 at.% Er: In_2O_3 ’.

CHAPTER 5

The devices were processed in the form of circular mesas with different diameters for the electrical characterization using the same method described in section 5.1.1.

It is worth to mention that these samples have been grown in collaboration with the group of Dr Aniruddha Mondal at National Institute of Technology Durgapur, India.

The following table shows all samples investigated in this thesis.

Sample	Description
PLD	In (50 nm)/TiO ₂ (380 nm)/Si (n-type)
Sputtered	In (50 nm)/TiO ₂ (300 nm)/Si (n-type)
PLD reference	TiO ₂ (380 nm)/Si (n-type)
Sputtered reference	TiO ₂ (300 nm)/Si (n-type)
(100)	TiO ₂ (380 nm)/GaAs (100) (n-type)
5 (100)	In (5 nm)/TiO ₂ (380 nm)/GaAs (100) (n-type)
15 (100)	In (15 nm)/TiO ₂ (380 nm)/GaAs (100) (n-type)
(311)B	TiO ₂ (380 nm)/GaAs (311)B (n-type)
5 (311)B	In (5 nm)/TiO ₂ (380 nm)/GaAs (311)B (n-type)
15 (311)B	In (15 nm)/TiO ₂ (380 nm)/GaAs (311)B (n-type)
Undoped TiO ₂ TF	TiO ₂ /Si (p-type)
Er: TiO ₂ TF (0.04 g Er ₂ O ₃)	Er (0.04 g) doped TiO ₂ /Si (p-type)
Er: TiO ₂ TF (0.06 g Er ₂ O ₃)	Er (0.06 g) doped TiO ₂ /Si (p-type)
Undoped In ₂ O ₃ TF	In ₂ O ₃ /Si (p-type)
0.15 at.% Er:In ₂ O ₃	Er (0.01 g) doped In ₂ O ₃ /Si (p-type)
0.18 at.% Er:In ₂ O ₃	Er (0.02 g) doped In ₂ O ₃ /Si (p-type)
0.22 at.% Er:In ₂ O ₃	Er (0.04 g) doped In ₂ O ₃ /Si (p-type)

5.2 MEASUREMENTS DETAILS

Details of all the measurements that have been carried out in this thesis are presented in this section.

5.2.1 I-V MEASUREMENTS

Conventional DLTS and Laplace DLTS measurements are mainly based on capacitance transients. Therefore, to avoid misinterpretation of DLTS data, low reverse current, in μA range, is needed for these measurements. I-V measurements were performed for all samples investigated in this thesis using a Keithley 236 source meter which is controlled by a computer using the provided software through GPIB interface. The reverse biases ranged from -1V up to -4V depending on the quality of Schottky diodes with increment of 0.01V. Moreover, the I-V measurements as function of temperature were also carried out to extract diode parameters, as described in Chapter 4.

5.2.2 C-V MEASUREMENTS

The C-V measurements are important for extracting the background doping concentration of a diode. This parameter is also important for DLTS analysis to calculate the trap concentrations. A Boonton 7200 capacitance meter, which operates at a fixed frequency (1MHz), was used to perform C-V measurements for all samples studied in this thesis.

5.2.3 DLTS MEASUREMENTS

DLTS technique, which was discussed in details in Chapter 4, was used to investigate the electrically active defects in the materials studied in this thesis. After

mounting a sample on a TO5 header, it is placed on a holder inside a He closed-loop cycle cryostat (JANIS CCS-450). The sample is cooled down to 10K and then the DLTS measurements started by ramping the temperature at a rate of 2K/min up to 450K (depending on the quality of Schottky diodes) while the sample is reversed biased at a chosen value (V_R). During the temperature scan, a train of electrical pulses, with a chosen value of filling pulse (V_P), generated by a National Instrument interface card is applied to the sample and a transient capacitance is monitored by a Boonton 7200 capacitance meter. The change in the capacitance transient is stored in a computer in a form of DLTS signal as a function of temperature.

5.2.4 LAPLACE DLTS MEASUREMENTS

Broad peaks are usually obtained for conventional DLTS measurements. Laplace DLTS technique, detailed in Chapter 4, is used in order to resolve these peaks. It is an isothermal technique where the sample's temperature is fixed during the measurements. The Laplace DLTS measurements are performed in a range of temperatures around the broad peak obtained from the conventional DLTS.

5.2.5 PHOTOLUMINESCENCE (PL) MEASUREMENTS

Photoluminescence (PL) is a powerful technique for studying the electronic structure of semiconductors. The PL measurements were carried out on the samples mentioned in section 5.1.1 and 5.1.2 in collaboration with the group of Prof. Yara Galvão Gobato at Federal University of São Carlos, Brazil. The PL spectra of In doped TiO₂ thin films were investigated as a function of temperature (12-300 K) using a laser (He-Cd) excitation wavelength of 325 nm.

5.2.6 XRD AND RAMAN MEASUREMENTS

X-ray diffraction (XRD) patterns were measured in a Bruker D8 Discover Diffractometer, using Cu K α radiation ($\lambda = 1.5418 \text{ \AA}$). The diffraction pattern was obtained at diffraction angles between 10° and 80° with geometry 2θ (the glancing angle X-ray diffraction-GAXRD method) and the conventional θ - 2θ techniques at room temperature. The Raman measurements were performed using a Renishaw micro Raman inVia spectrometer under ambient conditions. A laser with a wavelength of 514 nm was used as an excitation source. The XRD and Raman measurements were carried out on samples mentioned in section 5.1.1 whereas for samples mentioned in section 5.1.2, only XRD measurements have been carried out. All these measurements were carried out in collaboration with Dr Jorlandio Francisco Felix's group at University of Brasília, Brazil.

EFFECT OF GROWTH TECHNIQUES ON THE STRUCTURAL, OPTICAL AND ELECTRICAL PROPERTIES OF INDIUM DOPED TiO₂ THIN FILMS

In this chapter, the structural, optical and electrical properties of In-doped TiO₂ thin films grown by two different growth techniques, namely PLD and sputtering are investigated. XRD, PL, Raman, I-V, C-V, DLTS and Laplace DLTS techniques have used to study the effect of growth methods on the properties of In-doped TiO₂ thin films.

6.1 INTRODUCTION

Transparent conducting oxides (TCOs) materials have wide applications in terms of absorption, transparency of the visible light and electrical conductivity. They are used in optoelectronic, photovoltaic, photocatalytic and photoelectrochemical water splitting applications [1]. TiO₂ is a TCO material which has been extensively studied for photocatalysis and photovoltaic applications. This wide interest in TiO₂ is due to its efficient photoactivity, high stability, low cost and non-toxicity [2-4]. The large bandgap (3.0-3.4 eV) [5, 6] of TiO₂ makes it only sensitive to UV light and therefore it is not efficient for solar cell applications. Amongst a lot of approaches that have been used to modify the electrical and optical properties of TiO₂ in order to make it sensitive to visible light, metal ion doping has been proven to be one of the best methods [7]. Different metals have been used as dopants in TiO₂ to change its electronic and optoelectronic properties [8]. Using indium as a dopant has attracted a lot of attention as it can

modify some properties of TiO₂, such as bandgap, surface composition and charge transport.

Oxygen vacancies are well-known defects in TiO₂ which can alter the geometric structure and the chemical properties of the system [9]. In addition to the defects that may be introduced into the forbidden bandgap of TiO₂ due to the incorporation of indium, the growth methods can also provide defect levels within the bandgap. Understanding the deep and shallow level defects is essential for future devices [10]. Deep level transient spectroscopy (DLTS) and photoluminescence (PL) are powerful tools to investigate these defects in semiconductors. Particularly, by using DLTS, defects parameters such as activation energy, capture cross section and concentration can be determined. In this study, we investigated the effect of growth techniques, namely pulsed laser deposition (PLD) and sputtering, on structural, optical and electrical properties of indium doped TiO₂ thin films deposited on silicon substrates.

6.2 RESULTS AND DISCUSSION

6.2.1 SAMPLE DETAILS

In this study, two series of samples were prepared using two different growth methods. For the first series, a layer of 380 nm TiO₂ thin film was deposited on (100) n-type silicon substrate using pulsed laser deposition (PLD) techniques. This series of samples is named 'PLD sample'. In the second series, RF magnetron sputtering technique was employed to deposit a 300 nm thin film of TiO₂ on (100) n-type silicon substrate. The sample here is labelled as 'Sputtered sample'. By thermal evaporation, layers of indium (50 nm thick) were deposited on top of each set of samples. A third series of control samples, which do not contain In, were

grown by sputtering and PLD techniques and labelled here as ‘sputtered reference sample’ and ‘PLD reference sample’, respectively. Full details of fabrication the samples were presented in chapter 5, section 5.1.1.

6.2.2 STRUCTURAL AND OPTICAL INVESTIGATIONS

Fig. 6.1 shows the XRD patterns of the PLD and sputtered samples. The XRD θ - 2θ pattern of the sputtered reference sample, shown in Fig. 6.2, exhibited diffraction peaks at 25.4° and 25.5° corresponding to the (011) and (110) lattice planes revealing the anatase and rutile phases, respectively. Fig. 6.1 (a) shows the XRD pattern of the sputtered sample and the data shows the presence of anatase and rutile phases of TiO_2 , however, an additional signature of indium oxide phase can be noticed with the main peaks at 22.5° , 30.6° , 35.6° , 47.3° , 51.1° , and 60.9° corresponding to the (211), (222), (400), (431), (440), and (622) lattice planes of cubic In_2O_3 . These peaks are in good agreement with the standard spectrum according to the Joint Committee on Powder Diffraction Standards (JCPDS File no.: 06-0416), respectively. Additionally, the precipitation and formation of a second phase may contribute to the increase of trap defects, as will be shown later using the DLTS technique. TiO_2 thin films grown by the sputtering technique and composed of rutile and anatase phases have also been observed by Huang et al. [11].

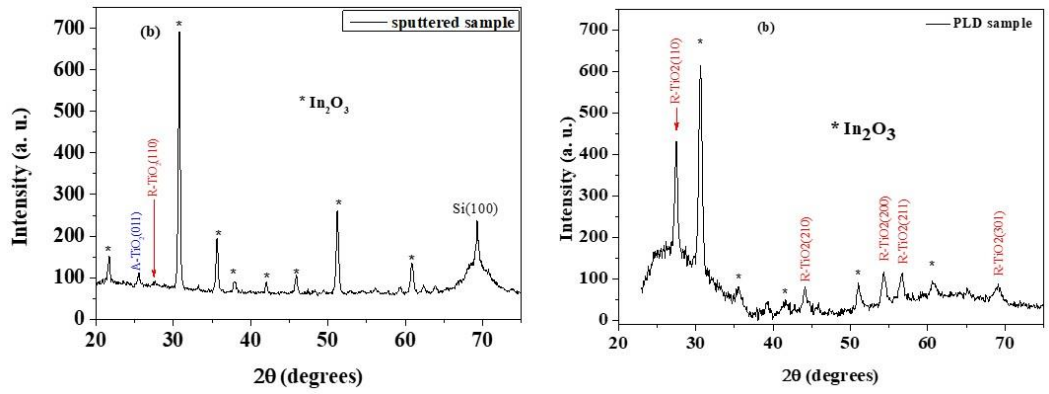


Fig. 6.1: Room temperature XRD pattern of In-doped TiO_2 thin films prepared by (a) sputtering and (b) PLD.

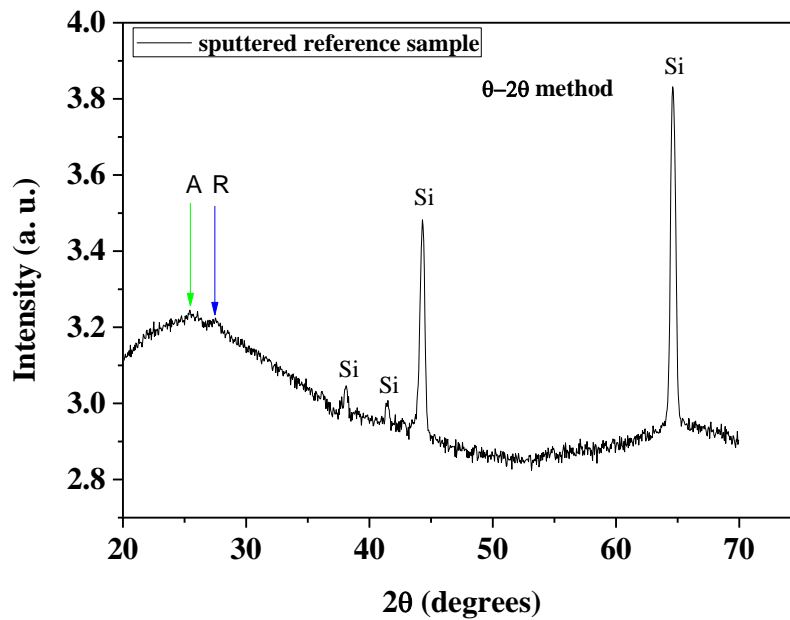


Fig. 6.2: XRD pattern of sputtered reference sample.

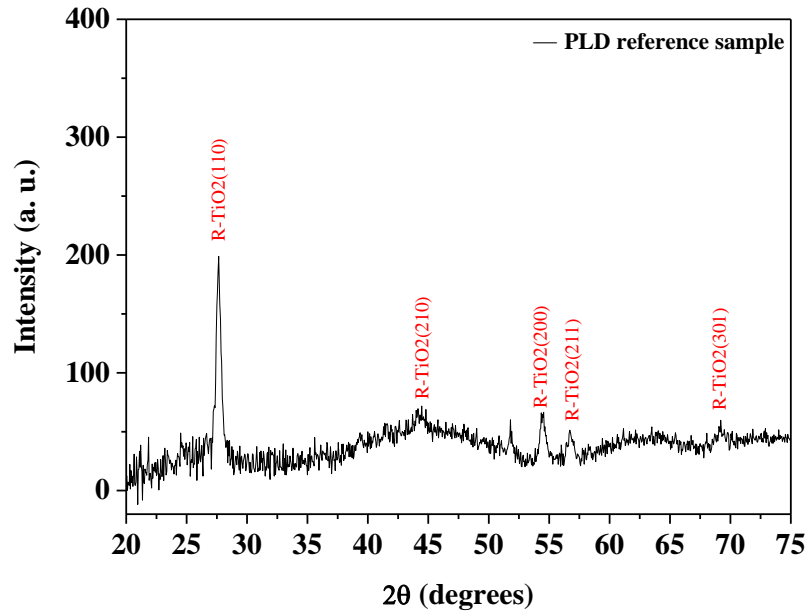


Fig. 6.3: XRD pattern of PLD reference sample.

For the PLD reference sample, Fig. 6.3 shows a single rutile phase characteristic of TiO_2 thin films. Fig. 6.1 (b) shows the XRD pattern of the PLD sample where the peaks are in good agreement with the standard XRD patterns of TiO_2 found in the literature [11]. It can be seen that the peak R(110) strongly dominates over the other peaks related to rutile TiO_2 structure, indicating the preferential orientation. However, in the PLD sample, the presence of both indium oxide phase and TiO_2 pure rutile phase are observed (see Fig. 6.1 (b)). From the XRD results, it is possible to conclude that for the sputtered reference sample both rutile and anatase phases are present, while only the rutile phase was detected in the PLD reference sample. Moreover, the presence of a layer of indium (50 nm thickness) causes the formation of In_2O_3 phases in both the sputtered and PLD samples. However, the polycrystalline character of the In_2O_3 phase is more intense in the sputtered samples. This latter behaviour will have a strong influence on the electrical properties of the devices, as will be shown later.

CHAPTER 6

In order to confirm the XRD results, Raman studies have been performed. Fig. 6. 4 (a) shows the Raman spectra of the sputtered samples where both rutile and anatase phases are observed. The sputtered sample shows an intense peak at $E_g=142\text{ cm}^{-1}$ from an anatase phase. The inset of Fig. 6. 4 (a) shows a weak peak at $B_{1g}=399\text{ cm}^{-1}$ and $E_g=638\text{ cm}^{-1}$ that are characteristics of anatase phase of TiO_2 [12]. A single band at $E_g=446\text{ cm}^{-1}$ from a TiO_2 rutile phase is also observed. Finally, a weak vibrational band was observed for cubic In_2O_3 at 197 cm^{-1} which is assigned to the O–In–O bending modes of cubic In_2O_3 . The most intense peak at 520 cm^{-1} is due to the Raman signal from Si(100) substrates. The results from XRD also show similar behavior. The same Raman bands are also observed in the sputtered reference sample as shown in Fig. 6.5.

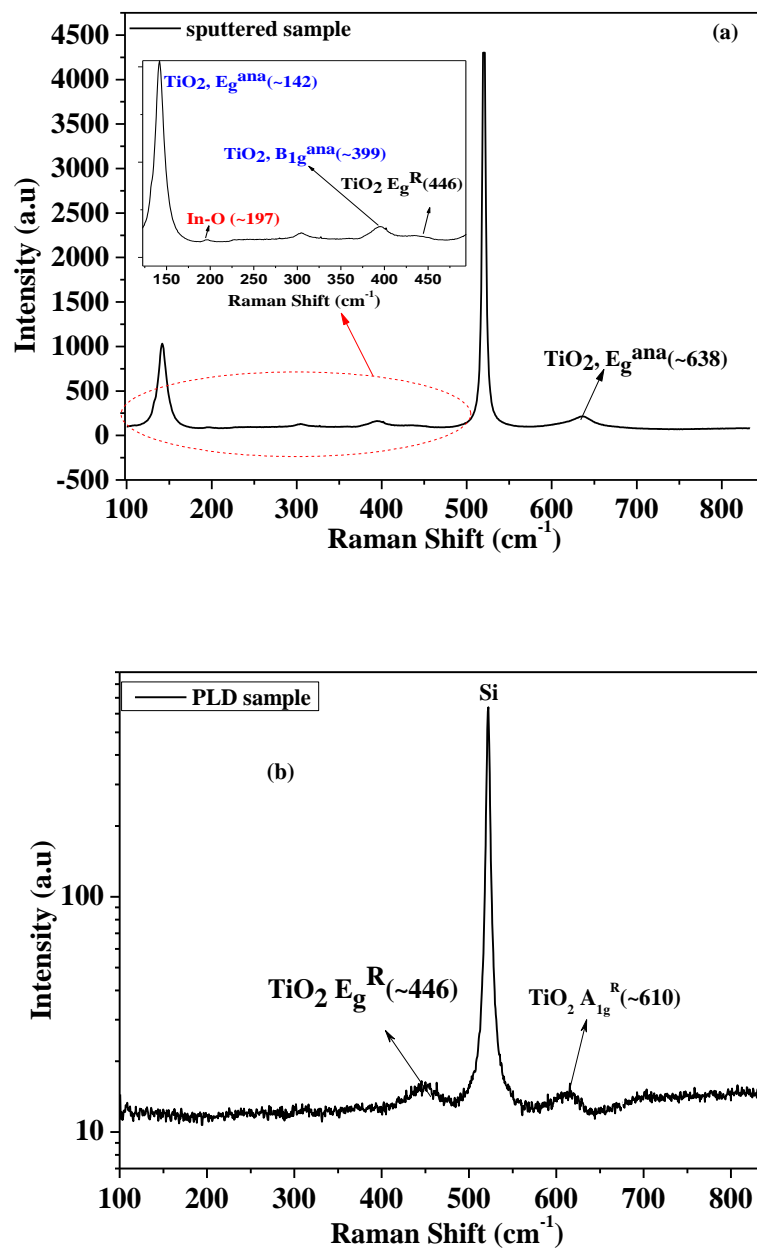


Fig. 6. 4: Raman spectrum of In-doped TiO_2 thin films prepared by (a) sputtering and (b) PLD.

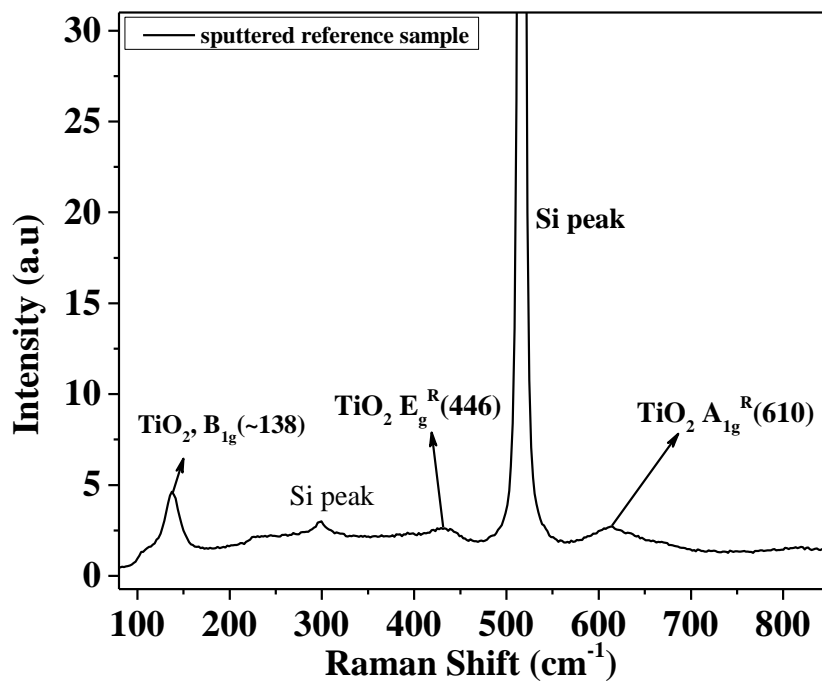


Fig. 6.5: Raman spectrum of sputtered reference sample.

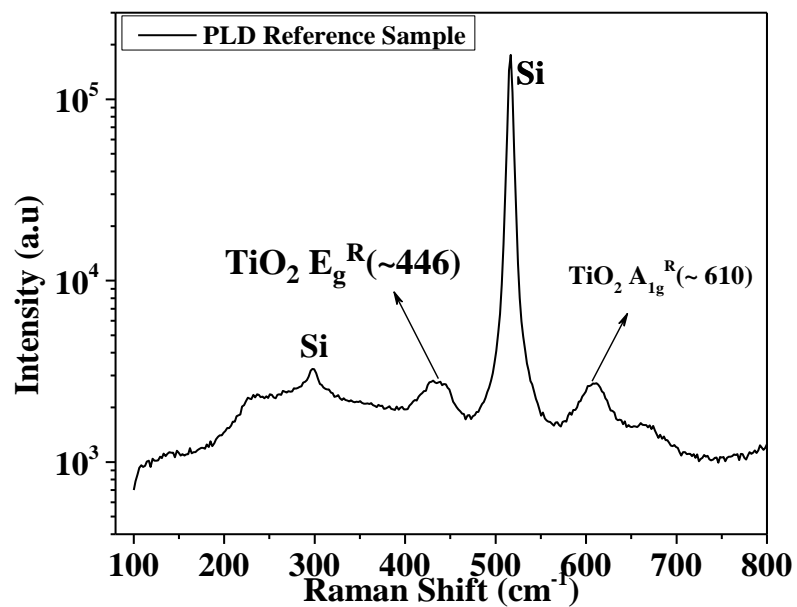


Fig. 6.6: Raman spectrum of PLD reference sample.

CHAPTER 6

Fig. 6. 4 (b) shows the Raman spectra of PLD samples. As can be seen in Fig. 6. 4 (b), only two peaks at $E_g=446 \text{ cm}^{-1}$ and $E_g=610 \text{ cm}^{-1}$ are observed which are related to rutile phase of TiO_2 [13]. These results are in good agreements with XRD results, where only the rutile phase was observed. The Raman spectrum for PLD reference samples, illustrated in Fig. 6.6, showed the same characteristics.

6.2.3 CURRENT-VOLTAGE MEASUREMENTS

I-V measurements as a function of temperature (20-440 K with 20 K intervals) were performed in PLD and sputtered samples in order to determine the diode parameters such as ideality factor (n), barrier height (ϕ_b) and series resistance (R_s). Fig. 6.7 shows the room temperature semi-logarithmic plot of I-V characteristics for both samples. It can be seen from the figure that the reverse current of the sputtered sample is higher than that of PLD sample. In particular, the reverse bias leakage current at -4 V for PLD and sputtered samples are $1.3 \times 10^{-7} \text{ A}$ and $5.9 \times 10^{-7} \text{ A}$, respectively. This may indicate the presence of more defects in the sputtered samples than PLD samples. These defects which act as generation-recombination centres and contribute to the tunnelling process in reverse bias can be probed by DLTS technique [8]. In addition, from the linear I-V plot (inset of Fig. 6.7) a turn-on voltage (V_{on}) of 0.26 V and 0.77 V were obtained for the sputtered and PLD samples, respectively.

The I-V characteristics of an ideal diode including series resistance (R_s) can be described by the thermionic emission model [14] as:

$$I = I_0 \left[\exp \left(\frac{q(V - IR_s)}{nKT} \right) - 1 \right] \quad (6.1)$$

where I_0 is the saturation current and is given by:

$$I_0 = AA^*T^2 \exp \left(\frac{-q\phi_b}{KT} \right) \quad (6.2)$$

CHAPTER 6

In Equations (6.1) and (6.2) A is the effective diode area ($A = 6.362 \times 10^{-3} \text{ cm}^2$ for both samples), A^* is the effective Richardson's constant ($A^* = 671 \text{ A cm}^{-2} \text{ K}^{-2}$ [15]), k is Boltzmann's constant, T is the temperature, q is the elementary charge, n is the ideality factor, ϕ_b is the barrier height and R_s is the series resistance. In order to improve the accuracy of calculating the diode parameters (n , ϕ_b , R_s and I_0), the Werner's method [16] was used which was explained in chapter 4, section 4.3. Fig. 6.8 shows the plot of G/I versus G and the plot of $\ln(I)$ versus $(V-IR_s)$ that are used to extract the diode parameters for PLD and sputtered samples. These parameters for PLD and sputtered samples at room temperature are shown in Table 6.1.

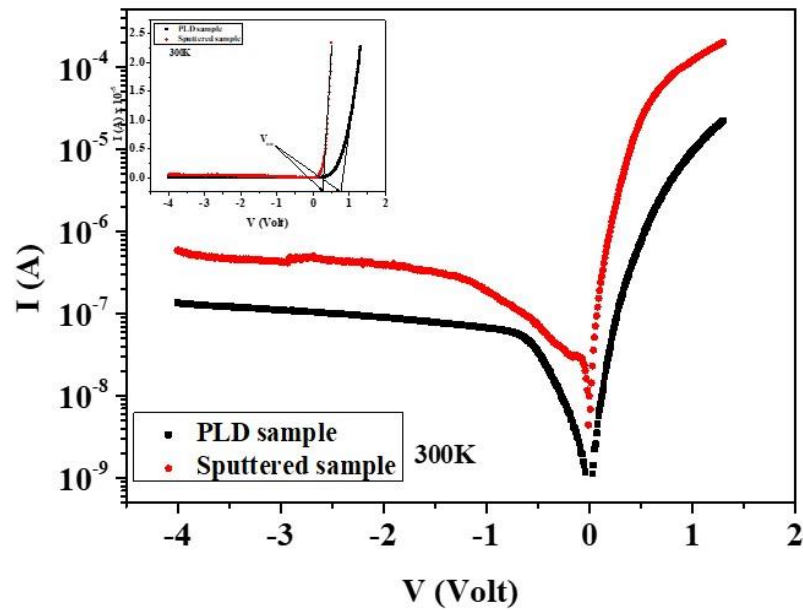


Fig. 6.7: Semi-logarithmic I-V plots for PLD and sputtered samples. The inset shows the linear I-V plots.

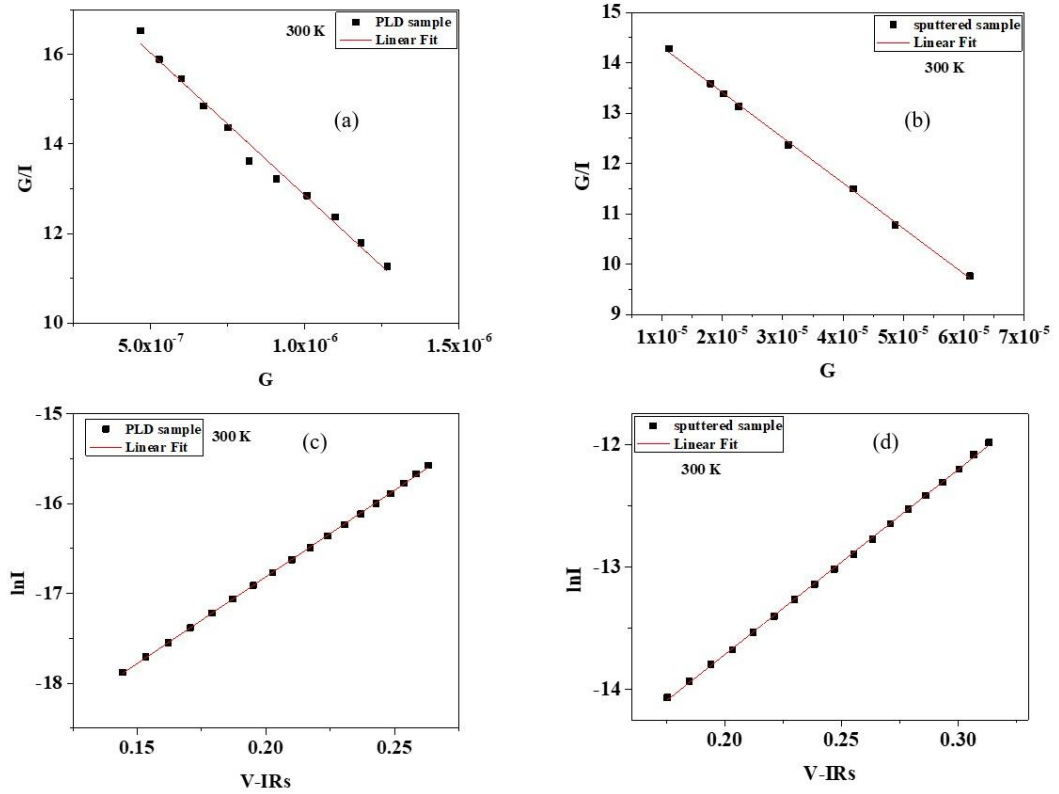


Fig. 6.8: The plot of G/I versus G for (a) PLD and (b) sputtered samples. The plot of $\ln(I)$ versus $(V-IR_s)$ for (c) PLD and (d) sputtered samples.

Table 6.1: Ideality factor (n), barrier height (ϕ_b) and series resistance (R_s) at room temperature for PLD and sputtered samples.

Sample	n	ϕ_B (eV)	R_s (k Ω)
PLD	2.01 ± 0.02	0.8671 ± 0.0007	330 ± 11
sputtered	2.542 ± 0.007	0.7654 ± 0.0008	5.92 ± 0.08

The plot of $\ln(I_0/T^2)$ versus $1000/T$ for PLD sample (Fig. 6.9 (a)) in the temperature range 100-420 K follows a straight line. This behaviour suggests that the conduction mechanism could be governed by thermionic emission and the saturation current can be obtained using Equation (6.2) [17]. A similar behaviour

CHAPTER 6

was observed in the sputtered sample in the temperature range 160-420 K (Fig. 6.9 (b)). The Richardson constants that are calculated from the intercept of the straight line of $\ln(I_0/T^2)$ versus $1000/T$ plot for PLD sample ($A^* = 1.917 \times 10^{-6} \text{ A/K}^2 \text{ cm}^2$) and sputtered sample ($A^* = 4.956 \times 10^{-8} \text{ A/K}^2 \text{ cm}^2$) are much lower than the well-established value ($A^* = 671 \text{ A/K}^2 \text{ cm}^2$). This deviation from the Richardson constant value may be due to the spatial inhomogeneous barrier and potential fluctuations at the interface that consist of low and high barrier areas [18, 19]. It is worth mentioning that a deviation from linearity is noticed for both sample at low temperature and that could be due to a contribution of additional current as a result of the reduction in the barrier height [18].

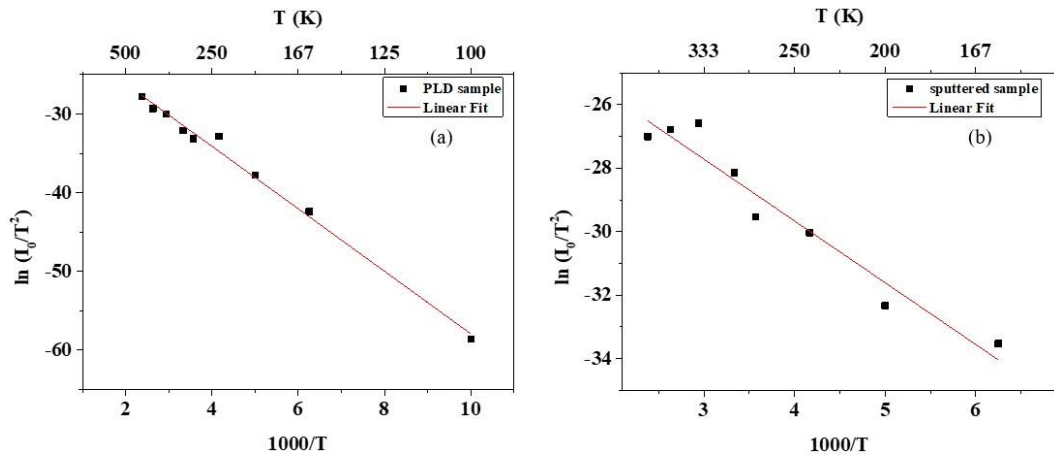


Fig. 6.9: Plots of $\ln(I_0/T^2)$ versus $1000/T$ for (a) PLD and (b) sputtered samples.

Fig. 6.10 shows the temperature dependence of the barrier height (ϕ_B) and ideality factor (n) for both samples. As the temperature increases, the barrier height increases while the ideality factor decreases. This behaviour is known to be due to nonuniformity of interfacial charges. At low temperatures, carriers are frozen and

CHAPTER 6

therefore the current does not follow the thermionic emission mechanism. At low temperatures, the current flows through the interface states and this results in higher values of the ideality factor [20]. Note that the carriers, at low temperatures, can overcome the lower barriers and the mechanism of transport will be dominated by the current flowing through the region with lower barrier height. As the temperature increases, carriers gain sufficient energy to overcome the higher barriers, which results in an increase of the barrier height with temperature [21].

The barrier height and ideality factor behaviour with temperature have been attributed to the barrier inhomogeneity. This inhomogeneity of barrier height was also confirmed by the almost linear relationship between barrier height and ideality factor for both samples as shown in Fig. 6.11 [22]. It is worth noting that deviation from a linear relationship has been attributed to uncertainties in the calculation of the ideality factor [23].

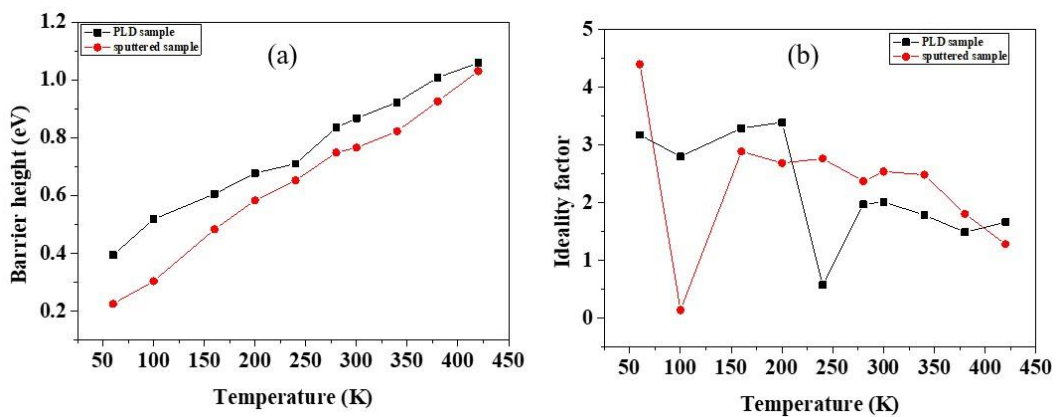


Fig. 6.10: In-doped TiO₂ samples grown by PLD and sputtering (a) barrier height (ϕ_B) versus temperature; (b) ideality factor (n) versus temperature.

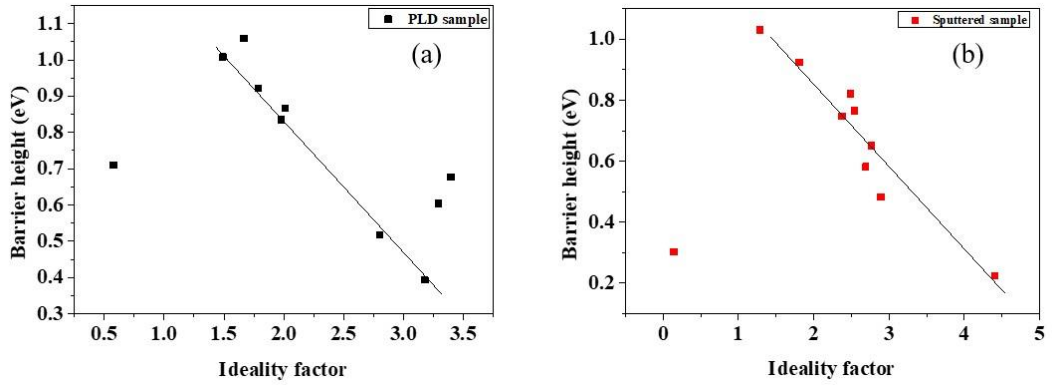


Fig. 6.11: Barrier height (ϕ_B) versus ideality factor (n) for (a) PLD sample and (b) sputtered sample.

The main trap which contributes to the leakage current can be calculated using I-V measurements at different temperatures by plotting the reverse current versus inverse temperature [20]. Fig. 6.12 shows the plot of reverse current versus $1000/T$ for -1 V bias voltage for both samples. One main trap has been found in PLD sample with an activation energy $E_{\text{PLD}} = 0.492 \pm 0.007$ eV. However, two traps have been detected in sputtered sample, namely $E_{\text{SP1}} = 0.100 \pm 0.005$ eV and $E_{\text{SP2}} = 0.51 \pm 0.04$ eV. Note that E_{PLD} and E_{SP2} have similar activation energies and the origin of this trap may be due to oxygen vacancy [7] or a deep donor Ti^{+3} state [10]. E_{SP1} may be related to oxygen vacancies or interstitial Ti ion [24]. A large number of defects determined from I-V measurements could account for the high value of the reverse current [20]. The larger value of the reverse current observed in the sputtered sample could be explained by the larger number of defects detected in the sputtered sample than the PLD sample. It is worth noting that the numbers of traps found using the I-V measurements are consistent with those found by using optical technique, as will be shown later.

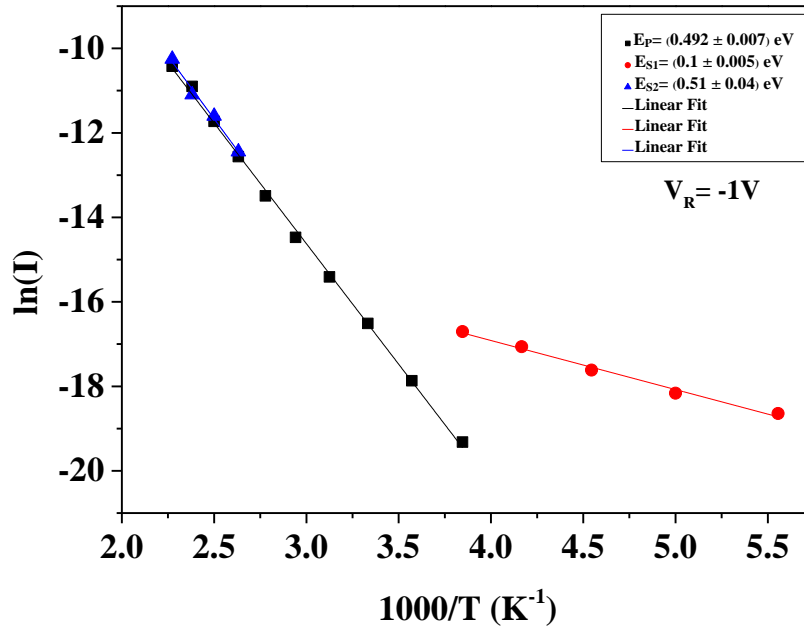


Fig. 6.12: Reverse current versus $1000/T$ for reverse bias voltage $V_R = -1$ V for In-doped TiO_2 samples prepared by PLD and sputtering

6.2.4 CAPACITANCE-VOLTAGE MEASUREMENTS

The C-V measurements for both samples at room temperature are shown in Fig. 6.13 (a). It is clear from the figure that the sputtered sample has higher capacitance than the PLD sample and this could be due to shallow ionised impurity levels. Also, a small shoulder can be seen in both samples, at -0.6 V and at -1.3 V for PLD and sputtering, respectively. This behaviour could be due to a poor interface quality and drift in carriers [8]. The slope of the best fit of the plot $1/C^2$ versus reverse bias, shown in Fig. 6.13 (b), was used to calculate the free carrier concentrations, N_d , for both samples at room temperature. For the PLD sample, the doping concentration was found to be uniform as evidenced by the linear behaviour of the plot of $1/C^2$ versus applied bias. The free carrier concentration is about $5.4 \times 10^{13} \text{ cm}^{-3}$. However, as depicted in Fig. 6.13 (b), for the sputtered sample, two lines

CHAPTER 6

were fitted to the C-V data, confirming two different doping concentrations of $1.0 \times 10^{14} \text{ cm}^{-3}$ and $\sim 3.0 \times 10^{14} \text{ cm}^{-3}$. The free carrier concentration is higher near the junction interface than in the bulk.

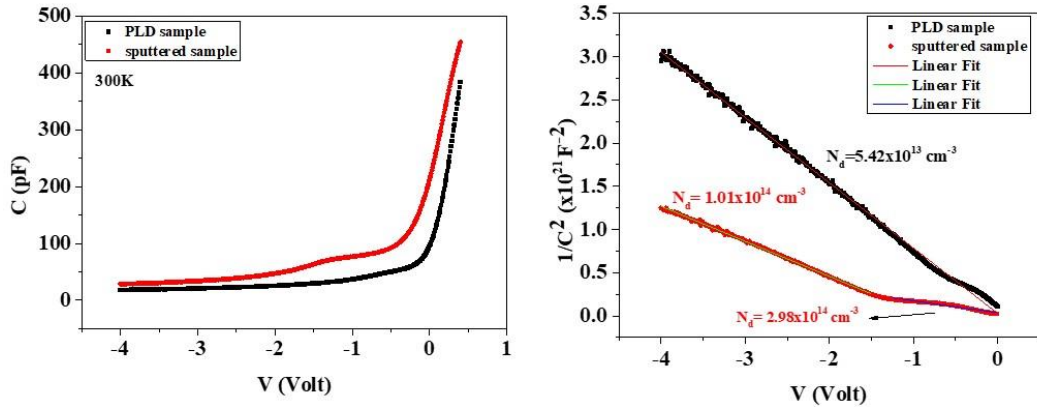


Fig. 6.13: (a) C-V plot and (b) $1/C^2$ versus V plot at room temperature of In-doped TiO_2 samples prepared by PLD and sputtering.

6.2.5 OPTICAL PROPERTIES

Fig. 6.14 (a) and (b) show typical normalized PL spectra at 12K and 300K for both samples prepared by sputtering and PLD. It was observed that the PL spectrum of the sputtered sample consists of only one broad band emission around 1.95 eV. This result is similar to the one previously reported for In-doped TiO_2 films prepared by e-beam evaporation [8]. The nature of this emission band was previously attributed to the In^{3+} cation, which may produce a radiative transition between In (5P) and oxygen defect level [8]. However, the observed broad PL band could also be associated with optical transitions related to anatase and rutile phases. It can also include an important contribution of In_2O_3 which can be formed during the thermal annealing of the samples to incorporate In. On the other hand, the PLD

sample revealed several peaks. In order to understand the contribution of In doping we have also studied PL from reference samples prepared by sputtering and PLD. Fig. 6.14 (c) and (d) show the normalized PL spectra at 300K for the reference and doped TiO₂ samples prepared by both techniques. We remark that for the reference sample prepared by sputtering the PL spectra shows four emission peaks (Fig. 6.14 (d)) at 300K. As will be discussed below, the anatase phase of TiO₂ usually shows PL bands around 1.9 and 2.4eV while the rutile phase usually shows PL bands around 1.5 and 1.7eV [25]. Therefore, the PL peaks observed at 300K for the reference sample prepared by sputtering are fully consistent with the presence of anatase and rutile phases which were also evidenced by XRD and Raman results.

As mentioned previously several bands were observed for the PLD sample in the visible and infrared region at 12K and 300K (Fig. 6.14 (a) and 8(b)) which are labelled as P₁ (1.93 eV), P₂ (2.52 eV), P₃ (2.90 eV), and P₄ (3.25 eV) at 12 K. In the following, a detailed discussion is presented about the nature of these emission bands and possible interpretation of PL peaks observed in our PLD sample.

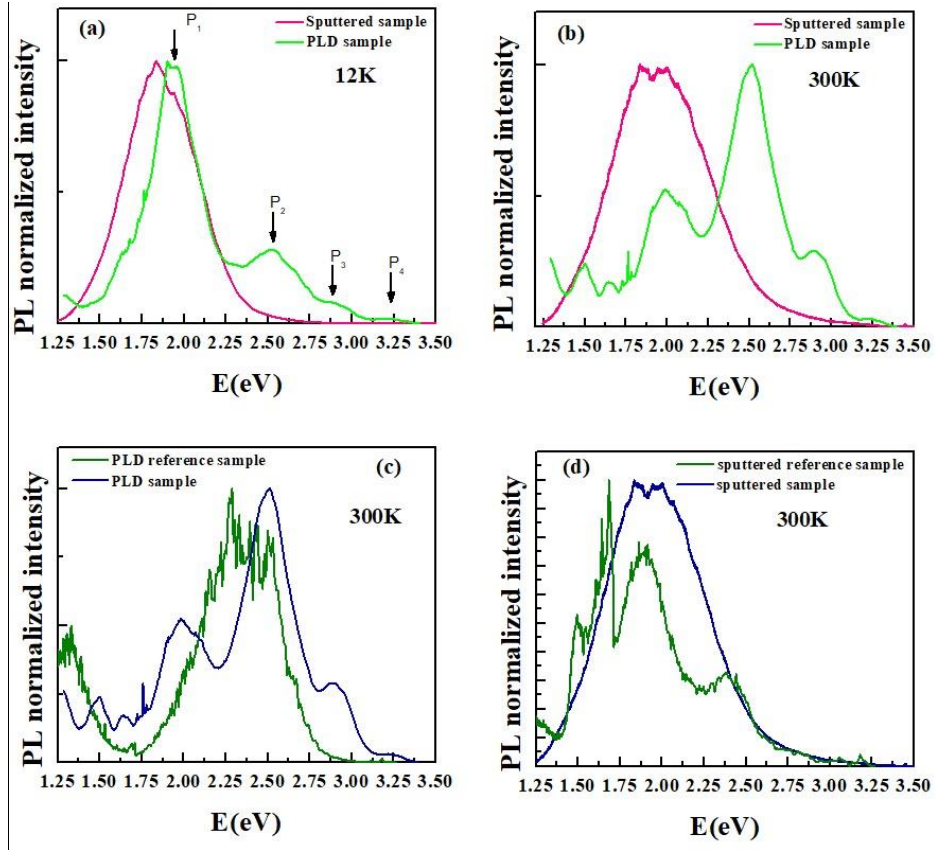


Fig. 6.14: Normalized PL spectra of In-doped TiO₂ thin films grown by PLD and sputtering at (a) 12K and (b) 300K. Comparison between PL emission at 300K for undoped and In-doped TiO₂ grown by (c) PLD and (d) sputtering.

As mentioned previously the PL spectra of TiO₂ material usually depends on the crystal phase (anatase, rutile or mixed phases) [25]. It was reported [25] that the TiO₂ PL spectrum shows green (around 2.5 eV) and red (around 1.9 eV) emissions for the anatase phase and only a near-infrared emission (NIR) band around 1.5 eV for the rutile phase. The green PL emission is usually attributed to self-trapped excitons [26], oxygen vacancies [27] and surface states [28]. However, a detailed study of these emissions has demonstrated that the green emission could also be related to radiative recombination of free electrons with trapped holes. These trapped holes could be localized at oxygen vacancies sites (V_O) or at Ti sites adjacent to V_O [25]. The red PL emission is usually related to recombination between trapped electrons and free holes [25]. On the other hand, the nature of NIR

emission in TiO_2 is more difficult to explain [25]. Usually, the rutile samples are less sensitive to prolonged exposure to UV illumination in oxygen environment than anatase samples, which suggests that the NIR PL could be associated to a possible radiative recombination between midgap trapped electrons and free holes at the valence band. Moreover, our XRD and Raman spectroscopy results have revealed both TiO_2 and In_2O_3 phases for the In-doped TiO_2 samples. The formation of In_2O_3 after the thermal annealing process which was used to incorporate In in the TiO_2 lattice could also contribute to the PL bands observed in the In-doped TiO_2 samples. It is well known that In_2O_3 oxide is also a wide bandgap (~ 3.6 eV) semiconductor [29]. It was previously reported that the PL spectra displayed a near band edge (NBE) emission around 3.23 eV and a defect-related emission at ~ 1.98 eV [30]. The PL peak in the visible region (defect-related emission) was previously associated to the transition from the oxygen vacancy level to the valence band [31]. In addition, this red emission was also previously associated with deep level states (1.94 eV) which can be present in In_2O_3 [32].

As mentioned above our In-doped TiO_2 PLD samples revealed four emission bands (labelled P_1 , P_2 , P_3 and P_4). It was found that as the temperature increases, a gradual reduction of P_1 emission band was observed as expected. However, additional weak emissions bands located around 1.5eV and 1.6eV were also detected. The PL peak energies of most of these bands are smaller than the energy gap of TiO_2 and In_2O_3 . Therefore, all these emission bands were attributed to the localized levels in the bandgap and could be due to intrinsic defects in both TiO_2 and In_2O_3 . As mentioned above, the observed defect emission peaks for TiO_2 and In_2O_3 usually have emissions in the same energy range. Therefore, it is difficult to separate the contribution of defect-related emissions from the In_2O_3 and TiO_2 .

In order to investigate which peak could be associated to the TiO₂, we have also studied a reference sample, i.e. undoped TiO₂ sample. Fig. 6.14 (c) shows the 300 K PL spectra of undoped and 50nm In-doped TiO₂ samples prepared by PLD.

As can be seen in Fig. 6.14 (c), the PL peaks of the undoped TiO₂ thin film have a smaller intensity in the range of about 1.8-2.9 eV and around 1.35 eV as compared to those in In-doped TiO₂ samples. The observed bands of 1.8-2.9 eV and ~1.35 eV are assigned to the anatase and rutile phases (mixed phase), respectively [25]. The visible emission was associated to a combination of two bands previously reported in the literature for the anatase phase, namely the green band (~2.5 eV) and the red band (~1.9 eV) [25]. However, the anatase phase was not evidenced in the XRD and Raman results. This band, which is prominent in the PL spectra, could be associated to a small contribution from the anatase phase (mixed phase sample) that cannot be evidenced by XRD and Raman results. Additionally, emissions around 1.5 and 1.7 eV have been observed only for the rutile phase and associated with the radiative recombination between midgap trapped electrons and free holes at the valence band [25] and Ti³⁺ ions [33]. We attribute the broad band around 1.2-1.6eV to the rutile phase. On the other hand, additional PL peaks (P₁, P₂, P₃ and P₄) were observed in PLD sample which could be associated to the formation of In₂O₃. Particularly, the P₄ band that was observed around 3.25 eV at 12 K can be associated to the band edge emission of In₂O₃ [32]. The other PL peaks (P₁, P₂ and P₃) have important contribution of defect emission due to In₂O₃.

We have also investigated the temperature dependence of the emission bands for both PLD and sputtering samples. Fig. 6.15 shows a typical temperature dependence of PL spectra for these samples. It was found that the emission intensity of the peak at 1.93 eV (P_1) decreases considerably with the increase of temperature for both sputtering and PLD samples (Fig. 6.15 (a)) as expected. However, the intensities of the other emissions of the PLD sample increase when the temperature increases (in the range of 100 to 300K). We believe that this effect could be associated to charge transfer, or traps due to the presence of defects or some disorder in TiO_2 and/or In_2O_3 . Traps could localize carriers non-radiatively and the trapped carriers are thermally activated and contribute to the optically active states. We have also estimated the activation energy using a double-channel activation energies function [34, 35].

$$I(T) = \frac{I_0}{1 + \gamma_1 \exp(-E_{a1}/(k_B T)) + \gamma_2 \exp(-E_{a2}/(k_B T))} \quad (6.3)$$

where I_0 is the PL intensity at $T = 0$ K, $\gamma_{1,2}$ are two constants related to the ratio between radiative and non-radiative recombination processes, $E_{a1,2}$ are the activation energies corresponding to the non-radiative recombination process, and k_B is the Boltzmann constant.

CHAPTER 6

The inset in Fig. 6.15 (a) and (b) shows the temperature ($1/k_B T$) dependence of the integrated PL intensity (I) (Arrhenius plot) in the temperature range $T = 12\text{--}300\text{ K}$ for PLD sample ($P_1=1.93\text{ eV}$) and sputtered sample (peak at 1.95 eV). Clearly, the emission intensity decreases with increasing temperature following an Arrhenius-like function. Equation (6.3) has been used to fit the PL intensity in the whole measured temperature range (dashed line). Activation energies of $E_{SP\alpha 1}=82.0\text{ meV}$ and $E_{SP\alpha 2}=12.0\text{ meV}$, and $E_{PLD\alpha 1}=22.3\text{ meV}$ were obtained for sputtering and PLD thin films, respectively. Al Saqri et al. [8] reported a defect in In-doped TiO_2 thin films with an activation energy of 62 meV . They attributed this defect to the intrinsic Ti atoms and ionization energies of oxygen vacancies. In our case, the calculated activation energy could also be related to the similar nature which has already been evidenced from emission processes.

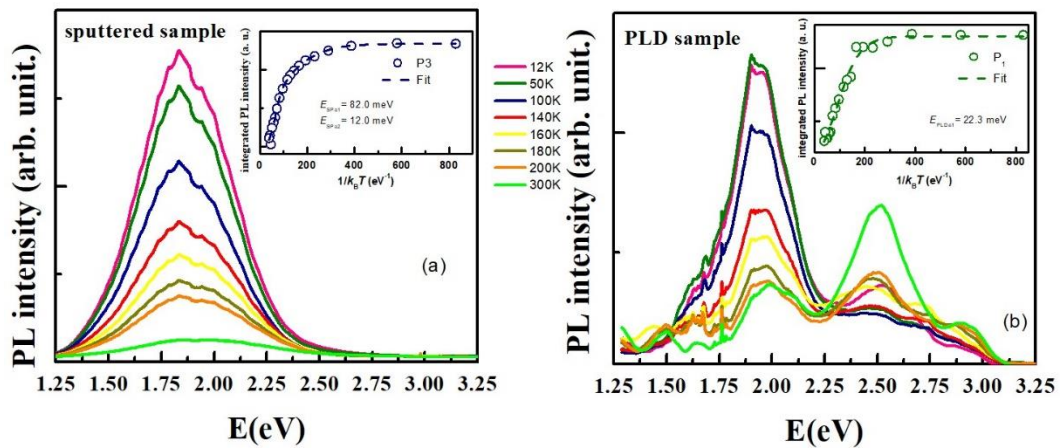


Fig. 6.15: PL spectra of (a) sputtered sample and (b) PLD sample at different temperatures in the range 12-300K. The insert shows the integrated Arrhenius plot for both samples.

In conclusion, well resolved PL bands in the PLD sample and a broad PL band in the sputtered sample were observed. These results provide strong evidence that PLD samples are of higher quality than sputtered samples. However, important contribution defect emission from the formation of In_2O_3 was observed in the PL from PLD samples. These results are also consistent with the I-V results for PLD samples which have shown better performance than the sputtered samples. The optical results are also consistent with the DLTS results which will be presented below.

6.2.6 DLTS AND LAPLACE DLTS MEASUREMENTS

In order to investigate the effect of the growth techniques on the electrically active defects, DLTS technique has been used [36]. The experiment was carried out with a reverse bias, $V_R = -1\text{V}$, a filling pulse height, $V_P = 0\text{V}$, a filling pulse time, $t_P = 1\text{ msec}$ and a rate window of 200 s^{-1} for both samples. Fig. 6.16 shows the DLTS signals versus temperature for both samples over the scanned temperature range 10K-450 K. Broad peaks due to electron traps have been detected in both samples as shown in Fig. 6.16. Laplace DLTS measurements [37] have been carried out on both samples in order to resolve the broader peaks. From the Laplace DLTS measurements, only one electron trap (E_P) and five electron traps (E_{s1} , E_{s2} , E_{s3} , E_{s4} , and E_{s5}) were detected in the PLD and sputtered samples, respectively. The activation energies of these traps were calculated from the Arrhenius plots as shown in Fig. 6.17. The trap parameters, such as activation energies, trap concentrations and capture cross sections are summarised in Table 6.2.

As seen in Table 6.2, traps E_P and E_{s4} have the same energies so they may have the same origin which could be assigned to oxygen vacancy as reported by E.

CHAPTER 6

Wang *et al.* [7] in their study of In-doped TiO₂ using the sol-gel method. However, B. Morgan and G. Watson have investigated the formation of native defects in anatase TiO₂ using the density functional theory [10] and assigned a trap at 0.5 eV to Ti⁺³ state. So, traps E_p and E_{s4} could be assigned to oxygen vacancy or Ti⁺³ state. It is worth mentioning that trap E_{s4} has higher concentration (1.59×10^{14}) when compared to trap E_p (3.75×10^{13}). Moreover, the capture cross-section of trap E_{s4} (5.92×10^{-13}) is higher than that of trap E_p (4.00×10^{-16}). E_{s1} is a shallow level trap and E_{s2} may be related to oxygen vacancy or interstitial Ti ion [24]. The E_{s2} trap was also observed using PL measurement, labeled as E_{SPa1}. E_{s3} and E_{s5} may be assigned to a Ti donor level [38].

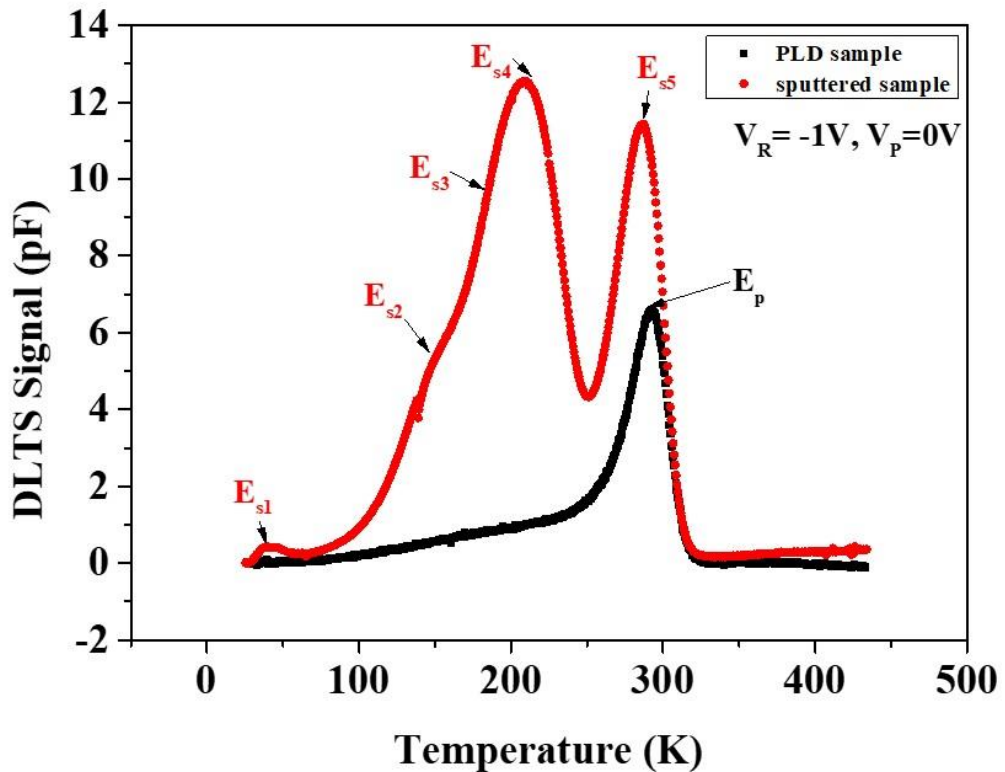


Fig. 6.16: DLTS signal for PLD and sputtered samples.

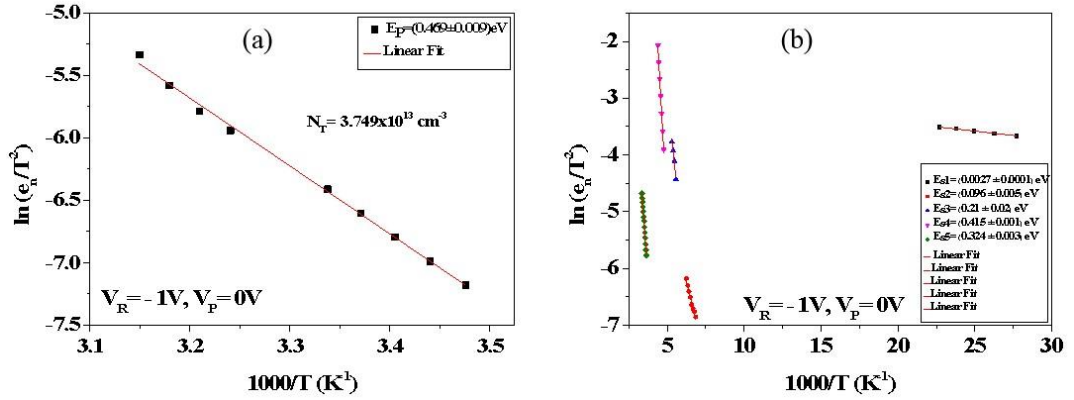


Fig. 6.17: Arrhenius plots from Laplace DLTS with reverse biases, $V_R = -1$ V, filling pulse height, $V_P = 0$ V, and filling pulse time, $t_P = 1$ msec, for (a) PLD sample and (b) sputtered sample

Table 6.2: Traps parameters for PLD and sputtered samples at $V_R = -1$ V, $V_P = 0$ V and $t_P = 1$ msec.

Sample	Trap	Activation Energy (eV)	Capture Cross-Section (σ_∞) (cm^2)	Trap Concentration (cm^{-3})
PLD	E_p	0.469 ± 0.009	4.00×10^{-16}	3.75×10^{13}
sputtered	E_{s1}	0.0027 ± 0.0001	1.96×10^{-22}	5.03×10^{12}
	E_{s2}	0.096 ± 0.005	6.63×10^{-21}	3.94×10^{13}
	E_{s3}	0.21 ± 0.02	4.01×10^{-17}	9.19×10^{13}
	E_{s4}	0.415 ± 0.001	5.92×10^{-13}	1.59×10^{14}
	E_{s5}	0.324 ± 0.003	8.98×10^{-18}	1.34×10^{14}

DLTS measurements using different reverse biases are usually performed to control the depletion region width (moving it away or close to the interface) where the process of trapping and de-trapping of carriers happen. DLTS measurements have been carried out for PLD sample at different reverse biases $V_R = -1, -3,$ and -4 V, as shown in Fig. 6.18. The filling pulse height, $V_P = 0$ V, and the filling pulse time, $t_P = 1$ msec, were kept the same for all measurements. As the reverse bias V_R is changed, only one trap has been detected for each reverse bias.

CHAPTER 6

Table 6.3 shows the trap parameters for $V_R = -1, -3$ and -4 V. Arrhenius plots for $V_R = -3$ and -4 V are displayed in Fig. 6.19. The trap found at $V_R = -3$ V has the same activation energy as that at $V_R = -4$ V whose origin could be related to the Ti donor [38]. Note that the amplitude of the DLTS signal is decreasing as the reverse bias increases (away from the interface). This means that the concentration of the trap is decreasing as moving away from the interface.

Table 6.3: Traps parameters for PLD sample at $V_R = (-1, -3$ and $-4)$ V, $V_P = 0$ V and $t_p = 1$ msec.

Reverse bias (V)	Trap	Activation Energy (eV)	Capture Cross-Section (σ_∞) (cm^2)	Trap Concentration (cm^{-3})
-1	E_p	0.469 ± 0.009	4.00×10^{-16}	3.75×10^{13}
-3	E_{p1}	0.335 ± 0.003	1.17×10^{-17}	2.85×10^{13}
-4	E_{p1}	0.318 ± 0.002	7.78×10^{-18}	2.10×10^{13}

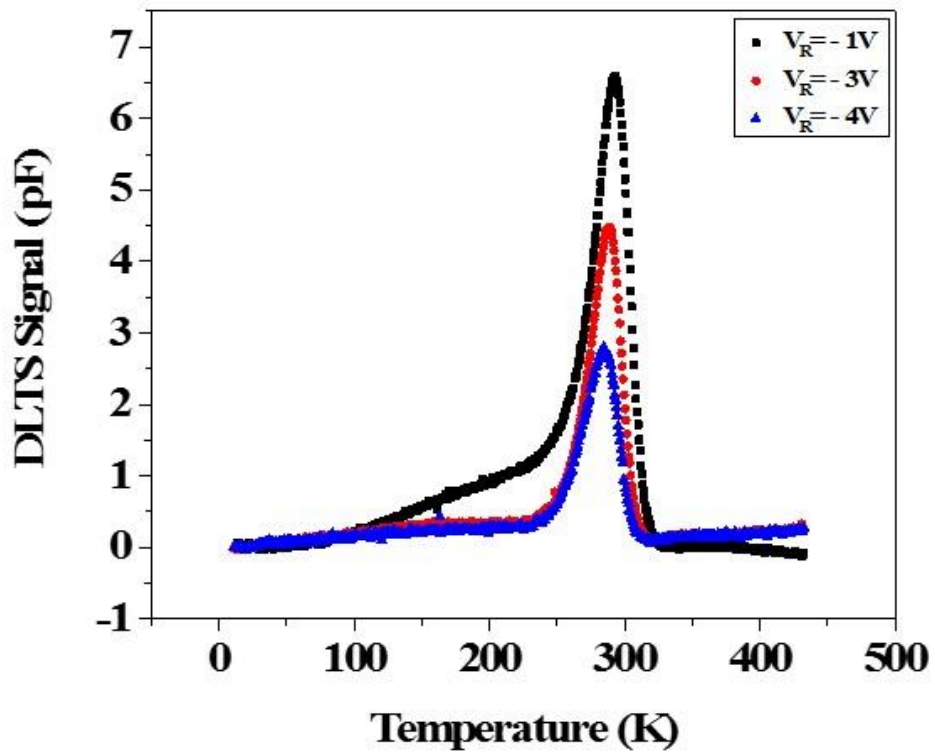


Fig. 6.18: DLTS signal for PLD sample at $V_R = -1, -3,$ and $-4V$

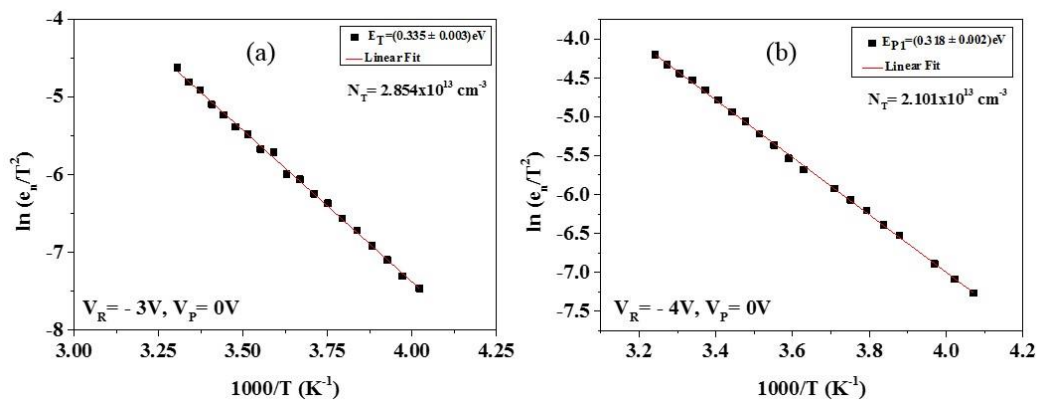


Fig. 6.19: Arrhenius plots for PLD sample obtained from Laplace DLTS at (a) $V_R = -3$ V and (b) $V_R = -4$ V.

6.3 CONCLUSION

The effect of the growth technique on the structural, electrically and optically active defects in In-doped TiO₂ has been investigated using two TiO₂ sample sets prepared by PLD and sputtering techniques. The samples grown by sputtering technique have shown more defects than those grown by PLD. This could be related to the coexistence of both anatase and rutile phases present in the thin film deposited by sputtering. As a consequence, the I-V characteristics show lower reverse current for PLD sample as compared with the sputtered sample. PLD sample has a smaller value of ideality factor and higher value of barrier height than the sputtered sample. One defect has been found in PLD samples whereas five defects have been detected in the sputtered samples. Due to the lower leakage currents and less number of defects in PLD samples, it is concluded that the PLD technique is better suited for the growth of In-doped TiO₂.

REFERENCES

1. Stadler, A., *Transparent conducting oxides—An up-to-date overview*. Materials, 2012. **5**(4): p. 661-683.
2. Hashimoto, K., H. Irie, and A. Fujishima, *TiO₂ photocatalysis: a historical overview and future prospects*. Japanese journal of applied physics, 2005. **44**(12R): p. 8269.
3. Sarkar, M.B., et al., *Enlarged broad band photodetection using Indium doped TiO₂ alloy thin film*. Journal of Alloys and Compounds, 2014. **615**: p. 440-445.
4. Chinnamuthu, P., et al., *Band gap enhancement of glancing angle deposited TiO₂ nanowire array*. Journal of Applied Physics, 2012. **112**(5): p. 054315.
5. Amtout, A. and R. Leonelli, *Optical properties of rutile near its fundamental band gap*. Physical Review B, 1995. **51**(11): p. 6842.
6. Tang, H., et al., *Urbach tail of anatase TiO₂*. Physical Review B, 1995. **52**(11): p. 7771.
7. Wang, E., W. Yang, and Y. Cao, *Unique surface chemical species on indium doped TiO₂ and their effect on the visible light photocatalytic activity*. The Journal of Physical Chemistry C, 2009. **113**(49): p. 20912-20917.
8. Al Saqri, N.A., et al., *Investigation of defects in indium doped TiO₂ thin films using electrical and optical techniques*. Journal of Alloys and Compounds, 2017. **698**: p. 883-891.
9. Nowotny, J., T. Bak, and M.A. Alim, *Dual mechanism of indium incorporation into TiO₂ (Rutile)*. The Journal of Physical Chemistry C, 2014. **119**(2): p. 1146-1154.

CHAPTER 6

10. Morgan, B.J. and G.W. Watson, *Polaronic trapping of electrons and holes by native defects in anatase TiO₂*. Physical Review B, 2009. **80**(23): p. 233102.
11. Huang, H.-H., et al., *Preparation of rutile and anatase phases titanium oxide film by RF sputtering*. Journal of nanoscience and nanotechnology, 2008. **8**(5): p. 2659-2664.
12. Mikami, M., et al., *Lattice dynamics and dielectric properties of TiO₂ anatase: a first-principles study*. Physical Review B, 2002. **66**(15): p. 155213.
13. Lukačević, I., et al., *Lattice dynamics and Raman spectrum of rutile TiO₂: The role of soft phonon modes in pressure induced phase transition*. Materials Chemistry and Physics, 2012. **137**(1): p. 282-289.
14. Sze, S.M. and M.K. Lee, *Semiconductor devices : physics and technology*. 2013, Singapore: Wiley.
15. Pillai, P., et al., *Extraction of Schottky barrier at the F-doped SnO₂/TiO₂ interface in Dye Sensitized solar cells*. Journal of Renewable and Sustainable Energy, 2014. **6**(1): p. 013142.
16. Werner, J.H., *Schottky barrier and pn-junction I/V plots—Small signal evaluation*. Applied Physics A: Materials Science & Processing, 1988. **47**(3): p. 291-300.
17. Van, C.N. and K. Potje-Kamloth, *Electrical and NO_x gas sensing properties of metallophthalocyanine-doped polypyrrole/silicon heterojunctions*. Thin Solid Films, 2001. **392**(1): p. 113-121.

CHAPTER 6

18. Jameel, D., et al., *Electrical performance of conducting polymer (SPAN) grown on GaAs with different substrate orientations*. Applied Surface Science, 2016. **387**: p. 228-236.
19. Aydoğan, Ş., M. Sağlam, and A. Türüt, *On the barrier inhomogeneities of polyaniline/p-Si/Al structure at low temperature*. Applied surface science, 2005. **250**(1): p. 43-49.
20. Aziz, M., et al., *Electrical Behavior of MBE Grown Interfacial Misfit GaSb/GaAs Heterostructures With and Without Te-Doped Interfaces*. IEEE Transactions on Electron Devices, 2015. **62**(12): p. 3980-3986.
21. Tripathi, S. and M. Sharma, *Analysis of the forward and reverse bias IV and CV characteristics on Al/PVA: n-PbSe polymer nanocomposites Schottky diode*. Journal of Applied Physics, 2012. **111**(7): p. 074513.
22. Korucu, D., A. Turut, and H. Efeoglu, *Temperature dependent I–V characteristics of an Au/n-GaAs Schottky diode analyzed using Tung's model*. Physica B: Condensed Matter, 2013. **414**: p. 35-41.
23. Al Saqri, N., et al., *Investigation of the effects of gamma radiation on the electrical properties of dilute GaAs 1– x N x layers grown by Molecular Beam Epitaxy*. Current Applied Physics, 2015. **15**(10): p. 1230-1237.
24. Miyagi, T., et al., *Photocatalytic property and deep levels of Nb-doped anatase TiO₂ film grown by metalorganic chemical vapor deposition*. Japanese journal of applied physics, 2004. **43**(2R): p. 775.
25. Pallotti, D.K., et al., *Photoluminescence Mechanisms in Anatase and Rutile TiO₂*. The Journal of Physical Chemistry C, 2017. **121**(16): p. 9011-9021.
26. Skowronski, L., R. Szczesny, and K. Zdunek, *Optical and microstructural characterization of amorphous-like Al₂O₃, SnO₂ and TiO₂ thin layers*

- deposited using a pulse gas injection magnetron sputtering technique. Thin Solid Films, 2017. 632: p. 112-118.*
27. Iijima, K., et al., *Influence of oxygen vacancies on optical properties of anatase TiO₂ thin films.* Journal of Luminescence, 2008. **128**(5): p. 911-913.
 28. Yang, Y., et al., *Visible and near-infrared electroluminescence from TiO₂/p⁺-Si heterostructured device.* AIP Advances, 2014. **4**(4): p. 047109.
 29. Kim, H.S., et al., *High performance solution-processed indium oxide thin-film transistors.* Journal of the American Chemical Society, 2008. **130**(38): p. 12580-12581.
 30. Chan, C.-H., et al., *Optical characterization of structural quality in the formation of In₂O₃ thin-film nanostructures.* The Journal of Physical Chemistry C, 2016. **120**(38): p. 21983-21989.
 31. Meléndez, J.J. and M. Wierzbowska, *In₂O₃ doped with hydrogen: electronic structure and optical properties from the pseudopotential Self-Interaction Corrected Density Functional Theory and the Random Phase Approximation.* The Journal of Physical Chemistry C, 2016. **120**(7): p. 4007-4015.
 32. Ghosh, A., et al., *Detailed investigation of defect states in Erbium doped In₂O₃ thin films.* Materials Research Bulletin, 2018. **99**: p. 211-218.
 33. Johannsen, S.R., et al., *Influence of TiO₂ host crystallinity on Er³⁺ light emission.* Optical Materials Express, 2016. **6**(5): p. 1664-1678.
 34. Krustok, J., H. Collan, and K. Hjelt, *Does the low-temperature Arrhenius plot of the photoluminescence intensity in CdTe point towards an erroneous activation energy?* Journal of applied physics, 1997. **81**(3): p. 1442-1445.

CHAPTER 6

35. Wang, X., et al., *Trap states and carrier dynamics of TiO₂ studied by photoluminescence spectroscopy under weak excitation condition*. Physical Chemistry Chemical Physics, 2010. **12**(26): p. 7083-7090.
36. Lang, D., *Deep-level transient spectroscopy: A new method to characterize traps in semiconductors*. Journal of applied physics, 1974. **45**(7): p. 3023-3032.
37. Dobaczewski, L., A. Peaker, and K. Bonde Nielsen, *Laplace-transform deep-level spectroscopy: The technique and its applications to the study of point defects in semiconductors*. Journal of Applied Physics, 2004. **96**(9): p. 4689-4728.
38. Salama, A. and L. Cheng, *The Effects of Titanium Impurities in N+/P Silicon Solar Cells*. Journal of The Electrochemical Society, 1980. **127**(5): p. 1164-1167.

INVESTIGATION OF THE STRUCTURAL, OPTICAL AND ELECTRICAL PROPERTIES OF INDIUM-DOPED TiO₂ THIN FILMS GROWN BY PULSED LASER DEPOSITION TECHNIQUE ON LOW AND HIGH INDEX GaAs PLANES

In this chapter, the electrical properties of In-doped TiO₂ thin films grown by pulsed laser deposition (PLD) on low and high index GaAs substrates, namely (100) and (311)B, are investigated. I-V, C-V, DLTS and Laplace DLTS techniques were used to study the effect of the substrates on the properties of In-doped TiO₂ thin films.

7.1 INTRODUCTION

TiO₂ is a transparent conducting oxide (TCO) material which has been widely studied due to its remarkable properties, such as efficient photoactivity, high stability, low cost and non-toxicity [1-3]. It has been used in many applications such as photocatalysis [4], water and air purification [5], photo-electrochemical (PEC) water splitting [6], UV sensors [7-9] and as a solar cell [10, 11]. TiO₂ is a wide bandgap oxide semiconductor material which exists in nature in three polymorphs, namely: anatase, rutile and brookite [12, 13]. Its wide bandgap (3.0-3.4 eV) [14, 15] makes it sensitive to UV light and not to visible light which degraded its use as a solar cell. To overcome this limitation, surface modification, combination with other semiconductors, in addition to metal and non-metal ion doping have been used to make the TiO₂ sensitive to the visible light [16]. Different metal ions such as Ag [17], Sb [18], Fe³⁺, Mo⁵⁺, Ru³⁺, Os³⁺, Re⁵⁺, V⁴⁺, Rh³⁺ [19] and In [20, 21]

have been used as dopant in TiO₂ with the aim to increase the absorption of the visible light by modifying its electronic and optoelectronic properties. In the studies of indium doping of TiO₂ [20, 21], different growth techniques have been used to synthesise TiO₂ thin films on Si substrates.

GaAs is a direct bandgap semiconductor and one of the most studied III-V compound semiconductors [22]. The direct bandgap of GaAs makes it suitable for optoelectronics as compared to Si. Moreover, due to higher carrier mobility of GaAs as compared to Si, GaAs draws much attention for making high frequency devices [23, 24]. Furthermore, as GaAs has higher bandgap energy compared to Si that makes GaAs more suitable for devices that operate at high temperatures. Additionally, the electrical, structural and optical properties of devices grown on high index planes of GaAs, i.e. (n11) where n is an integer, are improved when compared to the same devices grown on the conventional (100) plane [25]. For example, the morphological and optical properties of (InGa)As QDs have been improved when grown on (311)B GaAs substrates as compared to the same devices grown on a (100) GaAs substrates [26]. Additionally, the structural characteristics of InAs quantum dots (QDs) grown on (311)B orientation are better than those grown on low index plane (100) [27]. All the above provide a great motivation to investigate the electrical and optical properties of In-doped TiO₂ grown on GaAs substrates, low and high index, rather than Si. Recently, TiO₂ has been employed as a gate oxide in GaAs metal-oxide-semiconductor field-effect transistor (MOSFET) due to its high dielectric constant [23, 28, 29]. In addition, TiO₂ was grown on GaAs substrates to study its photocatalytic applications [30]. The structure of TiO₂ grown by PLD on semi-insulating (100) GaAs substrates was also investigated [31]. To the best our knowledge, there is no single study of the

CHAPTER 7

electrically active defects in In-doped TiO₂ thin films grown by PLD technique on GaAs substrates.

Oxygen vacancies are well-known defects in TiO₂ which can alter the geometric structure and the chemical properties of the system [32]. Furthermore, incorporating indium into the TiO₂ host lattice could create defects within the forbidden bandgap of TiO₂. Understanding the deep and shallow level defects is essential for future devices [33]. By using DLTS, defects parameters, such as energy, capture cross section and its concentration can be calculated. Additionally, XRD, I-V, C-V and photoluminescence (PL) measurements have been performed.

In this study, In-doped TiO₂ thin films have been grown on (100) and (311)B n-type GaAs substrates. The aim was to investigate the effect of the orientation of the GaAs substrates, i.e. (100) and (311)B, on the structural, optical and electrical (especially the electrically active defects) properties in In-doped TiO₂ thin films.

7.2 RESULTS AND DISCUSSION

7.2.1 SAMPLE DETAILS

Two series of samples were prepared by pulsed laser deposition (PLD) technique using low and high index planes, (100) and (311)B, of GaAs as substrates. For the first series, a layer of 380 nm TiO₂ thin film was deposited on (100) n-type GaAs substrate. Then, it cut into two halves and via thermal evaporation, a layer of indium (15 nm thick) was deposited on top of one half while the other half was deposited with a 5 nm thick layer of indium. In order to incorporate indium into the TiO₂ lattice, samples were annealed under oxygen flow with a temperature ramp rate of 15 °C/minute and a dwelling temperature of 500 °C for 30 minutes. Therefore, this

series consists of two samples which were labelled as 15 (100) and 5 (100) for In (15 nm) doped TiO₂/GaAs (100) n-type and In (5 nm) doped TiO₂/GaAs (100) n-type, respectively. The second series is similar to the first series except that the GaAs substrate orientation is (311)B. Also for this series, the two samples were labelled as 15 (311)B and 5 (311)B. A third series of control samples, which do not contain indium, were grown by the same technique using the same procedures as described above. This will allow us to investigate the effect of In doping on the electrically active defects of TiO₂. These control samples are referred to as (100) and (311)B samples for TiO₂/(100) GaAs and TiO₂/(311)B GaAs, respectively. The full samples fabrication details were presented in chapter 5, section 5.1.2.

7.2.2 STRUCTURAL MEASUREMENTS

The x-ray diffraction spectra of all doped samples are shown in Fig. 7.1. As illustrated in Fig. 7.1 (a) and (b), both anatase and rutile phases of TiO₂ are present in sample 5 (100) and 5 (311)B although the rutile phase is dominant. However, for sample 15 (100) and 15 (311)B, only a single-phase rutile was obtained as revealed in Fig. 7.1 (c) and (d). Moreover, the crystallographic properties of the samples in series (311)B, i.e. 5 (311)B and 15 (311)B, are clearly better than the samples in series (100). The peaks shown in Fig. 7.1 are in good agreement with the standard spectrum (JCPDS no.: 84-1286 and ICDD File No: 96-900-4142 for anatase and rutile phases, respectively). Finally, XRD results show that the thickness of the indium film has a remarkable influence on the structural properties of the TiO₂ thin films, as both anatase and rutile phases can be observed for the low doped samples whereas only one phase, i.e. rutile, could be detected for both highly doped samples.

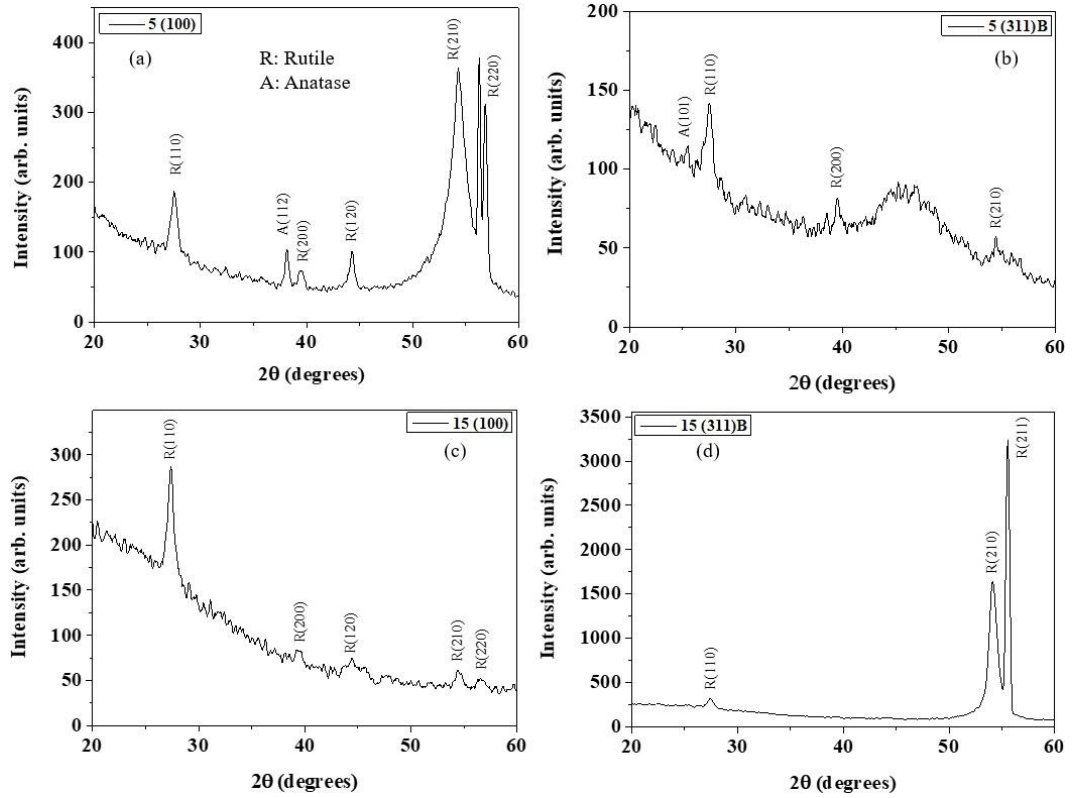


Fig. 7.1: The x-ray diffraction pattern of sample (a) 5 (100), (b) 5 (311)B, (c) 15 (100) and (d) 15 (311)B.

Fig. 7.2 shows the absorption spectra measured at room temperature for all doped samples. As Fig. 7.2 depicts, an absorption band centred at 3.65 eV is observed for sample 5 (311)B and at 3.30 eV for sample 15 (311)B. This redshift in the absorption is an indication that the increase in the thickness of the indium film contributes to the increase of doping concentration of the TiO_2 films. However, for samples in (100) series, a small absorption band that is centred at approximately 3.65 eV is observed for sample 5 (100) and no relevant change was observed in the absorption spectra with increasing indium, i.e. sample 15 (100). From the results of Fig. 7.2, the absorption coefficient (α) above the threshold of fundamental absorption has been calculated using the $(E-E_g)^2$ energy dependence characteristic for indirect allowed transitions (equation 4.34 in Chapter 4) to obtain $(\alpha h\nu)^{1/2}$ versus

photon energy (E) plot (h is Planck's constant and ν is the frequency). Fig. 7.3 shows the $(\alpha h\nu)^{1/2}$ versus photon energy (E) plot and the values of optical absorption gaps obtained by extrapolation are 3.39, 3.34, 3.40 and 2.94 eV for sample 5 (100), 5 (311)B, 15 (100) and 15 nm (311)B, respectively. It is clear that due to the increase of indium content in series (311)B samples, the bandgap has been reduced from 3.34 eV for sample 5 (311)B to 2.94 eV for sample 15 (311)B. However, no significant change has been noticed in series (100). Therefore, the doping process of indium into the TiO_2 host lattice has a remarkable influence on the bandgap in the samples grown on the (311)B GaAs substrate.

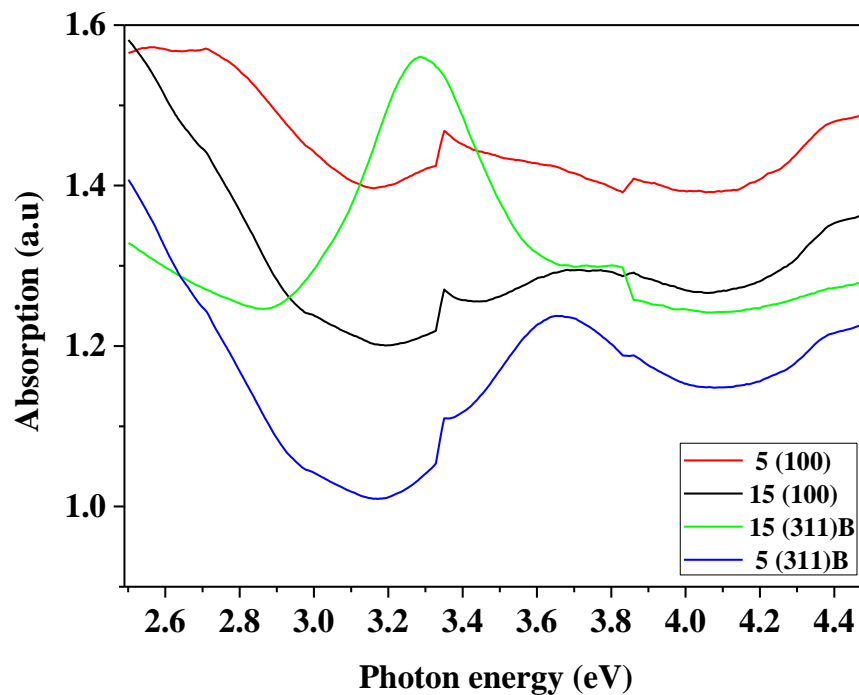


Fig. 7.2: Optical absorption spectra at room temperature for all doped samples.

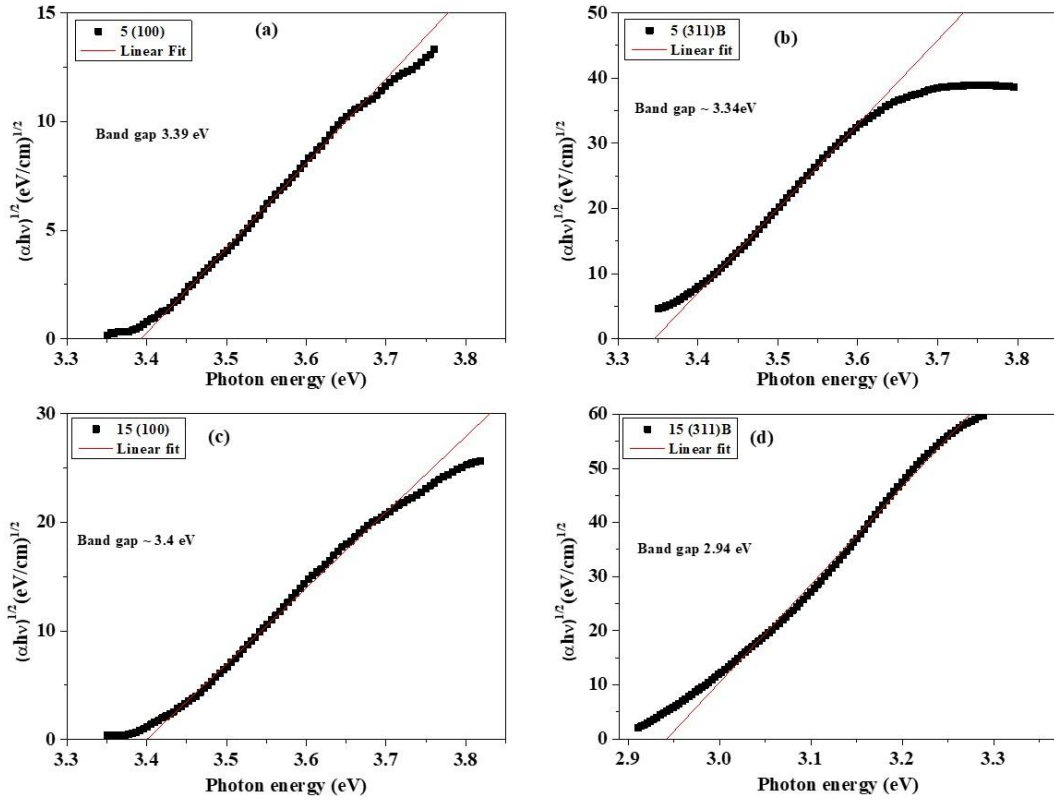


Fig. 7.3: $(\alpha h\nu)^{1/2}$ versus photon energy (E) plots for samples (a) 5 (100), (b) 5 (311)B, (c) 15 (100) and (d) 15(311)B samples.

7.2.3 CURRENT-VOLTAGE MEASUREMENTS

The semi-logarithmic plot of current density (J) versus applied bias (J-V) measurements at room temperature for all samples are shown in Fig. 7.4. As can be seen in this figure for the doped samples, samples grown on GaAs (100) have higher reverse current density as compared to GaAs (311)B samples. In particular, sample 15 (311)B has the lowest reverse current and sample 15 (100) has the highest reverse current. However, for the control samples (undoped), sample (100) has the lowest reverse current and samples (311)B has the highest reverse current when compared to all other samples. Current density-voltage (J-V) measurements as function of temperature have been carried out for all samples in the range of 20-300 K (with 20 K intervals) to extract the diode parameters.

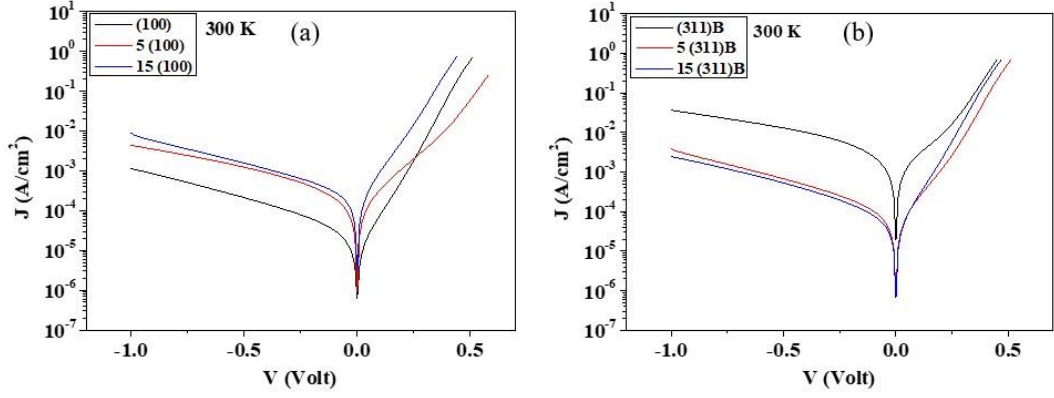


Fig. 7.4: Semi-logarithmic J-V plots for (a) series (100) samples and (b) series (311)B samples.

The thermionic emission model describes the I-V characteristics, including series resistance (R_s), of an ideal diode as follows[34]:

$$I = I_0 \left[\exp \left(\frac{q(V - IR_s)}{nKT} \right) - 1 \right] \quad (7.1)$$

where I_0 is the saturation current and is given by:

$$I_0 = AA^*T^2 \exp \left(\frac{-q\phi_b}{KT} \right) \quad (7.2)$$

In Equations (7.1) and (7.2), q is the elementary charge, n is the ideality factor, k is Boltzmann's constant, T is the temperature, ϕ_b is the barrier height, R_s is the series resistance, A is the effective diode area ($A = 3.85 \times 10^{-3} \text{ cm}^2$ for sample 5 (100) and $A = 1.26 \times 10^{-3} \text{ cm}^2$ for the other samples) and A^* is the effective Richardson's constant ($A^* = 671 \text{ A.cm}^{-2}.\text{K}^{-2}$ for TiO_2 [35]). Werner's method, which was explained in details in Chapter 4, section 4.3, was used to calculate the diode parameters (n , ϕ_b and R_s) [36]. Fig. 7.5 and Fig. 7.6 show the plot of G/I versus G and the plot of $\ln(I)$ versus $(V - IR_s)$, respectively, that are used to extract the diode parameters for all samples. These parameters for all samples at room temperature are summarised in Table 7.1. As Table 7.1 shows, for samples grown on GaAs (100) substrates, the (100) control sample has the lowest ideality factor (1.56) and

CHAPTER 7

highest barrier height (0.79 eV) values as compared to all samples [(100) and (311)B] investigated here. Sample 15 (100) has a lower ideality factor and barrier height as compared to sample 5 (100) whereas the series resistance is lower for sample 5 (100). Therefore, doping indium has adversely affected the electrical properties of TiO₂ thin films grown on (100) GaAs substrates. However, for samples grown on GaAs (311)B substrates, as the concentration of indium decreases, the barrier height increases and the ideality factor decreases. In particular, for sample 5 (311)B, the barrier height and ideality factor are 0.77 eV and 1.64, respectively. However, for sample 15 (311)B, the barrier height and ideality factor are 0.74 eV and 1.74, respectively. It is worth mentioning that the (311)B control sample has the lowest barrier height (0.70 eV) and the highest ideality factor (1.87) when compared to the doped samples in series (311)B. Thus, the electrical properties of TiO₂ thin films grown on (311)B GaAs substrates have been enhanced by indium doping. Among all doped samples, sample 5 (311)B has the highest barrier height and the lowest ideality factor which may indicate the best electrical properties of sample 5 (311)B as compared to all other doped samples.

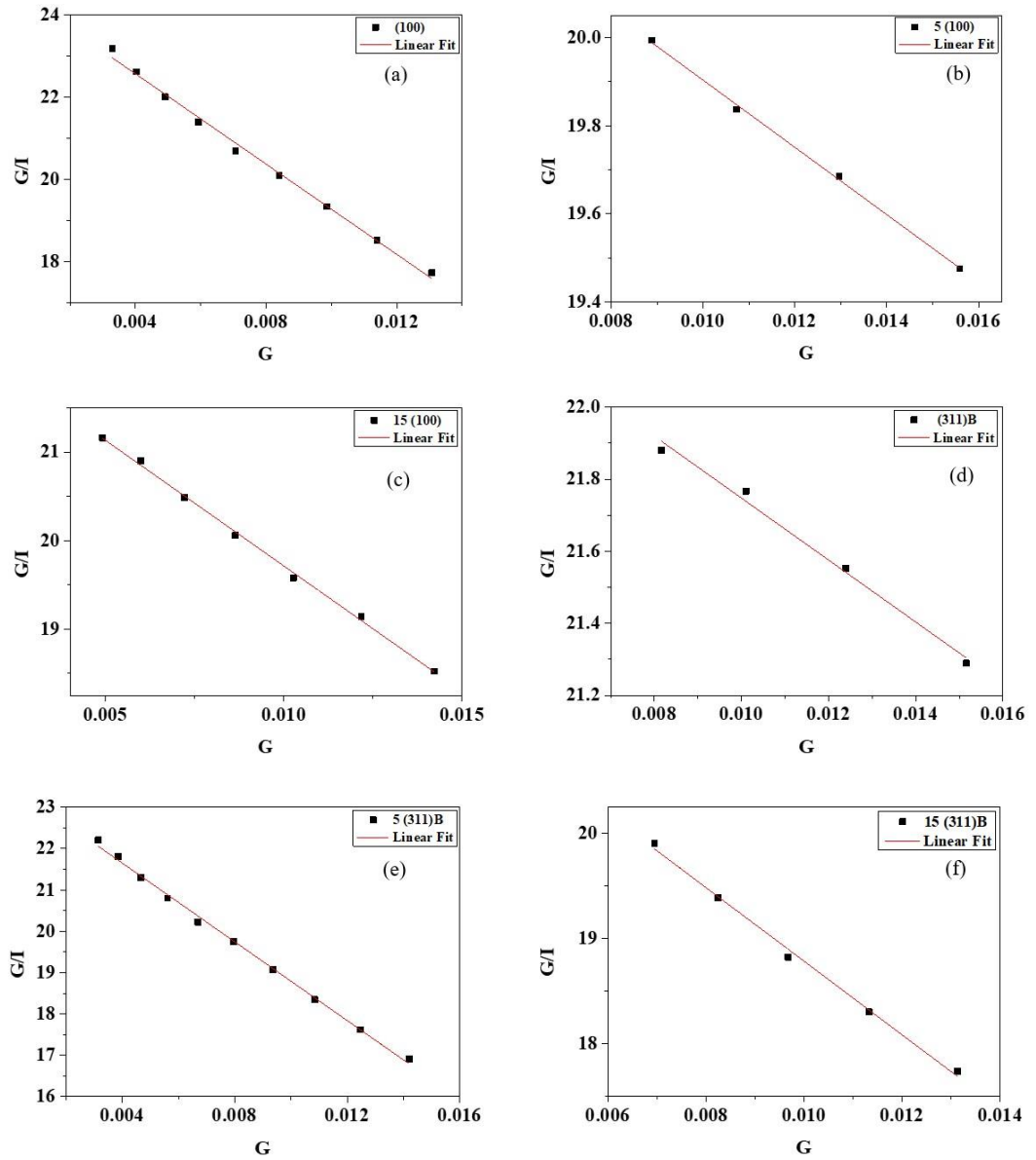


Fig. 7.5: G/I versus G plot for (a) control (100), (b) 5 (100), (c) 15 (100), (d) control (311)B, (e) 5 (311)B and (f) 15 (311)B samples.

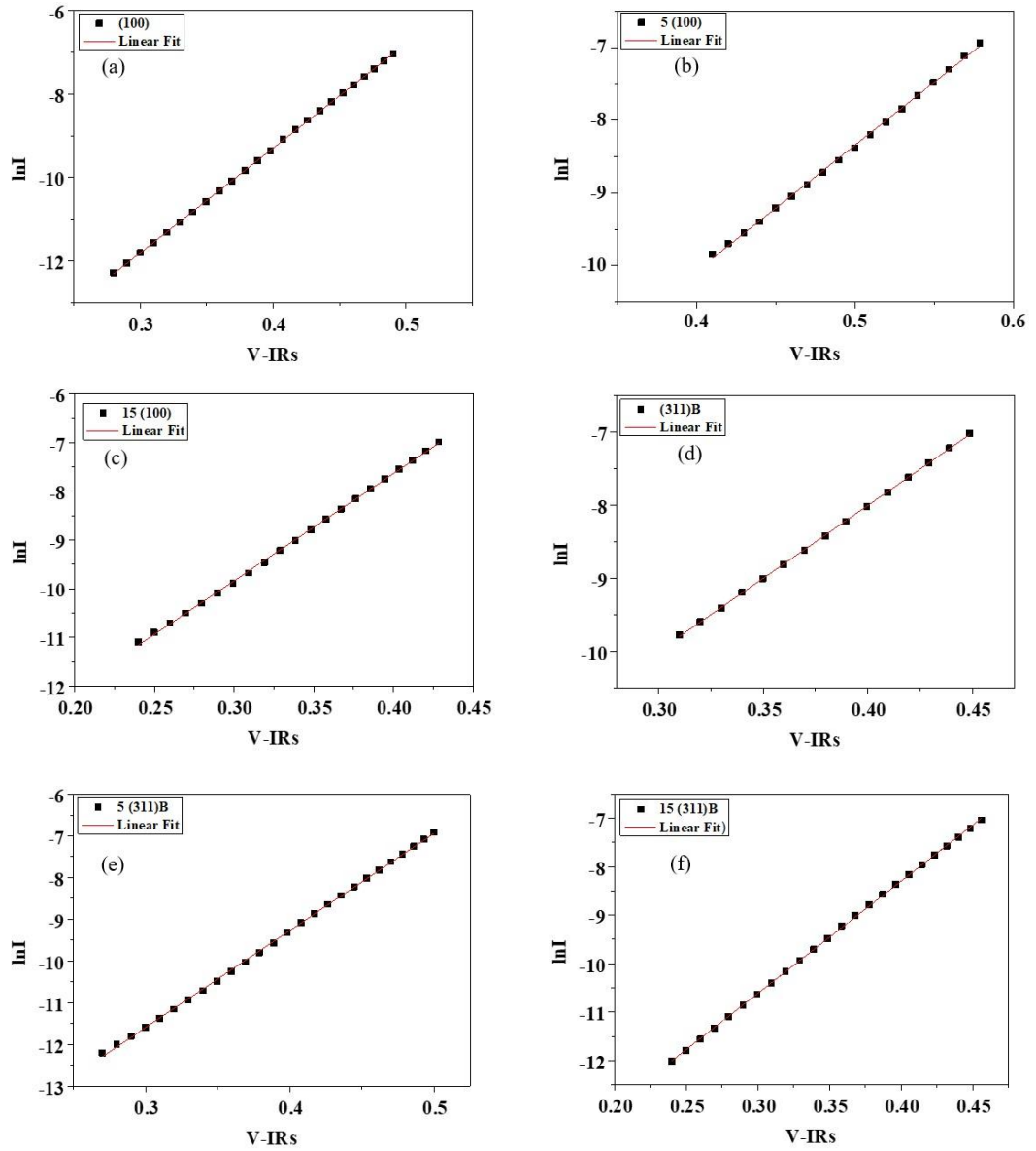


Fig. 7.6: The plot of $\ln(I)$ versus $(V \cdot IR_s)$ for (a) control (100), (b) 5 (100), (c) 15 (100), (d) control (311)B, (e) 5 (311)B and (f) 15 (311)B samples.

CHAPTER 7

Table 7.1: Ideality factor (n), barrier height (ϕ_b) and series resistance (R_s) at room temperature for samples 15 (100), 5 (100), 15 (311) and 5 (311)B.

Sample	n	ϕ_b (eV)	R_s (Ω)
(100)	1.561 ± 0.007	0.7902 ± 0.0006	22.2 ± 0.6
5 (100)	2.067 ± 0.002	0.757 ± 0.003	1.46 ± 0.04
15 (100)	1.715 ± 0.004	0.716 ± 0.002	12.6 ± 0.2
(311)B	1.872 ± 0.005	0.704 ± 0.001	1.43 ± 0.09
5 (311)B	1.642 ± 0.005	0.771 ± 0.001	20.2 ± 0.4
15 (311)B	1.74 ± 0.01	0.745 ± 0.001	15.7 ± 0.6

The plot of $\ln(I_0/T^2)$ versus $1000/T$ follows a straight line for samples (100), 15 (100), 5 (100), (311)B, 15 (311)B and 5 (311)B in a temperature range of 220-300 K, 180-300 K, 220-300 K, 180-300 K, 240-300 K and 200-300 K, respectively, as shown in Fig. 7.7. The straight line behavior indicates that the conduction mechanism could be governed by thermionic emission and the saturation current (I_0) can be obtained by Equation (7.2) [37]. However, at low temperature a deviation from linearity is noticed for each sample and that could be due to a contribution of additional current as a result of the reduction in the barrier height [25]. The experimental Richardson's constant, calculated from the y-intercept of the straight line, was found to be 6.4×10^{-7} , 2.5×10^{-4} , 3.0×10^{-4} , 3.6×10^{-6} , 7.4×10^{-4} and $1.8 \times 10^{-7} \text{ A cm}^{-2} \text{ K}^{-2}$ for samples (100), 15 (100), 5 (100), (311)B, 15 (311)B and 5 (311)B, respectively. The Richardson's constants that are obtained from all samples are much lower than the well-established value $A^* = 671 \text{ A cm}^{-2} \text{ K}^{-2}$ for TiO_2 . This deviation could be due to the spatial inhomogeneous barrier heights and

CHAPTER 7

potential fluctuations at the interface [38]. This behaviour has also been observed in a previous study of In-doped TiO₂ grown by PLD on Si substrates [21].

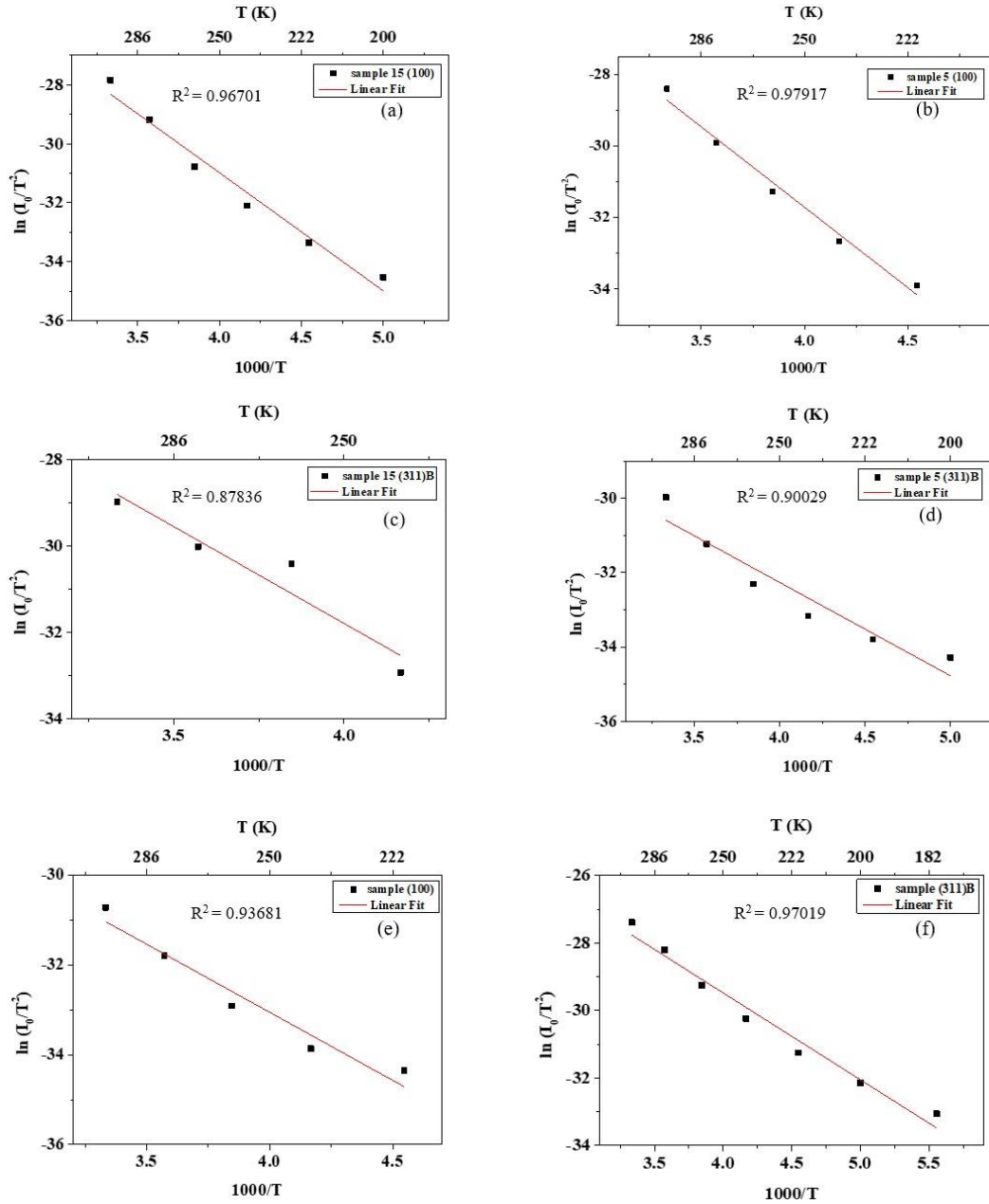


Fig. 7.7: The plot of $\ln(I_0/T_2)$ versus $1000/T$ for sample (a) 15 (100), (b) 5 (100), (c) 15 (311)B, (d) 5 (311)B, (e) control (100) and (f) control (311)B.

CHAPTER 7

The temperature dependence of barrier height and ideality factor for all samples are illustrated in Fig. 7.8. The variation of barrier height and ideality factor with temperature is usually observed in many metal-semiconductors interfaces [39]. Fig. 7.8 (a) shows that the barrier height increases with increasing temperature while, in Fig. 7.8 (b), the ideality factor decreases as temperature increases for all samples. This behaviour is well-known and is due to nonuniformity of interfacial charges and barrier inhomogeneity [21, 40, 41]. Similar behaviour of ideality factor and barrier height with temperatures has also been observed and discussed in chapter 6, section 6.2.3.

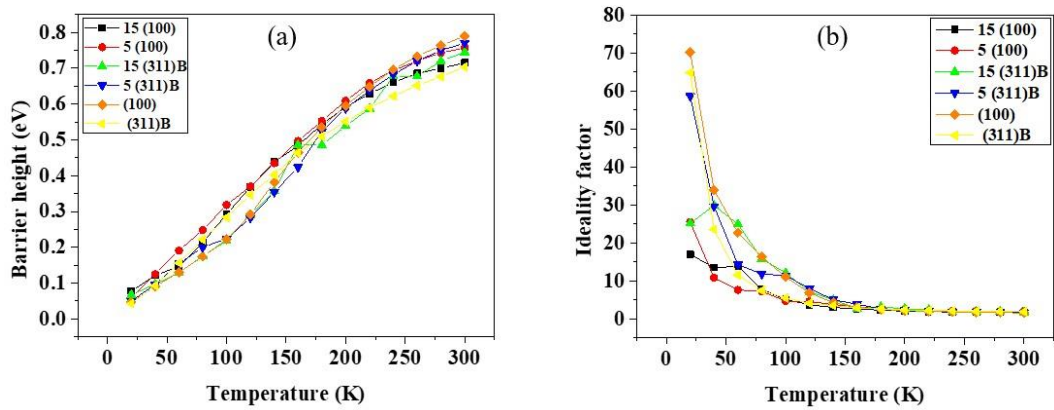


Fig. 7.8: (a) barrier height versus temperature and (b) ideality factor versus temperature for all samples.

The plots of the reverse current versus inverse temperature could be used to calculate the main traps which contributes to the leakage current [42]. The plots of reverse current versus $1000/T$ at -1 V voltage bias for all doped samples are illustrated in Fig. 7.9. Only one trap was detected for each sample and its activation energy was found to be 0.11 ± 0.01 , 0.09 ± 0.01 , 0.14 ± 0.01 and 0.15 ± 0.01 eV for 15 (100), 5 (100), 15 (311)B and 5 (311)B samples, respectively. As seen above,

CHAPTER 7

a similar trap is observed in each series of (100) and (311)B but the activation energy is higher in series (311)B. T. Miyagi, *et al.* in their study of photocatalytic property and deep levels of Nb-doped anatase TiO₂ film grown by metal organic chemical vapor deposition have assigned a defect with energy of 0.13 eV in undoped TiO₂ to oxygen vacancies or interstitial Ti ion [43]. Therefore, the origin of the defect that has been detected in 15 (311)B and 5 (311)B samples could also originate from oxygen vacancies or interstitial Ti ion.

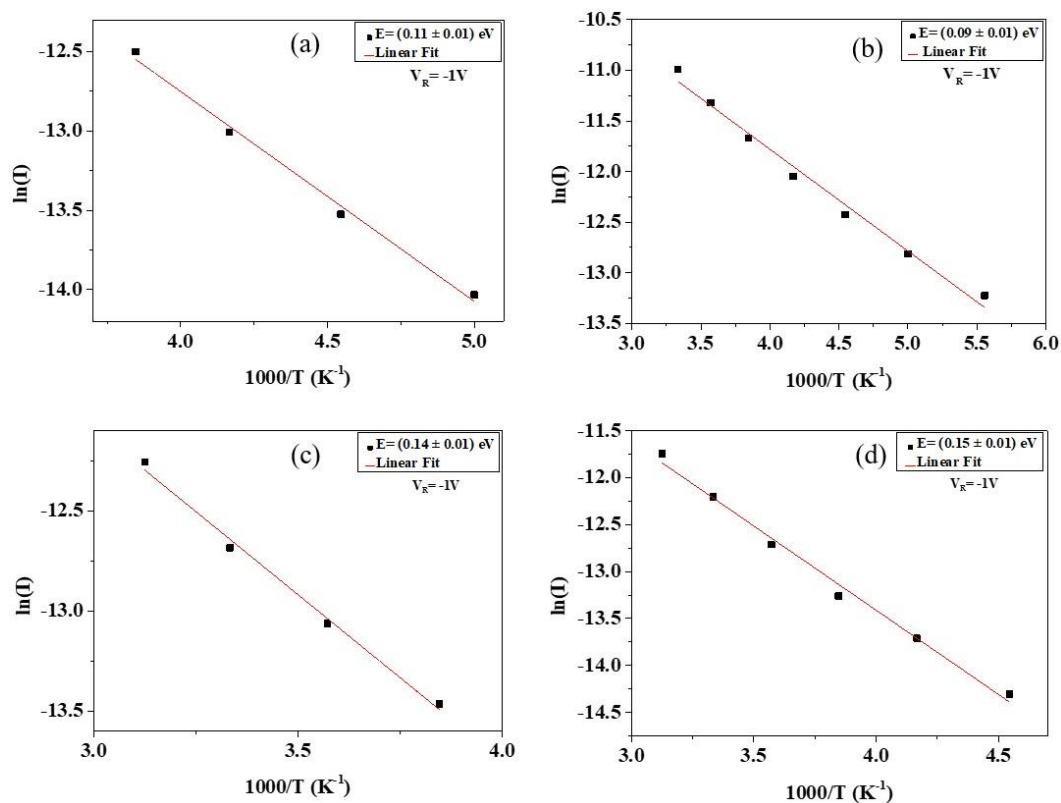


Fig. 7.9: Reverse current versus $1000/T$, for $V_R = -1 \text{ V}$, for samples (a) 15 (100), (b) 5 (100), (c) 15 (311)B and (d) 5 (311)B.

7.2.4 CAPACITANCE-VOLTAGE MEASUREMENTS

The capacitance-voltage (C-V) measurements at room temperature, Fig. 7.10, have been carried out for all doped samples in order to calculate the free carrier concentrations. As Fig. 7.10 shows, sample 5 (100) has the highest capacitance while sample 15 (311)B has the lowest capacitance. The free carrier concentrations, N_d , for all doped samples were calculated using the slope of the best fit of the plot $1/C^2$ versus reverse bias, as shown in Fig. 7.11. The doping concentration is found to be uniform for all doped samples as proven by the linear behaviour of the plot of $1/C^2$ versus applied bias and the free carrier concentration is about $3.44 \times 10^{17} \text{ cm}^{-3}$, $3.63 \times 10^{17} \text{ cm}^{-3}$, $4.98 \times 10^{17} \text{ cm}^{-3}$ and $6.41 \times 10^{17} \text{ cm}^{-3}$ for samples 15 (100), 5 (100), 15 (311)B and 5 (311)B, respectively. Moreover, Fig. 7.12 shows the C-V and the plot of $1/C^2$ versus reverse bias for the control samples, i.e. sample (100) and (311)B. As found for the doped samples, the doping concentration in the control samples is also uniform and the free carrier concentration is found to be $1.14 \times 10^{18} \text{ cm}^{-3}$ and $2.96 \times 10^{17} \text{ cm}^{-3}$ for sample (100) and (311)B, respectively.

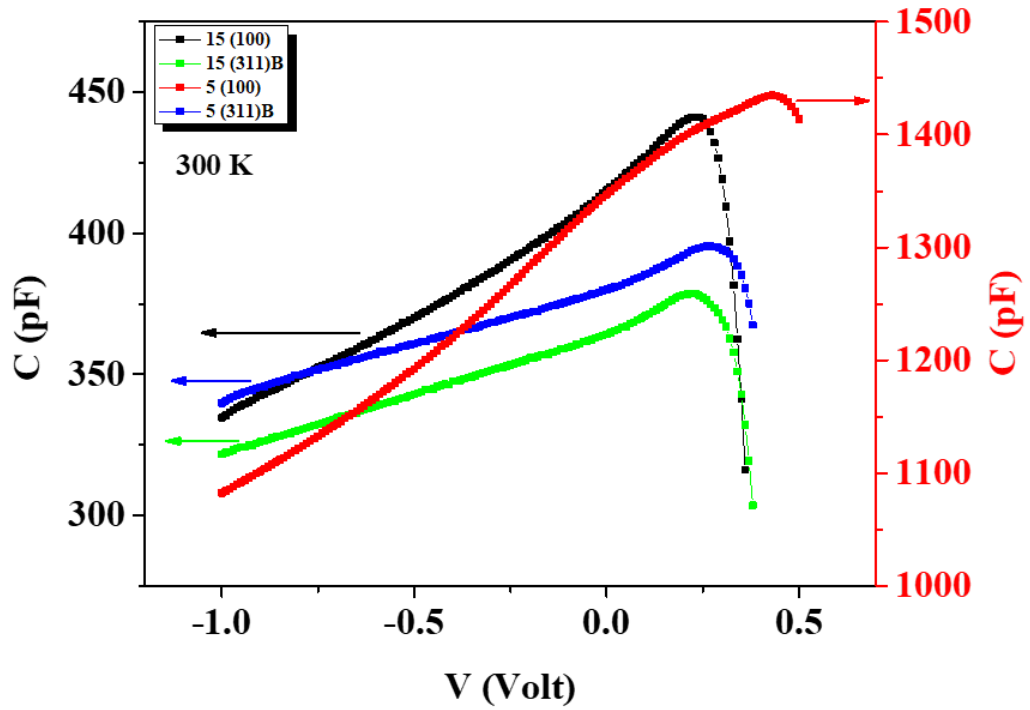


Fig. 7.10: C-V plot at room temperature for all doped samples.

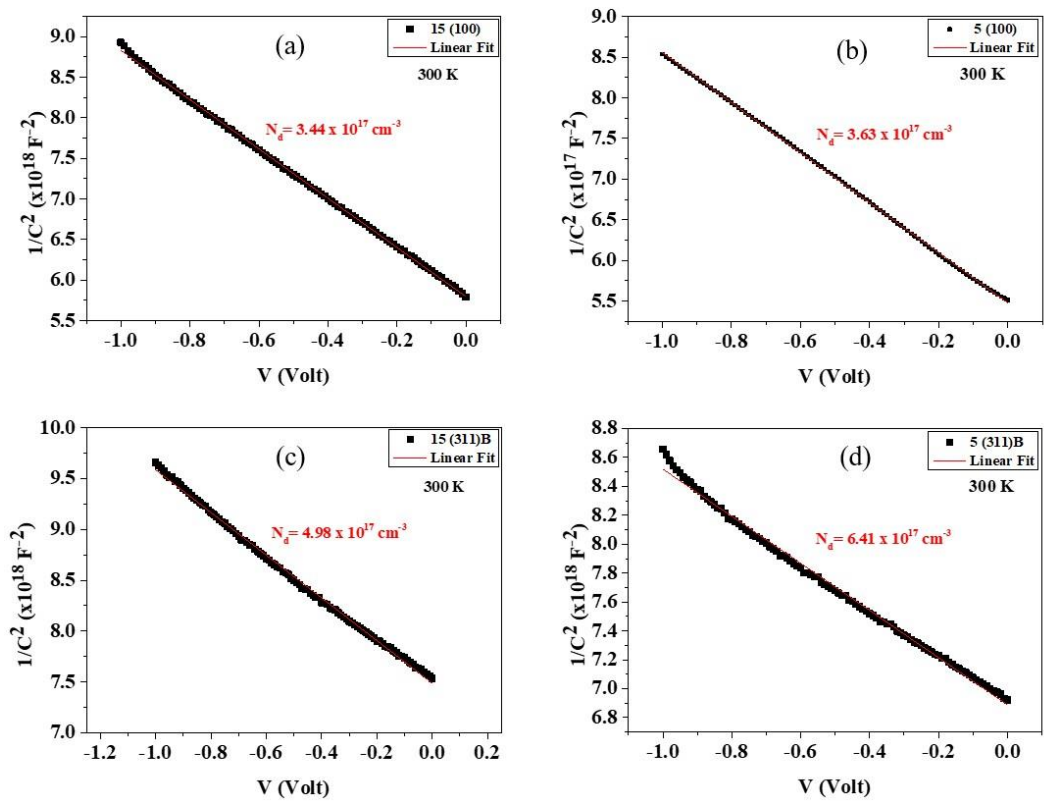


Fig. 7.11: $1/C^2$ versus applied bias plots at room temperature for (a) 15 (100), (b) 5 (100), (c) 15 (311)B and (d) 5 (311)B samples.

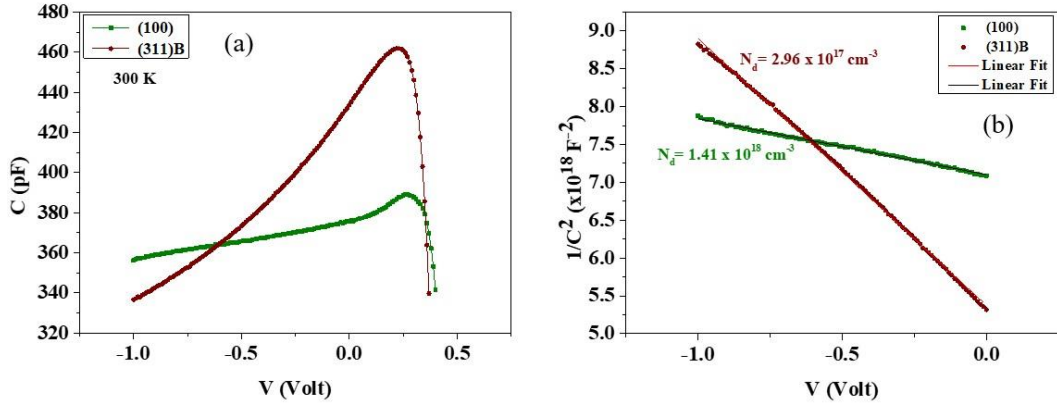


Fig. 7.12: (a) C-V and (b) $1/C^2$ versus applied bias plots at room temperature for control samples.

7.2.5 PL MEASUREMENTS

Fig. 7.13 (a) and (b) show typical PL spectra at different temperatures for sample 5 (100) and 5 (311)B, respectively. For both samples, the PL spectra clearly shows a visible broad band around 2.2 eV. This emission is usually associated with the presence of anatase phase of TiO_2 thin films [21, 44, 45]. Moreover, it is also observed that both samples, i.e. 5 (100) and 5(311)B, also exhibit a broad near infra-red (NIR) band at 300 K around 1.5 eV, which could be associated with an emission due to the rutile phase [44, 45]. Actually, several previous works have reported that the anatase phase of TiO_2 usually exhibits PL bands around 1.9 eV (red emission) and 2.4 eV (green emission) while the rutile phase usually exhibits PL bands around 1.5 and 1.7 eV [44]. The green emission associated with the anatase phase is usually attributed to self-trapped excitons [46], oxygen vacancies [47] or to a radiative recombination of free electrons with trapped holes. These trapped holes could be localized at oxygen vacancies sites (V_O) or at Ti sites adjacent to V_O [44]. On the other hand, the red PL emission observed for the anatase phase is usually assigned to the optical recombination between trapped electrons and free holes [44]. Particularly, it was also previously shown that the rutile phase samples are less

CHAPTER 7

sensitive to prolonged exposure to UV illumination in oxygen environment than anatase samples. This fact could support the possible interpretation that the NIR PL could be associated with a possible radiative recombination between midgap trapped electrons and free holes at the valence band [44]. However, the nature of NIR emission associated with the rutile phase and the visible emission associated with the anatase phase in TiO_2 are not well understood. In general, our PL results for both 5 (100) and 5 (311)B samples, which are fully consistent with the presence of mixed anatase and rutile phases, are in good agreement with XRD results.

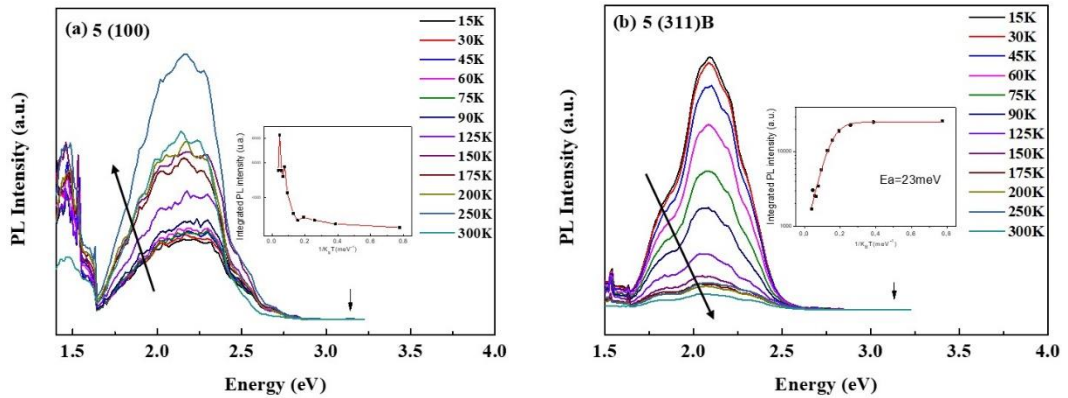


Fig. 7.13: Temperature dependence of PL spectra for sample (a) 5 (100) and (b) 5 (311)B. The arrows show the increasing of temperature. The inset shows the Arrhenius plots.

The PL spectra of sample 15 (100) and 15 (311)B are shown in Fig. 7.14. For both samples, emissions in visible and infrared regions have also been observed. This observation is fully consistent with the presence of anatase and rutile phases, as observed in the low doped samples, which indicates a mixed phase for these samples. However, only rutile phase was detected using XRD technique in both 15 (100) and 15 (311)B. A possible explanation is that the PL technique is more sensitive for probing structural phases of thin films than XRD technique.

CHAPTER 7

Therefore, although not be detected by XRD, the anatase phase is present in both samples. Another possible explanation is that the visible emission in both samples is not due to the presence of anatase phase but could be related to a possible formation of In_2O_3 phase or doping effects [20, 21, 48].

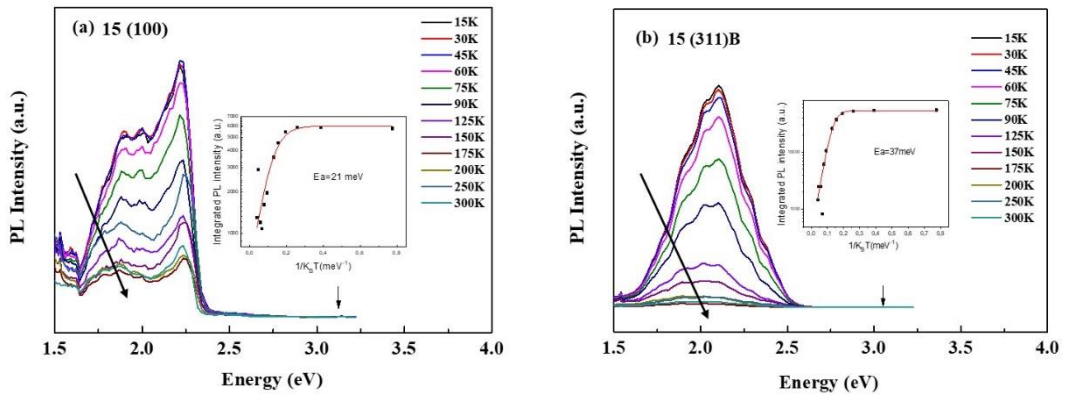


Fig. 7.14: Temperature dependence of PL spectra for sample (a) 15 (100) and (b) 15 (311)B. The arrows show the increasing of temperature. The inset shows the Arrhenius plots.

Furthermore, It was also observed that the PL bands are more intense in (311)B samples as compared with (100) samples (not shown here). These results seems to be consistent with the crystallographic properties of the samples in series (311)B that are clearly better than the samples in series (100).

In addition, for all doped samples at low temperatures, sharp peaks were also observed around 1.5 eV and were associated with typical emissions from the GaAs substrates as expected [49]. Moreover, all doped samples have also shown a small peak around 3.14 eV which could be associated with a small contribution of the brookite bandgap of TiO_2 or In doping effects[50].

The temperature dependence of the emission bands shows that the emission intensity of the PL peaks increases considerably with the decrease of temperature

CHAPTER 7

as expected. The activation energy have been estimated using the standard Arrhenius equation [51]:

$$I(T) = \frac{I_0}{1 + \gamma \exp(-E_a/(k_B T))} \quad (7.3)$$

where k_B is the Boltzmann constant, I_0 is the PL integrated intensity at 0 K, γ is the ratio between radiative and non-radiative lifetimes and E_a is an activation energy.

The Arrhenius plots are shown in the inset of Fig. 7.13 and 7.14. An activation energy of around 23 meV and 37 meV have been observed for sample 5 (311)B and 15 (311)B, respectively. Therefore, an increase of the activation energy was observed with the increase of indium content. Similar behaviour was observed previously by N. Al Saqri, *et al.* in their study of In-doped TiO₂ grown by e-beam evaporation on Si substrates [20]. However, for the sample 5 (100), an anomalous behaviour was observed for the temperature dependence of PL spectrum. It was observed that the PL intensity increases as the temperature increases up to 250 K and then decreases with increasing temperature in the range of 250 to 300 K as expected. This behaviour could be associated to a possible charge transfer or traps due to the presence of defects or some disorder in TiO₂ which could localize the carriers non-radiatively. As the temperature increases, the trapped carriers can be thermally activated and could contribute to the optically active states which lead to an increase of the intensity of the PL with increasing temperature up to 250 K [52]. In contrast, for sample 15 (100), a standard behaviour was observed and an activation energy of about 21 meV was obtained.

Finally, it is worth mentioning that a possible formation of In₂O₃ after the thermal annealing treatment, especially for samples with high indium content, could also contribute to the observed PL bands. Thus, all these observed emission bands were attributed to the localized levels in the bandgap and could be due to

intrinsic defects in TiO₂ and/or In₂O₃ as both usually have emissions in the same energy ranges. A possible contribution of In₂O₃ is particularly important for the In (15 nm)-doped TiO₂ samples. Therefore, it is difficult by using only PL measurements to separate between the contributions of defect-related emissions in TiO₂ and In₂O₃.

7.2.6 DLTS AND LAPLACE DLTS MEASUREMENTS

DLTS measurements have been performed for all samples, as Fig. 7.15 shows, over the scanned temperature range of 10 -300 K with a reverse bias $V_R = -1$ V, filling pulse height $V_P = 0$ V, filling pulse time $t_P = 1$ msec and rate windows of 200 s⁻¹. A very broad peak has been detected in each sample as shown in Fig. 7.15. Laplace DLTS [53], which is a powerful technique for resolving the broader peaks, has been used. Laplace DLTS measurements have revealed two traps in samples 15 (100), 5 (100) and 5 (311)B whereas three traps have been observed in sample 15 (311)B. It is worth mentioning that all these traps are shallow traps. Fig. 7.16 illustrates the Arrhenius plots for the traps in each sample which have been calculated from Laplace DLTS measurements. The parameters of all traps in each sample are summarised in Table 7.2.

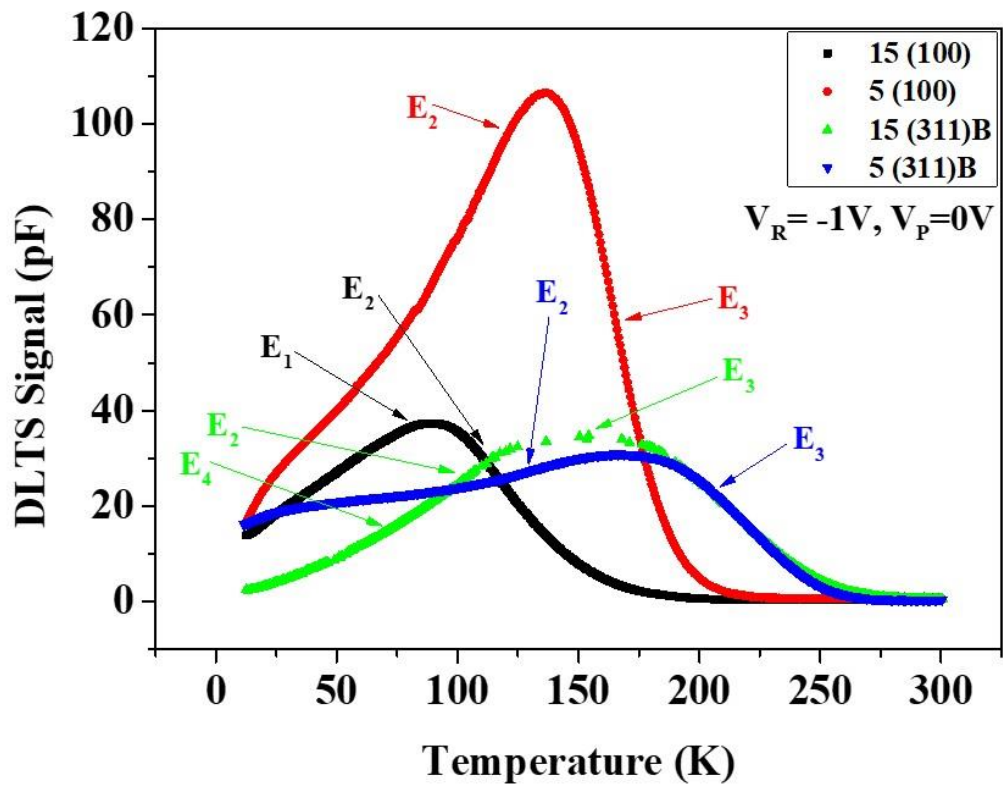


Fig. 7.15: DLTS signal for 15 (100), 5 (100), 15 (311)B and 5 (311)B samples.

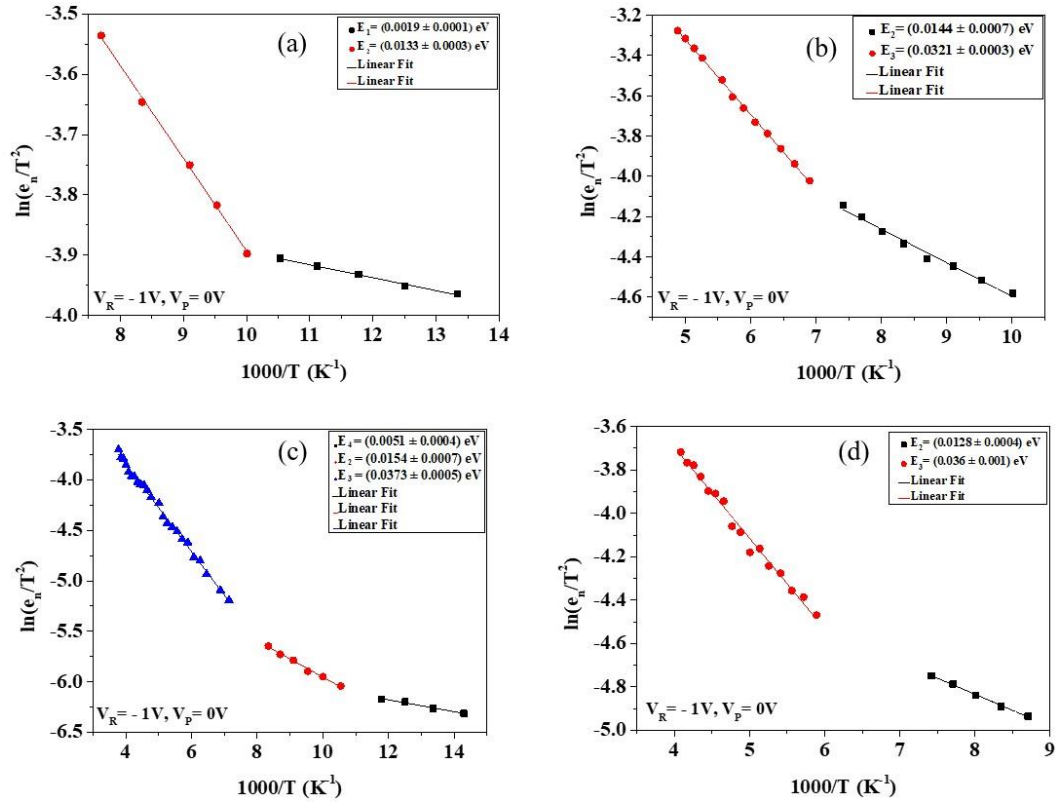


Fig. 7.16: Arrhenius plots from Laplace DLTS with reverse biases, $V_R = -1$ V, filling pulse height, $V_P = 0$ V, and filling pulse time, $t_p = 1$ msec, for sample (a) 15 (100), (b) 5 (100), (c) 15 (311)B and (d) 5 (311)B.

Table 7.2: Traps parameters for 15 (100), 5 (100), 15 (311)B and 5 (311)B samples at $V_R = -1$ V, $V_P = 0$ V and $t_p = 1$ msec.

Sample	Trap	Activation Energy (eV)	Capture Cross-Section (σ_∞) (cm^2)	Trap Concentration (cm^{-3})
15 (100)	E ₁	0.0019 ± 0.0001	8.17×10^{-23}	4.50×10^{16}
	E ₂	0.0133 ± 0.0003	3.08×10^{-22}	2.31×10^{16}
5 (100)	E ₂	0.0144 ± 0.0007	1.73×10^{-22}	6.05×10^{16}
	E ₃	0.0321 ± 0.0003	7.55×10^{-22}	3.36×10^{15}
15 (311)B	E ₄	0.0051 ± 0.0004	1.36×10^{-23}	3.85×10^{16}
	E ₂	0.0154 ± 0.0007	5.04×10^{-23}	4.60×10^{16}
	E ₃	0.0373 ± 0.0005	3.92×10^{-22}	8.04×10^{16}
5 (311)B	E ₂	0.0128 ± 0.0004	8.43×10^{-23}	8.17×10^{16}
	E ₃	0.036 ± 0.001	4.31×10^{-22}	6.65×10^{16}

CHAPTER 7

As shown in Table 7.2, trap E_2 is present in each sample but with higher concentration, $\sim 8.165 \times 10^{16}$, in sample 5 (311)B, while trap E_3 is detected in each samples except sample 15 (100). Trap E_3 has the highest concentration ($\sim 8.037 \times 10^{16} \text{cm}^{-3}$) in sample 15 (311)B . Trap E_1 is found only in sample 15 (100) and trap E_4 has been detected only in sample 15 (311)B. Trap E_1 was detected for the first time in our previous study of In-doped TiO_2 grown on Si substrate [21]. The origin of this trap is still unknown. To the best of our knowledge, the other defects, i.e. E_2 , E_3 and E_4 , are new and observed here for the first time. A theoretical model is needed to understand the origin of these defects.

DLTS measurements have been also carried out on control samples, (100) and (311)B, in order to investigate the effect of In incorporation on the traps. In other words, to find out if the traps, E_1 , E_2 , E_3 and E_4 , are present in the control samples or not. Fig. 7.17 (a) and (b) show the DLTS measurements whereas the Arrhenius plots, which were obtained from Laplace DLTS measurements, are depicted in Fig. 7.17 (c) and (d) for control samples. In sample (100), two traps were detected by Laplace DLTS, namely $E_2 = 0.017 \pm 0.001$ and $E_3 = 0.038 \pm 0.001$ eV. Incorporating 5 nm of indium into sample 5 (100) has not introduced any additional trap as the traps E_2 and E_3 in sample 5 (100) were also detected in the control sample (100). However, as indium doping increases, 15 nm, trap E_2 still could be detected but trap E_3 has been annihilated in sample 15 (100). In addition, trap E_1 in sample 15 (100) could not be detected in the control sample (100) nor in sample 5 (100), and hence it could be attributed the larger indium incorporation which may form some complexes. For sample (311)B, a broad peak has been resolved by Laplace DLTS and two traps were detected, namely $E_4 = 0.0068 \pm 0.0003$ and $E_3 = 0.034 \pm 0.004$ eV. In sample 5 (311)B, trap E_4 is removed and a

CHAPTER 7

new trap, E_2 , was created as compared to the control sample (311)B. However, as indium doping increases, 15 nm, the same traps detected in the control sample are still observed in sample 15 (311)B, i.e. E_4 and E_3 , in addition to the new trap E_2 . Therefore, for the samples grown on (311)B plane, the creation of trap E_2 could be due to incorporating indium into TiO_2 lattice.

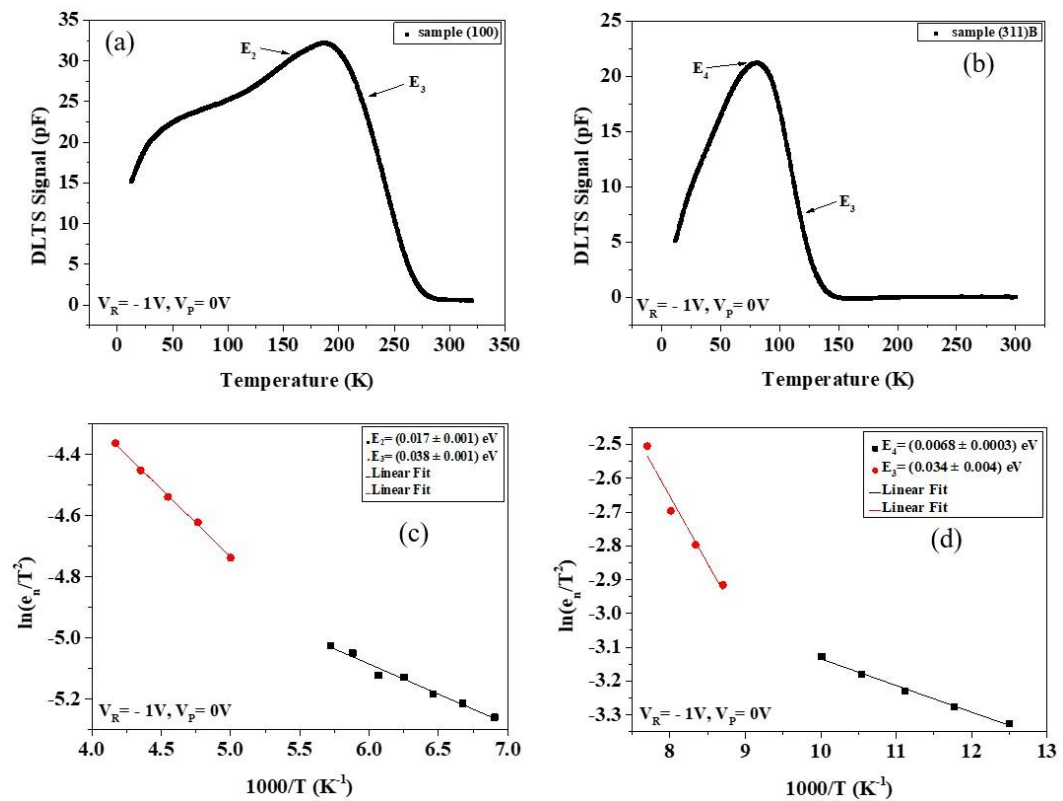


Fig. 7.17: DLTS signals for control samples (a) (100) and (b) (311)B. Arrhenius plots from Laplace DLTS measurements for (c) (100) and (d) (311)B control samples.

It is worth mentioning that the defects detected from I-V measurements could not be identified using DLTS techniques and that could be due to small concentrations of these defects. The broad DLTS peaks and the small

concentrations of the defects detected from I-V measurements could be the reason of not observing such defects even when Laplace DLTS has been employed.

The formation of more shallow defects in sample 15 (311)B which has been proven by DLTS could be correlated with the reduction of its optical absorption gap (2.94 eV) as compared to the other doped samples. This low emission energy observed only in sample 15 (311)B could be accounted for by the presence of more shallow defects that form a band under the conduction band, i.e. emission from valence band to donor states.

7.3 CONCLUSION

In this study, In-doped TiO₂ thin films were grown by PLD technique on low, (100), and high, (311)B, index planes of GaAs. Two contents of indium, 5 and 15 nm, have been used. The I-V measurements at different temperatures were performed for all samples. At room temperature, sample 5 (311)B exhibits the lowest ideality factor, 1.64, and highest barrier height, 0.77 eV as compared to the other doped samples. DLTS technique has been used to investigate the electrically active defects in all samples. Two shallow traps have been detected in all samples except sample 15 (311)B where three shallow traps have been observed. To the best of our knowledge, all these shallow traps are reported here for the first time except for trap E₁. The XRD and PL measurements have shown that the samples grown on (311)B planes have better crystallographic properties when compared to samples grown on the conventional plane (100). A lower emission energy (less than the expected bandgap energy) has been observed in sample 15 (311)B and this was attributed with the presence of more shallow donor defects as compared to the other samples. As there is no significant difference in the electrical properties of all

CHAPTER 7

samples, it could be concluded that sample 15 (311)B is the best among all other samples investigated in this work because its absorption energy has the largest red-shift meaning that it is a more suitable material for solar cells with enhanced efficiency.

REFERENCES

1. Hashimoto, K., H. Irie, and A. Fujishima, *TiO₂ photocatalysis: a historical overview and future prospects*. Japanese journal of applied physics, 2005. **44**(12R): p. 8269.
2. Sarkar, M.B., et al., *Enlarged broad band photodetection using Indium doped TiO₂ alloy thin film*. Journal of Alloys and Compounds, 2014. **615**: p. 440-445.
3. Chinnamuthu, P., et al., *Band gap enhancement of glancing angle deposited TiO₂ nanowire array*. Journal of Applied Physics, 2012. **112**(5): p. 054315.
4. Henderson, M.A., *A surface science perspective on photocatalysis*. Surface Science Reports, 2011. **66**(6): p. 185-297.
5. Fujishima, A., X. Zhang, and D.A. Tryk, *TiO₂ photocatalysis and related surface phenomena*. Surface Science Reports, 2008. **63**(12): p. 515-582.
6. Fujishima, A. and K. Honda, *Electrochemical photolysis of water at a semiconductor electrode*. nature, 1972. **238**(5358): p. 37-38.
7. Xie, T., et al., *UV-assisted room-temperature chemiresistive NO₂ sensor based on TiO₂ thin film*. Journal of alloys and compounds, 2015. **653**: p. 255-259.
8. Liu, L., et al., *Room temperature impedance spectroscopy-based sensing of formaldehyde with porous TiO₂ under UV illumination*. Sensors and Actuators B: Chemical, 2013. **185**: p. 1-9.
9. Cao, C., et al., *UV sensor based on TiO₂ nanorod arrays on FTO thin film*. Sensors and Actuators B: Chemical, 2011. **156**(1): p. 114-119.
10. Diebold, U., *The surface science of titanium dioxide*. Surface science reports, 2003. **48**(5): p. 53-229.

CHAPTER 7

11. Park, N.v., J. Van de Lagemaat, and A. Frank, *Comparison of dye-sensitized rutile-and anatase-based TiO₂ solar cells*. 2000, National Renewable Energy Laboratory (NREL), Golden, CO.
12. Howard, C., T. Sabine, and F. Dickson, *Structural and thermal parameters for rutile and anatase*. Acta Crystallographica Section B: Structural Science, 1991. **47**(4): p. 462-468.
13. Reyes-Coronado, D., et al., *Phase-pure TiO₂ nanoparticles: anatase, brookite and rutile*. Nanotechnology, 2008. **19**(14): p. 145605.
14. Amtout, A. and R. Leonelli, *Optical properties of rutile near its fundamental band gap*. Physical Review B, 1995. **51**(11): p. 6842.
15. Tang, H., et al., *Urbach tail of anatase TiO₂*. Physical Review B, 1995. **52**(11): p. 7771.
16. Wang, E., W. Yang, and Y. Cao, *Unique surface chemical species on indium doped TiO₂ and their effect on the visible light photocatalytic activity*. The Journal of Physical Chemistry C, 2009. **113**(49): p. 20912-20917.
17. Gupta, K., et al., *Photocatalytic antibacterial performance of TiO₂ and Ag-doped TiO₂ against S. aureus, P. aeruginosa and E. coli*. Beilstein journal of nanotechnology, 2013. **4**(1): p. 345-351.
18. Bechstein, R., et al., *The effects of antimony doping on the surface structure of rutile TiO₂ (110)*. Nanotechnology, 2009. **20**(26): p. 264003.
19. Choi, W., A. Termin, and M.R. Hoffmann, *The role of metal ion dopants in quantum-sized TiO₂: correlation between photoreactivity and charge carrier recombination dynamics*. The Journal of Physical Chemistry, 1994. **98**(51): p. 13669-13679.

CHAPTER 7

20. Al Saqri, N.A., et al., *Investigation of defects in indium doped TiO₂ thin films using electrical and optical techniques*. Journal of Alloys and Compounds, 2017. **698**: p. 883-891.
21. Al mashary, F.S., et al., *Effect of growth techniques on the structural, optical and electrical properties of indium doped TiO₂ thin films*. Journal of Alloys and Compounds, 2018. **766**: p. 194-203.
22. Blakemore, J., *Semiconducting and other major properties of gallium arsenide*. Journal of Applied Physics, 1982. **53**(10): p. R123-R181.
23. Lee, M.-K., C.-F. Yen, and J.-J. Huang, *Electrical Characteristics of Liquid-Phase-Deposited TiO₂ Films on GaAs Substrate with (NH₄)₂S_x Treatment*. Journal of The Electrochemical Society, 2006. **153**(5): p. F77-F80.
24. Şafak-Asar, Y., et al., *Investigation of dielectric relaxation and ac electrical conductivity using impedance spectroscopy method in (AuZn)/TiO₂/p-GaAs (1 1 0) schottky barrier diodes*. Journal of Alloys and Compounds, 2015. **628**: p. 442-449.
25. Jameel, D., et al., *Electrical performance of conducting polymer (SPAN) grown on GaAs with different substrate orientations*. Applied Surface Science, 2016. **387**: p. 228-236.
26. Polimeni, A., et al., *Optical properties and device applications of (InGa)As self-assembled quantum dots grown on (311) B GaAs substrates*. Applied physics letters, 1998. **73**(10): p. 1415-1417.
27. Wang, L., et al., *Effect of interfacial bonds on the morphology of InAs QDs grown on GaAs (311) B and (100) substrates*. Nanoscale research letters, 2009. **4**(7): p. 689.

CHAPTER 7

28. Dutta, S., R. Pal, and R. Chatterjee, *Electrical properties of spin coated ultrathin titanium oxide films on GaAs*. Materials Research Express, 2015. **2**(4): p. 046404.
29. Yen, C.-F. and M.-K. Lee, *Low equivalent oxide thickness of TiO₂/GaAs MOS capacitor*. Solid-State Electronics, 2012. **73**: p. 56-59.
30. Qiu, J., et al., *Microscopic study of atomic layer deposition of TiO₂ on GaAs and its photocatalytic application*. Chemistry of Materials, 2015. **27**(23): p. 7977-7981.
31. Liu, X., et al., *Structural characterization of TiO₂ thin films prepared by pulsed laser deposition on GaAs (1 0 0) substrates*. Applied surface science, 2001. **174**(1): p. 35-39.
32. Nowotny, J., T. Bak, and M.A. Alim, *Dual mechanism of indium incorporation into TiO₂ (Rutile)*. The Journal of Physical Chemistry C, 2014. **119**(2): p. 1146-1154.
33. Morgan, B.J. and G.W. Watson, *Polaronic trapping of electrons and holes by native defects in anatase TiO₂*. Physical Review B, 2009. **80**(23): p. 233102.
34. Sze, S.M. and M.K. Lee, *Semiconductor devices : physics and technology*. 2013, Singapore: Wiley.
35. Pillai, P., et al., *Extraction of Schottky barrier at the F-doped SnO₂/TiO₂ interface in Dye Sensitized solar cells*. Journal of Renewable and Sustainable Energy, 2014. **6**(1): p. 013142.
36. Werner, J.H., *Schottky barrier and pn-junction I/V plots—Small signal evaluation*. Applied Physics A: Materials Science & Processing, 1988. **47**(3): p. 291-300.

CHAPTER 7

37. Van, C.N. and K. Potje-Kamloth, *Electrical and NO_x gas sensing properties of metallophthalocyanine-doped polypyrrole/silicon heterojunctions*. Thin Solid Films, 2001. **392**(1): p. 113-121.
38. Aydoğan, Ş., M. Sağlam, and A. Türüt, *On the barrier inhomogeneities of polyaniline/p-Si/Al structure at low temperature*. Applied surface science, 2005. **250**(1): p. 43-49.
39. Jameel, D., et al., *High-performance organic/inorganic hybrid heterojunction based on Gallium Arsenide (GaAs) substrates and a conjugated polymer*. Applied Surface Science, 2015. **357**: p. 2189-2197.
40. Korucu, D., et al., *Evaluation of lateral barrier height of inhomogeneous photolithography-fabricated Au/n-GaAs Schottky barrier diodes from 80 K to 320 K*. Materials Science in Semiconductor Processing, 2012. **15**(5): p. 480-485.
41. Chand, S. and J. Kumar, *Evidence for the double distribution of barrier heights in Schottky diodes from I-V-T measurements*. Semiconductor science and technology, 1996. **11**(8): p. 1203.
42. Aziz, M., et al., *Electrical Behavior of MBE Grown Interfacial Misfit GaSb/GaAs Heterostructures With and Without Te-Doped Interfaces*. IEEE Transactions on Electron Devices, 2015. **62**(12): p. 3980-3986.
43. Miyagi, T., et al., *Photocatalytic property and deep levels of Nb-doped anatase TiO₂ film grown by metalorganic chemical vapor deposition*. Japanese journal of applied physics, 2004. **43**(2R): p. 775.
44. Pallotti, D.K., et al., *Photoluminescence Mechanisms in Anatase and Rutile TiO₂*. The Journal of Physical Chemistry C, 2017. **121**(16): p. 9011-9021.

CHAPTER 7

45. Gallart, M., et al., *Temperature dependent photoluminescence of anatase and rutile TiO₂ single crystals: Polaron and self-trapped exciton formation*. Journal of Applied Physics, 2018. **124**(13): p. 133104.
46. Tang, H., et al., *Photoluminescence in TiO₂ anatase single crystals*. Solid State Communications, 1993. **87**(9): p. 847-850.
47. Iijima, K., et al., *Influence of oxygen vacancies on optical properties of anatase TiO₂ thin films*. Journal of Luminescence, 2008. **128**(5-6): p. 911-913.
48. Chan, C.-H., et al., *Optical characterization of structural quality in the formation of In₂O₃ thin-film nanostructures*. The Journal of Physical Chemistry C, 2016. **120**(38): p. 21983-21989.
49. Vurgaftman, I., J.á. Meyer, and L.á. Ram-Mohan, *Band parameters for III–V compound semiconductors and their alloys*. Journal of applied physics, 2001. **89**(11): p. 5815-5875.
50. Di Paola, A., M. Bellardita, and L. Palmisano, *Brookite, the least known TiO₂ photocatalyst*. Catalysts, 2013. **3**(1): p. 36-73.
51. Shioi, K., et al., *Photoluminescence and thermal stability of yellow-emitting Sr- α -SiAlON: Eu²⁺ phosphor*. Journal of materials science, 2010. **45**(12): p. 3198-3203.
52. de Castro, S., et al., *Defects-related optical properties of Zn_{1-x}Cd_xO thin films*. Materials Science and Engineering: B, 2016. **212**: p. 96-100.
53. Dobaczewski, L., A. Peaker, and K. Bonde Nielsen, *Laplace-transform deep-level spectroscopy: The technique and its applications to the study of point defects in semiconductors*. Journal of Applied Physics, 2004. **96**(9): p. 4689-4728.

INVESTIGATION OF ELECTRICAL PROPERTIES OF ERBIUM-DOPED TiO₂ THIN FILMS PREPARED BY SOL-GEL PROCESS

In this chapter, the effect of Er doping on the electrical properties of Er-doped TiO₂ thin films grown by a combination of an easy sol-gel process and spin coating method are investigated using I-V, C-V, DLTS and Laplace DLTS techniques.

8.1 INTRODUCTION

TiO₂ is a wide bandgap oxide semiconductor material which exists in nature in three polymorphs, namely: anatase (3.21 eV), rutile (3 eV) and brookite (3.13 eV) [1, 2]. TiO₂ has been widely studied due to its remarkable properties, such as efficient photoactivity, high stability, low cost and non-toxicity [3-5]. It has been used in several applications such as photocatalysis [6], water and air purification [7], solar cell [8, 9], photo-electrochemical (PEC) water splitting [10] and UV sensors [11-13]. UV sensors have attracted a lot of attention due to their wide applications such as flame detection [14], air quality monitoring and gas sensing [15]. Si-based UV detectors have been used widely as compared to wide bandgap semiconductor UV detectors [16]. However, Si UV detectors have a low responsivity and the performance of the devices degrades with temperature [16, 17]. Therefore, the idea of using wide bandgap semiconductors as UV detectors has proved to overcome such limitations [17]. SiC [18], ZnO [19], In₂O₃ [20] and TiO₂ [21] are some of the wide bandgap semiconductors which have been studied as UV

detectors. TiO_2 is a promising candidate for such application. However, oxygen vacancies are well-known defects in TiO_2 which can lead to detecting the visible light in addition to the UV light and hence degrades the performance of TiO_2 as a UV detector [22]. Doping of TiO_2 with rare earth metals, such as Er, could eliminate the oxygen-related defects and enhance the bandgap, hence increases the sensitivity of detecting the UV light [22]. Generally, defects can play an important role in the performance of the devices. Therefore, studying the defects, both deep and shallow levels, is vital for the future of manufacturing devices [23]. In this sense, DLTS is a powerful technique to investigate the electrically active defects [24]. The main defect parameters such as activation energy, capture cross section and concentration could be obtained by DLTS.

In this study, DLTS technique has been used to investigate electrically active defects within the bandgap of Er doped TiO_2 thin films (Er: TiO_2 TFs) grown by sol-gel technique on p-type silicon substrates. In addition, capacitance-voltage measurements were used to calculate the free carrier concentration. Furthermore, current-voltage measurements as a function of temperature have been carried out to determine the ideality factors and the barrier heights of Er: TiO_2 TFs.

8.2 RESULTS AND DISCUSSION

8.2.1 SAMPLE DETAILS

Er-doped TiO_2 TFs were deposited on p-type silicon (Si) substrates using sol-gel technique followed by spin coating. To make Er: TiO_2 solutions, 0.04 g and 0.06 g Er_2O_3 nanopowder were mixed into two different TiO_2 . The TFs were deposited by spin coating (spin NXG-P1, apexicindia) technique with substrate rotation speed of 4000 rpm for 1.5 mins on Si substrates. To obtain uniform TFs,

the entire coating and annealing process were repeated 3 times with final annealing at 450 °C for 1.5 hours in air atmosphere. The samples are labelled here as Er: TiO₂ TF (0.04 g Er₂O₃) and Er: TiO₂ TF (0.06 g Er₂O₃). Full samples fabrication details were presented in chapter 5, section 5.1.3.

8.2.2 CAPACITANCE -VOLTAGE MEASUREMENTS

The capacitance-voltage (C-V) measurements at room temperature are shown in Fig. 8.1(a) for Er: TiO₂ TF (0.04 g Er₂O₃) and Er: TiO₂ TF (0.06 g Er₂O₃) samples. The free carrier concentrations for both samples were calculated using the slope of the best fit of the plot 1/C² versus reverse bias, as shown in Fig. 8.1(b). For both samples, the doping concentration is found to be uniform as proven by the linear behaviour of the plot of 1/C² versus applied reverse bias. The calculated free carrier concentration is about 1.07 x 10¹⁵ cm⁻³ and 8.80 x 10¹⁴ cm⁻³ for Er: TiO₂ TF (0.04 g Er₂O₃) and Er: TiO₂ TF (0.06 g Er₂O₃), respectively. However, the free carrier concentration for the undoped TiO₂ TF sample (control sample) is found to be 1.23 x 10¹⁵ cm⁻³ as shown in Fig. 8.2.

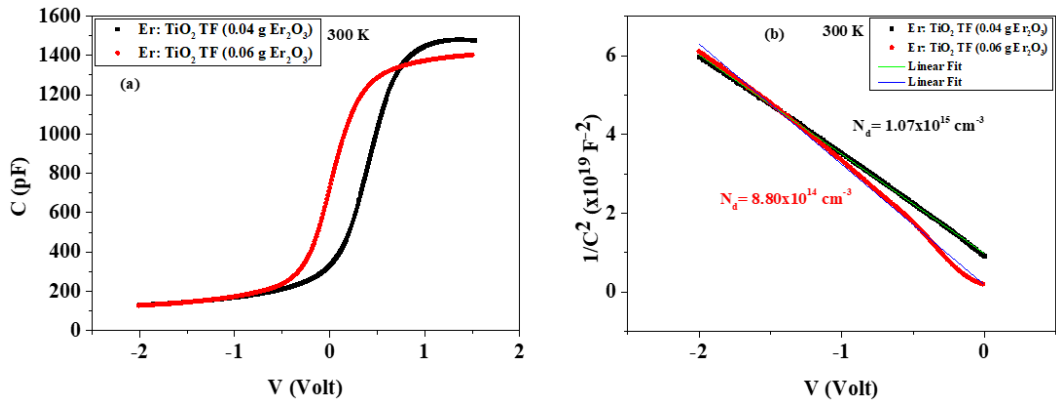


Fig. 8.1: (a) C-V plot and (b) 1/C² versus V plot at room temperature for Er: TiO₂ TF (0.04 g Er₂O₃) and Er: TiO₂ TF (0.06 g Er₂O₃) samples.

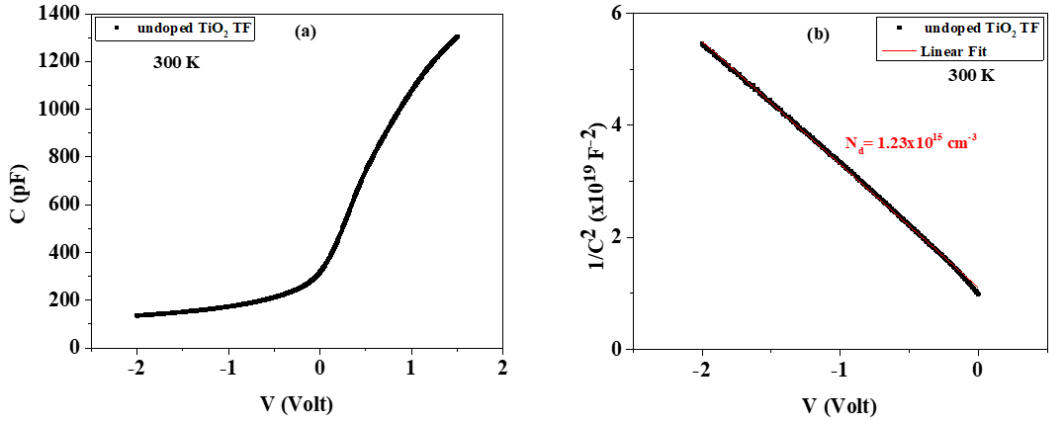


Fig. 8.2: (a) C-V plot and (b) $1/C^2$ versus V plot at room temperature for undoped TiO_2 TF sample.

8.2.3 CURRENT-VOLTAGE MEASUREMENTS

The current-voltage (I-V) measurements as a function of temperature (220-400 K with 20 K intervals) were measured for both samples in order to determine the diode parameters such as ideality factor (n), barrier height (ϕ_b) and series resistance (R_s). Fig. 8.3 shows the room temperature semi-logarithmic I-V plot for both samples. The rectification ratio at 1.5V for Er: TiO_2 TF (0.06 g Er_2O_3) sample is one order of magnitude lower than that of Er: TiO_2 TF (0.04 g Er_2O_3) sample, as shown in Fig. 8.3. However, the rectification ratio for the control undoped TiO_2 sample at the same voltage is around 2 orders of magnitude lower than the devices based on Er: TiO_2 (Fig. 8.4). This means that the doping process, independent of doping concentration, improves the electrical properties of the devices.

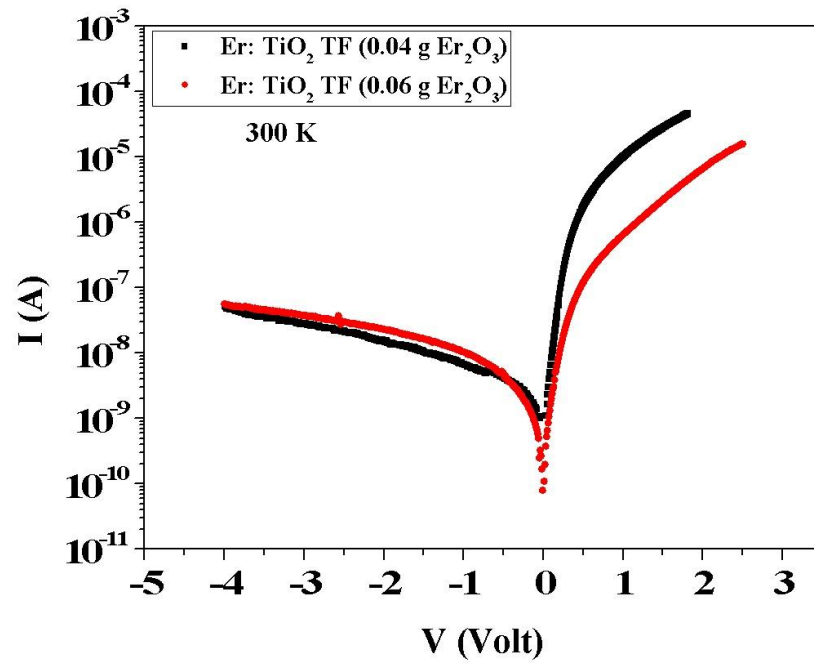


Fig. 8.3: Semi-logarithmic I-V plots for Er: TiO_2 TF (0.04 g Er_2O_3) and Er: TiO_2 TF (0.06 g Er_2O_3) samples.

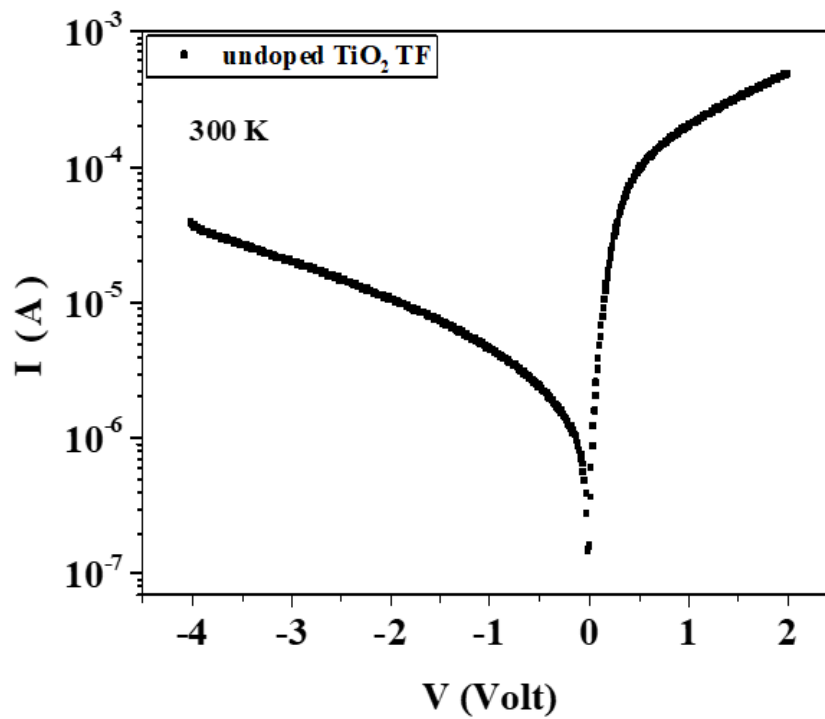


Fig. 8.4: Semi-logarithmic I-V plot for undoped TiO_2 TF sample.

CHAPTER 8

Considering the thermionic emission model, the I-V characteristics of an ideal diode including series resistance (R_s) could be described as [25]:

$$I = I_0 \left[\exp \left(\frac{q(V-IR_s)}{nKT} \right) - 1 \right] \quad (8.1)$$

where I_0 is the saturation current and is given by:

$$I_0 = AA^*T^2 \exp \left(\frac{-q\phi_b}{KT} \right) \quad (8.2)$$

In Equations (8.1) and (8.2), q is the elementary charge, n is the ideality factor, k is Boltzmann's constant, T is the temperature, ϕ_b is the barrier height, R_s is the series resistance, A is the effective diode area ($A = 7.85 \times 10^{-3} \text{ cm}^2$ for both samples) and A^* is the effective Richardson's constant ($A^* = 671 \text{ A cm}^{-2} \text{ K}^{-2}$ for TiO_2 [26]). Werner's method, which was explained in chapter 4, section 4.3, was used to calculate the diode parameters (n , ϕ_b , R_s and I_0) [27]. Table 8.1 shows the ideality factor, barrier height and series resistance for both samples at room temperature. Fig. 8.5 shows the plot of G/I versus G and the plot of $\ln(I)$ versus $(V-IR_s)$ that are used to extract the diode parameters for the doped samples. The ideality factor was found to be 2.21 and 2.02 for Er: TiO_2 TF (0.04 g Er_2O_3) and Er: TiO_2 TF (0.06 g Er_2O_3) samples, respectively. Moreover, sample Er: TiO_2 TF (0.06 g Er_2O_3) has higher barrier height (0.9 eV) as compared to Er: TiO_2 TF (0.04 g Er_2O_3) sample. This higher value of barrier height in addition to lower value of ideality factor may indicate better electrical properties of Er: TiO_2 TF (0.06 g Er_2O_3) sample when compared with Er: TiO_2 TF (0.04 g Er_2O_3) sample [28].

CHAPTER 8

Table 8.1: Room temperature Ideality factor (n), barrier height (ϕ_b) and series resistance (R_s) of Er: TiO₂ TF (0.04 g Er₂O₃) and Er: TiO₂ TF (0.06 g Er₂O₃) samples.

Sample	n	ϕ_B (eV)	R_S (k Ω)
Er: TiO ₂ TF (0.04 g Er ₂ O ₃)	2.21 ± 0.04	0.865 ± 0.002	78 ± 3
Er: TiO ₂ TF (0.06 g Er ₂ O ₃)	2.02 ± 0.09	0.9034 ± 0.0008	1840 ± 230

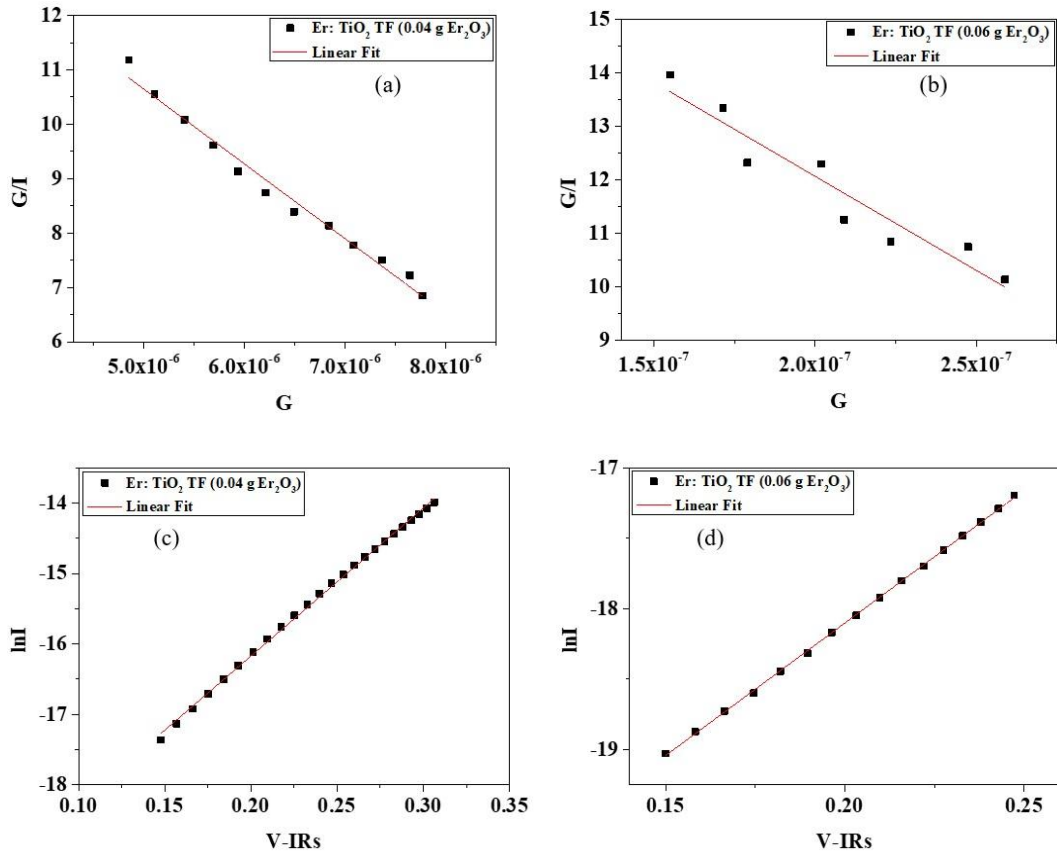


Fig. 8.5: G/I versus G plot for (a) Er: TiO₂ TF (0.04 g Er₂O₃) and (b) Er: TiO₂ TF (0.06 g Er₂O₃) samples. $\ln I$ versus ($V-IR_s$) plot for (c) Er: TiO₂ TF (0.04 g Er₂O₃) and (d) Er: TiO₂ TF (0.06 g Er₂O₃) samples.

CHAPTER 8

The saturation current equation (Eq. 8.2) could be rewritten as follows

$$\ln\left(\frac{I_0}{T^2}\right) = \ln(AA^*) - \left(\frac{-q\phi_b}{KT}\right) \quad (8.3)$$

The plot of $\ln(I_0/T^2)$ versus $1000/T$ for Er: TiO₂ TF (0.04 g Er₂O₃) sample, as shown in Fig. 8.6 (a), follows a straight line in the temperature range 260 – 400 K. This linear behaviour suggests that the conduction mechanism could be governed by thermionic emission and the saturation current (I_0) can be obtained by Equation (8.2) [29]. Fig. 8.6 (b) shows similar behaviour in the temperature range 220K - 400K for Er: TiO₂ TF (0.06 g Er₂O₃) sample. However, a deviation from linearity is observed in both samples at low temperature and this behaviour could be attributed to a contribution of additional current as a result of the reduction in the barrier height [30]. As Equation (8.3) shows, the Richardson constant can be extracted from the intercept of the straight line, and is found to be $9.9 \times 10^{-8} \text{ A cm}^{-2} \text{ K}^{-2}$ and $1.5 \times 10^{-9} \text{ A cm}^{-2} \text{ K}^{-2}$ for Er: TiO₂ TF (0.04 g Er₂O₃) and Er: TiO₂ TF (0.06 g Er₂O₃), respectively. The well-established value of Richardson constant is much higher than those found for both samples and that could be due to the spatial inhomogeneous barrier heights and potential fluctuations at the interface [31].

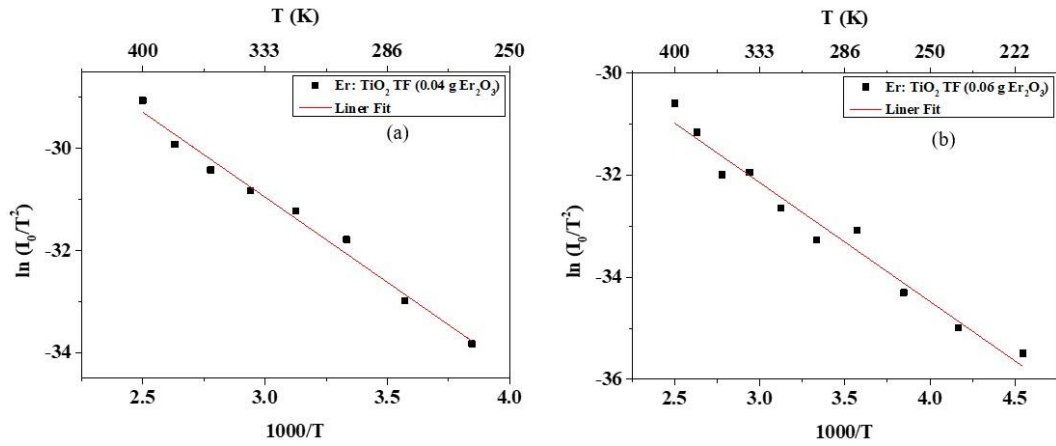


Fig. 8.6: Plot of $\ln(I_0/T^2)$ versus $1000/T$ for (a) Er: TiO₂ TF (0.04 g Er₂O₃) and (b) Er: TiO₂ TF (0.06 g Er₂O₃) samples.

The barrier height (ϕ_b) and ideality factor (n) as function of temperature for both samples are illustrated in Fig. 8.7. As shown in Fig. 8.7, the barrier height and ideality factor vary with temperature and this behaviour is generally found in many metal-semiconductors interfaces [32]. For both samples, as the temperature increases, the barrier height increases while the ideality factor decreases. This is well-known behaviour which is due to nonuniformity of interfacial charges and barrier inhomogeneity [33-35]. At low temperatures, carriers are frozen and therefore the current does not follow the thermionic emission mechanism. The current flows through the interface states and this results in higher values of the ideality factor [36]. Note that the carriers, at low temperature, can surmount the lower barriers and the mechanism of transport will be dominated by the current flowing through the regions with lower barrier heights. As temperature increases, additional carriers will gain sufficient energy to surmount regions with higher barrier heights. This charge emission process explains why the barrier height is temperature dependent [37].

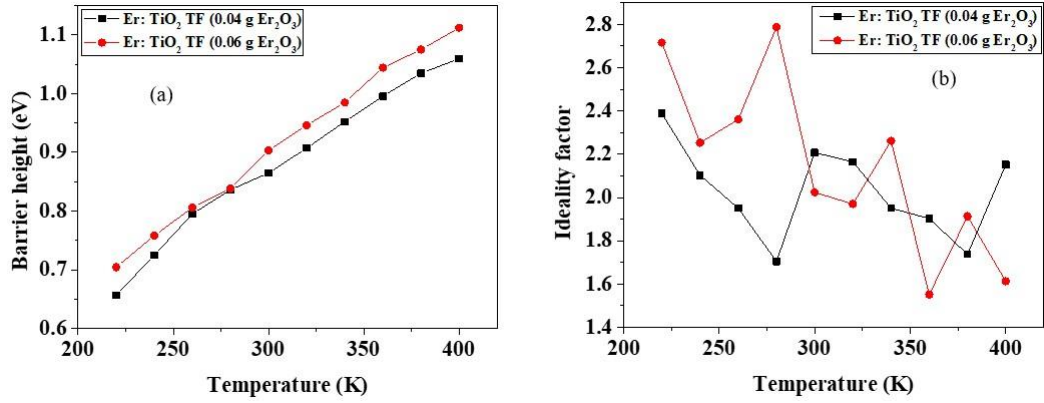


Fig. 8.7: (a) barrier height versus temperature and (b) ideality factor versus temperature for both samples.

8.2.4 DLTS AND LAPLACE DLTS MEASUREMENTS

Fig. 8.8 shows DLTS signals versus temperature for both doped samples over the scanned temperature range 10K-400 K. The DLTS measurements were carried out with a reverse bias, $V_R = -1V$, filling pulse height, $V_P = 0V$, filling pulse time, $t_P = 1$ msec and rate windows of 200 s^{-1} for both samples. As shown in Fig. 8.8, a small hump in the temperature range of 220-270 K is noticed in Er: TiO₂ TF (0.04 g Er₂O₃) sample, in addition to a broad peak in the temperature range of 300-380 K. Laplace DLTS measurements [38] have been carried out in order to resolve the broader peaks. One defect (E_1) has been revealed in the temperature range 220-270 K (the small shoulder) while two defects (E_2 and E_3) were detected under the broad peak in the temperature range of 300-380 K. On the other hand, in Er: TiO₂ TF (0.06 g Er₂O₃) sample, a broad shoulder in the temperature range 130-220 K and a small kink around 252 K were observed. However, Laplace DLTS could not resolve any real peak in those temperature ranges. A symmetric peak centred around 363 K is also observed in Er: TiO₂ TF (0.06 g Er₂O₃) sample. The full width at half maximum (FWHM) of this peak exceeds $0.1T_m$ (T_m is the temperature at the

maximum peak intensity), so Laplace DLTS has been used to resolve this peak and it is revealed that only one defect (E) is resolved. The activation energies and capture cross sections of traps detected in Er: TiO₂ TF (0.04 g Er₂O₃) and Er: TiO₂ TF (0.06 g Er₂O₃) samples were calculated from the Arrhenius plots as shown in Fig. 8.9. The trap parameters, i.e. activation energies, trap concentrations and capture cross sections are summarised in Table 8.2. The DLTS and Laplace DLTS measurements for the undoped TiO₂ TF sample (control), for the same measurement parameters used above, revealed five defects as shown in Fig. 8.10. Table 8.3 shows the activation energies, trap concentrations and capture cross sections for these traps. This higher number of defects in undoped sample as compared to doped samples are corroborating with the I-V results. Therefore, this high number of traps explains the poor electrical properties of the devices based on non-doped TiO₂ thin films.

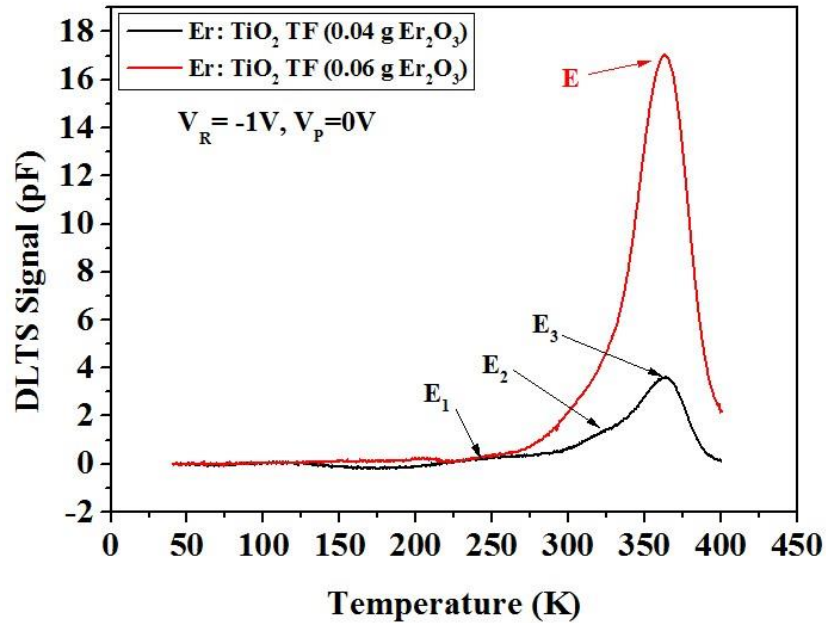


Fig. 8.8: DLTS spectra of Er: TiO₂ TF (0.04 g Er₂O₃) and Er: TiO₂ TF (0.06 g Er₂O₃) samples.

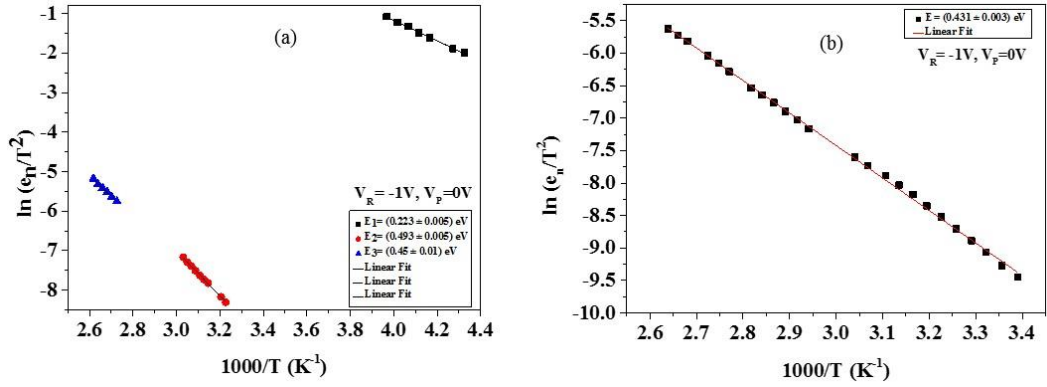


Fig. 8.9: Arrhenius plots from Laplace DLTS with reverse biases, $V_R = -1$ V, filling pulse height, $V_P = 0$ V, and filling pulse time, $t_P = 1$ msec, for (a) Er: TiO₂ TF (0.04 g Er₂O₃) and (b) Er: TiO₂ TF (0.06 g Er₂O₃) samples.

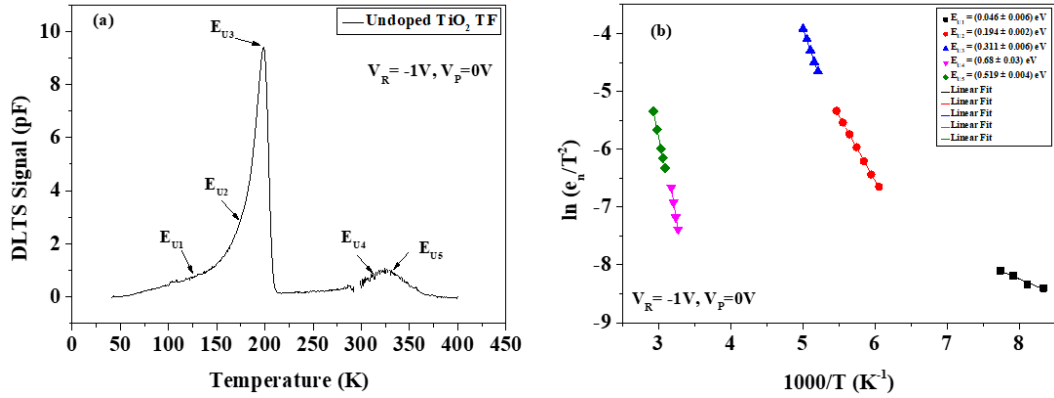


Fig. 8.10: (a) DLTS spectra and (b) Arrhenius plots from Laplace DLTS for undoped TiO₂ TF sample. The experiment parameters are reverse bias $V_R = -1$ V, filling pulse height, $V_P = 0$ V, and filling pulse time, $t_P = 1$ msec.

Table 8.2: Traps parameters of Er: TiO₂ TF (0.04 g Er₂O₃) and Er: TiO₂ TF (0.06 g Er₂O₃) samples at $V_R = -1$ V, $V_P = 0$ V and $t_P = 1$ msec.

Sample	Trap	Activation Energy (eV)	Capture Cross-Section (σ_∞) (cm ²)	Trap Concentration (cm ⁻³)
Er: TiO ₂ TF (0.04 g Er ₂ O ₃)	E ₁	0.223 ± 0.005	3.16 × 10 ⁻¹⁷	8.12 × 10 ¹²
	E ₂	0.493 ± 0.005	8.40 × 10 ⁻¹⁷	7.08 × 10 ¹²
	E ₃	0.45 ± 0.01	1.72 × 10 ⁻¹⁷	5.52 × 10 ¹³
Er: TiO ₂ TF (0.06 g Er ₂ O ₃)	E	0.431 ± 0.003	4.01 × 10 ⁻¹⁸	1.69 × 10 ¹⁴

CHAPTER 8

Table 8.3: Traps parameters of undoped TiO₂ TF sample at V_R= -1V, V_P= 0V and t_p= 1 msec.

Sample	Trap	Activation Energy (eV)	Capture Cross-Section (σ_{∞}) (cm ²)	Trap Concentration (cm ⁻³)
undoped TiO ₂ TF	E _{U1}	0.046 ± 0.006	5.92 x 10 ⁻²³	3.19 x 10 ¹²
	E _{U2}	0.194 ± 0.002	3.42 x 10 ⁻¹⁸	1.16 x 10 ¹⁴
	E _{U3}	0.311 ± 0.006	4.34 x 10 ⁻¹⁵	7.55 x 10 ¹³
	E _{U4}	0.68 ± 0.03	2.82 x 10 ⁻¹³	1.29 x 10 ¹³
	E _{U5}	0.519 ± 0.004	6.97 x 10 ⁻¹⁶	6.25 x 10 ¹²

The origin of E₁ trap could be assigned to a Ti donor level [39]. This trap (E₁) has also been observed as E_{s3} in the study of electrically active defects in indium doped TiO₂ with higher concentration than E₁ trap [35]. E₂ trap (0.49 eV) has an activation energy similar to a trap (0.5 eV) found in an investigation of the formation of native defects in anatase TiO₂ using the density functional theory [23]. The trap was assigned to Ti⁺³ state. However, E. Wang *et al.* [40] in a study of In-doped TiO₂ using the sol-gel method have assigned a trap of energy 0.51 eV to oxygen vacancies. Moreover, in another investigation T. Miyagi *et al.* [41] have found a trap with an energy 0.52 eV which was attributed to oxygen vacancies or interstitial Ti ions. Therefore, the origin of trap E₂ in this study could be assigned to Ti⁺³ state or oxygen vacancies. Trap E₃ in Er: TiO₂ TF (0.04 g Er₂O₃) sample and trap E in Er: TiO₂ TF (0.06 g Er₂O₃) sample may have the same origin as they have almost the same activation energies. As Fig. 8.8 shows, the amplitude of the DLTS signal for trap E is higher than that of trap E₃ which confirms the higher trap concentration of E (1.69 x 10¹⁴ cm⁻³) as compared to E₃ (5.52 x 10¹³ cm⁻³). However, the capture cross section of trap E (4.013 x 10⁻¹⁸ cm²) is smaller than that of trap E₃ (1.724 x 10⁻¹⁷ cm²). Traps E and E₃ may have the same origin as trap E₂, as they

have the same energies. However, for the control sample, trap E_{U1} is a shallow trap. Trap E_{U2} has the same activation energy as trap E_1 in Er: TiO₂ TF (0.04 g Er₂O₃) sample with higher concentration. Therefore, one may conclude that Er doping leads to a reduction of the concentration of this trap from $1.16 \times 10^{14} \text{ cm}^{-3}$ (E_{U2}) to $8.12 \times 10^{12} \text{ cm}^{-3}$ (E_1). However, as the doping increases (higher doped sample), E_{U2} trap is annihilated. K. Kobayashi *et al.* [42] have investigated the deep levels in Nb-doped rutile TiO₂ and found a deep level with an energy of 0.37 eV. They have assigned the origin of this trap to oxygen vacancy. Trap E_{U3} in the control sample has an energy of 0.311 eV and hence it could be due to an oxygen vacancy. A trap with an activation energy of 0.7 eV has been observed by B. Morgan and G. Watson in their study of intrinsic n-type defect formation in TiO₂ by density functional theory (DFT) and was attributed to an oxygen vacancy [43]. Trap E_{U4} which has an energy of 0.68 eV could also be due to an oxygen vacancy. Trap E_{U5} with an activation energy close to traps E , E_2 and E_3 , may have the same origin as these traps, i.e. Ti^{+3} state or oxygen vacancies. It is worth mentioning that some traps detected in the control sample are annihilated in the Er doped samples. In particular, all traps in the control sample are not detected in Er: TiO₂ TF (0.06 g Er₂O₃) sample except for trap E_{U5} . Note that traps E_{U3} and E_{U4} are due to oxygen vacancies, and therefore their absence in the Er-doped samples confirms the removal of oxygen-related defects by Er doping.

In order to control the depletion region width (moving it away or close to the interface) where the process of trapping and de-trapping of carriers happen, DLTS measurements with different reverse biases are usually performed. Fig. 8.11 (a) shows the DLTS signals for Er: TiO₂ TF (0.04 g Er₂O₃) sample at different reverse biases $V_R = -1$ and -4V . The filling pulse height, $V_P = 0\text{V}$ and the filling

CHAPTER 8

pulse time, $t_P = 1$ msec, were kept the same for all measurements. As Fig. 8.11 (a) shows, traps E_2 and E_3 which have been detected for $V_R = -1V$, are also observed at $V_R = -4V$. However, the amplitude of the DLTS signal decreases as the reverse bias increases (away from the interface). This means that the concentrations of both traps are decreasing away from the interface. In particular, the concentration of E_2 and E_3 decreased from $7.08 \times 10^{12} \text{ cm}^{-3}$ (at $V_R = -1V$) to $2.54 \times 10^{12} \text{ cm}^{-3}$ (at $V_R = -4V$), and from $5.52 \times 10^{13} \text{ cm}^{-3}$ (at $V_R = -1V$) to $2.25 \times 10^{13} \text{ cm}^{-3}$ (at $V_R = -4V$). Trap E_1 has disappeared at $V_R = -4V$ where two new shallow defects (E_4 and E_5) have been observed. These two new defects could not be detected at $V_R = -1V$, which means they are in the bulk away from the interface. Fig. 8.11 (b) shows the Arrhenius plots which are used to calculate the parameters of the traps detected at $V_R = -4V$. In Table 8.4, the parameters for the traps obtained at $V_R = -1V$ and $V_R = -4V$ are summarised.

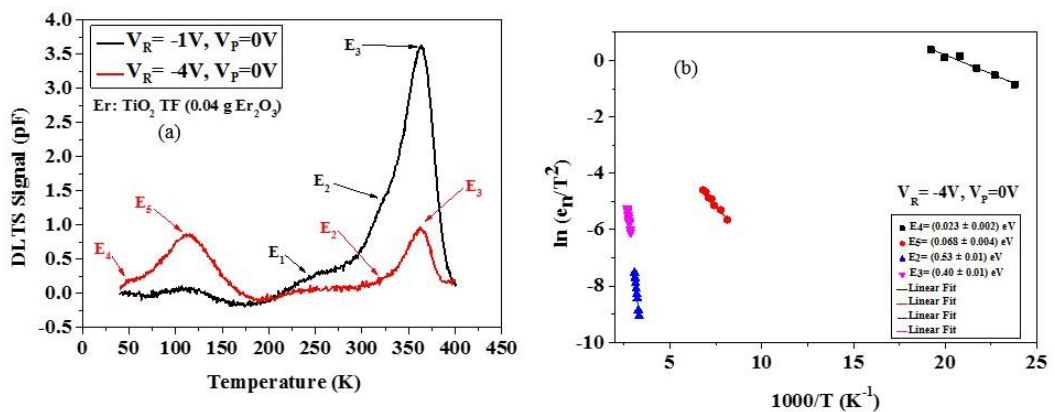


Fig. 8.11: (a) DLTS signals for $V_R = -1$ and -4 V. (b) Arrhenius plots from Laplace DLTS with reverse biases, $V_R = -4$ V, filling pulse height, $V_P = 0V$, and filling pulse time, $t_P = 1$ msec, for Er: TiO₂ TF (0.04 g Er₂O₃).

CHAPTER 8

Table 8.4: Traps parameters for Er: TiO₂ TF (0.04 g Er₂O₃) sample at V_R= -1V and -4V, V_P= 0V and t_p= 1 msec.

Reverse bias (V)	Trap	Activation Energy (eV)	Capture Cross- Section (σ_{∞}) (cm ²)	Trap Concentration (cm ⁻³)
-1	E ₁	0.223 ± 0.005	3.16 x 10 ⁻¹⁷	8.12 x 10 ¹²
	E ₂	0.493 ± 0.005	8.40 x 10 ⁻¹⁷	7.08 x 10 ¹²
	E ₃	0.45 ± 0.01	1.72 x 10 ⁻¹⁷	5.52 x 10 ¹³
-4	E ₄	0.023 ± 0.002	8.43 x 10 ⁻¹⁹	1.03 x 10 ¹³
	E ₅	0.068 ± 0.004	7.23 x 10 ⁻²¹	3.07 x 10 ¹²
	E ₂	0.539 ± 0.005	3.43 x 10 ⁻¹⁶	2.54 x 10 ¹²
	E ₃	0.395 ± 0.007	3.44 x 10 ⁻¹⁸	2.25 x 10 ¹³

For Er: TiO₂ TF (0.06 g Er₂O₃) sample, the DLTS and Laplace measurements at V_R = -4V reveal only one defect which is the same as the one detected at V_R = -1V. Fig. 8.12 (a) and Fig. 8.12 (b) show the DLTS spectra for Er: TiO₂ TF (0.06 g Er₂O₃) sample at V_R = -1V and -4V, and the Arrhenius plots that are used to calculate the energy of the trap detected at V_R = -4V, respectively. The trap concentration decreases from 1.69 x 10¹⁴ cm⁻³ (at V_R = -1V) to 1.54 x 10¹⁴ cm⁻³ (at V_R = -4V) which indicates that this trap is concentrated closer to the interface of the junction. The parameters of this trap are summarised in Table 8.5.

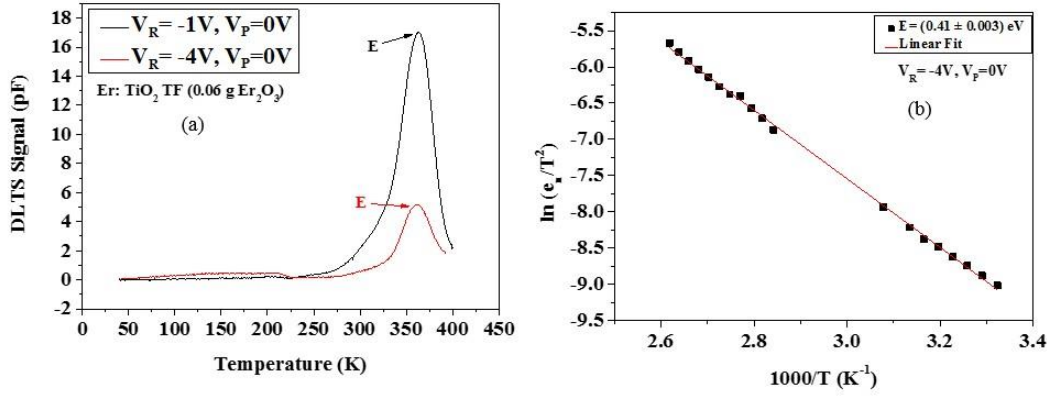


Fig. 8.12: (a) DLTS spectra at $V_R = -1$ and -4 V. (b) Arrhenius plots from Laplace DLTS at reverse bias $V_R = -4$ V, filling pulse height, $V_P = 0V$, and filling pulse time, $t_P = 1$ msec, for Er: TiO_2 TF (0.06 g Er_2O_3)

Table 8.5: Traps parameters for Er: TiO_2 TF (0.06 g Er_2O_3) sample at $V_R = -1V$ and $-4V$, $V_P = 0V$ and $t_P = 1$ msec.

Reverse bias (V)	Trap	Activation Energy (eV)	Capture Cross-Section (σ_∞) (cm^2)	Trap Concentration (cm^{-3})
-1	E	0.431 ± 0.003	4.01×10^{-18}	1.69×10^{14}
-4	E	0.409 ± 0.003	2.58×10^{-18}	1.54×10^{14}

8.3. CONCLUSION

The effect of Er content on the electrical properties of Er doped TiO_2 thin films has been investigated. Two doped structures have been prepared with different contents of Er, namely Er: TiO_2 TF (0.04 g Er_2O_3) and Er: TiO_2 TF (0.06 g Er_2O_3). Both samples show almost the same leakage current at room temperature. It was also found that the doping process improve the electrical properties of the devices as compared to the control undoped sample. The temperature behaviour of

CHAPTER 8

the ideality factor (decreases as temperature increases) and the barrier height (increases as temperature increases) have been investigated in both doped samples. At room temperature, Er: TiO₂ TF (0.06 g Er₂O₃) sample shows lower ideality factor and higher barrier height values as compared to Er: TiO₂ TF (0.04 g Er₂O₃) sample. By DLTS and Laplace DLTS measurements, only one defect has been detected in Er: TiO₂ TF (0.06 g Er₂O₃) sample while three defects were observed in Er: TiO₂ TF (0.04 g Er₂O₃) sample. On the other hand, five defects were observed in the control sample. Therefore, Er: TiO₂ TF (0.06 g Er₂O₃) sample exhibits better electrical properties as compared to Er: TiO₂ TF (0.04 g Er₂O₃) sample meaning that the electrical properties are improved by increasing Er doping. All the above findings would enhance the sensitivity UV detectors based on wide bandgap TiO₂ semiconductor materials.

REFERENCES

1. Howard, C., T. Sabine, and F. Dickson, *Structural and thermal parameters for rutile and anatase*. Acta Crystallographica Section B: Structural Science, 1991. **47**(4): p. 462-468.
2. Reyes-Coronado, D., et al., *Phase-pure TiO₂ nanoparticles: anatase, brookite and rutile*. Nanotechnology, 2008. **19**(14): p. 145605.
3. Hashimoto, K., H. Irie, and A. Fujishima, *TiO₂ photocatalysis: a historical overview and future prospects*. Japanese journal of applied physics, 2005. **44**(12R): p. 8269.
4. Sarkar, M.B., et al., *Enlarged broad band photodetection using Indium doped TiO₂ alloy thin film*. Journal of Alloys and Compounds, 2014. **615**: p. 440-445.
5. Chinnamuthu, P., et al., *Band gap enhancement of glancing angle deposited TiO₂ nanowire array*. Journal of Applied Physics, 2012. **112**(5): p. 054315.
6. Henderson, M.A., *A surface science perspective on photocatalysis*. Surface Science Reports, 2011. **66**(6): p. 185-297.
7. Fujishima, A., X. Zhang, and D.A. Tryk, *TiO₂ photocatalysis and related surface phenomena*. Surface Science Reports, 2008. **63**(12): p. 515-582.
8. Diebold, U., *The surface science of titanium dioxide*. Surface science reports, 2003. **48**(5-8): p. 53-229.
9. Park, N.-G., et al., *Comparison of dye-sensitized rutile-and anatase-based TiO₂ solar cells*. The Journal of Physical Chemistry B, 2000. **104**(38): p. 8989-8994.
10. Fujishima, A. and K. Honda, *Electrochemical photolysis of water at a semiconductor electrode*. nature, 1972. **238**(5358): p. 37-38.

CHAPTER 8

11. Xie, T., et al., *UV-assisted room-temperature chemiresistive NO₂ sensor based on TiO₂ thin film*. Journal of alloys and compounds, 2015. **653**: p. 255-259.
12. Liu, L., et al., *Room temperature impedance spectroscopy-based sensing of formaldehyde with porous TiO₂ under UV illumination*. Sensors and Actuators B: Chemical, 2013. **185**: p. 1-9.
13. Cao, C., et al., *UV sensor based on TiO₂ nanorod arrays on FTO thin film*. Sensors and Actuators B: Chemical, 2011. **156**(1): p. 114-119.
14. Cheong, P., et al., *A ZigBee-based wireless sensor network node for ultraviolet detection of flame*. IEEE transactions on industrial electronics, 2011. **58**(11): p. 5271-5277.
15. Razeghi, M. and A. Rogalski, *Semiconductor ultraviolet detectors*. Journal of Applied Physics, 1996. **79**(10): p. 7433-7473.
16. Shi, L. and S. Nihtianov, *Comparative study of silicon-based ultraviolet photodetectors*. IEEE Sensors Journal, 2012. **12**(7): p. 2453-2459.
17. Sang, L., M. Liao, and M. Sumiya, *A comprehensive review of semiconductor ultraviolet photodetectors: from thin film to one-dimensional nanostructures*. Sensors, 2013. **13**(8): p. 10482-10518.
18. Bertuccio, G., et al., *Silicon carbide detector for laser-generated plasma radiation*. Applied Surface Science, 2013. **272**: p. 128-131.
19. Yu, J., et al., *Enhanced responsivity of photodetectors realized via impact ionization*. Sensors, 2012. **12**(2): p. 1280-1287.
20. Mondal, A., et al., *Structural and optical properties of glancing angle deposited In₂O₃ columnar arrays and Si/In₂O₃ photodetector*. Applied Physics A, 2014. **115**(1): p. 353-358.

CHAPTER 8

21. Tiwari, A., et al., *Improved Photo-Detection Using Zigzag TiO₂ Nanostructures as an Active Medium*. Journal of nanoscience and nanotechnology, 2015. **15**(7): p. 5099-5104.
22. Lahiri, R., et al., *Performance of Erbium-doped TiO₂ thin film grown by physical vapor deposition technique*. Applied Physics A, 2017. **123**(9): p. 573.
23. Morgan, B.J. and G.W. Watson, *Polaronic trapping of electrons and holes by native defects in anatase TiO₂*. Physical Review B, 2009. **80**(23): p. 233102.
24. Lang, D., *Deep-level transient spectroscopy: A new method to characterize traps in semiconductors*. Journal of applied physics, 1974. **45**(7): p. 3023-3032.
25. Sze, S.M. and M.K. Lee, *Semiconductor devices : physics and technology*. 2013, Singapore: Wiley.
26. Pillai, P., et al., *Extraction of Schottky barrier at the F-doped SnO₂/TiO₂ interface in Dye Sensitized solar cells*. Journal of Renewable and Sustainable Energy, 2014. **6**(1): p. 013142.
27. Werner, J.H., *Schottky barrier and pn-junction I/V plots—Small signal evaluation*. Applied Physics A: Materials Science & Processing, 1988. **47**(3): p. 291-300.
28. Devi, V.L., et al., *Schottky barrier parameters and interfacial reactions of rapidly annealed Au/Cu bilayer metal scheme on n-type InP*. Open Applied Physics Journal, 2012. **5**(1).

CHAPTER 8

29. Van, C.N. and K. Potje-Kamloth, *Electrical and NO_x gas sensing properties of metallophthalocyanine-doped polypyrrole/silicon heterojunctions*. Thin Solid Films, 2001. **392**(1): p. 113-121.
30. Jameel, D., et al., *Electrical performance of conducting polymer (SPAN) grown on GaAs with different substrate orientations*. Applied Surface Science, 2016. **387**: p. 228-236.
31. Aydoğan, Ş., M. Sağlam, and A. Türüt, *On the barrier inhomogeneities of polyaniline/p-Si/Al structure at low temperature*. Applied surface science, 2005. **250**(1): p. 43-49.
32. Jameel, D., et al., *High-performance organic/inorganic hybrid heterojunction based on Gallium Arsenide (GaAs) substrates and a conjugated polymer*. Applied Surface Science, 2015. **357**: p. 2189-2197.
33. Korucu, D., et al., *Evaluation of lateral barrier height of inhomogeneous photolithography-fabricated Au/n-GaAs Schottky barrier diodes from 80 K to 320 K*. Materials Science in Semiconductor Processing, 2012. **15**(5): p. 480-485.
34. Chand, S. and J. Kumar, *Evidence for the double distribution of barrier heights in Schottky diodes from I-V-T measurements*. Semiconductor science and technology, 1996. **11**(8): p. 1203.
35. Al mashary, F.S., et al., *Effect of growth techniques on the structural, optical and electrical properties of indium doped TiO₂ thin films*. Journal of Alloys and Compounds, 2018. **766**: p. 194-203.
36. Aziz, M., et al., *Electrical Behavior of MBE Grown Interfacial Misfit GaSb/GaAs Heterostructures With and Without Te-Doped Interfaces*. IEEE Transactions on Electron Devices, 2015. **62**(12): p. 3980-3986.

CHAPTER 8

37. Tripathi, S. and M. Sharma, *Analysis of the forward and reverse bias IV and CV characteristics on Al/PVA: n-PbSe polymer nanocomposites Schottky diode*. Journal of Applied Physics, 2012. **111**(7): p. 074513.
38. Dobaczewski, L., A. Peaker, and K. Bonde Nielsen, *Laplace-transform deep-level spectroscopy: The technique and its applications to the study of point defects in semiconductors*. Journal of Applied Physics, 2004. **96**(9): p. 4689-4728.
39. Salama, A. and L. Cheng, *The Effects of Titanium Impurities in N+/P Silicon Solar Cells*. Journal of The Electrochemical Society, 1980. **127**(5): p. 1164-1167.
40. Wang, E., W. Yang, and Y. Cao, *Unique surface chemical species on indium doped TiO₂ and their effect on the visible light photocatalytic activity*. The Journal of Physical Chemistry C, 2009. **113**(49): p. 20912-20917.
41. Miyagi, T., et al., *Photocatalytic property and deep levels of Nb-doped anatase TiO₂ film grown by metalorganic chemical vapor deposition*. Japanese journal of applied physics, 2004. **43**(2R): p. 775.
42. Kobayashi, K., et al., *Investigation of trapping states in a Nb-doped rutile by admittance spectroscopy*. Journal of applied physics, 1986. **60**(12): p. 4191-4196.
43. Morgan, B.J. and G.W. Watson, *Intrinsic n-type defect formation in TiO₂: a comparison of rutile and anatase from GGA+ U calculations*. The Journal of Physical Chemistry C, 2010. **114**(5): p. 2321-2328.

INVESTIGATION OF THE ELECTRICAL PROPERTIES OF ERBIUM-DOPED In_2O_3 THIN FILMS

In this chapter, the effects of Erbium (Er) doping on the electrical properties of In_2O_3 thin films grown by spin-on technique are investigated using I-V, C-V, DLTS and Laplace DLTS techniques.

9.1 INTRODUCTION

Transparent conducting oxides (TCOs) thin films (TFs) have drawn so much attention due to their applications in optoelectronic devices [1]. Among these materials, Indium oxide (In_2O_3) is one of the most investigated TCOs material due to its high carrier mobility ($\sim 43.7 \text{ cm}^2/\text{V}\cdot\text{s}$) as compared to other TCOs materials [2]. It is intrinsically an n-type semiconductor with a direct wide bandgap of 3.5 – 3.75 eV [3-6]. In_2O_3 has been used as a gas sensor due to its sensitivity to the ambient conditions [7], in photovoltaic devices [8], in flat panel displays, electrochromic mirror [9] and UV light detectors [4]. The ability to detect UV light is very important in industry for device applications such as flame sensors, spatial optical communication, biological and chemical sensors etc. [4]. The main figures of merit of UV detectors are high sensitivity, low noise and high response time [10]. Si-based UV detectors have been used widely as compared to wide bandgap semiconductor UV detectors due mainly to their low cost. However, one of the major disadvantage of Si UV detectors is their low efficiency at high temperatures. Additionally, due to the small bandgap of Si, usually an optical filter is needed to block the low energy photons [11]. Wide bandgap semiconductors, such as SiC

[12], ZnO [13], In₂O₃ [14], TiO₂ [15] and GaN [16], have been explored as UV detectors because they are intrinsically solar-blind due to their large bandgap [17]. However, one of their disadvantages is the presence of defects within the bandgap which are sensitive to the visible light. These defects greatly affect the response to UV light [18] and therefore adversely affects their performance. Such defects are well known to be oxygen related defects in TCOs materials [2, 19], and their annihilation is very challenging. Doping In₂O₃ TFs with Er have been reported to remove the oxygen related defects and simultaneously increase the bandgap, and hence enhance the sensitivity of UV detection which has been proved by photocurrent measurements. A reduction in the rise and fall times which leads to a better response speed of the detector has been achieved by increasing Er [2]. An electrical investigation, including a study of the electrically active defects, on the samples studied by our collaborators in reference [2] is presented here.

Defects play an important role in the performance of the devices. Therefore, studying the defects, both deep and shallow levels, is vital for the future of manufacturing devices [20].

The main objective in this study is to investigate the electrically active defects in undoped In₂O₃ and Er doped In₂O₃ TFs by DLTS technique to confirm the removal of defects by adding erbium. Furthermore, the ideality factors and the barrier heights at different temperatures have been determined from the current-voltage measurements as a function of temperature.

9.2 RESULTS AND DISCUSSION

9.2.1 SAMPLE DETAILS

In_2O_3 and Er doped In_2O_3 (Er: In_2O_3) TFs were deposited on p-type Si (100) substrates by spin-on technique using chemical routes [4]. The atomic fraction of Er in the doped films is estimated, using the energy dispersive X-ray spectroscopy (EDX), to be 0.15, 0.18 and 0.22 at. % for the 0.01 g, 0.02 g and 0.04 g Er_2O_3 containing TFs [2]. Thus, the samples in this work are labelled as undoped In_2O_3 , 0.15 at.% Er: In_2O_3 , 0.18 at.% Er: In_2O_3 and 0.22 at.% Er: In_2O_3 . Full details of the fabrication of the samples were presented in Chapter 5, section 5.1.4.

9.2.2 CURRENT-VOLTAGE MEASUREMENTS

The room temperature semi-logarithmic plot of current density-voltage (J-V) of undoped sample and Er doped samples are shown in Fig. 9.1. A deviation from linearity as the forward bias increases is noticed for all samples. This deviation is due to series resistance [21]. The less doped sample, 0.15 at.% Er: In_2O_3 , has the lowest leakage current as compared to all other samples. The undoped In_2O_3 sample has the highest leakage current. In particular, the current density at - 4 V reverse bias for 0.15 at.% Er: In_2O_3 , 0.18 at.% Er: In_2O_3 and 0.22 at.% Er: In_2O_3 samples are $1.4 \times 10^{-6} \text{ A/cm}^2$, $1.0 \times 10^{-5} \text{ A/cm}^2$ and $1.4 \times 10^{-3} \text{ A/cm}^2$, respectively. However, for the undoped In_2O_3 sample, the current density at - 4 V is $3.7 \times 10^{-3} \text{ A/cm}^2$. The reduction of the leakage current as Er is incorporated in the lattice has been attributed to the removal of the oxygen related defects, which lead to a reduction of the generation-recombination centres and hence reduces the tunnelling process in reverse bias [2]. I-V measurements for all samples as function of temperature

have been carried out in the range of 220-400K (with 20 K intervals) to extract the diode parameters and study their behaviour with temperature.

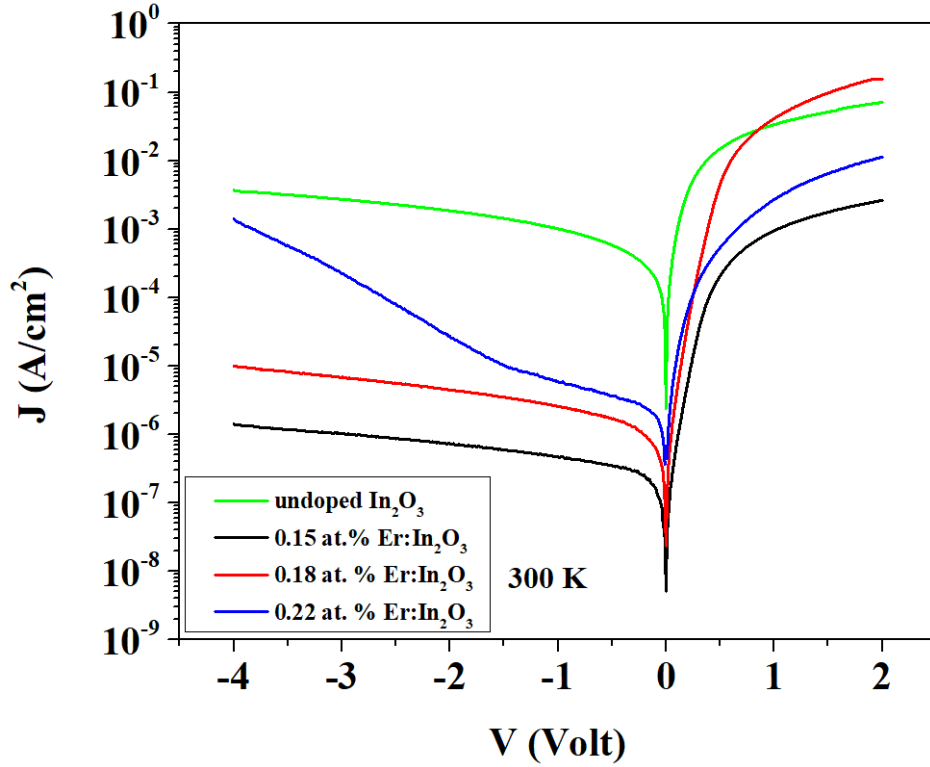


Fig. 9.1: Semi-logarithmic J-V plots for undoped In_2O_3 , 0.15 at.% $\text{Er}:\text{In}_2\text{O}_3$, 0.18 at.% $\text{Er}:\text{In}_2\text{O}_3$ and 0.22 at.% $\text{Er}:\text{In}_2\text{O}_3$ samples.

The I-V characteristics of an ideal diode, including series resistance (R_s), are described by the thermionic emission model [22]:

$$I = I_0 \left[\exp \left(\frac{q(V - IR_s)}{nKT} \right) - 1 \right] \quad (9.1)$$

where I_0 is the saturation current and is given by:

$$I_0 = AA^*T^2 \exp \left(\frac{-q\phi_b}{KT} \right) \quad (9.2)$$

CHAPTER 9

The effective diodes area are $A = 1.59 \times 10^{-3}$, 7.85×10^{-3} , 6.36×10^{-3} and $3.85 \times 10^{-3} \text{ cm}^2$ for undoped In_2O_3 , 0.15 at.% Er: In_2O_3 , 0.18 at.% Er: In_2O_3 and 0.22 at.% Er: In_2O_3 samples, respectively and the effective Richardson's constant is $A^* = 36 \text{ A cm}^{-2} \text{ K}^{-2}$ for In_2O_3 [23]. Werner's method was used in order to improve the accuracy of calculating the diode parameters (ideality factor (n), barrier height (ϕ_b) and series resistance (R_s)) [24]. A detailed explanation of this method and definition of all variables in the above equations were covered in Chapter 4, section 4.3. G/I versus G plot (Fig. 9.2) and $\ln(I)$ versus $(V-IR_s)$ plot (Fig. 9.3) are used to extract the diode parameters for all samples. These parameters calculated at room temperature for all samples are summarised in Table 9.1.

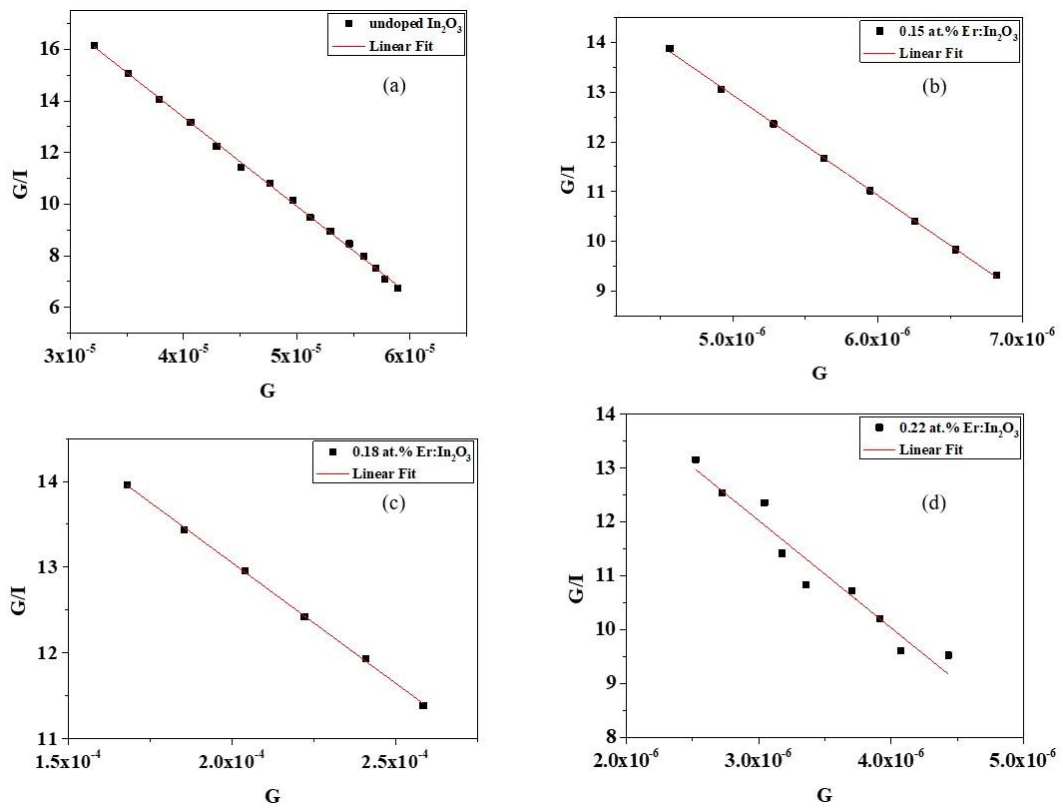


Fig. 9.2: G/I versus G plot for (a) undoped In_2O_3 , (b) 0.15 at.% Er: In_2O_3 , (c) 0.18 at.% Er: In_2O_3 and (d) 0.22 at.% Er: In_2O_3 samples.

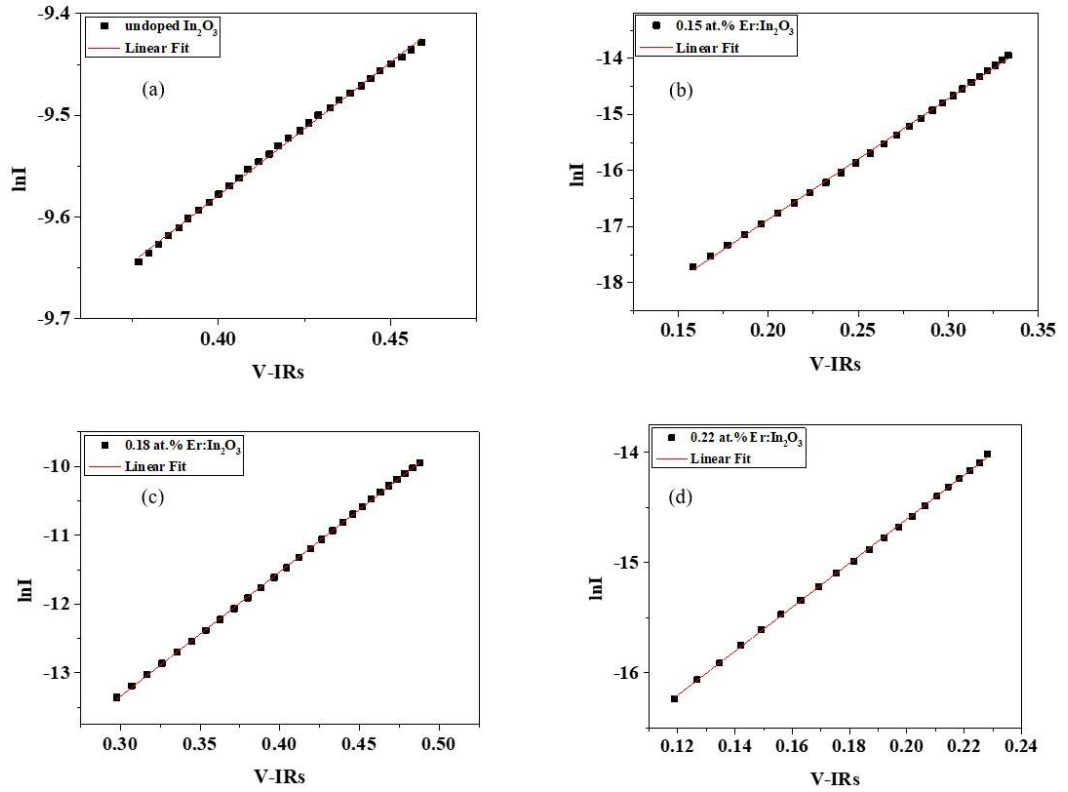


Fig. 9.3: $\ln(I)$ versus $(V-IR_s)$ plot for (a) undoped In_2O_3 , (b) 0.15 at.% Er: In_2O_3 , (c) 0.18 at.% Er: In_2O_3 and (d) 0.22 at.% Er: In_2O_3 samples.

Table 9.1: Ideality factor (n), barrier height (ϕ_b) and series resistance (R_s) at room temperature for all samples.

Sample	n	ϕ_B (eV)	R_S (k Ω)
Undoped In_2O_3	1.423 ± 0.008	0.4977 ± 0.0004	12.7 ± 0.1
0.15 at.% Er: In_2O_3	1.679 ± 0.008	0.809 ± 0.001	87.5 ± 0.8
0.18 at.% Er: In_2O_3	2.072 ± 0.008	0.7421 ± 0.0007	1.50 ± 0.01
0.22 at.% Er: In_2O_3	2.15 ± 0.07	0.7248 ± 0.0005	110 ± 9

Among all doped samples, the less doped sample, 0.15 at.% Er: In_2O_3 , has the lowest ideality factor and the highest barrier height. As the concentration of Er increases, the ideality factor increases and the barrier height decreases. In

CHAPTER 9

particular, at room temperature the ideality factor is about 1.68, 2.07 and 2.15 for 0.15 at.% Er:In₂O₃, 0.18 at.% Er:In₂O₃ and 0.22 at.% Er:In₂O₃, respectively. The barrier height is about 0.81, 0.74 and 0.72 eV for 0.15 at.% Er:In₂O₃, 0.18 at.% Er:In₂O₃ and 0.22 at.% Er:In₂O₃, respectively. However, the undoped In₂O₃ sample has the smallest ideality factor (1.42) and barrier height (0.5 eV). The higher value of barrier height and small ideality factor of the 0.15 at.% Er:In₂O₃ sample may indicate better electrical properties when compared with all other samples [25].

The behaviour of barrier heights and ideality factors as function of temperature for all samples is shown in Fig. 9.4. The variation of barrier height and ideality factor with temperature is usually observed in many metal-semiconductors interfaces [26]. As can be seen in Fig. 9.4 (a), the barrier height increases as temperature increases for all samples. However, as seen in Fig. 9.4 (b), the ideality factor decreases with increasing temperature for all doped samples, whereas for the undoped sample the ideality factor increases as temperature increases which is an unusual behaviour. This behaviour of ideality factor with temperature of the undoped sample could be a sign of a poor device performance at high temperatures. The increase of the barrier height with temperature is a well-known behaviour and usually is due to nonuniformity of interfacial charges and barrier inhomogeneity [27-29]. Similar behaviour of ideality factor and barrier height with temperatures has also been observed and discussed in chapter 6, section 6.2.3. It is worth mentioning that the less doped sample, 0.15 at.% Er:In₂O₃, has shown generally the best values of ideality factor and barrier height as function of temperature when compared to all other samples as clearly shown in Fig. 9.4.

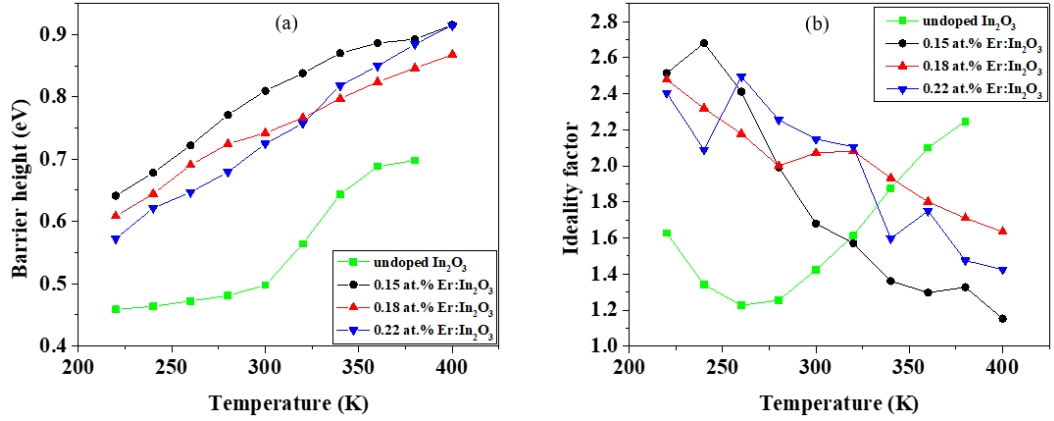


Fig. 9.4: (a) barrier height versus temperature and (b) ideality factor versus temperature for all samples.

The saturation current equation (9.2) could be rewritten as following

$$\ln\left(\frac{I_0}{T^2}\right) = \ln(AA^*) - \left(\frac{-q\phi_b}{KT}\right) \quad (9.3)$$

The plot of $\ln(I_0/T^2)$ versus $1000/T$, as shown in Fig. 9.5, shows the best line fit for 0.15 at.% Er:In₂O₃, 0.18 at.% Er:In₂O₃ and 0.22 at.% Er:In₂O₃ samples in the temperature range of 280-400K, 260-400K and 340-400K, respectively. This behavior suggests that the conduction mechanism could be governed by thermionic emission and the saturation current (I_0) can be obtained by Equation (9.2) [30]. However, a deviation from linearity at low temperature is observed for all samples and that could be attributed to a contribution of extra current as a result of the reduction in the barrier height [31]. The Richardson constant could be extracted from the y-intercept of the straight line and is found to be 3.06×10^{-5} , 1.44×10^{-5} and $2.07 \times 10^{-7} \text{ A cm}^{-2} \text{ K}^{-2}$ for 0.15 at.% Er:In₂O₃, 0.18 at.% Er:In₂O₃ and 0.22 at.% Er:In₂O₃ samples, respectively. The experimental values of Richardson constant obtained here are much lower than the well-established value of In₂O₃ ($36 \text{ A cm}^{-2} \text{ K}^{-2}$). This deviation of the experimental values is usually attributed to the spatial

CHAPTER 9

inhomogeneous barrier heights and potential fluctuations at the interface [32]. Moreover, the mean barrier height, which can be extracted from the slope of the best line fit, was found to be 0.45, 0.36 and 0.26 eV for 0.15 at.% Er:In₂O₃, 0.18 at.% Er:In₂O₃ and 0.22 at.% Er:In₂O₃ samples, respectively. The higher barrier height value of sample 0.15 at.% Er:In₂O₃ could be an indication of less defects in this sample which will be investigated by DLTS measurements.

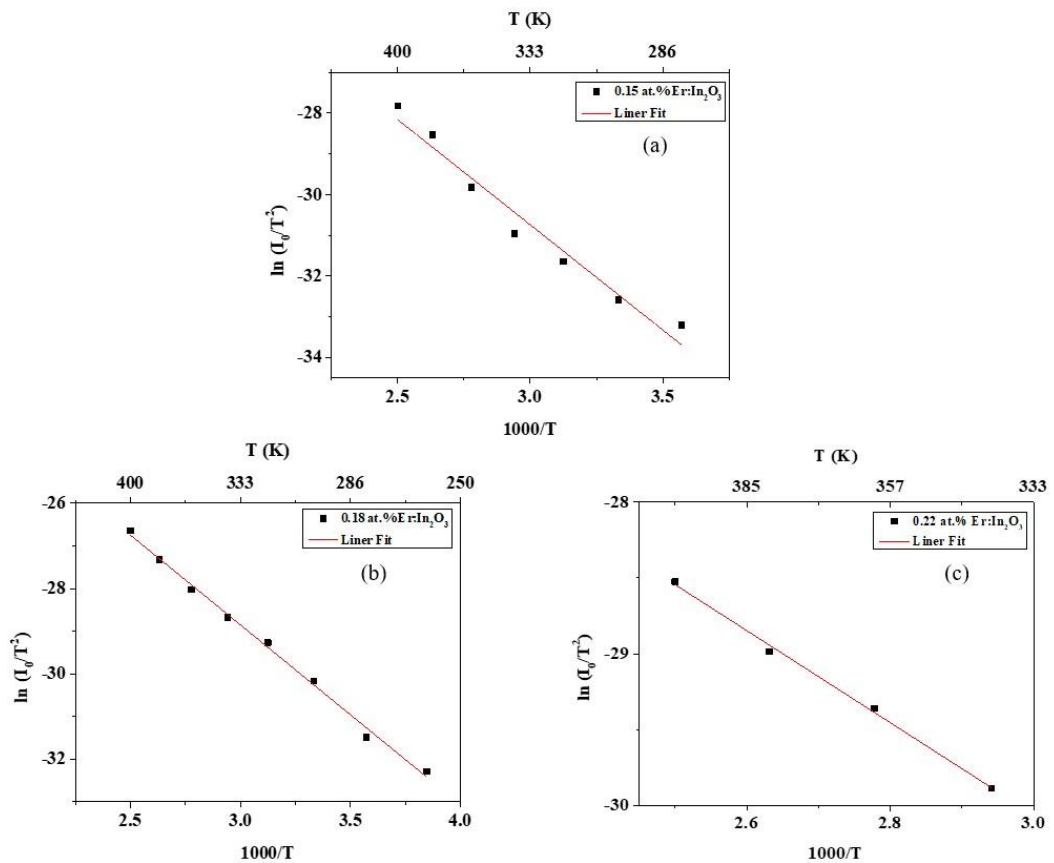


Fig. 9.5: The plot of $\ln(I_0/T^2)$ versus $1000/T$ for (a) 0.15 at.% Er:In₂O₃, (b) 0.18 at.% Er:In₂O₃ and (c) 0.22 at.% Er:In₂O₃ samples.

9.2.3 CAPACITANCE-VOLTAGE MEASUREMENTS

The capacitance-voltage (C-V) measurements at room temperature are shown in Fig. 9.6 (a) for all doped samples. The free carrier concentrations for all samples were calculated using the slope of the best fit of the plot $1/C^2$ versus reverse bias, as shown in Fig. 9.6 (b). The doping concentration, for all samples, is found to be uniform as confirmed by the linear behaviour of the plot of $1/C^2$ versus applied reverse bias, and the free carrier concentration is found to be about $8.33 \times 10^{15} \text{ cm}^{-3}$, $1.67 \times 10^{16} \text{ cm}^{-3}$ and $2.77 \times 10^{16} \text{ cm}^{-3}$ for 0.15 at.% Er:In₂O₃, 0.18 at.% Er:In₂O₃ and 0.22 at.% Er:In₂O₃ samples, respectively. However, the free carrier concentration for the undoped In₂O₃ sample is found to be $3.61 \times 10^{16} \text{ cm}^{-3}$ as shown in Fig. 9.7. As observed in Fig. 9.6 (b) and Fig. 9.7 (b) the undoped sample has the highest capacitance as compared to the doped samples and this could be due to shallow ionised impurity levels present in the undoped sample.

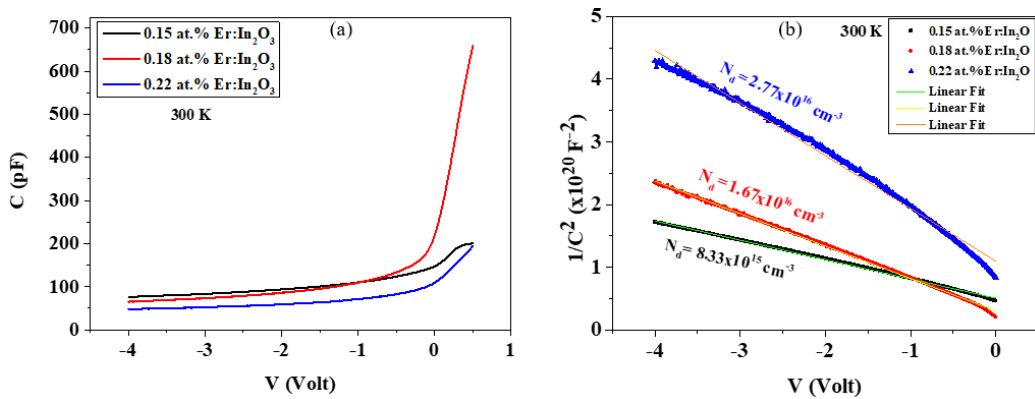


Fig. 9.6: (a) C-V plots and (b) $1/C^2$ versus V plots at room temperature for all doped samples.

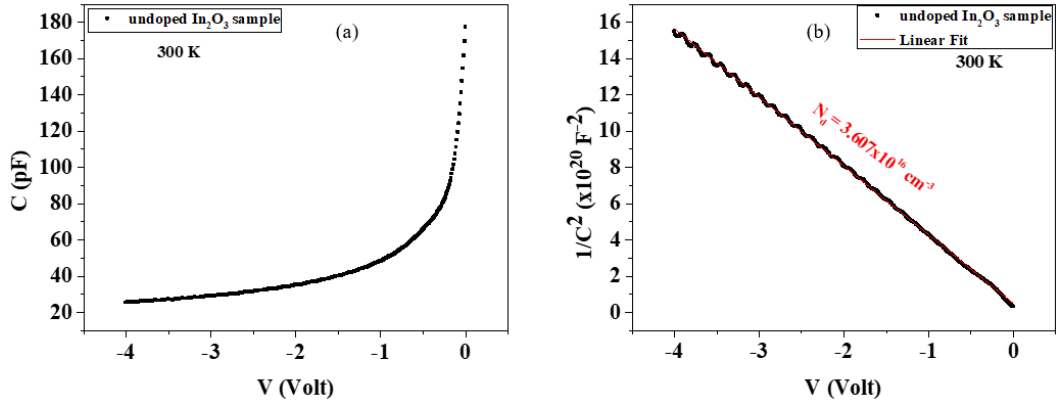


Fig. 9.7: (a) C-V plot and (b) $1/C^2$ versus V plot at room temperature for the undoped sample.

9.2.4 DLTS AND LAPLACE DLTS MEASUREMENTS

DLTS technique has been used to study the electrically active defects in the samples under investigation. Fig. 9.8 shows the DLTS spectra as function of temperature scanned over the range of 50-400K for all samples. The DLTS experiment was carried out with a reverse bias of $V_R = -1\text{V}$, filling pulse height of $V_P = 0\text{V}$, filling pulse time of $t_P = 1 \text{ msec}$ and rate windows of 200 s^{-1} . As Fig. 9.8 depicts, a negative peak in the temperature range of 50-80K has been observed for the undoped In_2O_3 sample and an asymmetric broad positive peak in the temperature range of 280-400K. In addition, sample 0.15 at.% Er: In_2O_3 reveals a broad peak in the temperature range 170-245K. For sample 0.18 at.% Er: In_2O_3 , also a broad peak is noticed in the range of 50-165K and a hump around 300K. A wide peak has also been detected in the 0.22 at.% Er: In_2O_3 sample in the temperature range 180-280K. Laplace DLTS technique [33] is used to resolve the broad DLTS peaks, which are usually formed due to defects having closely spaced energy levels.

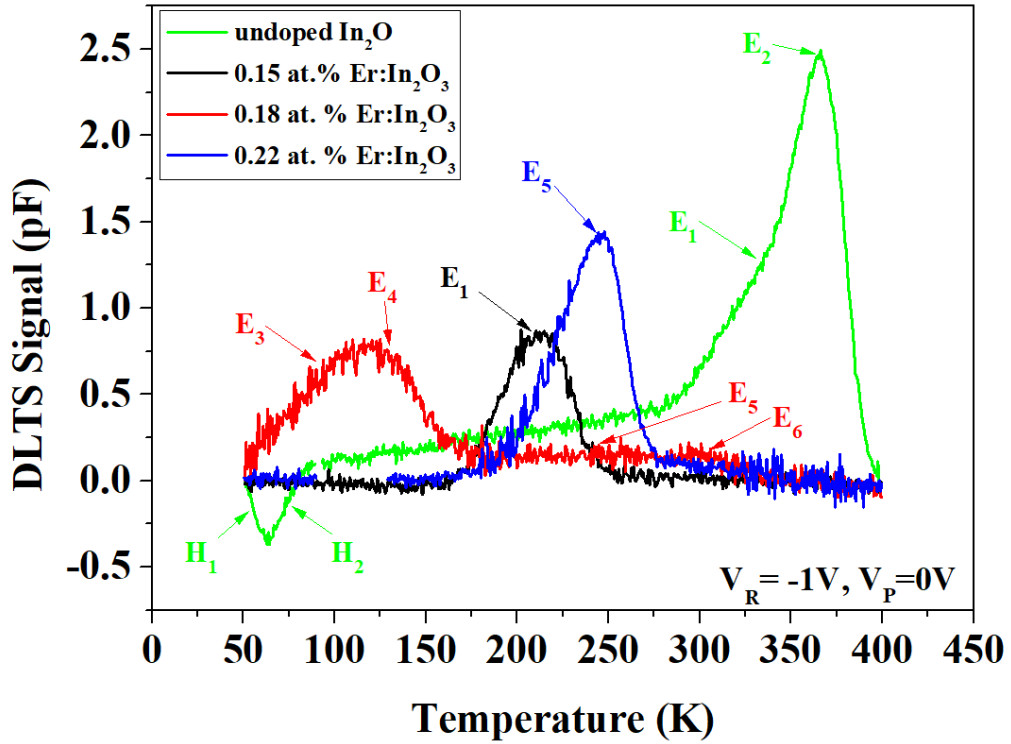


Fig. 9.8: DLTS spectra for undoped In_2O_3 , 0.15 at.% $\text{Er}:\text{In}_2\text{O}_3$, 0.18 at.% $\text{Er}:\text{In}_2\text{O}_3$, and 0.22 at.% $\text{Er}:\text{In}_2\text{O}_3$ samples.

For the undoped In_2O_3 sample, Laplace DLTS measurements reveal two negative peaks which are minority shallow hole traps. The energies of these defect levels are $H_1 = 0.033 \pm 0.001$ and $H_2 = 0.008 \pm 0.001$ eV. Resolving the broad positive peak reveals two electron defects, namely $E_1 = 0.238 \pm 0.008$ and $E_2 = 0.50 \pm 0.01$ eV. However, in sample 0.15 at.% $\text{Er}:\text{In}_2\text{O}_3$, only one defect, $E_1 = 0.204 \pm 0.001$ eV, could be detected. In sample 0.18 at.% $\text{Er}:\text{In}_2\text{O}_3$, two shallow defects, $E_3 = 0.011 \pm 0.001$ and $E_4 = 0.028 \pm 0.001$ eV, and two deep level defects, $E_5 = 0.111 \pm 0.004$ and $E_6 = 0.39 \pm 0.03$ eV, have been observed. Finally, only one defect, $E_5 = 0.09 \pm 0.004$ eV, has been detected in sample 0.22 at.% $\text{Er}:\text{In}_2\text{O}_3$. The activation energies of all these defects were calculated from Arrhenius plots shown in Fig. 9.9, which are obtained from Laplace DLTS measurements. All defects parameters are summarised in Table 9.2.

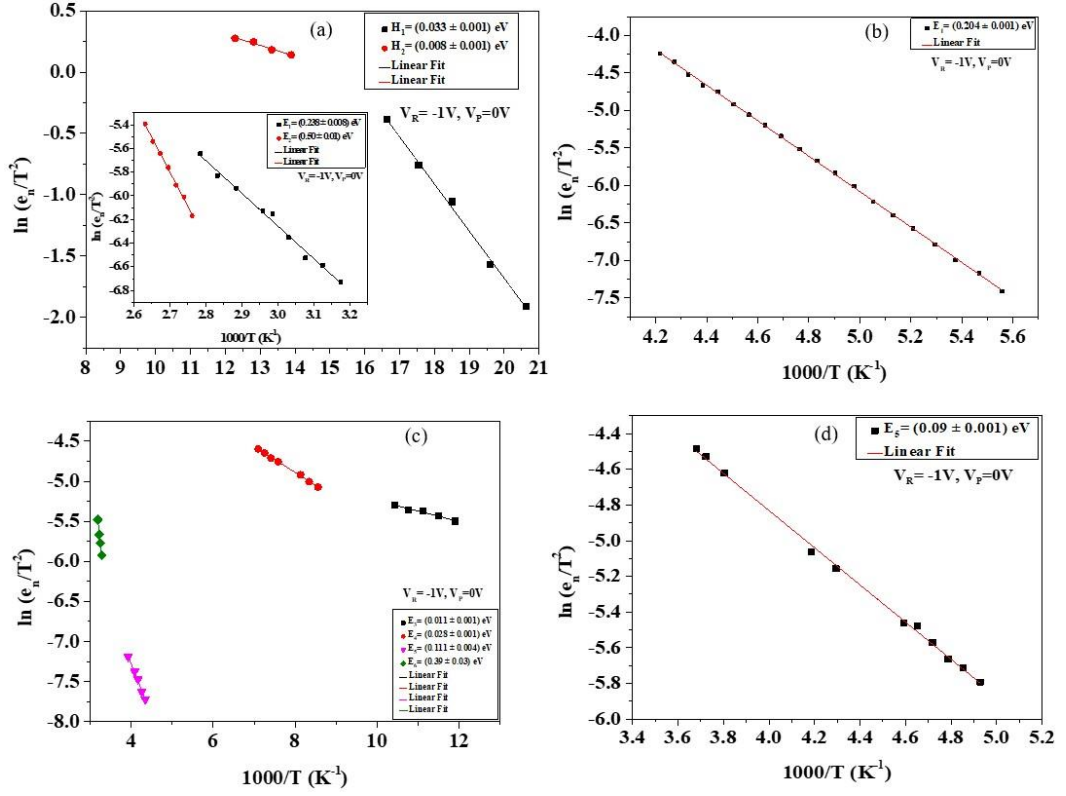


Fig. 9.9: Arrhenius plots from Laplace DLTS measurements for (a) undoped In₂O₃, (b) 0.15 at.% Er:In₂O₃, (c) 0.18 at.% Er:In₂O₃ and (d) 0.22 at.% Er:In₂O₃ samples. The inset of (a) shows the Arrhenius plots of E₁ and E₂.

Table 9.2: Traps parameters for undoped In₂O₃, 0.15 at.% Er:In₂O₃, 0.18 at.% Er:In₂O₃, and 0.22 at.% Er:In₂O₃ samples at $V_R = -1V, V_P = 0V$ and $t_P = 1$ msec.

Sample	Trap	Activation Energy (eV)	Capture Cross-Section (σ_∞) (cm ²)	Trap Concentration (cm ⁻³)
Undoped In ₂ O ₃	H ₁	0.033 ± 0.001	4.15 x 10 ⁻¹⁹	2.43x 10 ¹⁵
	H ₂	0.008 ± 0.001	3.99 x 10 ⁻²¹	4.38 x 10 ¹⁵
	E ₁	0.238 ± 0.008	7.76 x 10 ⁻²¹	3.01 x 10 ¹⁵
	E ₂	0.50 ± 0.01	2.07 x 10 ⁻¹⁷	5.03 x 10 ¹⁵
0.15 at.% Er:In ₂ O ₃	E ₁	0.204 ± 0.001	3.17 x 10 ⁻¹⁹	6.56 x 10 ¹⁴
0.18 at.% Er:In ₂ O ₃	E ₃	0.011 ± 0.001	2.00 x 10 ⁻²³	2.60 x 10 ¹⁴
	E ₄	0.028 ± 0.001	1.01 x 10 ⁻²²	3.19 x 10 ¹⁴
	E ₅	0.111 ± 0.004	1.22 x 10 ⁻²²	2.61 x 10 ¹³
0.18 at.% Er:In ₂ O ₃	E ₆	0.39 ± 0.03	7.80 x 10 ⁻¹⁸	3.74 x 10 ¹³
	E ₅	0.09 ± 0.001	5.27 x 10 ⁻²²	2.04 x 10 ¹⁴

P. Reunchan et al. [34] in their study of electronic and structural properties of oxygen and indium vacancies in In_2O_3 by first-principles calculations which are based on density functional theory (DFT) have observed a defect level at 0.2 eV and attributed it to an oxygen vacancy. This defect could be the same as defect E_1 observed in our study and hence the origin of the E_1 could be allocated to an oxygen vacancy. However, in another study of intrinsic point defects in indium oxide also using first-principles calculations and DFT, P. Angoston et al. [35] have assigned a point defect with an energy of 0.49 eV to be due to indium interstitial. Therefore, indium interstitial could be the origin of defect E_2 in our study as it has an energy similar to that observed by P. Angoston et al. Tomita et al. have studied the origin of n-type conductivity in undoped In_2O_3 and found that the oxygen vacancies are deep levels and hence cannot act as native donors. However, indium interstitials can form shallow donor levels which act as native donors [36]. Therefore, the origin of E_3 and E_4 in our study could be allocated to indium interstitials as they are shallow levels. R. Weiher in his investigation of electrical properties of single crystals of indium oxide has found a defect with an energy of 0.093 eV [37]. This defect is in a good agreement with the defect of 0.1 eV found by Tomita et al. which was assigned to a complex of oxygen vacancy-indium interstitial [36]. Thus, it is possible to assign defect E_5 , detected in 0.18 at.% Er: In_2O_3 and 0.22 at.% Er: In_2O_3 samples, to complex point defects of oxygen vacancy-indium interstitial. In our study, two shallow acceptors (hole traps), namely H_1 and H_2 , levels have been detected in the undoped In_2O_3 . According to Tomita et al., only indium vacancies can form shallow acceptor levels and hence H_1 and H_2 could be due to indium vacancies [36]. It is worth mentioning that Er doping leads to a reduction of oxygen related defects present in the In_2O_3 host lattice as confirmed by DLTS and Laplace

CHAPTER 9

DLTS measurements. In particular, sample 0.15 at.% Er:In₂O₃ has only one defect where four defects have been detected in the undoped sample. Although, the defect remaining (E₁) in sample 0.15 at.% Er:In₂O₃ is an oxygen vacancy but its concentration ($6.56 \times 10^{14} \text{ cm}^{-3}$) has been reduced by a factor of five when compared to the same defect in the undoped sample ($3.01 \times 10^{15} \text{ cm}^{-3}$). However, the capture cross-section is $3.17 \times 10^{-19} \text{ cm}^2$ in sample 0.15 at.% Er:In₂O₃ which higher than its value in the undoped sample ($7.76 \times 10^{-21} \text{ cm}^2$).

The process of trapping and de-trapping of carriers in a Schottky diode happens in the depletion region, which is in the semiconductor side. In order to control the depletion region width (moving it away or close to the interface between the metal and semiconductor), DLTS measurements at different reverse biases were performed. Sample 0.15 at.% Er:In₂O₃ has been selected for DLTS measurement at $V_R = -4\text{V}$. The filling pulse height, $V_P = 0\text{V}$ and the filling pulse time, $t_P = 1 \text{ msec}$, were kept the same for all measurements. Fig. 9.10 (a) depicts the DLTS spectra for sample 0.15 at.% Er:In₂O₃ measured at two different reverse biases, $V_R = -1$ and -4 V . As illustrated in Fig. 9.10 (a), the peaks at $V_R = -1$ and $V_R = -4 \text{ V}$ occur at the same temperature, but the peak at $V_R = -4 \text{ V}$ has higher amplitude, meaning that the concentration of this trap is not uniform and it is higher away from the interface. Laplace DLTS measurement has been carried out at $V_R = -4 \text{ V}$ and only one defect has been detected. Fig. 9.10 (b) shows the Arrhenius plot obtained from Laplace DLTS for $V_R = -4 \text{ V}$.

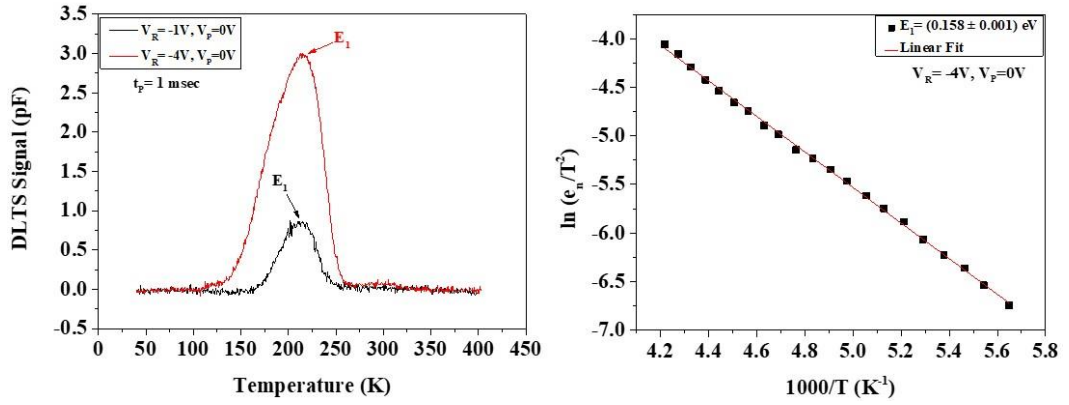


Fig. 9.10: (a) DLTS spectra for sample 0.15 at.% Er:In₂O₃ measured at two different reverse biases (b) Arrhenius plot obtained from Laplace DLTS measurement at $V_R = -4V$ for sample 0.15 at.% Er:In₂O₃.

Table 9.3 shows the trap parameters for $V_R = -1$ and -4 V. The capture cross-section of the trap at $V_R = -4$ V is $3.86 \times 10^{-20} \text{ cm}^2$ whereas it is higher ($3.17 \times 10^{-19} \text{ cm}^2$) at $V_R = -1$ V. However, the concentration of the trap detected at $V_R = -4$ V is $\sim 1.73 \times 10^{15} \text{ cm}^{-3}$ which is higher than its concentration ($6.56 \times 10^{14} \text{ cm}^{-3}$) at $V_R = -1$ V. This result confirms that the higher amplitude of DLTS signal means higher concentration and indicates that the trap is more concentrated away from the interface of the junction.

Table 9.3: Traps parameters for 0.15 at.% Er:In₂O₃ sample at $V_R = -1$ and -4 V, $V_P = 0V$ and $t_P = 1$ msec.

Reverse bias (V)	Trap	Activation Energy (eV)	Capture Cross-Section (σ_∞) (cm ²)	Trap Concentration (cm ⁻³)
-1	E ₁	0.204 ± 0.001	3.17×10^{-19}	6.56×10^{14}
-4	E ₁	0.158 ± 0.001	3.86×10^{-20}	1.73×10^{15}

It is worth mentioning that an increase of the bandgap with Er content has been confirmed by our collaborators using optical absorption measurements [2]. The bandgap increased from 3.53 eV for undoped samples to 3.77, 3.80 and 3.83 eV for 0.15, 0.18 and 0.22 at.% Er doped TFs, respectively. This enhancement of the bandgap has been assigned to the removal of oxygen related deep level defects as a result of increasing Er doping which may occupy the defects sites and contribute to their neutralization by forming In-O-Er compound material [2]. The suggestion of removing oxygen related defect by our collaborators [2] was confirmed here by DLTS measurements. However, in our study, sample 0.15 at.% Er:In₂O₃, the less doped sample, is found to have the best electrical properties and the lowest number of defects whereas our collaborators have found that the highest doped sample, 0.22 at.% Er:In₂O₃, has the better optical properties.

9.3 CONCLUSION

The electrically active defects in undoped In₂O₃ and Er doped In₂O₃ thin films (TFs) grown by spin-on technique have been investigated. The atomic fraction of Er in the doped films was estimated to be 0.15, 0.18 and 0.22 at. % for the 0.01 g, 0.02 g and 0.04 g Er₂O₃ containing TFs. At room temperature, sample 0.15 at.% Er:In₂O₃ has the lowest leakage current whereas the undoped sample has the highest leakage current. The highest value of leakage current in the undoped In₂O₃ may indicate the presence of more defects as compared to sample 0.15 at.% Er:In₂O₃. It was found that as Er content increases both the leakage current and the ideality factor increase, and the barrier height decreases. DLTS and Laplace DLTS show that the undoped In₂O₃ has four defects while only one defect could be detected in sample 0.15 at.% Er:In₂O₃ and this confirms the reduction of oxygen

CHAPTER 9

related defect as a result of incorporating Er. Due to the lower leakage current, lower values of ideality factor and higher values of barrier height and less number of defects in sample 0.15 at.% Er:In₂O₃, it is concluded that sample 0.15 at.% Er:In₂O₃, the less doped sample, has the best electrical properties among all other samples investigated in this work. It is also worth mentioning that the removal of oxygen related defects and the improvement of the electrical properties of the doped samples, specially sample 0.15 at.% Er:In₂O₃, would enhance the sensitivity of UV detectors for Er doped samples as compared to the undoped In₂O₃ samples.

REFERENCES

1. Ellmer, K., *Past achievements and future challenges in the development of optically transparent electrodes*. Nature Photonics, 2012. **6**(12): p. 809.
2. Ghosh, A., et al., *Removal of oxygen related defects from chemically synthesized In₂O₃ thin film doped with Er by spin-on technique*. Journal of Alloys and Compounds, 2017. **695**: p. 1260-1265.
3. Hamberg, I., et al., *Band-gap widening in heavily Sn-doped In₂O₃*. physical Review B, 1984. **30**(6): p. 3240.
4. Ghosh, A., et al., *Detailed investigation of defect states in Erbium doped In₂O₃ thin films*. Materials Research Bulletin, 2018. **99**: p. 211-218.
5. Ko, T.-S., et al., *Tunable light emissions from thermally evaporated In₂O₃ nanostructures grown at different growth temperatures*. Journal of crystal growth, 2008. **310**(7-9): p. 2264-2267.
6. Kim, H.S., et al., *High performance solution-processed indium oxide thin-film transistors*. Journal of the American Chemical Society, 2008. **130**(38): p. 12580-12581.
7. Li, C., et al., *In₂O₃ nanowires as chemical sensors*. Applied Physics Letters, 2003. **82**(10): p. 1613-1615.
8. Granqvist, C.G. and A. Hultåker, *Transparent and conducting ITO films: new developments and applications*. Thin solid films, 2002. **411**(1): p. 1-5.
9. Murali, A., et al., *Synthesis and characterization of indium oxide nanoparticles*. Nano Letters, 2001. **1**(6): p. 287-289.
10. Sze, S.M. and K.K. Ng, *Physics of semiconductor devices*. 2006: John wiley & sons.

11. Sang, L., M. Liao, and M. Sumiya, *A comprehensive review of semiconductor ultraviolet photodetectors: from thin film to one-dimensional nanostructures*. *Sensors*, 2013. **13**(8): p. 10482-10518.
12. Bertuccio, G., et al., *Silicon carbide detector for laser-generated plasma radiation*. *Applied Surface Science*, 2013. **272**: p. 128-131.
13. Yu, J., et al., *Enhanced responsivity of photodetectors realized via impact ionization*. *Sensors*, 2012. **12**(2): p. 1280-1287.
14. Mondal, A., et al., *Structural and optical properties of glancing angle deposited In₂O₃ columnar arrays and Si/In₂O₃ photodetector*. *Applied Physics A*, 2014. **115**(1): p. 353-358.
15. Tiwari, A., et al., *Improved Photo-Detection Using Zigzag TiO₂ Nanostructures as an Active Medium*. *Journal of nanoscience and nanotechnology*, 2015. **15**(7): p. 5099-5104.
16. Li, D., et al., *Realization of a high-performance GaN UV detector by nanoplasmonic enhancement*. *Advanced Materials*, 2012. **24**(6): p. 845-849.
17. Shi, L. and S. Nihtianov, *Comparative study of silicon-based ultraviolet photodetectors*. *IEEE Sensors Journal*, 2012. **12**(7): p. 2453-2459.
18. Liao, M., et al., *Comprehensive investigation of single crystal diamond deep-ultraviolet detectors*. *Japanese Journal of Applied Physics*, 2012. **51**(9R): p. 090115.
19. Lahiri, R., et al., *Performance of Erbium-doped TiO₂ thin film grown by physical vapor deposition technique*. *Applied Physics A*, 2017. **123**(9): p. 573.

CHAPTER 9

20. Morgan, B.J. and G.W. Watson, *Polaronic trapping of electrons and holes by native defects in anatase TiO₂*. Physical Review B, 2009. **80**(23): p. 233102.
21. Tung, R., J. Sullivan, and F. Schrey, *On the inhomogeneity of Schottky barriers*. Materials Science and Engineering: B, 1992. **14**(3): p. 266-280.
22. Sze, S.M. and M.K. Lee, *Semiconductor devices : physics and technology*. 2013, Singapore: Wiley.
23. Bong, J., et al., *Fabrication of Highly Transparent Nanowire Transistors with One-Step-Processed Graphene Gate–Source–Drain Electrodes*. Applied Physics Express, 2013. **6**(5): p. 055103.
24. Werner, J.H., *Schottky barrier and pn-junction I/V plots—Small signal evaluation*. Applied Physics A: Materials Science & Processing, 1988. **47**(3): p. 291-300.
25. Devi, V.L., et al., *Schottky barrier parameters and interfacial reactions of rapidly annealed Au/Cu bilayer metal scheme on n-type InP*. Open Applied Physics Journal, 2012. **5**(1).
26. Jameel, D., et al., *High-performance organic/inorganic hybrid heterojunction based on Gallium Arsenide (GaAs) substrates and a conjugated polymer*. Applied Surface Science, 2015. **357**: p. 2189-2197.
27. Korucu, D., et al., *Evaluation of lateral barrier height of inhomogeneous photolithography-fabricated Au/n-GaAs Schottky barrier diodes from 80 K to 320 K*. Materials Science in Semiconductor Processing, 2012. **15**(5): p. 480-485.

CHAPTER 9

28. Chand, S. and J. Kumar, *Evidence for the double distribution of barrier heights in Schottky diodes from I-V-T measurements*. Semiconductor science and technology, 1996. **11**(8): p. 1203.
29. Al mashary, F.S., et al., *Effect of growth techniques on the structural, optical and electrical properties of indium doped TiO₂ thin films*. Journal of Alloys and Compounds, 2018. **766**: p. 194-203.
30. Van, C.N. and K. Potje-Kamloth, *Electrical and NO_x gas sensing properties of metallophthalocyanine-doped polypyrrole/silicon heterojunctions*. Thin Solid Films, 2001. **392**(1): p. 113-121.
31. Jameel, D., et al., *Electrical performance of conducting polymer (SPAN) grown on GaAs with different substrate orientations*. Applied Surface Science, 2016. **387**: p. 228-236.
32. Aydoğan, Ş., M. Sağlam, and A. Türüt, *On the barrier inhomogeneities of polyaniline/p-Si/Al structure at low temperature*. Applied surface science, 2005. **250**(1): p. 43-49.
33. Dobaczewski, L., A. Peaker, and K. Bonde Nielsen, *Laplace-transform deep-level spectroscopy: The technique and its applications to the study of point defects in semiconductors*. Journal of Applied Physics, 2004. **96**(9): p. 4689-4728.
34. Reunchan, P., et al., *Vacancy defects in indium oxide: An ab-initio study*. Current Applied Physics, 2011. **11**(3): p. S296-S300.
35. Ágoston, P., et al., *Geometry, electronic structure and thermodynamic stability of intrinsic point defects in indium oxide*. Journal of Physics: Condensed Matter, 2009. **21**(45): p. 455801.

CHAPTER 9

36. Tomita, T., et al., *The origin of n-type conductivity in undoped In₂O₃*. Applied Physics Letters, 2005. **87**(5): p. 051911.
37. Weiher, R., *Electrical properties of single crystals of indium oxide*. Journal of Applied Physics, 1962. **33**(9): p. 2834-2839.

CONCLUSION AND FUTURE WORK

In this chapter, an overall summary of the work carried out in this thesis is presented. Doped transparent conductive oxides (TCO) thin semiconductor films (i.e. TiO_2 and In_2O_3) have been investigated. Specifically, this thesis dealt with In-doped TiO_2 grown on Si substrates by different growth techniques, namely PLD and sputtering, In-doped TiO_2 grown by PLD on low and high index GaAs substrates, Er doped TiO_2 and Er doped In_2O_3 both grown by a combination of an easy sol-gel process and spin coating method. The main objective of this work was to investigate the electrically active defects. The electrical properties of the samples were investigated using DLTS, Laplace DLTS, I-V and C-V. Moreover, suggestions for future characterizations based on the work accomplished in this thesis are discussed.

10.1 CONCLUSION

10.1.1 INDIUM DOPED TiO_2 THIN FILMS GROWN BY PLD AND SPUTTERING TECHNIQUES ON SILICON SUBSTRATES

TiO_2 thin films were synthesised by two different techniques, namely PLD and sputtering, followed by thermally evaporating deposition of layers of indium (50 nm thick) on top of the TiO_2 surface of each sample. Then the indium was incorporated into the TiO_2 lattice by using a rapid thermal annealing (RTA) process, both samples were annealed under a flow of oxygen with a temperature ramp rate of $15^\circ\text{C}/\text{minute}$ and a dwelling temperature of 500°C for 30 minutes. The aim was to investigate the effect of the growth techniques on the electrical,

optical and structural properties of In-doped TiO₂ thin films. XRD measurements revealed the coexistence of anatase and rutile phases of TiO₂ in the sample grown by sputtering technique whereas only rutile phase has been observed in PLD sample. The presence of mixed phases in the sputtered sample may contribute to forming more defects in the sputtered sample as compared to the PLD sample. Furthermore, an In₂O₃ phase has been observed in both sputtered and PLD samples. As confirmed by XRD results, the In₂O₃ phase is more dominant in the sputtered sample than in the PLD sample. The existence of this phase could be due to the high thickness of indium (50 nm). The I-V characteristics showed that the sputtered sample have higher reverse current when compared to those of PLD sample, which may indicate the presence of more defects in the sputtered sample than the PLD sample. In particular, at room temperature the reverse bias leakage current at – 4 V for sputtered and PLD samples are 5.9×10^{-7} A and 1.3×10^{-7} A, respectively. Additionally, the PLD sample has lower ideality factor and higher barrier height values than those of the sputtered sample, indicating the PLD sample has better electrical properties. C-V measurements showed that the sputtered sample has higher capacitance than the PLD sample and this could be due to shallow ionised impurity levels. Moreover, the PLD sample displayed a uniform doping concentration as compared with the sputtered sample. The PL characterization of both samples has shown well resolved PL bands in the PLD sample and a broad PL band in the sputtered sample. This finding demonstrates that the quality of PLD sample is higher than that of the sputtered sample. Finally, the DLTS and Laplace DLTS measurements have detected five defects and only one defect in the sputtered and PLD samples, respectively. All the above findings strongly suggest that the

PLD technique is better than sputtering technique for the growth of In-doped TiO₂ thin films.

10.1.2 INDIUM DOPED TiO₂ THIN FILMS GROWN BY PLD TECHNIQUE ON LOW AND HIGH INDEX GaAs PLANES

In-doped TiO₂ has been grown by PLD technique on low and high index GaAs planes, namely (100) and (311)B, using the same growth and characterisation procedures explained in section 5.1.1 of Chapter 5. The thicknesses of the thermally evaporated indium were 5 and 15 nm. Hence, four samples with different content of indium grown on (100) and (311)B GaAs substrates, labelled as 15 (100), 5 (100), 15 (311)B and 5 (311)B were investigated. The motivation was to study the effect of the orientation of the GaAs substrates on the optical and electrical properties of In-doped TiO₂ thin films. The I-V characteristics showed that sample 15 (311)B has the lowest reverse current while sample 15 (100) has the highest reverse current when compared to all doped samples. However, sample 5 (311)B has the lowest ideality factor and the highest barrier height values as compared to all doped samples. It was important here to investigate the control samples (undoped samples), labelled as (100) and (311)B, in order to understand the effect of indium on the electrical properties of TiO₂. The investigation of the control samples has shown that the electrical properties of samples grown on (100) were adversely affected by adding indium. In particular, sample (100) has lower reverse current, lower ideality factor and higher barrier height as compared to the doped samples, i.e. 5 (100) and 15 (100) samples. In contrast, the electrical properties of samples grown on (311)B substrates have been enhanced by indium doping. By using DLTS and Laplace DLTS measurements, very shallow defects have been

CHAPTER 10

detected on all samples. In particular, three defects have been observed in sample 15 (311)B whereas two defects have been detected in all other samples. PL measurements have shown emissions in visible and infrared regions for all doped samples. XRD characteristics have revealed that both anatase and rutile phases of TiO_2 are present in the low doped samples, i.e. sample 5 (100) and 5 (311)B, whereas only a single-phase rutile was observed in the high doped samples, i.e. sample 15 (100) and 15 (311)B. Both XRD and PL measurements have shown that the samples grown on (311)B planes have better crystallographic properties when compared with samples grown on the conventional plane (100). The absorption measurements have shown that sample 15 (311)B has the lowest emission energy of 2.94 eV as compared to 3.39, 3.34 and 3.40 eV for sample 5 (100), 5 (311)B and 15 (100), respectively. This red-shift emission observed in sample 15 (311)B was attributed to the presence of more shallow donor defects as compared to the other samples. As there is no significant difference in the electrical properties of all samples, it could be concluded that sample 15 (311)B is the best among all other samples investigated in this work because its absorption energy has the largest red-shift, meaning that it is a more suitable material for solar cells with enhanced efficiency.

10.1.3 ERBIUM DOPED TiO₂ THIN FILMS GROWN BY A COMBINATION OF AN EASY SOL-GEL PROCESS AND SPIN COATING METHOD

Undoped TiO₂ and Er-doped TiO₂ thin films were grown on silicon substrates using a sol-gel technique followed by spin coating to investigate the effect of Er doping on the electrical properties, especially the electrically active defects. During the growth process, 0.04 g and 0.06 g Er₂O₃ nanopowder were mixed into two different TiO₂ solutions to obtain two samples of Er-doped TiO₂ with different Er contents. Both doped samples showed almost the same leakage current at room temperature, which was lower than the leakage current observed in the undoped sample. Moreover, the rectification ratio for the control undoped TiO₂ sample at the same voltage was found to be around 2 orders of magnitude lower than that for doped samples which evidences an improvement of the electrical properties of the doped samples as compared with the undoped sample. The high doped sample has higher barrier height and lower ideality factor values as compared to the low doped sample which suggest better electrical properties of the high doped sample when compared with the low doped sample. In addition, the undoped sample has the highest capacitance which could be due to the presence of more shallow ionised impurity levels in the undoped sample than in the doped samples. The investigation of the electrically active defects using DLTS technique showed five defects in the undoped sample whereas three and one defects have been observed in the low and high doped samples, respectively. The removal of oxygen related defects due to Er doping has been confirmed by DLTS technique. It was found that Er doping of TiO₂ not only improved the electrical properties of the

devices but resulted in the eliminating of oxygen related defects as confirmed by DLTS. Therefore an enhancement of the sensitivity of UV detectors is expected.

10.1.4 ERBIUM DOPED In_2O_3 THIN FILMS GROWN BY SPIN-ON TECHNIQUE

In_2O_3 and Er-doped In_2O_3 (Er: In_2O_3) thin films were deposited on silicon substrates by spin-on technique. The effect of Er doping on the electrical properties of In_2O_3 thin films has been investigated. Three Er-doped samples have been grown with different content of Er and the Er atomic fraction in the doped films was estimated to be 0.15, 0.18 and 0.22 at. % for the 0.01 g, 0.02 g and 0.04 g Er_2O_3 containing TFs. The I-V measurements at room temperature showed that the undoped In_2O_3 sample has the highest reverse current when compared to the doped samples which may indicate the presence of more defects in the undoped sample as compared with the doped samples. It is worth mentioning that the less doped sample, 0.15 at.% Er: In_2O_3 , has the lowest reverse current. It was found that this leakage current increased as the Er content increased. Additionally, the low doped sample has the lowest ideality factor and highest barrier height values which may indicate better electrical properties than the higher doped samples. C-V measurements revealed that the undoped sample has the highest capacitance which could be due to shallow ionised impurity levels present in the undoped sample.

DLTS measurements were performed in order to provide evidence of a reduction of oxygen related defects as a result of Er doping. Four defects have been detected in the undoped sample while only one defect has been observed in the lowest and highest doped samples, namely 0.15 at.% Er: In_2O_3 and 0.22 at.% Er: In_2O_3 . However, in 0.18 at.% Er: In_2O_3 sample, four defects were detected. It was

observed that Er doping of In_2O_3 thin films led to the removal of oxygen related defects as confirmed by DLTS measurements. However, it was found that the lowest Er-doped sample (0.15 at.% Er: In_2O_3) showed better electrical properties than the higher doped samples (0.18 and 0.22 at.% Er: In_2O_3). Therefore, one could conclude that the content of Er is critical for the achievement of optimal device quality. In general, the removal of oxygen related defects and the improvement of the electrical properties of In_2O_3 using Er doping especially sample 0.15 at.% Er: In_2O_3 , would enhance the sensitivity of UV detectors.

10.2 SUGGESTIONS FOR FUTURE WORK

Suggestions for further work based on the results obtained from this thesis are discussed in the following:

- Reducing the indium content in the In-doped TiO_2 thin film grown on silicon substrates by PLD and sputtering could lead to a removal of the In_2O_3 phase. Hence a clearer picture of the effect of the growth techniques could be obtained.
- Use Molecular Beam Epitaxy (MBE) which is a material fabrication process used to produce high-purity nano-scale materials.
- The parameters of the annealing process which has been used to incorporate the indium into the TiO_2 host lattice could be varied to reach better electrical properties, especially for the samples grown on GaAs substrates as they generally have high reverse currents.

- Different annealing processes can be used, e.g. Furnace annealing, that may improve the electrical properties of In-doped TiO₂ samples grown on GaAs substrates.
- The content of Er in Er-doped In₂O₃ samples is critical as the lowest doped sample (0.15 at.% Er:In₂O₃) showed better electrical properties. Hence, lower content of Er (lower than 0.15 %) could be used to achieve devices with better electrical properties.